RECONSTRUCTING SPATIALLY HETEROGENEOUS THERMAL MAPS USING LIGHT-BASED METROLOGY SENSORS

Ainsley Miller

Department of Electronic and Electrical Engineering

University of Strathclyde

A thesis submitted for the degree of

Doctor of Philosophy

2019

Copyright Declaration

This thesis is submitted to the University of Strathclyde for the degree of Doctor of Philosophy in the Faculty of Engineering

This thesis is the result of the author's original research. It has been composed by the author and has not been previously submitted for examination which has led to the award of a degree.

Date:

Signed: Ainsley Miller

In loving memory of Gran Janice and Auntie Eileen.

I know that you would both be so proud of me.

Acknowledgements

I would like to express my sincere gratitude to my supervisors Anthony Mulholland, Gareth Pierce, Ben Hughes and Alistair Forbes. In particular I would like to thank Anthony Mulholland for his patience guidance and support throughout the PhD programme, I definitely would not have got to this stage without you. I would also like to extend my thanks to Katy Tant for her support and guidance throughout. I would also like to thank the National Physical Laboratory for providing me with my PhD studentship.

I would also like to thank my colleagues in the Department of Mathematics and Statistics and the Centre for Ultrasonic Engineering. In particular, a special thank you to Marcus Ingram for keeping me motivated throughout the PhD process, and to Russell Niven for his patience, support and friendship throughout this process.

Lastly, I would like to thank my parents for supporting me throughout my PhD studies. If it was not for them encouraging me to be the first in my family to go to university, then this thesis would not exist.

Abstract

Modern manufacturing increasingly utilises automated systems for component positioning and assembly. Industries are interested in autonomous manufacturing as it can reduce costs and increase productivity. A vital aspect of autonomous precision manufacturing is large volume metrology. One popular approach to large volume or large scale metrology involves using light rays which travel through the air to calculate the position of an object of interest. Optical-based metrology systems like photogrammetry and laser trackers are crucial in improving the accuracy and quality associated with robotic assembly. In an industrial setting these positional measurements are subject to uncertainties which can in many instances be greater than the required tolerances. One source of uncertainty that arises when considering large scale industrial settings is light refraction (bending of the light ray path) due to temperature fluctuations in the air. This thesis will report on the recent work in using light-based sensor data to reconstruct the heterogeneous spatial map of the refractive index in the air. This is then used to discount the refractive effects and thereby reduce the uncertainty of this positioning problem.

The finite element model software COMSOL Multiphysics was used to simulate light ray paths in complex, two dimensional, spatially varying temperature fields. These simulations provided a sense of the typical measurement uncertainties associated with deploying photogrammetry sensors in environments with spatially heterogeneous temperature distributions. Following this, physical experiments were carried out to assess the sensitivity of the Vicon T160 Photogrammetry system.

Later chapters look at solving the inverse problem using Voronoi tessellations to spatially parameterise the refractive index map. A Bayesian approach, namely the reversible jump Markov Chain Monte Carlo method (rj-MCMC), is then used as the optimisation method in the inversion. Using the recovered refractive index map led to improvements in discounting the refractive effects by up to 54 % and the uncertainty of this positioning problem was reduced by up to 89 %. Following this, a second method was employed to reduce computational times, improve the sensitivity of the objective function and further reduce the positioning errors of the photogrammetry system. Using this second method, errors in this positioning problem were reduced by up 67 % and the uncertainty was also reduced by up to 89 %.

Contents

Contents **vi**

1 Background **1**

1.1 Robotics and Manufacturing . . . 2
1.2 Metrology . . . 4
1.3 Optical based Metrology Systems . . . 6
    1.3.1 Laser Tracking . . . 6
    1.3.2 Photogrammetry . . . 8
1.4 Refraction Effects in Large Volume Metrology . . . 12
1.5 Refractive Index Modelling . . . 14
1.6 Techniques for Recovering a Spatial Map of the Refractive Index . 18
1.7 Inverse Problems . . . 21
1.8 Parametrisation of the Spatial Domain . . . 22
1.9 Mathematical Modelling of Light Rays in Heterogeneous Media . 23
1.10 Optimisation . . . 29
1.11 Use of rj-MCMC in Inverse Problems . . . 32
1.12 Outline of Thesis . . . 33

1.13 Publications Arising from this Thesis 35

2 Mathematical Modelling of Light Rays in Heterogeneous Media 36

2.1 Positional Errors Associated with Light-based Sensors 37

2.2 Modelling of Light Rays in Heterogeneous Media 39

2.2.1 Ray Tracing Using Finite Elements 46

2.2.2 Test Cases 50

2.2.3 Results of COMSOL Simulations 51

2.3 Chapter Summary 56

3 An Experimental Investigation into the Effects of a Localised Heat Source on Photogrammetry Measurement Errors 58

3.1 Experimental Setup 59

3.2 Experiment 1 63

3.3 Experiment 2 66

3.4 Experiment 3 68

3.5 Conclusions and Limitations of the Experiment 69

3.6 Discussion 71

3.7 Conclusions 78

4 The Inverse Problem of Reconstructing Refractive Index Maps from Photogrammetry Data 82

4.1 Parametrisation of The Refractive Index Map 83

4.2 Modelling the Light Ray Propagation in a Heterogeneous Refractive Index Map 84

4.2.1 The Fast Marching Method 86
4.3 Objective function between the Modelled and Measured Data . . 87
4.4 Recovery of the Refractive Index Map via a Bayesian Approach . 92
4.5 Quantifying the Measurement Uncertainty 96
4.6 Generation of Simulated Data 99
4.7 Numerical Experiment A 101
4.7.1 Discussion of the optimal method to calculate the estimate of the initial ray-angle from the FMM 107
4.7.2 Investigation into perturbing the initial refractive index index map to assess the sensitivity of the objective function 114
4.7.3 Numerical Experiment A: The Inversion Process 116
4.7.4 Numerical Experiment A: Results 118
4.8 Numerical Experiment B 131
4.9 Numerical Experiment C 139
4.10 Numerical Experiment D 145
4.11 Chapter Summary 153

5 Using Time Fields to Reconstruct Refractive Index Maps from Photogrammetry Data 157

5.1 Using the Time Field to Trace the Ray-paths 157
5.2 Numerical Experiment A 169
5.3 Numerical Experiment B 178
5.4 Numerical Experiment C 186
5.5 Numerical Experiment D 192

5.6 Chapter Summary 196

6 Conclusions and Future Work **201**

6.1 Final Conclusions 201

6.2 Future Work 206

References **208**

List of Symbols

a Index of the laser tracker

b Ray length between camera c_k and reflector r_i

$\bar{c}$ Velocity of the homogeneous domain

c_k Camera, where $i = k \ldots C$

c_∞ Speed of light in a vacuum

$d_{a,i}$ Distance from the laser tracker, l_a to the reflector r_i

$\mathbf{d}Q$ Small displacement along the ray

f Focal length of the camera

j Realisation index of the model $m^{(j)}$

m^* True refractive index map

$\hat{m}$ Recovered refractive index map

m^h Homogeneous refractive index map

$m^{(j)}$ Map realisation at iteration j

$m^{(j+1)}$ Map realisation at iteration $j+1$

n Side length of the square cluster of pixels

p Number of pixels along $\beta_{k,i}$

$p(m^{(j)})$ Prior knowledge of the model $m^{(j)}$

$p(m^{(0)})$ Initial prior probability density function

$p\left(\theta^*_{k,i} \mid m^{(j)}\right)$ Likelihood of observing the true data given model $m^{(j)}$

$p\left(m^{(j)} \mid \theta^*_{k,i}\right)$ Posterior distribution which describes the probability of $m^{(j)}$ being the refractive index map m^* given the data $\theta^*_{k,i}$

q Gradient between each adjacent point

r_i Reflector, where $i = 1 \ldots R$

$\hat{r}_l$ Estimated position of reflector when laser tracker is used

$\hat{r}_c$ Estimated position of reflector when the photogrammetry system is used

s^* Co-ordinates of an object of known position in the domain e.g. a retroreflector mimicking a robot

$\bar{s}^*$ New centroid position of reflector s^* when an additional pixel is added

$\hat{s}_h$ Estimated position of s^* when the domain is assumed to be homogeneous

$\hat{s}_\alpha$ Estimated position of s^* when the domain is the recovered refractive index map

$\hat{s}^*$ An estimate of the object of known position in the known refractive index index map domain, e.g. a retro-reflector mimicking a robot

$\hat{s}$ Estimated position of s^* in an experimental setting

t Time taken for light ray to reach a point $\mathbf{p}$

t_i^h Times of arrival (on the discretised grid used by the FMM) of the spherical wave from c_k on the line $\beta_{k,i}$ when the refractive index map is homogeneous

$t_i^{(j)}$ Times of arrival at iteration j of the inversion process (when the material is heterogeneous).

$(t_{k,i})$ Time of arrival between the camera c_k and reflector r_i

$t(\tau_{(x,y)})$ Desired travel time field

u Arc-length of light ray

v Velocity

w Grid side length for Fast Marching Method

x Horizontal direction

x_i Initial horizontal component of the light ray

x_f Final horizontal component of the light ray

$\underline{x}_p^{(j)}$ Position of Voronoi cell seed p at realisation j

$\underline{x}_p^{(0)}$ Position of Voronoi cell seed p at realisation zero

$\underline{x}_p^*$ Position of Voronoi cell seed p of the known refractive index map m^*

y Vertical direction

z Depth component of (x, y, z) co-ordinates

$\mathbf{a}$ Amplitude of the wave

$\mathbf{k}$ Wave vector

$\mathbf{p}$ Position vector of the ray

A Total number of laser trackers

B Depth of the charged coupled device

C Total number of cameras

$D^-_{x,y}$ Standard backward finite difference operator

$D^+_{x,y}$ Standard forward finite difference operators

$F_{x,y}$ Speed at position $\tau_{x,y}$

$G_{x,y}$ Horizontal (x) or vertical (y) dimension of the sensor

k Range of refractive indices expressed as a percentage of the mean refractive index for the reconstructed refractive index map

L_x Domain length in the horizontal direction

L_y Domain length in the vertical direction

N_x Digitised sensor size in x (horizontal direction)

N_y Digitised sensor size in y (vertical direction)

N_{rays} Number of rays

P Number of Voronoi seeds

Q Length of the ray measured from a fixed point

$P^{(j)}$ Set of randomly chosen seeds of the Voronoi tessellation at iteration j

R Number of reflectors

S Optical path length

T Temperature of the ray at each point

$T(x, y)$ Temperature at point (x, y) in the domain, measured in Kelvin

$T_{\max}$ Maximum temperature in the domain, measured in Kelvin

$T_{\min}$ Minimum temperature in the domain, measured in Kelvin

V Number of pixels in horizontal direction of the recovered refractive index map image reconstruction

W Number of pixels in vertical direction of the recovered refractive index map image reconstruction

$\mathbf{E}$ Electric field

$\mathcal{C}$ Set of cameras in the mapping Φ

$\mathcal{L}$ Likelihood function

$\mathcal{R}$ The set of reflectors in the mapping Φ

$\mathcal{V}$ Variance

$\mathcal{V}_{imp}$ Percentage improvement of the uncertainty in the position of the object of interest when compared to the homogeneous case

$\mathcal{V}(\varepsilon_\alpha)$ Variance in the error of the position when the recovered refractive index map is used

$\mathcal{V}(\varepsilon_h)$ Variance in the error of the position when there is a homogeneous refractive index map

$\alpha_{(x,y)}$ Horizontal (x) and vertical (y) angular field of view

$\beta_{k,i}$ The line that lies perpendicular to the straight ray path between c_k and r_i

$\gamma^{(j)}$ Misfit at refractive index map realisation j

δ Percentage of points used to calculate the angles $\theta_{k,i}$ and θ_β

ϵ Perturbation factor to assess the sensitivity of the misfit function

ε_α Error in the position of an object at position s^* when the domain is the recovered refractive index map

ε_c^* Error in the estimated position of s^* when photogrammetry system is used

ε_h Error in position of an object at position s^* when the domain is assumed to be homogeneous

ε_{imp} Percentage improvement of the error in the position of the object of interest when compared to the homogeneous case

ε_l^* Error in the estimated position of s^* when laser tracker is used

ζ System noise parameter

$\zeta^{(j)}$ System noise parameter at realisation j

η Refractive index

$\eta(\mathbf{p})$ Refractive index at position $\mathbf{p}$

$\eta_p^{(0)}$ Refractive index in Voronoi cell p at realisation 0

$\eta_p^{(j)}$ Refractive index in Voronoi cell p at realisation j

η_p^* Refractive index in Voronoi cell p of known map

η_{range} Range of values which the refractive index can take

$\eta_{x,y}$ Refractive index at point (x, y)

$\theta_{k,i}$ Estimated angle from the camera c_k to the reflector r_i

$\theta_{k,i}^{(j)}$ Estimation of the angle from camera c_k to the reflector at iteration r_i at model realisation j

$\theta^h_{k,i}$ Straight ray angle between the camera c_k and the reflector r_i

$\theta^*_{k,i}$ Measured angle (from experimentation or simulation) estimate from camera c_k to reflector r_i

$\theta^*_{k,s}$ Angle from the cameras c_k to the known reflector positioned at s^*

$\theta^*_{s,k}$ Angle from the reflector mimicking the robot s^* to the camera c_k

$\theta_{x,y}$ Angular field of view per pixel in the horizontal (x) and vertical (y) direction

$\kappa^{(0)}$ Mean material map difference between the known refractive index map and any other refractive index map at iteration zero

$\kappa^{(j)}$ Mean material map difference between the known refractive index map and any other refractive index map at iteration j

κ_{mean} Relative difference between the initial refractive index map m^* and the mean of the posterior recovered refractive index map

κ_{median} Relative difference between the initial refractive index map m^* and the median of the posterior recovered refractive index map

κ_{max} Relative difference between the initial refractive index map m^* and the maximum of the posterior recovered refractive index map

$\lambda_{x,y}$ Intersection point on the Fast Marching Method grid

ν Range of positions captured by one pixel in the Charged Coupled Device (CCD)

$\xi^{(0)}$ Average relative error in the camera-reflector ray angles at iteration zero (of the inversion algorithm)

ρ Point on the ray

σ Variance of the temperature distribution $T(x, y)$

$\tau_i^{(j)}$ Difference between $t_i^{(j)}$ and t_i^h

$\phi_{k,i}^*$ Difference between $\theta_{k,i}^*$ and $\theta_{k,i}^h$

χ Pearson correlation coefficient

ω Angular frequency

Δ Change in optical path length

Δs Difference between the centroid position of $\bar{s}^*$ and $\bar{s}$

Δy Vertical displacement of the light ray

Δ_x Change in the position in the centroid position of the target in the horizontal x direction

Δ_y Change in the position in the centroid position of the target in the vertical y direction

Φ Set of camera reflector pairs

$\boldsymbol{\Psi}$ Phase of the wave

Chapter 1

Background

Almost half of UK exports are from manufacturing [1] and, as the world enters the fourth industrial revolution, the autonomous age, it is crucial that the UK continues to manufacture high value goods quickly, to a high standard and at a low cost to sustain this income. As a result, modern manufacturing increasingly utilises automated systems for component positioning and assembly [2, 3]. Industries are interested in autonomous manufacturing, for example robotic systems, as they potentially reduce costs and increase productivity [4]. A key component of autonomous manufacturing is large volume metrology. Robots require sensors to allow them to accurately position themselves and the component they are working on; this can be thought of as a local GPS system. Large volume or large-scale metrology typically involves using light rays which gather data on the distance, and/or the direction between measurement apparatus and an object being measured [5].

1.1 Robotics and Manufacturing

The use of robotics in manufacturing is on the rise. In 2018, it was reported that the global average was 74 robotic units per 10,000 employees, compared with only 66 robotic units in 2015 [6]. South Korea and Singapore are the world's most automated countries with 631 and 488 robotic units per 10,000 employees in 2018 [6]. Whereas the United Kingdom is slightly below the world average with 71 robotic units per 10,000 employees [6].

This rise in the use of robotics within manufacturing is leading to some of the general public questioning their job security, with 23 % of participants questioning this in a recent 2018 study [7]. However, researchers found that industrial robots lead to workers having increased wages without impacting total number of hours worked by an employee [8]. In addition, it has been shown that fewer jobs in manufacturing were lost when a country invested in manufacturing robots compared to those that did not [9]. A study by Barclays Bank suggested that an investment of £1.24 billion into autonomous manufacturing between 2015 and 2025 could protect over 70,000 jobs and lead to the creation of 30,000 jobs in new sectors [10].

Depending on a robot's configuration, it can be classed as Cartesian, spherical, or cylindrical [11, 12]. Cartesian robots are often referred to as gantry robots and these are commonly used in industry [12]. Gantry robots move in straight lines rather than rotating [12]. Due to their simple design, they have low manufacturing costs. Their rigid structure also allows these robots to perform to a high level of accuracy with a high repeatability [13]. Gantry robots are suitable to work with heavy objects [12, 13].

Cylindrical robots have two translational and one rotational degree of freedom and are mainly used for welding [13]. Spherical or polar robots are the oldest of the robotic configurations; they have two rotational and one translational degree of freedom [13]. Although these are still found in manufacturing floors, few spherical robots are manufactured today [12].

The most typical industrial robot are those which have six degrees of freedom in their motion range as this allows maximum flexibility to complete tasks [11]. These robots are used mainly for welding [12, 14] particularly in the automotive assembly line, with six workers to every one robot in the automotive industry [13]. Robots are also used for assembly [12], component positioning, and inspection, with researchers developing a climbing robot to inspect bridges in Madrid [15]. Robots can also be involved in the manufacture of clothing [16, 17] with clothing giant Adidas stating that they will be able to produce 800,000 t-shirts per day by implementing robotic sewing machines [18].

Additionally, the collaborative robot or cobot are robots designed to work with a human operator [19]. KUKA Robotics have developed a cobot which can slow down their working speed when unexpected contact is made with the robot in order to safeguard the human employee [20].

1.2 Metrology

Metrology is arguably the oldest study of mathematics, with the earliest recorded use being approximately 2900 BC, where an Egyptian Pharaoh wanted to have a standard unit of length which would aid in the construction of his pyramid [21]. The word metrology means the science of measurement [22], with the National Physical Laboratory (NPL) maintaining the measurement standards for the UK. The International System of Units (SI) is the most widely used system of measurement, however in November 2018 a vote was held to redefine the kilogram, kelvin, mole and ampere so that their values are in keeping with fundamental constants: Planck, Boltzmann, Avogadro and elementary electrical charge respectively [23, 24].

Many companies may be unaware that they are doing metrology in their day-to-day roles; companies employ quality control practises to reduce flaws in the production of goods and to keep batch uniformity of goods, which is a form of metrology [22, 25]. Since metrology is the science of measurement, it is important to note that all measurements have a degree of uncertainty surrounding them, and in particular, there is a subtle difference between error and uncertainty within metrology. The error is the difference between the true value of the object being measured and the measured value. There are two main types of error, systematic and random error [22, 25]. Systematic errors can be controlled and are reproducible, which means that they can be corrected for by using a suitable method, for example, calibration of software helps to reduce systematic errors. Systematic errors can arise from poor maintenance of environmental factors; for example, not maintaining a constant temperature in the laboratory. Whereas, random errors vary inconsistently but are generally straightforward to detect [22, 25]. Uncertainty on the other hand is the estimated range of values which the true value of the measured quantity lies in [25, 26]. Sources of error will be discussed further in Subsection 1.3.2.

In manufacturing settings, robots need a sensing system to help them position themselves and the component they are working on. The most well-known positioning system is the global positioning system (GPS) which uses satellite signals, however these signals often can't be well received indoors [27]. For this reason, there have been many advancements in indoor positioning systems (IPS) and some of these systems typically use ultrasound [27, 28]. For mobile robots, the most commonly used navigation method is odometry, although this can prove problematic in outdoor terrains and can lead to large errors [29–31]. Odometry is the measure of distance and the most well-known example of this is within a car [31]. Visual odometry uses photographs taken from one or more cameras to determine the position and orientation of the robot [32]. Another popular sensing modality uses light rays, which travel through the volume of air, to undertake this. These systems are called optical based metrology systems [33].

1.3 Optical based Metrology Systems

Optical metrology is the science of using light to make measurements, and optical based systems allow this to happen. Optical based metrology systems might be distance based, angle based, or focussed on surface form measurement [34]. Two types of optical based metrology systems: laser trackers and photogrammetry systems are now considered.

1.3.1 Laser Tracking

Laser trackers use interferometry to measure lengths. Interferometry is a measuring technique where the analysis of the interference between two or more light beams is used for precision measurements [22]. In the past laser metrology systems worked on a fixed axis, but since the invention of the laser tracker, which gives displacement and angular based measurements they are able to be used for long distance metrology [35, 36]. Laser trackers use range and two angles to determine the co-ordinate of the reflector [37, 38]. Laser trackers operate using a laser beam which is split in two, one part of the beam stays within the tracker and is used as reference point, the second beam reflects off the target and back into the instrument. This secondary beam is called the measurement beam. When these two beams interfere with one another this results in a cyclic change, which is often called a fringe count. Circuitry inside the tracker uses the fringe counts to determine how far the tracker is from the reflector [33]. One disadvantage with these systems is beam breakages as the home position of the target needs to be re-evaluated [37, 38]. For this reason absolute distance meters (ADM) are being increasingly built into laser trackers to provide absolute measurements as the beam does not break and ADMs work on a “point and shoot” basis, however these are less accurate [34, 35, 37].

The laser tracker tracks a target, also called a retroreflector and the most common type of retroreflector is the spherically mounted reflector (SMR), which is also known as the corner cube reflector (CCR) [34, 35, 39]. SMRs are spherical in shape which means that they can be seen from more positions compared to a flat target; a flat target can only be located over an angle of ± 45 ° whereas a spherical target can be located over a range of 240 ° [39]. SMRs can range in diameter from 10 mm to larger than 100 mm [40]. Previously, these types of retroreflectors were made out of solid glass but now SMRs are hollow and made from steel [5], however they have high manufacturing cost. To keep costs down there are some retroreflectors on the market which are made of plastic [39].

In terms of the accuracy of the laser tracker, the typical accuracy for the Leica Absolute Laser Tracker is $\pm$ 7.5 μm + 3 μm/m for angular measurements and $\pm$ 0.2 μm + 0.15 μm/m for interferometer measurements [41]. Laser trackers can be used in many technical disciplines such as aerospace and civil engineering [5, 42, 43]. Laser trackers can also be used to inspect surfaces, such as dish antennas. Additionally, laser trackers have also been used to track space debris [43, 44]. Aside from using a laser tracker in an engineering environment, they have also been used to digitally archive the architecture of historical buildings [45]. This thesis will focus mainly on the optical based metrology system of photogrammetry.

1.3.2 Photogrammetry

Photogrammetry is an optical-based metrology system used particularly in the fields of engineering and metrology [5, 46, 47]. Photogrammetry can be thought of as using a set of photographs taken from different positions to produce positional measurements [46]. It is possible to obtain robust and dependable data about the surface, shape, size and position of an object without touching it using photogrammetry [34]. These sizes and shapes are calculated from measurements made using 2-D photographs. By using two or more images of the object of interest from different angles, it is possible to find the three dimensional co-ordinates using optical triangulation [5, 46]. Optical triangulation calculates where two or more straight rays meet in space. However, due to thermal fluctuations in the air, the light can be refracted and this can lead to significant positioning errors in the triangulation calculation [48].

Photogrammetry systems can use two methods of optical triangulation, these are intersection and bundle adjustment. In fact some photogrammetry systems may deploy both an intersection method and bundle adjustment to increase the accuracy of the position of the object of interest. We have already mentioned that intersection as a triangulation solution finds the location of a point by finding where the light-ray paths intersect and then finds the mean of these intersections [39, 49].

Bundle adjustment is used to produce the final (x, y, z) co-ordinates of the object of interest. To do this process there are three steps: triangulation using intersections, resection and self-calibration. The process of triangulation finds the measured points, whereas resection determines the orientation of the image [49]. Generally speaking, it is not possible to triangulate without knowing the orientation of the image and vice versa. Bundle adjustment does these two things simultaneously and also self-calibrates the camera. For the bundle adjustment method to be successful it requires an initial orientation to get the process started [39]. In this thesis, only intersection as a triangulation solution is considered.

These techniques are used to increase the accuracy of the resulting image or reconstruction. However, target image measurements in particular sub pixel accuracy can also introduce errors. When the locations of subpixels within the target image are being calculated it is crucial that the targets are detected and accurately located. One way to increase detection, which is currently used in industrial metrology, is to make the targets the brightest or darkest object in the image [50, 51]. In terms of optimising the accuracy of the location of the target blob testing can be carried out. This is where outlying pixels are removed which are not part of the so called “blob” of the target image and have a high contrast value. The resulting blob is then checked to determine if it is the correct shape given the known target shape [50, 52]. In citeclarke1995analysis Fourier transforms are used to determines if the target location errors are effected by background noise and ambient conditions. In Chapter 3, a simple mathematical approach to increase sub pixel accuracy is introduced.

Photogrammetry systems have many applications in industry and manufacturing [5, 53, 54]. In medical applications and navigation [53], photogrammetry systems with more than one camera are used. These systems are called multi-sensor [53]. Photogrammetry is also used in civil engineering, particularly in structural assessment [54]. In addition, photogrammetry systems have also been used to monitor the structure of an ore crusher, the PI Truss of the International Space Station and the Arecibo Primary Reflector Surface, which is the biggest single-dish radio telescope in the world located at Arecibo Observatory in Puerto Rico [5]. A photogrammetry system was used to examine a footbridge in Aveiro, Portugal [54]. The footbridge is circular with a radius of 13 m and the path for pedestrians is 2 m wide [54]. Images were captured before a weight was added to the bridge, when the weight was on the bridge and after the weight had been taken off the bridge. The researchers concluded that photogrammetry can be used for structural assessment and they reported an accuracy of lower than 2 mm [54].

Generally speaking, photogrammetry systems are not as accurate as laser trackers. In idealised working conditions, the V-STARS/N-Platinum photogrammetry system has an absolute accuracy of ± 5 μm + 5 μm/m [55], whilst in a large working volume 100 m^3, the Vicon T160 photogrammetry system has average errors of 1.48 mm to 3.95 mm in a working volume [56]. This paper used six Vicon T160 cameras, but the errors found may not be reliable. This is due to the fact that the cameras are mounted on a scaffold and this structure vibrates due to traffic and underground trains.

Photogrammetry systems experience intrinsic and extrinsic errors [56]. Intrinsic errors are those related to the optical parameters such as the focal length, image sizing and the principal point [56, 57]. Extrinsic errors are those related to the position and orientation of the camera [56, 57]. There is also an error associated with the distortion of the lens, this occurs when the incident angle is not equal to the emergence angle [39, 56]. When there is no distortion in an image it is referred to as orthoscopic [39].

More generally, metrology systems can experience random and systematic errors and these have been briefly introduced in Section 1.2. Systematic errors fall into four main categories: errors in instrument calibration, environmental conditions, deformation of equipment and errors which cannot be avoided [22]. One example of deformation of equipment is that the photogrammetry cameras can warm up, particularly those which use infra-red [58, 59]. This heating up of the exterior of the camera can lead to errors, as the beam will experience refraction from the outset. Random errors cannot be reproduced and deviate randomly from the true value, these cannot be corrected for by repeating the reading many times [22, 25].

The types of errors explored in this thesis are systematic errors caused by environmental conditions, in particular, errors caused by refractive index fluctuations.

1.4 Refraction Effects in Large Volume Metrology

A photogrammetry system's ability to measure accurately depends on many factors, including, the ability to take into account the atmospheric effects such as temperature, pressure, refractive index and humidity [60, 61]. If the volume being measured is extended to that of an industrial setting, light refraction due to temperature variations within the volume has to be addressed. A factory environment does not have a constant temperature as machines and operators emit heat. This therefore means that the first order approximation, which says that rays of light move in straight lines, is not applicable [5]. The thermal fluctuations within the air cause the rays of light to bend. This bending of light-rays introduces errors in the received measurements (that is, the angle measurements of the photogrammetry system) and consequently, as the volume measured increases, these errors grow and can severely affect the accuracy of the coordinate positioning [61]. Accounting for the refractive index effects is a key step to improving accuracy and quantifying uncertainties.

If laser tracker systems are considered, the role that the refractive index of air plays is crucial to improving the accuracy of laser interferometers [62]. Most laser interferometers can monitor the environmental conditions and use this information to compensate the wavelength [33, 35]. The relationship between wavelength and refractive index can be expressed by the following

$$\lambda_{air} = \lambda_0/\eta_{air} \tag{1.1}$$

where, λ_{air} is the wavelength of the laser in air, λ_0 is the wavelength of a laser in a vacuum and η_{air} is the refractive index of air [62]. Therefore, an accurate way of calculating the refractive index of air is crucial for accurate laser interferometry measurements.

The "Large volume unified metrology for industry and novel applications and research (LUMINAR)" project is a recently completed (2016) international collaboration between the National Physical Laboratory and other institutions which focused on tackling refraction effects in industrial settings [63]. Researchers on the project found that in a typical aircraft industrial space the positional measurement uncertainty can be significant, 0.26 mm for full aircraft measurements [64, 65]. In addition, [66] found that a light beam will deviate from a straight line by 0.2 mm for every 15 m it travels horizontally when there is a vertical temperature gradient of approximately 2 K/m (and a vertical height of 6 m).

Additionally, researchers found that when a VICON T160 photogrammetry system was operating in a working volume of 100 m^3 the average positional error was millimetre scale [56].

1.5 Refractive Index Modelling

Increasingly optical based metrology systems are required to accurately measure distances to a desired order of 10^{-7} m, and therefore, it is important to be able to calculate the refractive index of air accurately [67]. Typically, the Edlén and Ciddor equations can be used to calculate the refractive index of air, with the typical refractive index of air at room temperature (21 °C) being approximately 1.00028 [33, 42, 68]. The Edlén equation was first published in 1966 and it has been updated many times since then. The original Edlén equation for standard air, $\eta_{T\rho}$, where T is temperature (measured in degrees Celsius) and ρ is pressure (measured in torr) is given by [69]

$$(\eta_{T\rho} - 1) = \frac{\rho(\eta_s - 1)}{720.775} \frac{1 + \rho(0.817 - 0.0133T)10^{-6}}{1 + 0.0036610T}. \tag{1.2}$$

In the above, η_s is standard air (also referred to as dry air) with a pressure of 760 torr and a temperature of 15 °C [69] is defined as

$$\begin{aligned}(\eta_s - 1) \times 10^8 = 8342.13 &+ 2406030(130 - \sigma^2)^{-1} \\ &+15997(38.9 - \sigma^2)^{-1},\end{aligned} \tag{1.3}$$

where σ is the vacuum wave number expressed in $\mu\mathrm{m}^{-1}$ [33, 69, 70]. The Edlén equation has been modified since it was first published [70, 71], with the form in reference [70] being the most commonly used. To improve the accuracy of the results, the Edlén equation can include the carbon dioxide content of air [61, 69, 70]. Researchers at NPL updated the Edlén equation [70] as the original equation was not in keeping with the International System of Units (SI). This updated Edlén equation, which takes into account conversion to SI units, uses a correction factor of 1.000079923 which is a ratio of the refractivities of dry air containing 450 ppm carbon dioxide and 300 ppm carbon dioxide. This updated formula also has a revision of the dispersion term; this is because when Edlén originally created his formula the carbon dioxide concentrations were lower than those measured today so this is corrected for. The refractive index for dry air ($\eta_{T\rho}$), which is air that has no water vapour or a low relative humidity, is given by the revised formula

$$(\eta_{T\rho} - 1) = \frac{\rho(\eta_s - 1)}{96095.43} \times \frac{[1 + 10^{-8}(0.613 - 0.00998T)\rho]}{(1 + 0.0036610T)} \tag{1.4}$$

where ρ is now measured in Pascals [33, 70].

In recent years, researchers have experimentally tested the Edlén equation [67, 72]. In 1986, researchers found that when the CO_2 content was accounted for the agreement with the Edlén equation was better than 5×10^{-8} [67]. This is very good agreement as researchers state that the refractive index of air should be known to a few parts in 10^{-8} to keep uncertainties of a laser interferometer at the desired 1 part in 10^{-7} [67]. More recently, researchers developed a method that used both laser synthetic wavelength interferometry and the Edlén equation to give a very accurate reading for the refractive index of air, with the measurement accuracy being approximately 3.7 $\times 10^{-8}$ [62, 72].

Ciddor was able to find two ways to evaluate an estimate for the refractive index of moist air, η_{prop}, using the following,

$$\eta_{prop} - 1 = \left(\frac{\rho_\alpha}{\rho_{\alpha xs}}\right)(\eta_{\alpha xs} - 1) + \left(\frac{\rho_\omega}{\rho_{\omega s}}\right)(\eta_{\omega s} - 1), \tag{1.5}$$

where ρ_α is the density of dry air, $\rho_{\alpha xs}$ is the density of dry air at 15 °C with pressure 101.325 kPa, $\eta_{\alpha xs}$ is the refractive index of dry air at 15 °C, 101.325 kPa and 0% humidity, ρ_ω is the water vapour component of moist air, $\rho_{\omega s}$ is the density of pure water vapour at 20 °C and $n_{\omega s}$ is the refractive index of standard air at 15 °C, 101.325 Pa, 0 % humidity and 450 ppm of CO_2 [68]. The second estimate Ciddor created for the refractive index in moist air, η_{LL}, which uses the Lorentz-Lorenz (LL) relationship is given by [68],

$$\eta_{LL} = \left(\frac{1 + 2L}{1 - L}\right)^{1/2} \tag{1.6}$$

where L is

$$L = \left(\frac{\rho_\alpha}{\rho_{\alpha xs}}\right)L_a + \left(\frac{\rho_\omega}{\rho_{\omega s}}\right)L_w \tag{1.7}$$

and

$$L_i = \frac{{\eta_i}^2 - 1}{{\eta_i}^2 + 2}, \tag{1.8}$$

where i = a(air), w(water) and η is the refractive index in each of these substances [68].

In terms of relating the refractive index of air with light ray propagation, the most simple and well-known equation is arguably Snell's Law

$$\eta_1 \sin\theta_1 = \eta_2 \sin\theta_2, \tag{1.9}$$

where η_1 and η_2 are the refractive indices in media 1 and 2 respectively and θ_1 and θ_2 are the angles of incidence and refraction that the light ray makes with the normal [73]. The main problem with Snell's Law is that it breaks down when θ_1 is small and can also only be used in layered media. To better account for these measurement errors one must include transverse gradients [42]. In Chapter 2, a full comparison is carried out between the displacement of a light beam in the y (vertical) direction when the light ray is propagating through transverse temperature gradients when the ray is in a simulated environment and when the calculation is carried out using equations found in [42, Appendix E].

Another way to model a light ray propagating through a spatial domain with transverse temperature gradients is the Williams' equation [33, 74]. The refraction angle, θ_R, can be expressed as

$$\theta_R = \frac{1}{\ell}\frac{\rho_0}{T_0}\int_0^{\ell} \frac{\partial T}{\partial z} s \ \mathrm{d}s \tag{1.10}$$

where ℓ is the complete light ray path, ρ_0 and T_0 are the standard values of pressure and temperature respectively, z is the direction normal to the ray and s is expected length of the light ray [74].

1.6 Techniques for Recovering a Spatial Map of the Refractive Index

Since the refractive index is typically inhomogeneous in a material or object, and it can significantly affect the path of light traversing it, researchers are interested in modelling it [5, 75–83]. Pollen grains have had the spatial distribution of the refractive index modelled using digital holographic microscopy to an accuracy of around 98 % [81], and researchers have used refractometry to generate a tomographic image of the refractive index of human tissue cells [82]. Researchers have also developed an optical microscope which provides a three dimensional spatial map of the refractive index of polystyrene beads and living cells [77]. Methods to calculate the refractive index of a solid material or aqueous solution can include non-linear interferometry [75, 76], using different coloured lasers [5, 77–79, 84] and microscopy [77, 80, 81].

Researchers are also interested in the refractive index distribution that occurs in aqueous solutions [85]. Image plane holographic tomography was used in [85] to reconstruct the refractive index in an aqueous solution of photo sensitizer. A Least-Squares Estimation approach was used to analyse the data from the digital holograms which allowed the fluctuations of the refractive index to be calculated. The researchers were able to obtain reproducible results with an average percentage error of 6.1 % when they were reconstructing the temperature profile of an observable volume compared with a reference method [85]. This system would not be suitable for use in air as the difference in the refractive indices used in the researcher's simulation was up to 0.05 [85], whereas in air a temperature change of 1 °C corresponds to an approximate refractive index change of 9.5×10^{-7}; so the system is not sensitive enough to pick up the small refractive index changes in a robot's environment in a factory setting.

Due to the inhomogeneous nature of air, researchers found that using sensors based on interferometric displacement to measure distances greater than 50 mm resulted in errors caused by fluctuations in the refractive index [61]. When operating over larger distances the increase in refractive index fluctuations was linearly proportional to the distance being measured [61]. To reduce the effect that the refractive index has on laser based distance measurements, a two-colour heterodyne laser interferometer with two distinct wavelengths has been developed

[79]. The wavelengths used were 1555 nm and 777.5 nm. This method is suitable for measuring distances in open air conditions and the results obtained were in keeping with the Ciddor Equation. However, this method has only been shown to work for distances of up to 2.5 m which is not in keeping with the dimensions of large volume metrology which are usually greater than 10 m in length [63]. This method was tested at 2.5 m due to space restrictions in the laboratory and the authors have not commented on whether or not this technique would work over large distances (10 m) [79]. A two colour interferometry approach to find the refractive index has also been used [84]. Experiments showed that for distances less than 30 m there is a length-dependent measurement uncertainty of below 1.2×10^{-7} per metre measured over. The results are very encouraging but cannot be used in an industrial setting as this technique can only be used in dry air (air that has no water vapour or a low relative humidity). For this technique to be implemented in moist air the air humidity would have to be accurately measured, and this would require a series of humidity sensors on the optical path which would be impractical in a manufacturing environment.

It is clear from the literature discussed above that there is currently no light based sensor system (or otherwise) capable of reconstructing the refractive index map of air in a large three dimensional volume to an accuracy of $1\ \times10^{-5}$. Establishing such a capability is vital to the successful deployment of this technology in a manufacturing setting, and so the work in this thesis is of substantial importance. The next Sections of this Chapter provide some introductions to key methodologies which will be used in Chapter 4 and 5.

1.7 Inverse Problems

Chapter 4 and 5 will look at solving an inverse problem and using the results to reconstruct a refractive index map of the spatial domain. When given a set of data or a series of observations the inverse problem entails determining what specific parameters or factors produced these specific results [86]. Related to this is the so called forward problem. This is a mathematical model which given a set of inputs (parameters or causal factors) produces an output (data set) which can then be compared with experimental observations. It is sometimes tricky to determine which is the inverse problem and which is the forward problem, the inverse problem is widely regarded as the one which is more difficult to solve [87].

An inverse problem is often ill-posed [88]. In order to define an ill-posed problem, it is more intuitive to define a well-posed problem. A problem is well posed if there exists a unique solution that continuously depends on the data [88, 89]. In an ill-posed problem the solution may not be unique and is sensitive to small changes in the data [88–90]. As will be shown later, using this definition, the inverse problem being solved is ill-posed as refractive index changes of the order of 10^{-5} lead to positional uncertainties in large volume metrology, and even the smallest amount of noise can lead to significant disruptions in the reconstruction of the refractive index map.

Inverse problems can be applied to a large number of disciplines, and most commonly used as an imaging technique [86]. In an inverse problem measurements are most commonly taken on the exterior of an object in order to make reference about the inside of the object, which in most cases is inaccessible [91]. Inverse problems are commonly used in medical applications, with computerised tomography (CT) scans being the most well-known [91]. A CT scan works by measuring the attenuation of many X-rays positioned at different sources and measuring the intensity of the attenuation on a computer [92]. Researchers solve inverse problems in order to reconstruct the spatial map of a flaw within a weld as a method of non-destructive testing [90].

1.8 Parametrisation of the Spatial Domain

Arguably the most straightforward way to parameterise a spatial domain is with a regular grid; a well-known example being the parametrisation of the Earth using a latitude longitude spherical grid [93, 94]. The issue with this grid is that there can be sharp discontinuities and the model may need to be spatially smoothed, this is particularly true in the Earth where there is a singularity at the poles [93, 95].

In this thesis, the refractive index map was parametrised using a space-filling polygon tessellation, known as a Voronoi tessellation; this is related to Delaunay triangulation [96, 97]. A Voronoi tessellation starts with a set of randomly chosen seeds; these are the black dots inside each of the Voronoi cells in Figure 1.1. The partitioning into cells is achieved by ensuring that every point inside each cell is closer to the seed associated with that cell than to any other seed in the tessellation [98, 99]. Voronoi tessellations can achieve adaptive and irregular partitions which in turn provide a low dimensional model (lower degrees of freedom) whilst affecting large regions with a single perturbation. For example, the removal of a single Voronoi cell can completely change the parametrisation of the space due to the irregular shapes that Voronoi cells can have [100, 101].

Voronoi tessellations are used in many applications [90, 102–105]. The first documented use of Voronoi tessellations was in 1855 when they were used to model the spread of cholera in London [104]. Researchers have used Voronoi tessellations to spatially parametrise a crystal orientation map in the application of ultrasonic non-destructive testing [90]. In biological applications, researchers have used Voronoi tessellations to model tissue cells [102] and to determine the optimal positions to site wireless local area networks for Wi-Fi signal coverage [103]. In seismology, researchers have used a generalised version of a Voronoi tessellation called a random Johnson Mehl tessellation to estimate the velocity of seismic waves [106]. This method gives a more generalised shape of the Voronoi cell which allows them to reduce the computational time.

1.9 Mathematical Modelling of Light Rays in Heterogeneous Media

In Chapter 2 COMSOL Multiphysics is introduced as the software which will be used in this thesis to simulate ray light ray propagation and hence generate simulated photogrammetry data. This has several advantages including complete

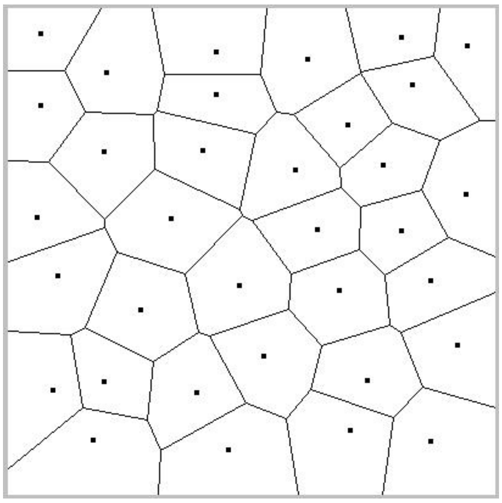

Figure 1.1: A Voronoi tessellation of the spatial domain in two dimensions where the black dots are the cell seeds [107].

ground-truth on the refractive index map to be reconstructed. The ray-tracing package in COMSOL firstly assumes that the electric field $\mathbf{E}$ of an electromagnetic wave can be expressed as

$$\mathbf{E} = \mathbf{a}e^{i\boldsymbol{\Psi}}, \tag{1.11}$$

where $\mathbf{a}$ is the amplitude of the wave and $\boldsymbol{\Psi}$ is the phase of the wave which is a function of the position vector of the wave $\mathbf{p}$ and the time t taken for the wave to reach $\mathbf{p}$. In this work, the media is locally isotropic and so the angular frequency ω can be expressed by

$$\omega(\mathbf{k}, \mathbf{p}) = \frac{v|\mathbf{k}|}{\eta(\mathbf{p})}, \tag{1.12}$$

where v is the velocity, $\mathbf{k}$ is the wave vector and $\eta(\mathbf{p})$ is the refractive index at position $\mathbf{p}$. In this initial value problem (Equation (1.12)) the user inputs the directional vector $\mathbf{k}$, the initial point of the ray $\mathbf{p}$ and the refractive index at position $\mathbf{p}$, that is $\eta(\mathbf{p})$. The wave vector $\mathbf{k}$ and angular frequency ω can be written in terms of the phase $\boldsymbol{\Psi}$, which is

$$\begin{aligned} \mathbf{k} &= \frac{\partial \boldsymbol{\Psi}}{\partial \mathbf{q}} \\ \omega &= -\frac{\partial \boldsymbol{\Psi}}{\partial t}, \end{aligned} \tag{1.13}$$

where t is time [108, 109].

COMSOL traces the ray by solving six (there are six if the ray is propagating in three dimensions and four if the ray is propagating in two dimensions) coupled first-order ordinary differential equations for the components of $\mathbf{k}$ and $\mathbf{q}$

$$\begin{aligned} \frac{\partial \mathbf{p}}{\partial t} &= \frac{\partial \omega}{\partial \mathbf{k}} \\ \frac{\partial \mathbf{k}}{\partial t} &= \frac{\partial \omega}{\partial \mathbf{p}}. \end{aligned} \tag{1.14}$$

As will be discussed in Section 4.2, COMSOL is not suitable to be used within the inversion algorithm due to the computational overhead and instead the Fast Marching Method (FMM) will be used as the Forward Solver. The Fast Marching Method (FMM) is a numerical algorithm which is grid based. It is used for finding the arrival time of a wave at each point in a discretized spatial domain (typically on a square grid) [110]. The FMM has been used in non-destructive testing to obtain the travel time field of an ultrasonic ray [90], and has also been used in robotic navigation to find the safest and shortest path a robot should take [111].

Consider a uniform grid with grid side length w, with each intersection point on the grid denoted by $\lambda_{x,y}$, where x represents the horizontal direction and y is the vertical direction. The FMM is used to solve a boundary value problem of the Eikonal equation [112]

$$|\nabla t(\lambda_{x,y})|\frac{c_{\infty}}{\eta_{x,y}} = 1, \tag{1.15}$$

where $t(\lambda_{x,y})$ is the desired travel time field (the time at which the light ray crosses a point $\lambda_{x,y}$ in the spatial domain) and η is the refractive index at $t(\lambda_{x,y})$. Once the travel time field is calculated, the ray that takes the shortest time to travel between the start of the ray (source) and the end point of the ray (receiver), can be found using Fermat's Principle of the Shortest Path [73]. This principle states that light travelling between the source and the receiver will always take the path that takes the least amount of time compared to the optical length of any other curve which joins the source and the receiver. To calculate the time field each grid point, $\lambda_{x,y}$, is initially assigned a classification of *far* and as the algorithm iterates this classification will eventually switch to *narrow band* and then *known* [113, 114]. Once assigned, the *known* grid points, $\lambda_{x,y}$, have fixed travel times and cannot be changed, *narrow band* grid points are assigned a temporary travel time which may be changed and *far* grid points travel times have not yet been calculated. Firstly, the grid points on the boundary where the camera is positioned are categorised as *known* and given a travel time of zero. The arrival times of neighbouring grid points are then calculated using a discretised form of Equation (1.15)

$$\begin{aligned}\Big[&\max\left(\max\left(D^{-x}_{f,g}t,0\right),-\min\left(D^{+x}_{f,g}t,0\right)\right)^2\\ &+\max\left(\max\left(D^{-y}_{f,g}t,0\right),-\min\left(D^{+y}_{f,g}t,0\right)\right)^2\Big]=\frac{1}{F^2_{f,g}}\end{aligned}\tag{1.16}$$

where $F_{x,y}$ is the speed at position $\lambda_{f,g}$, $D^{-}_{f,g}$ and $D^{-}_{f,g}$ are the standard backward and forward finite difference operators [113, 114], and the neighbouring grid points are defined as *narrow band*. Then, among all the *narrow band* points, the grid point with the smallest arrival time is updated to be *known* and its arrival times fixed. The set of nearest neighbour grid points that are *narrow band* are then updated and the arrival times for these subsequent points is found by solving Equation (1.16). This process is then repeated until every grid point has a travel time associated with it [113].

The optical ray path travelled by the light-ray between the source to the receiver is then calculated using the travel time field created by the FMM, and then the optical path with the shortest travel time is found. The algorithm begins at the known end point of the ray (the receiver) and calculates the optical path to the start point (the source). From the previous step of the FMM, the time ($t_{k,i}$) between the source and the receiver is known. The nearest neighbour grid points of the reflector are considered and the one which satisfies the following is chosen: (time at grid point) + (the time between it and the reflector) = $t_{k,i}$. The grid point which satisfies this condition is then added to the ray path and the process is repeated until it traces back to the camera grid point [113, 114].

Researchers have extended the grid based system that the FMM uses to a multi-stencil fast marching method; as the standard FMM has reduced accuracy in diagonal directions [90, 113]. The original stencil in FMM is a four point stencil, however in multi-stencil fast marching this grid is rotated by 45 ° and added to the original stencil which introduces four additional points to the stencil [90, 113].

This project will use COMSOL and the Fast Marching Method throughout (see Chapter 2 for further discussions on COMSOL and Chapter 4 for more details on the FMM). Although, the two methods are generally referred to separately, COMSOL solves the Eikonal equation (Equation (1.15) and Equation (1.16)) numerically on a grid [109]. The Eikonal equation is solved at the front of the ray to calculate the direction that the ray will take in its next time step. It uses the refractive indices in the local grid to perform this calculation and then solves the Eikonal equation to provide the position of the ray and its wave vector [109].

COMSOL assumes that the propagating light waves are locally plane. COMSOL also neglects diffraction effects (slight bending of light as it passes around an object) at the corners and edges of the geometry [73, 109].

1.10 Optimisation

Within the inversion method an optimisation technique is needed. Optimisation is the study of trying to minimise or maximise a function by selecting values (real or integer) of variables from a set [115–117]. The function that is being minimised/maximised is called the objective or misfit function (in the study of business and finance this may be referred to as the cost or utility function). To undertake an optimisation exercise, the problem must be defined and an objective function is then formulated mathematically. This initial model is then evaluated for a given set of parameter values. These parameter values are then perturbed and a second value (or several values) for the objective function is obtained. The optimisation method then decides whether or not to accept one of these new parametrisations and another perturbation is performed. This method iterates in this way until some prescribed stopping condition is reached [116, 117].

Optimisation methods can either be deterministic or stochastic [118]. A deterministic optimisation generates a sequence of points which converge to the optimal solution by assuming that there is no uncertainty associated with the model parameters, and if the process changes through time then these changes are known [119]. The most basic type of deterministic optimisation is linear programming [115–117]. Linear programming can be used when the objective function is a linear combination of variables and the constraints are all inequalities involving linear combinations of the variables [117, 120].

If the objective function of the problem being solved has many local minima and is non differential and discontinuous, optimisation algorithms based on random variables have some advantages. This technique is called stochastic optimisation. In this thesis, the objective function meets these conditions and therefore a stochastic optimisation approach is implemented. Some examples of stochastic optimisation techniques include simulated annealing and genetic algorithms [117]. Simulated annealing is an iterative stochastic method which is based on the physics involved with the slow cooling of metals [116, 121]. In the simulated annealing algorithm it is possible to accept an inferior solution so that the algorithm has a reduced probability of getting stuck in a local minima/maxima. This decision is conducted using the Metropolis Hastings criterion, which will be discussed shortly. Genetic algorithms are based on Darwin's theory of survival of the fittest [122, 123]. They work by changing a population of solutions at each model iteration. *Parents* (solutions at iteration n) are randomly selected and these *parents* are combined to produce *children* (solutions at iteration $n+1$) for the next generation of the problem. As the number of generations increase the population converges towards the optimal solution [123].

The most well-known stochastic optimisation method is arguably the Markov Chain Monte Carlo (MCMC) method [124]. This approach relies on Bayesian statistics, which uses known data to estimate parameters of interest. Unlike frequentist statistics, Bayesian statistics assumes the parameters of interest follow some fixed unknown distribution. Bayesian statistics relies on three main statistical concepts: the prior, the likelihood and the posterior. The prior is a probability distribution which reflects prior knowledge or beliefs about the parameters of interest in the experiment. The prior can be chosen such that it is either informative or uninformative; an uninformative prior is a wide distribution to reflect that there is no prior knowledge about the process. In this thesis, a prior which follows a uniform distribution will be chosen, as it will be assumed that the refractive index has a finite range of values and each are equally likely. The likelihood is the probability distribution which quantifies how well a given model with a particular set of parameter values can reproduce the observed data. The posterior distribution is the distribution of the parameters which we wish to recover which is obtained by updating the prior based on the results of the likelihood, where updating is done using Bayes' Theorem [125].

The posterior distribution is integrated using Monte Carlo methods in order to obtain estimates of interest from the posterior distribution. This method is also called Monte Carlo integration [124]. This method generates random variables with a probability density function which is approximate to the density function being integrated, that is, the posterior [126]. However it can be difficult to generate these samples and the most common method is to use a Markov Chain [124]. A Markov chain is a stochastic process where the probability of the next event depends only on the previous event. In Chapter 4, the Metropolis Hastings algorithm is used as the means of generating the Markov Chains. The Metropolis Hastings criterion is made up of two key components: a proposal distribution and an acceptance probability [127, 128]. The acceptance probability for the inversion algorithm is given in Equation (4.10). The main ideology of the Metropolis Hastings criterion is that at every iteration of the model the solution should be closer to the posterior density function.

Another method would be to use Gibbs Sampling which is a special case of the Metropolis Hastings algorithm. Gibbs sampling is used when sampling from a multivariate posterior is not feasible, but sampling from the conditional distributions for each parameter can be done [124]. Gibbs sampling works by assigning a start value to the parameter of interest, then draws samples from the parameter's conditional distribution, or the probability distribution of the parameter given a specific value of another parameter [124, 129].

In Chapter 4 the reversible jump Markov Chain Monte Carlo (rj-MCMC) method is introduced as the optimisation method of the inversion process in this thesis. The rj-MCMC builds on the aforementioned MCMC and further particulars of this method in relation to the problem are discussed in Chapter 4.

1.11 Use of rj-MCMC in Inverse Problems

As far as the author is aware the use of photogrammetry data to reconstruct a refractive index map is a completely new inverse problem. However, the inversion method employed has found success in other applications. For example, ultrasonic tomography for flaw detection in non-destructive testing [90]. These researchers used Voronoi tessellations to parametrise the geometry and the rj-MCMC method as their optimisation technique. The data these researchers obtain is time of flight from the ultrasonic sensor (as opposed to the angular direction to a target in photogrammetry) and the material map is locally anisotropic (whereas the refractive index is locally isotropic). The approach has also been used by researchers to obtain a spatial map of the wave speed within the Earth's crust [100, 130–132].

1.12 Outline of Thesis

Chapter 1 provides a review of the effects of refraction in large volume metrology. It also introduces current techniques used to recover the refractive index map in other materials with other sensing techniques and ways to model the refractive index maps. An introduction to inverse problems was given along with the key components: parametrisation of the spatial domain, forward solvers and optimisation techniques.

The original work in this thesis is presented in Chapters 2 to 5. Chapter 2 provides discussions of the positional errors associated with optical based metrology systems (photogrammetry and laser tracker) but mainly focuses on photogrammetry systems. This Chapter discusses the role that transverse gradients in the temperature field have in the displacement of a light ray. An empirical comparison is carried out between a finite element solver (COMSOL) and an analytical formulation [42] to determine the robustness of COMSOL as a ray tracing software. This Chapter ends with the introduction of three test cases which have light rays propagating through a Gaussian temperature profile; the aim of these test cases is to determine the effect that the initial angle of the ray, the maximum temperature and the temperature variance has on the positional errors of the light ray.

Chapter 3 builds from Chapter 2 and aims to determine the sensitivity of the Vicon T160 photogrammetry system when positioning a cluster of retroreflectors in a spatially heterogeneous refractive index volume; created by applying a localised heat source to the volume. The results from this experiment are then used to comment on the validity of the simulations described in Chapter 2. Following the results from the experimentation an investigation into the angular field of view was carried out to obtain a better understanding of the variation in the estimated position of the cluster of retroreflectors by looking at perturbations within the digitised images.

Chapter 4 outlines a methodology to reconstruct the refractive index maps. The methodology uses Voronoi tessellations to parametrise the refractive index map, the Fast Marching Method is used as the forward solver and the reversible jump Markov Chain Monte Carlo is used as the optimisation technique. This Chapter also details how the results from the inversion will be quantified by taking the reader through the triangulation process. Since photogrammetry systems use angular based measurements the objective function uses an estimated angle calculated by the forward solver and an investigation into how this angle is calculated is given in this Chapter. This Chapter introduces four numerical experiments with each having a more industrially relevant refractive index map than the previous. These numerical experiments all use simulated photogrammetry data to ensure ground truth within the results. The aim of the numerical experiments (and indeed this thesis) is that the positional error (absolute error and variance) of the target is reduced when the light rays are traced through the recovered refractive index compared to a homogeneous refractive index map.

Chapter 5 builds on the methodology of the previous Chapter and aims to reduce computational time and improve the sensitivity of the objective function. This novel methodology uses the time field as calculated using the FMM rather than by ray tracing. This Chapter revisits the four numerical experiments presented in Chapter 4 and aims to improve upon those initial results.

This thesis concludes with a summary of the key findings presented in this work and then finishes with an overview of the future work for this research.

1.13 Publications Arising from this Thesis

The work presented in Section 2.2 was published in *Acta Imeko* in 2018 and is titled *Positional uncertainty in optical-based metrology systems in large volume manufacturing* [133].

The work presented in Section 3.1- 3.3 and Chapter 4 has been submitted to *Inverse Problems in Science and Engineering* [134].

Chapter 2

Mathematical Modelling of Light Rays in Heterogeneous Media

This Chapter will discuss the positional error associated with a laser tracker system and a photogrammetry system. By examining a simplified mathematical model of light ray propagation it will be seen that the gradients in the refractive index that run transverse to the ray path direction have a critical role to play. Following that, it will be shown how to simulate light ray paths in complex, two dimensional, spatially varying temperature fields using a finite element model (COMSOL Multiphysics [135]). COMSOL Multiphysics was chosen as the finite element software as there is a large user base within the research group. COMSOL provides excellent technical support and offers users a free trial prior to purchasing the software to determine if it is appropriate for use, this free trial also includes access to the technical support. Other packages were considered for example Lambda Trace Pro, however due to the reasons mentioned above, COMSOL Multiphysics was chosen as the finite element software. The advantage of using simulated photogrammetry data is that it provides complete ground truth on the refractive index field in the volume. This will provide large volumes of carefully controlled photogrammetry data sets to be generated so that any subsequent methods that are developed to circumvent these effects can be carefully honed and tested. To illustrate this modelling framework, an investigation into the dependence of the positional error on the initial ray angle, the maximum temperature of the domain and the variance of a Gaussian temperature profile is performed.

2.1 Positional Errors Associated with Light-based Sensors

Optical-based metrology systems assume that the volume of air is homogeneous and that light-rays travel in straight lines (so no refractive effects). In addition to an angular measurement, the laser tracker system calculates the lengths ($d_{a,i}$) of the light-rays from the laser trackers, l_a, where $a = 1, \ldots, A$ to the reflectors, r_i, where $i = 1, \ldots, R$.

For example, in a two dimensional plane, two laser trackers can be deployed (l_1 and l_2 in Figure 2.1) to track a reflector s^* (of known position). The red dashed lines show the true ray path where the light-rays bend away from the localised heat source and have lengths d_{1,s^*} and d_{2,s^*} respectively. The circles in blue have radii d_{1,s^*} and d_{2,s^*}. The intersection of these circles gives the estimated position of the reflector ($\hat{r}_l$). This method of using the intersection points of the rays is similar to trilateration used in GPS systems [39, 48] and it assumes a spatially homogeneous refractive index and hence no refraction takes place. The error in the estimated position (as shown in Figure 2.1) is ε_l^* where $\varepsilon_l^* = \|s^* - \hat{r}_l\|_2$. These errors will typically be much smaller than the errors caused by using a photogrammetry system as photogrammetry systems use angular based calculations (triangulation) [39, 48].

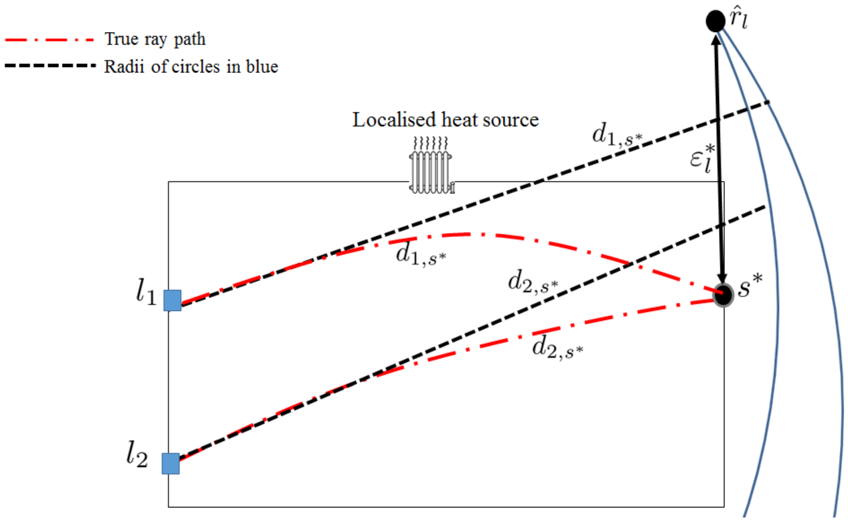

Figure 2.1: Figure showing the errors caused by using just the ray length measurement in the laser tracker system when the volume is assumed to be homogeneous. Two laser trackers (l_1 and l_2) are tracking a reflector s^*. The red dashed lines show the true ray path where the light-rays bend away from the localised heat source and have lengths d_{1,s^*} and d_{2,s^*} respectively. The black lines use these lengths for the radii of the blue circles. The intersection of those circles gives the estimated position of the reflector ($\hat{r}_l$) and from this the positional error ε_l^* can be calculated.

The photogrammetry system calculates the angle ($\theta^*_{k,i}$) that the light ray enters camera, c_k, where $k = 1, \dots, C$ from the reflector r_i (with respect to the normal to the camera plane). The photogrammetry system assumes a homogeneous medium and so the predicted ray path is a straight line (see the straight dashed lines in Figure 2.2). As in the case of the laser tracker, two cameras (or more) can be deployed (c_1 and c_2 in Figure 2.2) which track reflector s^* (of known position). The red dashed lines in Figure 2.2 show the true ray path where the light rays bend away from the localised heat and have initial angles $\theta^*_{1,1}$ and $\theta^*_{2,1}$. This triangulation method gives the estimated position of the reflector, $\hat{r}_c$, and from this the positional error can be calculated, via $\varepsilon^*_c = \|s^* - \hat{r}_c\|_2$. The laser tracker case is included here for completeness sake but the remainder of this thesis will focus on the photogrammetry case.

2.2 Modelling of Light Rays in Heterogeneous Media

As mentioned in Section 1.5, the positional errors obtained by simply using Snell's Law are far smaller than those observed in practice and to better account for these measurement errors one must include transverse gradients [42]. For example, if an additional camera is added to the lower right corner of Figure 2.2, the light ray will not experience transverse gradients and as a result the positional error will be much smaller than those observed in c_1 and c_2.

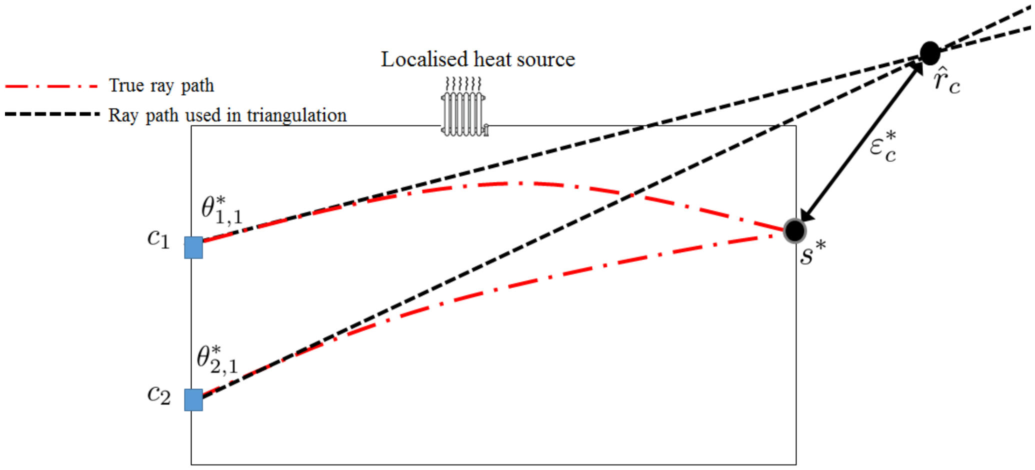

Figure 2.2: Figure showing the error caused by using the photogrammetry (angular) system when the geometry is assumed to be homogeneous. Two cameras (c_1 and c_2) track the reflector s^*. The red dashed lines show the true ray path where the light rays bend away from the localised heat source and have initial angles $\theta_{1,1}^*$ and $\theta_{2,1}^*$ (with respect to the normal to the camera plane). The black lines show the equivalent straight ray path that the photogrammetry system uses in its calculations since this assumes the volume is homogeneous (has a constant refractive index throughout and hence no refraction takes place). The triangulation method gives the estimated position of the reflector, $\hat{r}_c$, and from this ε_c^* can be calculated.

The general form of the ray [73] equation is given by

$$\frac{d}{du}\left(\eta\frac{d\mathbf{p}}{du}\right) = \nabla\eta, \tag{2.1}$$

where u is the arc-length of the ray, $\mathbf{p}$ is the position vector of point ρ on the ray and η is the spatially dependent refractive index [73]. Since the temperature fluctuations in a typical industrial environment are relatively small then the ray does not deviate much from a straight line. If Equation (2.1) is rewritten as two scalar equations in terms of Cartesian co-ordinates, the following is obtained,

$$\frac{d}{du}\left(\eta\frac{dx}{du}\right) = \frac{\partial\eta}{\partial x} \tag{2.2}$$

and

$$\frac{d}{du}\left(\eta\frac{dy}{du}\right) = \frac{\partial\eta}{\partial y}. \tag{2.3}$$

The right hand side of Equation (2.3) can be integrated from $x = x_i$ to $x = x'$ as follows

$$\int_{x_i}^{x'} \frac{d}{du}\left(\eta\frac{dy}{du}\right) du = \int_{x_i}^{x'} \frac{\partial\eta}{\partial y} du \tag{2.4}$$

and so

$$\eta\left(x'\right)\left.\frac{dy}{du}\right|_{x'} - \eta\left(x_i\right)\left.\frac{dy}{du}\right|_{x_i} = \int_{x_i}^{x'} \frac{\partial\eta}{\partial T}\frac{\partial T}{\partial y} du, \tag{2.5}$$

where T is the temperature of the ray at each point, $\partial\eta/\partial T$ is the Ciddor equation differentiated with respect to the temperature T and $\partial T/\partial y$ is the transverse gradient of the temperature [42, Appendix E]. For a ray that is propagating roughly parallel to the x direction (so that the arc-length u can be approximated by x) then

$$\left.\frac{dy}{dx}\right|_{x'} = \frac{\eta(x_i)}{\eta(x')}\left.\frac{dy}{dx}\right|_{x_i} + \frac{1}{\eta(x')}\int_{x_i}^{x'} \frac{\partial n}{\partial T}\frac{\partial T}{\partial y}dx. \tag{2.6}$$

Let the final point of the ray be denoted by x_f then

$$\left.\frac{dy}{dx}\right|_{x_f} = \frac{\eta(x_i)}{\eta(x_f)}\left.\frac{dy}{dx}\right|_{x_i} + \frac{1}{\eta(x_f)}\int_{x_i}^{x_f} \frac{\partial n}{\partial T}\frac{\partial T}{\partial y}dx. \tag{2.7}$$

Therefore, in two dimensions (x, y), the displacement of a light beam in the y direction, Δy, can be approximated by integrating Equation (2.6) equation from $x = x_i$ to $x = x_f$, where x_f is the final point of the ray

$$\int_{x_i}^{x_f} \left.\frac{dy}{dx}\right|_{x'} dx' = \int_{x_i}^{x_f} \left(\frac{\eta(x_i)}{\eta(x')}\left.\frac{dy}{dx}\right|_{x_i} + \frac{1}{\eta(x')}\int_{x_i}^{x'} \frac{\partial n}{\partial T}\frac{\partial T}{\partial y}dx \right) dx',$$

$$\int_{x_i}^{x_f} \left.\frac{dy}{dx}\right|_{x'} dx' = \eta(x_i)\left.\frac{dy}{dx}\right|_{x_i} \left(\int_{x_i}^{x_f} \left(\frac{1}{\eta(x')} + \frac{1}{\eta(x')}\int_{x_i}^{x'} \frac{\partial n}{\partial T}\frac{\partial T}{\partial y}dx \right) dx' \right),$$

$$\int_{x_i}^{x_f} \left.\frac{dy}{dx}\right|_{x'} dx' = \eta(x_i) \left.\frac{dy}{dx}\right|_{x_i} \left(\int_{x_i}^{x_f} \frac{1}{\eta(x')} dx' + \int_{x_i}^{x_f} \frac{1}{\eta(x')} \int_{x_i}^{x'} \frac{\partial n}{\partial T} \frac{\partial T}{\partial y} dx dx' \right). \tag{2.8}$$

The left hand side of Equation (2.8) reduces to $y(x_f) - y(x_i)$ which is equal to Δy, and this gives the following result

$$\Delta y = \eta\left(x_i\right) \left.\frac{dy}{dx}\right|_{x_i} \int_{x_i}^{x_f} \frac{dx'}{\eta\left(x'\right)} + \int_{x_i}^{x_f} \frac{1}{\eta\left(x'\right)} \int_{x_i}^{x'} \frac{\partial \eta}{\partial T} \frac{\partial T}{\partial y} dx dx'. \tag{2.9}$$

Consider an example [42, Appendix E] where a laser tracker sends a beam parallel to the x-axis and the laser is tracking a retroreflector 10 m away (see Figure 2.3). The vertical temperature gradients along the beam path are $\partial T/\partial y =$ 1°C/m in $x \in$ [0,4) $\cup$ (5,10] and $\partial T/\partial y = +10$°C/m in $x \in$ [4,5]. The refractive index η is approximately 1 at all distances x, $\partial\eta/\partial T$ is -1 $\times 10^{-6\circ}\mathrm{C}^{-1}$ and the initial angle of the beam with respect to the x-axis is zero. The angle of the laser beam in the y direction is found using Equation (2.7). Therefore, the angle of the laser beam in the y direction for $x \in [0, 4)$ is

$$\left.\frac{dy}{dx}\right|_4 = \frac{\eta(0)}{\eta(4)} \left.\frac{dy}{dx}\right|_0 + \frac{1}{\eta(4)} \int_0^4 -1 \times 10^{-6} dx = -4\ \mu\text{radians}. \tag{2.10}$$

Similarly the angle of the laser beam in the y direction for $x \in$ [4,5] and $x \in$ (5,10] are

$$\left.\frac{dy}{dx}\right|_5 = \frac{\eta(4)}{\eta(5)}\left.\frac{dy}{dx}\right|_4 + \frac{1}{\eta(5)}\int_4^5 -10\times10^{-6}dx = -14\ \mu\text{radians} \qquad (2.11)$$

and

$$\left.\frac{dy}{dx}\right|_{10} = \frac{\eta(5)}{\eta(10)}\left.\frac{dy}{dx}\right|_5 + \frac{1}{\eta(10)}\int_5^{10} -1\times10^{-6}dx = -19\ \mu\text{radians} \qquad (2.12)$$

respectively. From Equation (2.9) for $x \in [0,4)$

$$\Delta y = \eta(0)\left.\frac{dy}{dx}\right|_0\int_0^4 \frac{dx'}{\eta(x')} + \int_0^4 \frac{1}{\eta(x')}\int_0^{x'} -1\times10^{-6}\ dxdx' = -8\ \mu\text{m}. \qquad (2.13)$$

Similarly the displacement of the laser beam in the y direction for $x \in$ [4,5] and $x \in$ (5,10] are calculated as follows

$$\Delta y = \eta(4)\left.\frac{dy}{dx}\right|_4\int_4^5 \frac{dx'}{\eta(x')} + \int_4^5 \frac{1}{\eta(x')}\int_4^{x'} -10\times10^{-6}\ dxdx' = -9\ \mu\text{m} \qquad (2.14)$$

and

$$\Delta y = \eta(5) \left.\frac{dy}{dx}\right|_5 \int_5^{10} \frac{dx'}{\eta\left(x'\right)} + \int_5^{10} \frac{1}{\eta\left(x'\right)} \int_5^{x'} -1\times 10^{-6}\; dx dx' = -82.5\ \mu\text{m}, \quad (2.15)$$

respectively. Therefore, the total displacement of the ray in the y direction is 99.5 μm. This provides some information on the types of errors that are encountered for typical temperature gradients found in industrial settings. For more complex temperature profiles the finite element package COMSOL can be used [135]. As a first check on its performance, the above example was investigated and, as will be seen below, very good agreement was obtained.

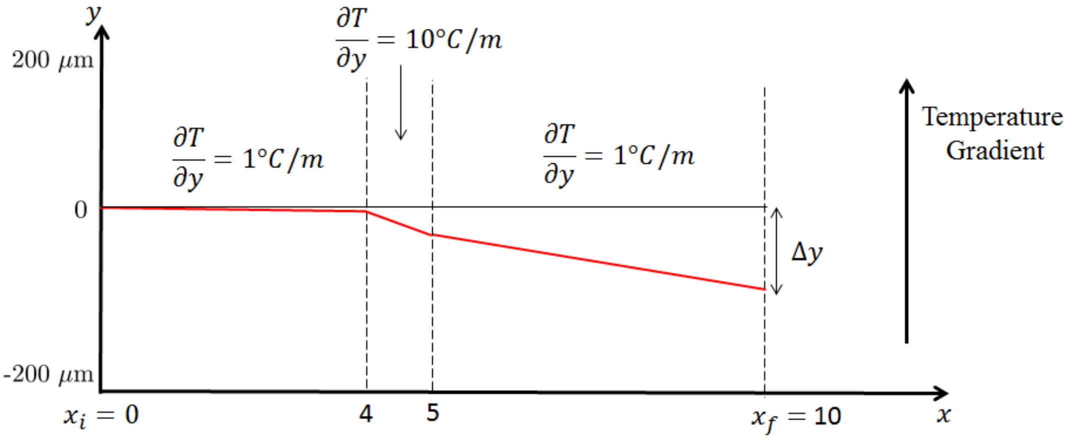

Figure 2.3: The bending of the light ray (in red) in accordance with the example above using Equation (2.9) to find the vertical displacement of the light ray Δy.

2.2.1 Ray Tracing Using Finite Elements

In order to simulate the example discussed in Section 2.2 using COMSOL, the underlying geometry needs to be created (recall that in Section 1.9 the mathematics of COMSOL Multiphysics were presented). In the aforementioned example there are three clear regions (0 to 4 m, 4 to 5 m and 5 to 10 m). In order to create these regions the *Geometry* node was selected and three rectangles were created. In the example the height of the rectangles is not given, it was decided to make the height of the rectangle 400 μm (there was no need to make it any larger as the light ray would still remain within the boundary). In COMSOL the position of each rectangle is defined by the lower left corner. The bottom left corners of each rectangle are as follows (0, 0.9998) m, (4, 0.9998) m and (5, 0.9998) m. In order to add the vertical temperature gradient to each rectangle, two *Variables* were created under the *Definitions* node, both variables were called T_domain (the reasoning behind this will be explained shortly). T_domain was firstly defined as 20[degC]+1[degC/m]*y where y corresponds to the vertical direction, the initial temperature is not defined in the example so 20 °C was chosen as it is commensurate with a laboratory. Under the *Geometric entity level* tab of *Variable*, *Selection* was 1 and 3, this represents the first and third rectangle mentioned above. The second T_domain was defined as 20[degC]+10[degC/m]*y and the *Geometric entity level Selection* was 2, to represent the second rectangle defined. In COMSOL the *Geometrical Optics* package is used. In this package all spatial regions must be defined using the refractive index (as opposed to velocity or temperature), this means that, an interpolation which reads in temperature values and converts to refractive indices needs to be included. To do this in COMSOL, an *Interpolation* function in the *Global Definitions* node is added and *file* is then selected. This command allows the user to read in a file containing temperatures in Kelvin and their corresponding refractive index using values calculated using NIST. This function is called n_int (this file would have to be created by the user). To make use of this file, *Refractive index, real part* is set to be *User defined* with value n_int(T_domain), within the *Medium Properties* of the *Geometrical Optics (gop)* node. To add the light ray the *Geometrical Optics (gop)* node is used again and add a *Release from Grid* since the height of the ray is not explicitly defined. The ray is defined to begin at (0,1) m and the ray direction vector is [1,0]. In order to output the (x, y) co-ordinates of the ray a *Ray Evaluation* in the *Derived values* of the *Results* node is required. To output the x co-ordinates qx is typed in the expression box (this is a built in COMSOL variable). To obtain the y coordinates qy is typed in the expression box (there is no need to create another *Ray Evaluation*). These (x, y) points were then plotted and the result is shown in Figure 2.4. The deflection of the ray using a COMSOL was approximately -92 μm.

Comparing Figure 2.3 (which is a schematic) to Figure 2.4 it can be seen that there is very good agreement which suggests that COMSOL has a variation of Equation (2.9) embedded within it as the software was able to account for the refraction effects caused by transverse gradients. The Δy value is also very similar, -99.5 μm in the analytical result and approximately -92 μm in the COMSOL simulation.

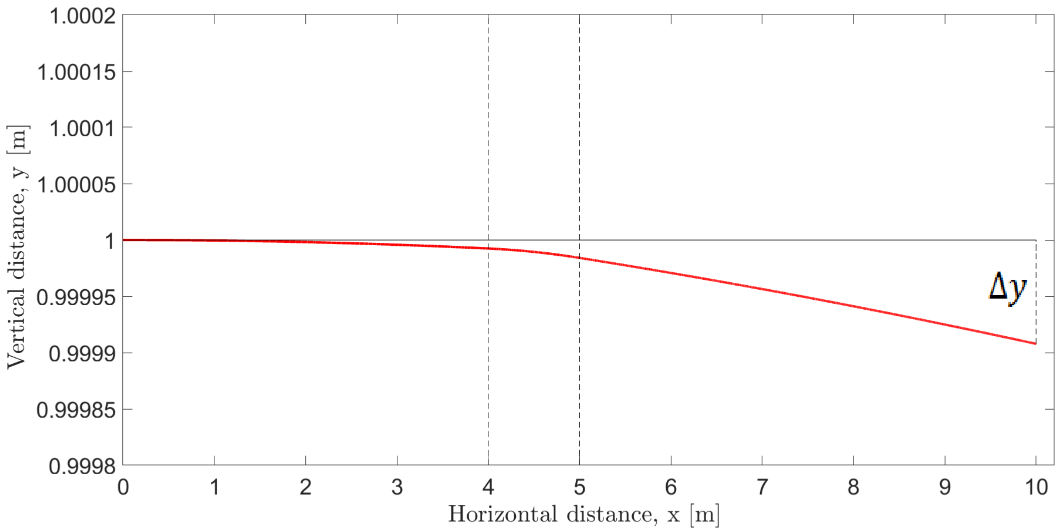

Figure 2.4: Light ray path produced from a COMSOL simulation of the example in Section 2.2 where various linear temperature gradients are applied to the geometry, with initial temperature of 20 °C. The red line shows the light ray which had starting point at (0,1) m.

To provide a more realistic example, COMSOL was used to examine the positional uncertainties that arise when a photogrammetry system is embedded in a spatial temperature profile that follows a two dimensional Gaussian distribution. The effect of the initial ray angle, the maximum temperature and the variance of the temperature distribution on the positional uncertainty was then assessed. In all of the simulations the size of the spatial domain was kept constant. The size chosen was commensurate with the laboratory photogrammetry system in Chapter 3 (3 m by 4 m).

In these simulations a localised heat source is placed at the centre of the domain and the Gaussian temperature distribution is then given by

$$T(x, y) = (T_{\max} - T_{\min}) \exp\left(-\frac{(x^2 + y^2)}{\sigma^2}\right) + T_{min}, \tag{2.16}$$

where σ is the variance of the temperature distribution measured in metres, $T_{\max}$ is the maximum temperature in the domain and similarly, $T_{\min}$ is the minimum temperature. To add this equation to the COMSOL simulation, the *component* option in the *Model Builder* window was accessed and a new *variable* was added in the *definitions* section. Once in this menu, the right hand side of Equation (2.16) was input into the *Expression* box and this *variable* was named as *T_domain*.

The next step was to convert the temperature map into a refractive index map. COMSOL requires the refractive index values in order to define the material properties. The temperature values in Equation (2.16) were transformed to a refractive index map using the Ciddor equation [68]; all other parameters in this equation were set at the NIST average values [136]. These values were simply collated as a two column table, temperature on the left and the corresponding refractive index on the right, and saved locally on the computer. In order to upload this file, an *Interpolation* was added to the model; this was accessed from the *Function* menu of the *Global Definitions* node. Once in this menu, the function was named *n_int* with temperatures ranging from ($T_{\min}$ to $T_{\max}$). To ensure that these refractive index values were used in the model the *Geometrical Optics (gop)* functionality was accessed. In this functionality the *Medium Properties* option was located and in the *Medium Properties* heading the *Refractive index real part* was defined as *user defined* from the drop-down menu. Finally, the refractive index was defined to take the values of *n_int(T_ domain)*.

Following this, the rays propagating within this geometry are defined. In the *Geometrical Optics (gop)* functionality of the *Model Builder* the *Release from Grid* option was used. This allows the user to prescribe the start point of a ray, its initial directional vector and its length.

2.2.2 Test Cases

In the first study (T1) 25 rays were simulated with the same starting point (position of the photogrammetry camera c_k) of (-1.5, 0) m, but each ray had a different initial direction. The vector describing the light rays initial direction is $x_0 = [1, y_0]$ where y_0 takes the values 0, ± 0.05, ± 0.10, ± 0.15, $\ldots$ ±, 0.6. The upper limit here is 0.6, as any higher values leads to the light ray not reaching the right hand boundary of the domain. Figure 2.5 shows the 25 rays propagating in the geometry. In this case, the values of $T_{\max}$ and σ were kept constant (314 K and 1.3107 respectively), the value for σ was chosen to ensure that at the four corners of the domain the temperature is approximately $T_{\min}$.

The second study (T2) examined the impact that $T_{\max}$ has on the positional error. In this case the number of rays propagating through the geometry was reduced to one. The chosen ray was the one whose initial ray angle led to the biggest positional error in the T1 study. All other parameters in this case remain as before apart from $T_{\max}$. In these simulations $T_{\max}$ takes values from 299 K to 374 K.

The final study (T3) examined the effect that varying the spread of the temperature profile (σ) had on the positional uncertainty. As in the second set of simulated experiments there was again only one ray propagating through the geometry (the same ray which was used in the T2 study). As in T1, $T_{\max}$ was set to 314 K but now the values for σ range from 0.5 to 3.5 m. In all of the simulations the COMSOL output was a set of (x, y) co-ordinates for each i^{th} ray, with the last value being the position of the reflector r_i.

2.2.3 Results of COMSOL Simulations

The photogrammetry camera is positioned at c_k and it is tracking each reflector at known position r_i as shown in Figure 2.6. The ray will take the path shown by the red dashed line (this ray path has been exaggerated for visual purposes) as the temperature distribution causes the light ray to bend away from the heat source (the red colours in Figure 2.6). As in Section 2.1, the photogrammetry system calculates the angle that the line from the camera (c_k) to the reflector (r_i) makes with the normal to the camera plane (denote by $\theta^*_{k,i}$). The straight dashed line in Figure 2.6 shows the straight ray path that the photogrammetry system adopts in its calculations; the associated triangulation algorithm assumes

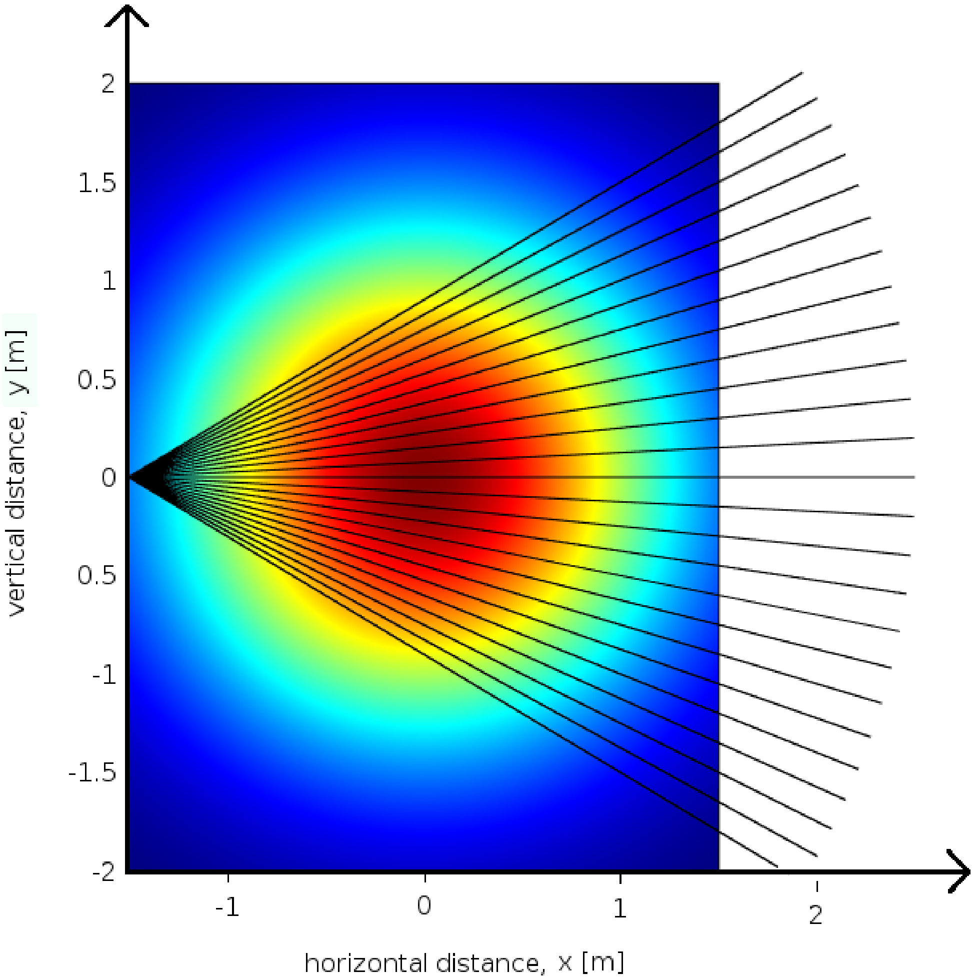

Figure 2.5: COMSOL simulation of the 25 light rays (black lines) propagating through the Gaussian temperature profile described by Equation (2.16). The size of the domain is 3 metres by 4 metres in the x and y directions, respectively. In this simulation the light rays have starting position $(-1.5, 0)$ m and the directional vector takes the values $\{(1, -0.6), (1, -0.55), (1, -0.50), \ldots (1.0), \ldots, (1, 0.55), (1, 0.6)\}$.

that the volume is homogeneous. The intersection of the dashed black line and the domain boundary gives the estimated position of the reflector $\hat{r}_c$. This value is then used to calculate the error in the position $\varepsilon_c^* = \|s^* - \hat{r}_c\|_2$.

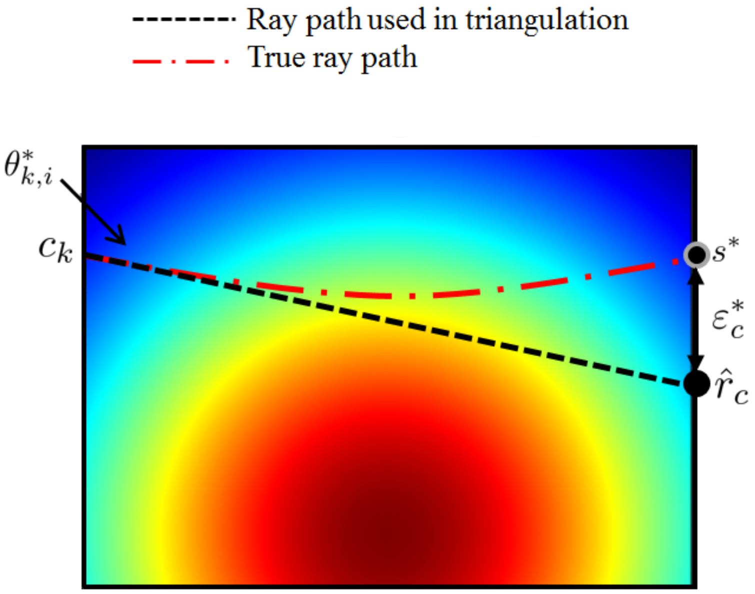

Figure 2.6: Figure showing the positional errors caused by refraction of a light ray traversing a Gaussian temperature profile. The red dashed line shows the true path of the light ray from camera c_k to reflector r_i (positioned at s^* on the right hand domain boundary). The dashed black line shows the equivalent straight ray path that the photogrammetry system uses in its calculations since this assumes the volume is homogeneous. The intersection of the dashed black line and the domain boundary gives the estimated position of the reflector ($\hat{r}_c$). The positional error is then given by ε^*_c.

In the first study (T1), the aim was to deduce if the initial ray angle impacted the positional error ε^*_c. The results (shown in Figure 2.7) are very intuitive; as the initial angle of the light ray increases so too does the positional error associated with this. The maximum value seen here is approximately $\varepsilon^*_c = 60\ \mu$m when the ray has an initial angle of approximately $\theta^*_{k,i} = 31$ °. At an initial angle of $\theta^*_{k,i} = 0$ ° the ray does not experience any transverse refractive index gradients. Since it is perpendicular to each isothermal contour, and the transverse temperature gradient is zero, then it does not undergo any refraction and so the positional uncertainty is zero.

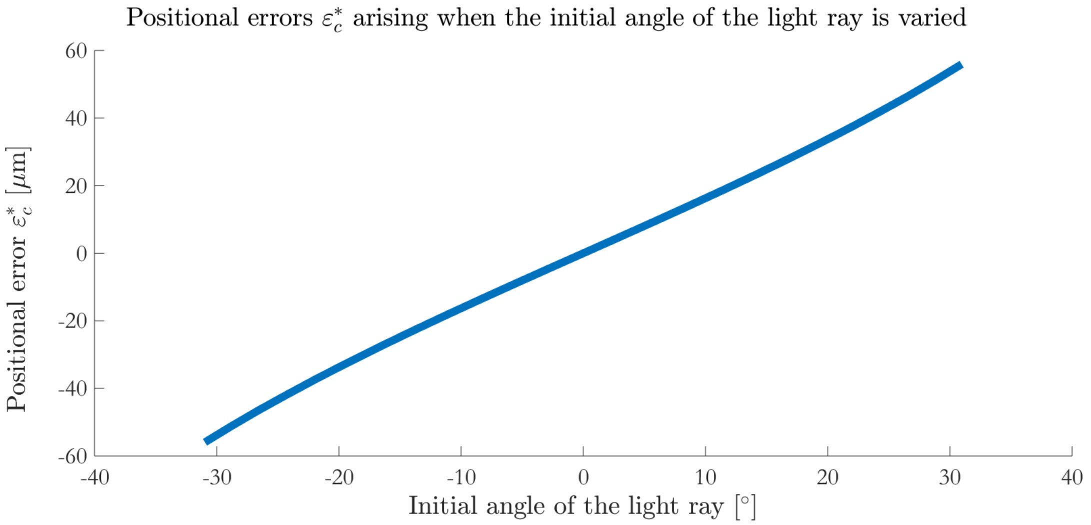

Figure 2.7: Graph showing the positional error ε_c^* of the light rays travelling through the Gaussian temperature profile described in Equation (2.16) when the initial ray angle is varying. The size of the domain is 3 metres by 4 metres in the horizontal (x) and vertical (y) direction respectively. There are 25 rays propagating the domain each with a starting position of (-1.5, 0) and directional vector $x_0 = [1, y_0]$ where x_0 takes the values $\{(1, -0.6), (1, -0.55), (1, -0.50), \ldots (1.0), \ldots, (1, 0.55), (1, 0.6)\}$. The parameters $T_{\max}$, $T_{\min}$ and σ are kept constant throughout at 295 K, 314 K and 1.3107 m respectively

The second study (T2) varied the maximum temperature of the domain, $T_{\max}$ (keeping all other variables constant). This simulation only had one ray propagating through the geometry and the ray that was chosen was the ray whose initial angle led to the largest positional error value in T1. The results in Figure 2.8 show that as $T_{\max}$ increases so too does the error. As $T_{\max}$ increases so too does the local transverse gradient of the temperature (refractive index) profile. It can be seen that the positional uncertainty is now of sub-millimetre scale and would start to cause concern in a high precision manufacturing setting (over tens of metres this would rise to be of millimetre scale).

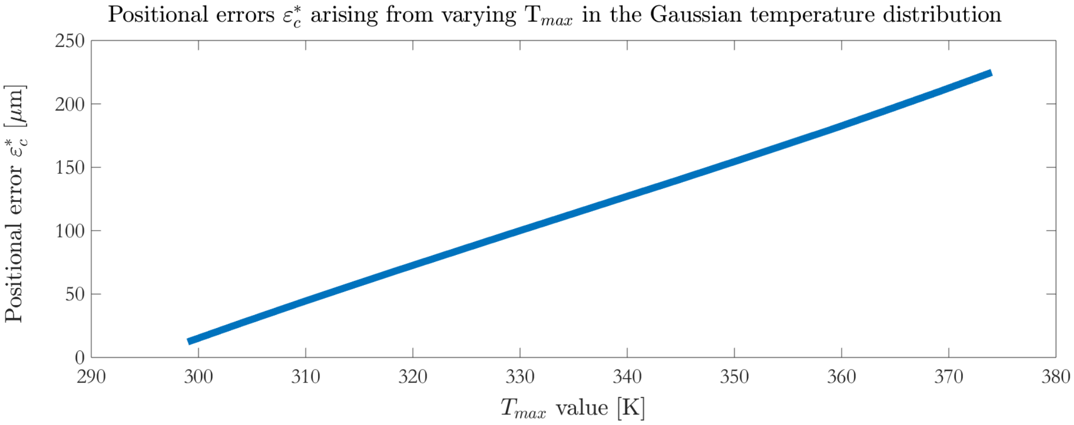

Figure 2.8: Graph showing the positional error ε_c^* of a light ray travelling through the Gaussian temperature described in Equation (2.16) when the range of the temperature profile is varied (via the parameter T_{max}) The size of the domain is 3 metres by 4 metres in the horizontal (x) and vertical (y) direction respectively. The ray in this instance has a directional vector of $x_0 = [1, 0.6]$ as this led to the largest positional uncertainty in T1. The parameters T_{min} and σ are kept constant throughout at 295 K and 1.3107 m respectively. The values for T_{max} are $\{299, 304, \ldots, 374\}$ K.

Finally the variance of the temperature profile was varied (study T3) via the parameter σ. The results (for the same ray direction used in T2) are shown in Figure 2.9. For σ values between 0.5 and 1.1 m the positional uncertainty ε_c^* value increases, until it reaches a maximum at around 60 μm when σ is approximately equal to 0.9 m. Thereafter, the ε_c^* value decreases as σ increases. As σ increases the temperature gradient spreads out becoming less steep in the spatial region considered, and so it is gradually approaching a constant temperature. So the temperature domain resembles that of a homogeneous one, resulting in reduced refractive index effects and hence a lower ε_c^* value. In a similar way when σ is decreased the temperature profile narrows until it forms an isolated peak in the spatial domain considered. The ray now traverses a domain that is far from

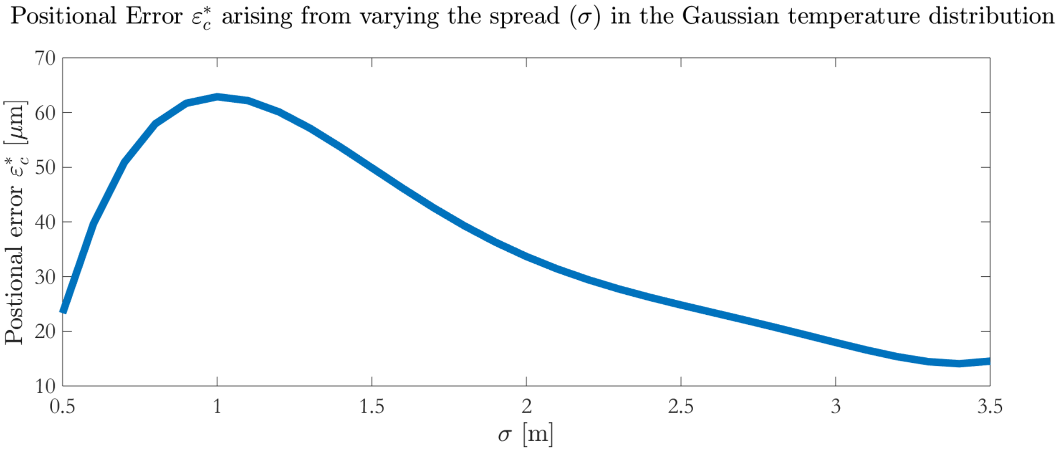

Figure 2.9: Graph showing the positional error ε_c^* of a light ray travelling through the Gaussian temperature described in Equation (2.16) when the spread of the profile (as determined via parameter σ) takes the values from 0.5 to 3.5 metres. The size of the domain is 3 metres by 4 metres in the horizontal (x) and vertical (y) direction respectively. In each of the simulations there is one light ray propagating the geometry, with initial position (-1.5, 0) and directional vector $x_0 = [1, 0.6]$. The variables T_{min} and T_{max} are kept constant throughout the simulations taking the values 295 K and 314 K respectively.

this peak and hence there is a very flat temperature profile; so the resulting positional error is significantly reduced. Hence there is an interim value for σ where the positional error is maximised.

2.3 Chapter Summary

This Chapter looked at how mathematical modelling, and in particular, how a finite element package (COMSOL Multiphysics) can be used to simulate light rays propagating through a spatially heterogeneous refractive index (temperature) map. The equations for calculating transverse temperature gradients (Equation (2.9)) were discussed and it was found that transverse gradients dominate ray refraction.

A simulation of a Gaussian temperature profile which has light rays propagating through it was studied. An investigation into the effect that varying three parameters (initial angle of the ray, the maximum temperature and the temperature variance) had on the positional error were discussed. It was found that changes in the maximum temperature led to the highest error (approximately 220 μm) relative to changes in the initial angle of the ray and the variance.

This Chapter provides some sense of the typical measurement uncertainties associated with deploying photogrammetry sensors in environments with spatially heterogeneous temperature distributions. In the next Chapter some experiments will be described which report on the measurement uncertainties that arise due to spatially varying temperature fluctuations.

Chapter 3

An Experimental Investigation into the Effects of a Localised Heat Source on Photogrammetry Measurement Errors

In the last Chapter it was observed from simulations that submillimetre sized positional errors can arise in industrial sized volumes with reasonable spatial temperature profiles. This Chapter will turn to physical experiments and starts by discussing an experiment to determine the sensitivity of the Vicon T160 Photogrammetry system. Following this, the results from this experiment will be discussed. Finally, this Chapter will introduce the angular field of view of the photogrammetry system and will derive mathematical equations to represent this.

An experiment was carried out to determine the sensitivity of the Vicon T160 photogrammetry system when positioning a cluster of retroreflectors in a spatially heterogeneous refractive index volume; created by applying a localised heat source to the volume. This experiment will be used to comment on the validity of the simulations described in Chapter 2. In order to do so it is also necessary to measure the temperature profile in the working geometry.

3.1 Experimental Setup

Two Vicon T160 cameras (16 megapixel (MP) with standard Vicon 18 mm focal length lens) (Vicon Motion Systems, LA, USA) were mounted on tripods, and these tripods were positioned approximately 3.5 m away from a group of reflectors as shown in Figure 3.1. The cameras were mounted on tripods to mitigate the vibrational effects and were positioned 2.5 m away from one another. Recall that in Subsection 1.3.2, the researchers in [56] observed large positional errors due to the cameras being affixed to a scaffold. There were five retroreflectors all of which were steel and spherical, each with a 3.81 cm diameter. These reflectors were mounted on to a plate attached to the top of a tripod which was approximately 1 m high, as shown in Figure 3.2. This configuration of retroreflectors and the plate they were attached to were manufactured by Vicon and sent to the research team for testing. The cameras will be denoted as c_1 and c_2 and the photogrammetry system records the estimated position of the cluster of the reflectors as the centroid of them; this estimated position will be denoted as $\hat{s}$. Photogrammetry systems use the method of triangulation to estimate the position of objects of interest [39, 48], and so in a two camera setting the intersection point of the light ray paths emitted from the cameras yields the estimated position $\hat{s}$. For the experiments below the two cameras and the cluster of retroreflectors remained in a fixed spatial position.

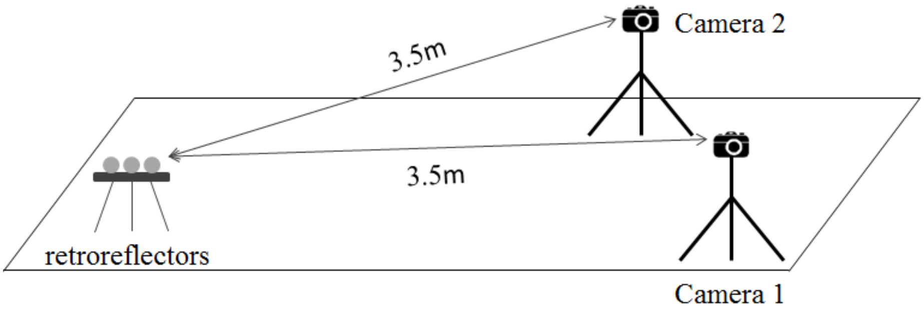

Figure 3.1: Baseline set up of experiment 1 which has two Vicon T160 cameras (16 MP with standard Vicon 18 mm focal length lens) tracking a cluster of stationary reflectors over time. Each camera is positioned approximately 3.5 m from the reflectors.

Figure 3.2: Five steel spherical reflectors of diameter 3.81 cm mounted on a plate on top of a tripod.

The cameras were recalibrated each time the experiments were carried out and, during each calibration of the cameras, 2000 frames were captured using the active wand; the active wand is a T-shaped calibration artefact that has 5 LED sensors. The active artefact minimises the number of data outliers captured as the number of data points that have an obstructed view are reduced as the LEDS are actively lit up [56]. In fact using an active calibration leads to an improvement in the accuracy of 13 % compared with using a passive calibration artefact [56]. A passive artefact is one which reflects infra-red light projected from the camera using standard retroreflectors [56]. The active wand was also used to set the geometry's origin, as shown in Figure 3.3. To set the origin of the geometry the active wand has to be placed in a position where both the cameras can see it; in this case it was placed on the ground. The origin remained in a fixed position throughout all experimentation.

Initially, the experiment was carried out at room temperature and the estimated position ($\hat{s}$) of the retroreflector centroid was monitored over approximately 8 minutes and 20 seconds (time step: 0.02 seconds, number of time steps: 25,000). The estimated position of the reflectors is output as a series of (x, y, z) co-ordinates. This experiment at room temperature can be thought of as a control as it is the closest to a homogeneous refractive index map that can be achieved in the laboratory. In addition to recording the co-ordinates, the temperature of the volume was also recorded throughout using a printed circuit board (PCB) with 8 MCP9808 Precision I2C temperature sensors. These temperate sensors have a typical accuracy of ± 0.5 °C and a maximum accuracy of ± 0.25 °C [137].

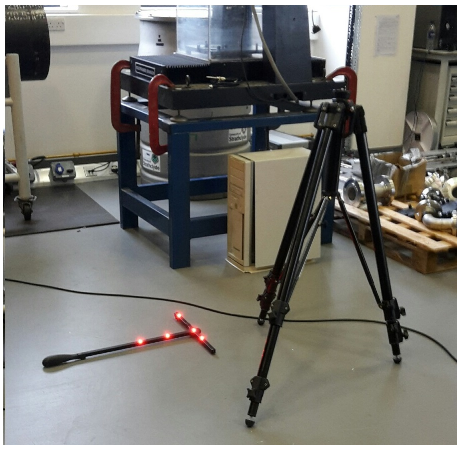

Figure 3.3: Active wand being used to set the origin for the experiment

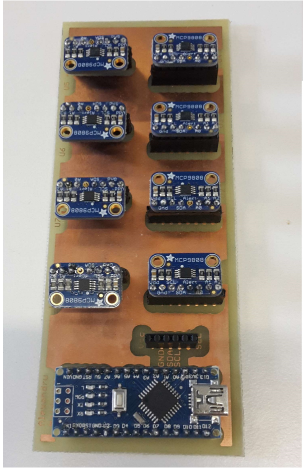

Figure 3.4: PCB board with 8 MCP9808 Precision I2C temperature sensors soldered to it.

This configuration of temperature sensors was designed by a final year project student at the University of Strathclyde, there are 8 temperature sensors on the PCB as this is the maximum number that can fit, and this increased number also increases the reliability of the experimental results. These sensors work by connecting them to a laptop via a MicroUSB cable and they populate a matrix which has 8 columns (one for each sensor) and the number of rows is determined by how long the sensor is plugged in, as readings are taken until the laptop connection is broken. On average the ambient temperature of the laboratory was between 21 °C and 22 °C and it took approximately 2 seconds for the temperature sensor to collect one set of readings. Once these baseline readings were collected, a localised heat source was then introduced to the volume. The heat source used in this experiment was a 1.6 kW halogen heater.

3.2 Experiment 1

Once the estimated position of the reflectors had been tracked over time for the homogeneous refractive index map, the experiment was then repeated but this time the localised heat source was switched on until the laboratory reached a steady state. In Experiment 1, the heat source was placed on the ground between camera c_1 and the cluster of retroreflectors as shown in Figure 3.5, a schematic of which is shown in Figure 3.6. As in the control, 25,000 data points were captured and this experiment was repeated 5 times to increase the reliability of the results. In Experiment 1 the mean temperature of the volume when there was a localised heat source applied to the volume was 51 °C and the maximum temperature was 55 °

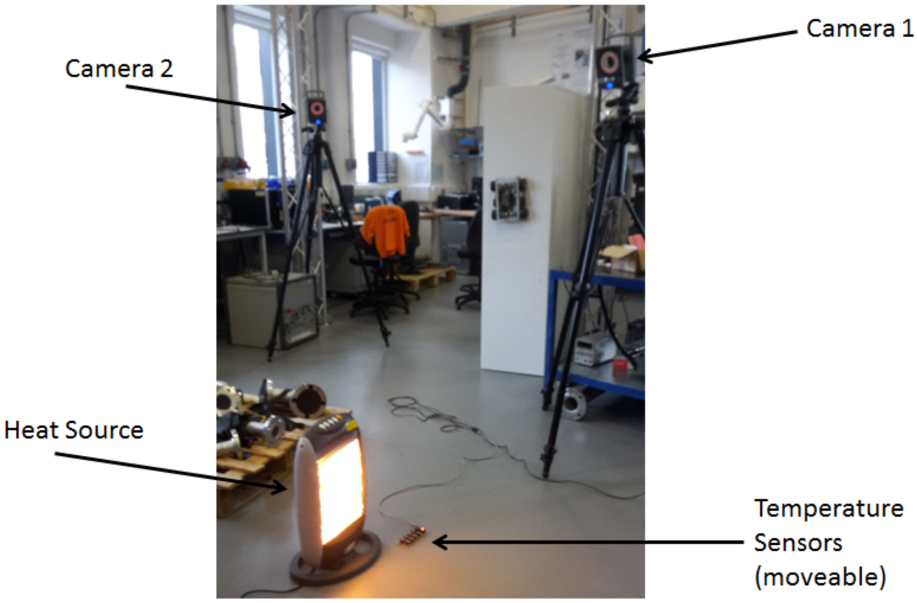

Figure 3.5: Set up of experiment 1 with two Vicon T160 cameras (16 MP with standard Vicon 18 mm focal length lens), the heat source (a 1.6kW Halogen Heater) and a temperature sensor board (a PCB board with 8 MCP9808 temperature sensors soldered to it, shown in Figure 3.4). The cameras are tracking the cluster of retroreflectors (which are out of shot and are pictured in Figure 3.2).

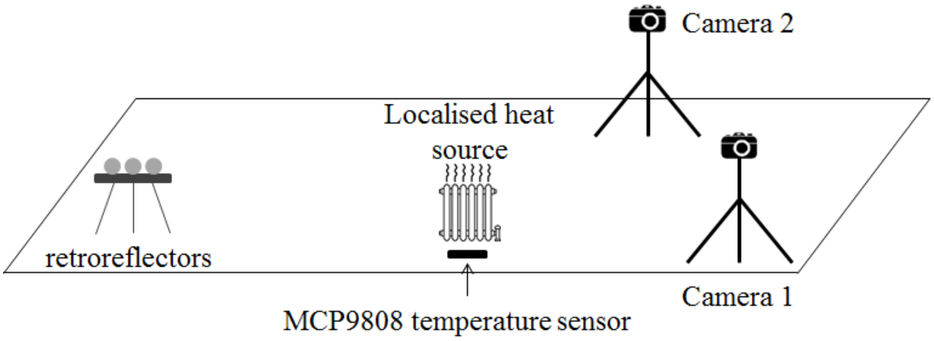

Figure 3.6: Set up of experiment 1, the 2 Vicon cameras and the retroreflectors are positioned in the same position for all experimental iterations. A localised heat source is placed on the ground directly impacting c_1. There is also an MCP9808 temperature sensor placed in front of the heat source measuring the temperature of the volume.

In order to analyse the impact that the heat source has on the estimated position of the cluster of reflectors the data was taken into MATLAB for analysis. The data-set comprised of 25,000 (x, y, z) co-ordinates of the estimated position of the cluster of reflectors when the geometry was a homogeneous refractive index map (localised heat source switched off) and when the geometry was a heterogeneous refractive index map (localised heat source switched on). Since the experiment was repeated five times for each case (the homogeneous and heterogeneous refractive index maps) the mean point at each of the 25,000 iterations was taken. From this a point cloud of the estimated position of the cluster of reflectors was plotted (at each of the 25,000 data points) for the control case (localised heat source switched off) and the heterogeneous (localised heat source switched on) and this point cloud is shown in Figure 3.7.

The positional error was then found for the heterogeneous refractive index map. Define the mean estimated position of the cluster of reflectors (denoted by s^*) for the homogeneous case is taken to be the true position of the reflectors. The mean estimated position of the cluster of reflectors for the heterogeneous case (denoted by $\hat{s}$) is then also calculated. Then the error in the estimated position is the Euclidean distance between these two points, that is, $\varepsilon_c = \|s^* - \hat{s}\|_2$ which was found to be 147 μm for Experiment 1.

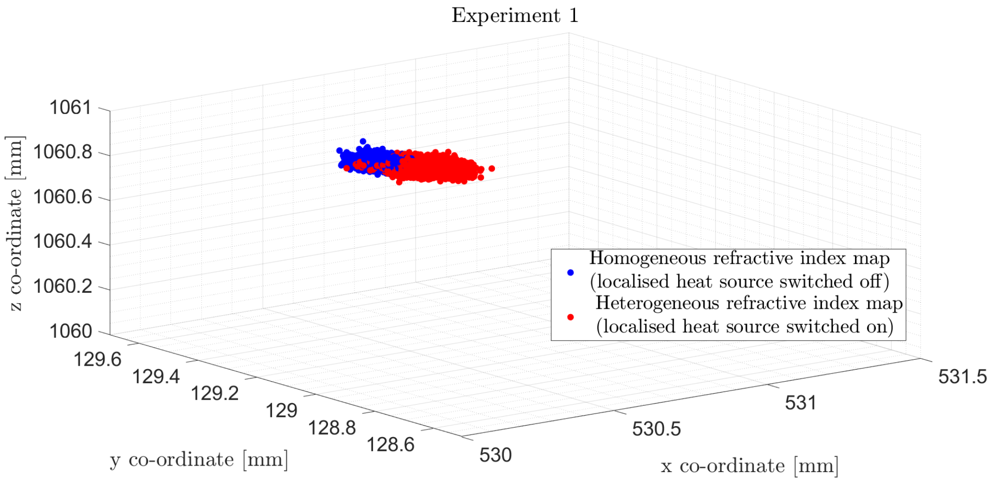

Figure 3.7: Experiment 1: Point cloud showing the (x,y,z) co-ordinates of the reflectors before heat was applied to the volume (blue dots) and after (red dots).

3.3 Experiment 2

Once the temperature of the laboratory had settled back to the ambient temperature of the lab, a new iteration of the experiment was carried out. As in Experiment 1 the position of the reflectors was firstly found in the homogeneous refractive index map (localised heat source switched off). However for the heterogeneous case (localised heat source switched on) this position of the heat source was moved in an attempt to maximise the positional error, ε_c. The heat source was placed in the same location as Experiment 1, that is, between camera c_1 and the reflectors. However, instead of being placed on the floor, the heat source was elevated approximately 70 cm, as shown in Figure 3.8. As in Experiment 1, the estimated position of the retroreflectors and the temperature of the working volume were recorded. As before, Experiment 2 was also repeated five times for increased reliability of results.

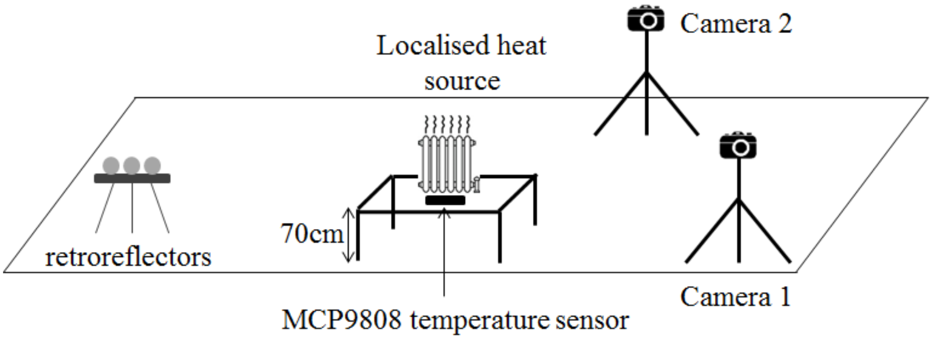

Figure 3.8: Experiment 2 Experimental Set up: The 2 Vicon cameras and the retroreflectors remain in the same position throughout the experiment. A localised heat source is placed 70 cm above the ground and is directly between camera c_1 and the retroreflectors. There is also an MCP9808 temperature sensor placed in front of the heat source measuring the temperature of the volume.

The point clouds depicting $\hat{s}$ for the homogeneous (localised heat source switched off) and heterogeneous (localised heat source switched on) refractive index maps are shown in Figure 3.9. The point cloud depicting the volume with no heat source (blue dots) is slightly more spread out (shows more variance) than that in the heated volume (red dots) in the x-y plane. The reasoning behind this is not clear at this stage, there could be random errors occurring here (see Section 1.2). One way of mitigating these errors would be to repeat the experiments more than 5 times. The point clouds do not overlap as they did in Figure 3.7. It is clear therefore that for Experiment 2 the positional error will be larger than in Experiment 1. The positional error for Experiment 2, ε_c was 679 μm.

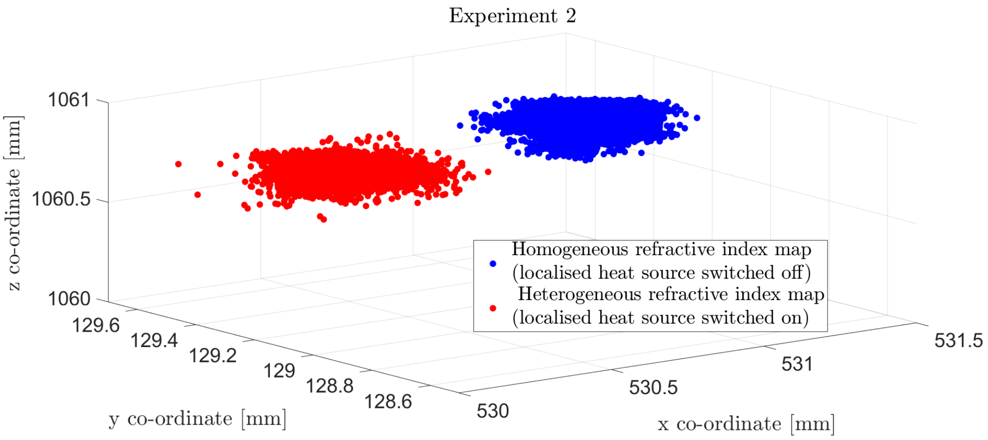

Figure 3.9: Experiment 2: Point cloud showing the (x,y,z) co-ordinates of the reflectors before heat was applied to the volume (blue) and after (red).

3.4 Experiment 3

In the last experiment, it was of interest to see what happens to the estimated position of the reflectors when both cameras were affected by the localised heat source. The heat source was again in an elevated position of approximately 70 cm (as in experiment 2), but, it was placed directly behind the reflectors. The heat source was not placed in front of the reflectors as this obscured the reflectors from the camera's view. Again the experiment was carried out for the spatially homogeneous (no heat source) and heterogeneous (heat source turned on) refractive index maps. As with the other iterations of this experiment, the experiment was repeated five times for the homogeneous and heterogeneous cases to increase reliability of the results. As in Experiments 1 and 2, 25,000 data points were recorded.

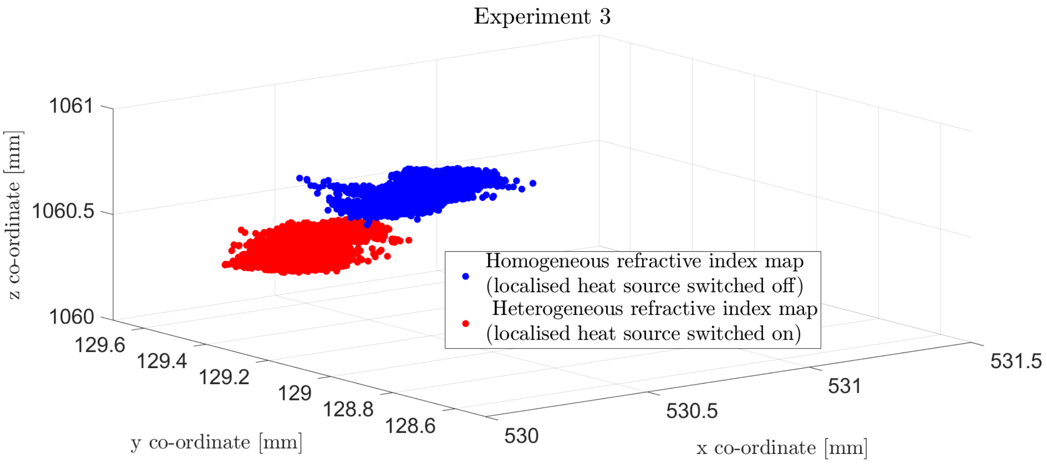

Figure 3.10: Experiment 3: Point cloud showing the centroid of the reflectors when heat is applied to the volume (red point cloud) and when there is no heat applied to the volume (blue point cloud). The distance between the mean centroid position of the reflectors when there is heat applied to the volume and when there is no heat applied to the volume is 421 μm

The point clouds for Experiment 3 are shown in Figure 3.10. It can be seen that the point cloud for the homogeneous refractive index map has more variation in the x-y plane than in the z direction. When the localised heat source is applied to the volume the range of z co-ordinates increases slightly. The mean positional error was found to be 421 μm, which is less than Experiment 2 and a summary of the results for Experiments 1 to 3 can be found in Table 3.1.

3.5 Conclusions and Limitations of the Experiment

This set of experiments showed that the Vicon T160 photogrammetry system is sensitive enough to detect significant positional errors in the retroreflectors caused by heat fluctuations in the working volume. These results are surpris-

Table 3.1: Summary of Experimental results

Experiment	Positional Error [μm]
1	147
2	679
3	421

ing as the VICON system is not optimised for positional accuracy, it is used mainly as a tracking camera in the film industry. However, from the results it can be seen that the VICON system shows a clear movement of a target cluster when the heat source is switched on (and left to stabilise the local temperature gradient). Importantly, the sizes of those errors are submillimetre over a relatively small distance (3.5 m) and such positional errors could be significant in high precision manufacturing scenarios. The positional errors were maximised when the heater was placed in an elevated position such that the region of increased temperature was directly in the path between one of the cameras and the cluster of retroreflectors. It would be expected that the largest positional error ε_c would be achieved when both of the cameras were impacted by the heat source. One reason that this did not happen in Experiment 3 is that the heat source position did not produce an increased transverse temperature gradient; recall from Chapter 2 that this dominates the positional errors. The errors obtained in Chapter 2 are generally smaller than those obtained in Table 3.1 one key reason for this is that the experiment is carried out in three dimensions whilst the simulation was only carried out in two. In addition the simulations allow complete ground truth meanwhile experimentation can introduce other errors (as discussed in Subsection 1.3.2). An additional limitation is that the temperature sensors only measure temperature locally and in subsequent experiments more temperature sensors would be required to measure the temperature dispersion throughout the laboratory. Additional sensors would require more computing power as they only work when connected to a computer or equivalent, this would lead to more computing equipment being required which may be costly.

3.6 Discussion

From the above experiment, it was determined that the Vicon T160 photogrammetry system was indeed capable of detecting a significant change in the observed position of a cluster of reflectors when heat was applied to the volume. However, the point clouds (Figure 3.7, Figure 3.9 and Figure 3.10) show a considerable variation over time. It was expected that the point cloud showing the centroid of the targets when no localised heat source was applied to the volume would have less variation than when there was a heat source applied to the volume. This was not the case and some explanation will be discussed in this section. This will be done by looking at the angular field of view (AFOV) of the Vicon T160 Photogrammetry system. The horizontal and vertical AFOV, $\alpha_{x,y}$, is defined as

$$\tan(\alpha_{x,y}) = \frac{G_{x,y}}{2f}, \tag{3.1}$$

where $G_{x,y}$ is the horizontal (x) or vertical (y) dimension of the sensor measured in millimetres and f is the focal length of the camera measured in millimetres [39, 138]. In the Vicon T160 photogrammetry system the physical sensor size of the camera is 18.35 mm horizontally and 13.48 mm vertically [139]. The digitised sensor size in the horizontal and vertical direction is $N_x = 4704$ and $N_y = 3456$ pixels respectively and the focal length of the camera is 584 pixels. Using ratios the focal length of the Vicon T160 Photogrammetry system is approximately 17.88 mm. Using Equation (3.1) the horizontal and vertical AFOV was calculated to be 0.9481 radians (54.3 °) and 0.7231 radians (41.53 °) respectively.

From Figure 3.11, which shows a schematic of the AFOV of the camera, $\theta_{x,y}$ is the AFOV per pixel and is defined as

$$\theta_{x,y} = \frac{\alpha_{x,y}}{N_{x,y}}. \tag{3.2}$$

From the experiments the distance between the camera and the reflector was roughly 3 m. Hence $\theta_{x,y}$ can also be expressed as

$$\tan\theta_{x,y} = \frac{\nu_{h,v}}{3+B} \approx \frac{y_{h,v}}{3}, \tag{3.3}$$

where B is the depth of the charged coupled device (CCD) and ν is the range of positions captured by one pixel in the CCD. A CCD is a type of sensor used to capture an image by taking light and converting it into digital data. Therefore,

$$\nu_{x,y} = 3 \tan \theta_{x,y} = 3 \tan \left(\frac{\alpha_{x,y}}{N_{x,y}} \right), \tag{3.4}$$

and this was calculated to be $\nu_h = 604.65$ μm in the horizontal direction and $\nu_v = 627.69$ μm in the vertical direction. These values quantify the amount that the targets can move without the photogrammetry system capturing it (the object remains in the same pixel). However, this does not agree with the results from Experiments 1 and 3 which reported positional errors of 147 μm and 421 μm respectively.

To begin to explain this, consider a simple case where a retroreflector is represented on the Vicon system by a square which is 2 pixels in size in both directions as shown in Figure 3.12. The location of each pixel is given by the co-ordinates of the bottom left corner. As mentioned previously, the centroid of the cluster of pixels is the Vicon's estimate of the reflector's position. Therefore, the centroid of the cluster of pixels representing the retroreflector, $\bar{s}$, is (2,2) as marked by the blue cross in Figure 3.12.

Now, consider the case that another pixel has been added to the image due to thermal fluctuations in the refractive index of the volume. Without loss of generality assume that this additional pixel has centroid position (n+1, 1), where

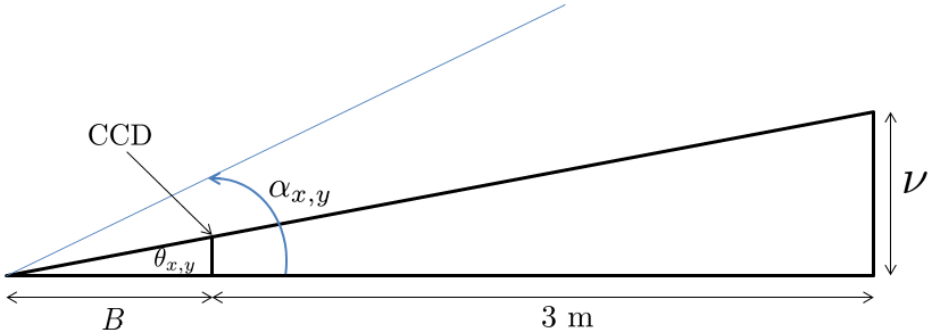

Figure 3.11: Schematic representing the angular field of view of the camera, where $\alpha_{x,y}$ is defined in Equation (3.1), $\theta_{x,y} = \alpha_{x,y}/N_{x,y}$, where $N_{x,y}$ is the number of pixels, B is the depth of the CCD and ν is the range of positions captured by one pixel in the CCD.

n is the side length of the square cluster of pixels. For example, when this additional pixel is added to Figure 3.12 it will have position (3,1) as shown in plot (a) of Figure 3.13. Therefore, the Vicon system will report a new centroid of the cluster, $\bar{s}^*$, which is equal to (2.3, 1.9), shown by the blue cross in the plot (b) of Figure 3.13. The difference between $\bar{s}^*$ and $\bar{s}$ (denoted by Δs), is (0.3, -0.1). This means that the addition of one more pixel caused the centroid of the targets to move by 0.3 pixels to the right and 0.1 pixel downward; a distance of 0.316 pixels which is approximately 190 μm.

To generalise this consider an image consisting of a square with side length n pixels with the bottom left pixel located at $(0.5, 0.5)$. Using the formula for the sum of an arithmetic progression the centroid of this image is $\bar{s} = ((1 + n)/2, (1 + n)/2)$.

Then, when one additional pixel is added with centroid position $(n+1,1)$ to the image the new x co-ordinate of centroid of the retroreflector, $\bar{s}_x^*$ can be expressed as

$$\begin{aligned}
\bar{s}_x^* &= \frac{1}{n^2+1}\left((1+2+\ldots+n)n+(n+1)\right)\\
&= \frac{1}{n^2+1}\left(\frac{n^2}{2}(1+n)+(n+1)\right)\\
&= \frac{(n+1)(n^2+2)}{2(n^2+1)},
\end{aligned} \tag{3.5}$$

Similarly, the y co-ordinate of the centroid of the target when one additional pixel is added to the geometry can be expressed as

$$\begin{aligned}
\bar{s}_y^* &= \frac{1}{n^2+1}\left((1+2+\ldots+n)n+1\right)\\
&= \frac{n^2(1+n)+2}{2(n^2+1)}.
\end{aligned} \tag{3.6}$$

The change in the position of the centroid of the x and y co-ordinates of the target can be expressed as Δ_x, where Δ_x=$\bar{s}_x^* - \bar{s}$, and Δ_y, where Δ_y=$\bar{s}_x^*$-$\bar{s}$ respectively,

$$\Delta_x = \frac{(n+1)(n^2+2)}{2(n^2+1)} - \frac{(1+n)}{2} = \frac{n+1}{2(n^2+1)} \tag{3.7}$$

and

$$\Delta_y = \frac{n^2(1+n)+2}{2(n^2+1)} - \frac{(1+n)}{2} = \frac{1-n}{2(n^2+1)}. \tag{3.8}$$

Now, if the limit as n gets large is considered, then

$$\Delta_x \approx \frac{1}{2n} \text{ , and } \Delta_y \approx \frac{-1}{2n}. \tag{3.9}$$

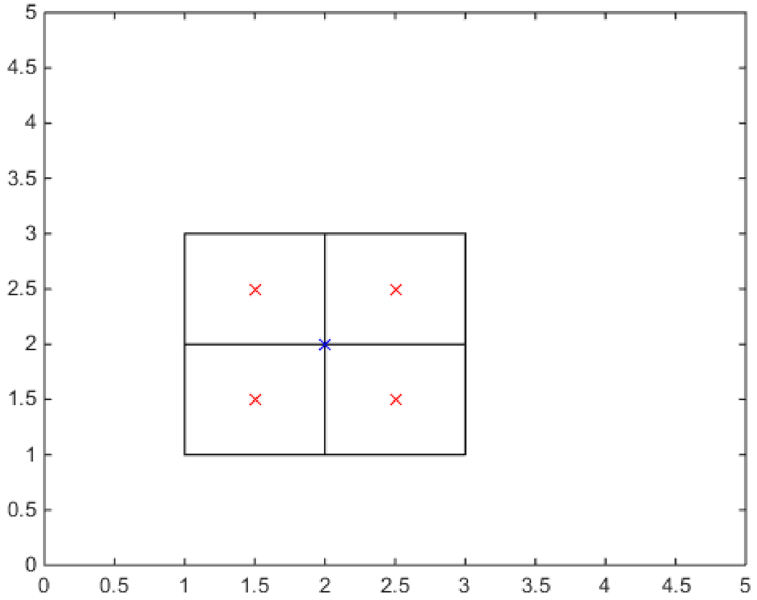

Figure 3.12: A digitised image of a square with side length 2 pixels. The red crosses indicate the centroid of each pixel and the blue cross indicates the centroid of the image. The centroid of the image is the position of the object that the Vicon system reports to the user; (2,2) in this example.

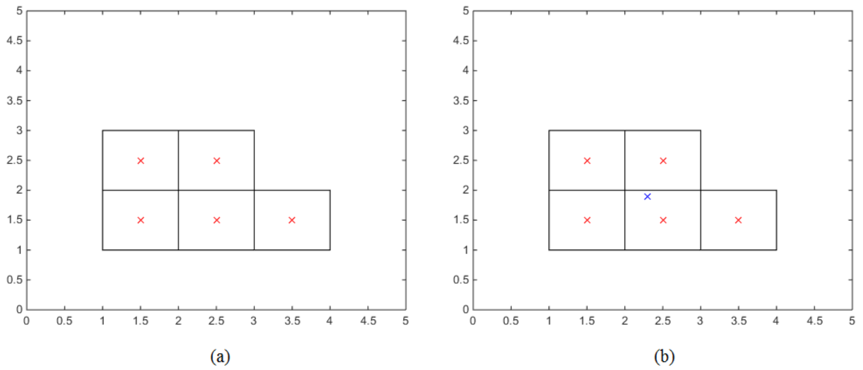

(a)

(b)

Figure 3.13: (a) One additional pixel has been added to the image shown in Figure 3.12. (b) The Vicon system will calculate a new centroid position (blue cross) of (2.3,1.9).

In the experiment a cluster of 5 retroreflectors were used as targets, each retroreflector had a diameter of 3.81 cm, and these were arranged as shown in Figure 3.2. The plate that the targets occupy has a side length of approximately 16 cm as shown schematically in Figure 3.14. Using the information above this equates to a side length of 265 pixels. Using Equation (3.9), with $n = 265$ then $\|\Delta_{x,y}\|_2 \approx 0.002668$ pixels ≈ 1.62 μm. This means that during the experiment the smallest movement that the photogrammetry equipment can detect is approximately 1.62 μm.

During the experiment 25,000 measurements of the position of this cluster of retroreflectors were recorded. The distance between each successive measurement was then calculated to monitor the fluctuations. These distances were then illustrated using two smoothed histograms for the case where no additional heat was added to the volume and when the heat source was added to the volume as shown in Figure 3.15 and Figure 3.16 respectively. If Figure 3.15 is considered firstly, the centroid of adjacent images is most likely to move by between 10 and 20 μm. It can also be seen that 162 distances out of the 24,999 calculated are less than the theoretical value that the centroid position can move by, which accounts for 0.648 % of the data. Secondly, if Figure 3.16 is now considered, it can be seen that the centroid of adjacent images is most likely to move by 10 and 20 μm. It transpires that fewer than 200 distances (0.65 % of the data) are less than the theoretical minimum value that the centroid position can move by, when no heat is applied 17 distances (0.07 % of the data) are less than the theoretical minimum value.

The addition of the localised heat source has resulted in some of the distances between adjacent readings being greater than 100 μm compared with the homogeneous (no localised heat source) case. The addition of the heat source causes the working volume to have larger temperature gradients which in turn causes the light rays to refract more which in turn leads to larger movements between the calculated positions of the adjacent centroids. Note that these calculations only take into account the successive distance between the centroid of the adjacent images and not the cumulative movement of the centroid.

3.7 Conclusions

This Chapter introduced physical experimentation, the aim of which was to show that the Vicon T160 photogrammetry system was sensitive enough to detect submillimetre errors in position caused by thermal fluctuations. The experiment

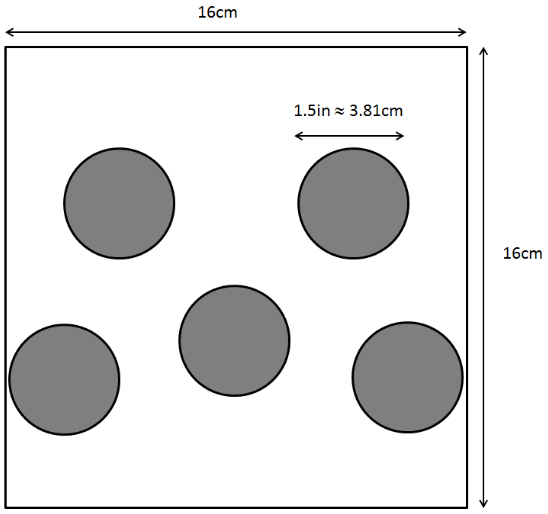

Figure 3.14: Schematic of the five targets used in the experiment. Each target had a diameter of 1.5 inches, the schematic shows a bounding box around the targets of 16 cm which is approximately 265 pixels.

used two Vicon T160 cameras tracked a cluster of retroreflectors. A 1.6 kW heater was used as the localised heat source and when this was switched on it generated a heterogeneous refractive index map. When the heater was switched off the spatial domain was assumed to have a homogeneous refractive index map.

It was found that when the heat source was affecting only one of the camera's light ray trajectory, the positional error was 679 μm. These positional errors confirm the findings of Chapter 2 and show that submillimetre sized positional errors can arise in laboratory sized volumes.

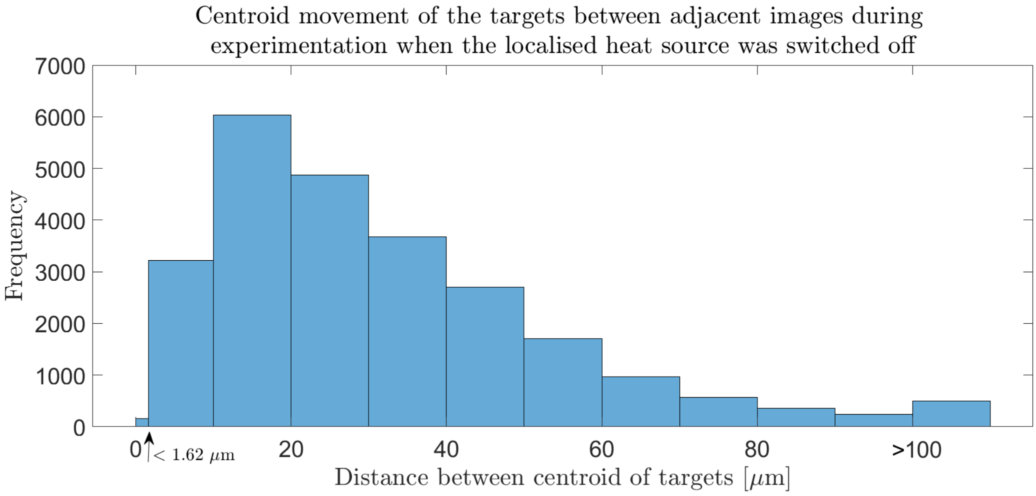

Figure 3.15: Histogram showing the frequency between the adjacent distances between the centroid of the pixel image. In this case the homogeneous refractive index case (no additional heat source) was considered

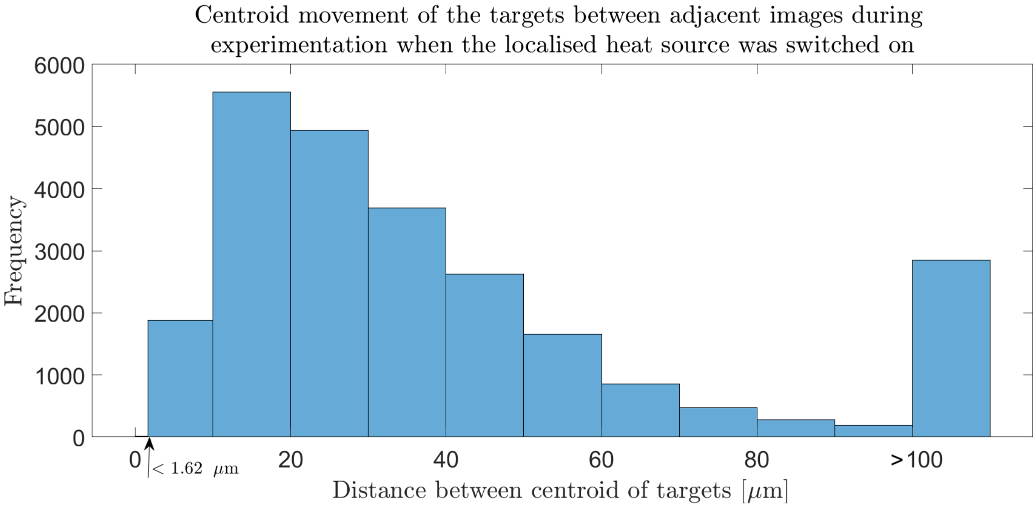

Figure 3.16: Histogram showing the frequency between the adjacent distances between the centroid of the pixel image. In this case the heterogeneous refractive index (additional heat source is switched on) case was considered.

Mathematical formulae were derived which illustrate the amount that the centroid of a target can move, following the addition of another pixel to the image of the retroreflector. It was found that approximately 99 % of the adjacent centroid movements of the data points captured by the cameras were within the range of movement calculated using the formulae.

The next Chapter will introduce a methodology to recover the spatial refractive index map and this map will be used to reduce these refraction effects.

Chapter 4

The Inverse Problem of Reconstructing Refractive Index Maps from Photogrammetry Data

This thesis endeavours to tackle a long-standing problem in large volume metrology. The challenge is to use photogrammetry sensor data to reconstruct the refractive index map in a 2D plane and in so doing reduce the measurement uncertainty arising from light refraction in heterogeneous media. From the literature it is known that sub-millimetre errors in the position of a target cause significant problems [56, 63, 64, 66]. This chapter will outline a methodology to reconstruct refractive index maps and will discuss preliminary results using this method on simulated data. The refractive index map is recovered by solving an inverse problem and a Bayesian approach, namely the reversible jump Markov Chain Monte Carlo method (rj-MCMC) [140], is used as the optimisation method in the inversion. This recovered refractive index map is then used to discount the effect of variations in this refractive index field in the positioning of reflector targets. This reduction in uncertainty in this metrology system will enable this technology to be used in large volume manufacturing environments for robot pose calculations. The pose of the robot is its location and orientation, which in this case, is reported in two dimensions.

The inverse problem will be tackled using five building blocks. To begin with the heterogeneous spatial domain will be parametrised. Then a fast forward solver to predict the ray paths is built. An objective function will be defined to measure the distance between the measured (synthetic) data and this modelled data. A means of minimising this objective function to reconstruct the refractive index maps will then be proposed. Finally, this recovered map will be used to produce an improved prediction of a given target in the spatial domain.

4.1 Parametrisation of The Refractive Index Map

As mentioned in Chapter 1, Voronoi tessellations will be used to parametrise the refractive index map. The method for generating Voronoi tessellations will be discussed in Section 4.6. In this case, the Voronoi tessellation will be generated from a set of $P^{(j)}$ randomly chosen seeds. The Voronoi seed locations are denoted by $\underline{x}_p^{(j)}$ and each Voronoi cell is assigned a single refractive index $\eta_p^{(j)}$, where $p = 1, \ldots, P^{(j)}$. Voronoi tessellations can achieve adaptive and irregular partitions which in turn produces a low dimensional model (low degrees of freedom) whilst affecting large regions with a single parameter perturbation. The map realisation at iteration j of the model is denoted by $m^{(j)}$. Since the Voronoi seeds are in two dimensions, they have two co-ordinates and within each Voronoi cell there is a constant refractive index, hence the dimension (degrees of freedom) of $m^{(j)}$ is $3P^{(j)}$.

4.2 Modelling the Light Ray Propagation in a Heterogeneous Refractive Index Map

For each camera (c_k, where $k = 1, \ldots, C$) and retroreflector (r_i, where $i = 1, \ldots, R$) the ray tracing algorithm (forward model) will generate an estimated angle denoted by $\theta_{k,i}$ with the measured (simulated) angle denoted by $\theta^*_{k,i}$. All angles are measured anticlockwise relative to the horizontal axis.

Using COMSOL for the forward model would be computationally prohibitive, would be difficult to automate and embed within the inversion algorithm, and would lead to the 'inverse crime' of using the same forward model as that used to generate the synthetic data. The Fast Marching Method (FMM) [114, 141] is used to calculate the ray paths through the Voronoi tessellation. The FMM is a fast means of calculating time fields, and this will enable the inversion algorithm to make many forward model calculations and have many model realisations. The FMM is used as an alternative to Dijkstra's algorithm [142]. One advantage of the FMM over Dijsktra's algorithm is that as the grid size tends to zero, the FMM converges towards the correct solution.

Fermat's Principle states that a light ray travelling between two points will take the path which takes the least amount of time [73]. Consider the light ray path between the camera, c_k, and the retro-reflector, r_i, and then using Fermat's principle the time taken, t, for the ray of light following path $r(Q)$, where Q is a length of the ray measured from a fixed point, is defined by

$$t = \frac{1}{c_\infty} \int_{c_k}^{r_i} \eta(r(Q))dQ, \tag{4.1}$$

where c_∞ is the speed of light in a vacuum, $\eta(r(Q))$ is the refractive index along the path which takes the shortest time between c_k and r_i, and dQ is a small displacement along the ray. Following this, the optical path length S between the camera, c_k, and the retro-reflector, r_i, is

$$S = \int_{c_k}^{r_i} \eta(r(Q))dQ, \tag{4.2}$$

where $S = c_\infty t$. Using the calculus of variations

$$\Delta S = \Delta \int_{c_k}^{r_i} \eta(r(Q))dQ = 0, \tag{4.3}$$

where Δ is the change in optical path length, and this means that the path $r(Q)$ satisfies Fermat's principle.

4.2.1 The Fast Marching Method

The mathematics behind the Fast Marching Method (FMM) have been discussed in Section 1.9, but a brief summary is provided here. However, this section builds from what was presented in Section 1.9 and puts it in the context of the inverse problem.

The FMM is used to solve a boundary value problem of the Eikonal equation(see Equation (1.15))to calculate the travel time field. Once the travel time field is calculated, the ray that takes the shortest time to travel between the camera c_k and the reflector r_i, can be found using Fermat's Principle of the Shortest Path. There is a uniform grid with grid side length w, and each intersection point on the grid is denoted by $\lambda_{x,y}$. Then the intersection points are classified into *far*, *narrow band* and *known* and a description of this process is presented in Section 1.9. Then using this travel time field the optical path which took the shortest time is found.

The Fast Marching Method code (and the entire inversion algorithm) is written in FORTRAN 90 and ran on the University of Strathclyde's super computer Archie West. This code was originally developed for the seismology community, in particular the University of Edinburgh's School of Geosciences [101, 131]. The algorithm was then passed on the University of Strathclyde where it was updated to be used within the field non-destructive testing for flaw detection using ultrasonics [90]. Then finally, the algorithm was edited so that it could be used within this thesis for large volume metrology. Due to this code originally being developed for seismology, the algorithm is optimised at large volumes (in the order of km). This meant that all dimensions within this algorithm had to be scaled by a factor of 1000. The size of w in the algorithm is 5 m. Using the aforementioned scaling this yields a grid size of 5 mm. An investigation into grid size and accuracy of results was carried out. It was found that a grid size within the algorithm of 5 m was the smallest grid size which did not cause the code to crash. It is for this reason that the grid size within the algorithm is 5 m.

4.3 Objective function between the Modelled and Measured Data

Photogrammetry systems output the angles, $\theta^*_{k,i}$, between each camera, c_k, and the objects it is tracking, r_i. The likelihood function which accounts for the misfit between the observed data, $\theta^*_{k,i}$, and the data arising from the model $\theta^{(j)}_{k,i}$, is denoted by

$$\mathcal{L} = \exp\left(\frac{-\gamma^{(j)}\left(\eta_p^{(j)}, \underline{x}_p^{(j)}\right)}{\left(\zeta^{(j)}\right)^2}\right). \tag{4.4}$$

where $\zeta^{(j)}$ is the noise parameter and $\gamma^{(j)}$ (measured in degrees) is the objective function (misfit) at iteration j given by

$$\gamma^{(j)}\left(\eta_p^{(j)}, \underline{x}_p^{(j)}\right) = \frac{\sum_{(k,i)\in\Phi}^{N_{rays}}\left(\left|\theta^*_{k,i} - \theta^{(j)}_{k,i}\left(\eta_p^{(j)}, \underline{x}_p^{(j)}\right)\right|\right)^2}{N_{rays}}. \tag{4.5}$$

The set of camera-reflector pairs is denoted by Φ, where $\Phi : \mathcal{C} \rightarrow \mathcal{R}$ maps the set of cameras $\mathcal{C} = \{c_1, c_2, \dots c_C\}$ to the set of reflectors $\mathcal{R} = \{r_1, r_2, \dots r_R\}$ and $N_{rays} = |\Phi|$.

Given the discretised ray-path the angle $\theta_{k,i}^{(j)}$ is calculated using what will be referred to in subsequent chapters as the δ method. To begin with, the agreement between the known angle $\theta_{k,i}^{*}$ and the estimated angle at model iteration zero, $\theta_{k,i}^{(0)}$ (calculated from the FMM applied to the known refractive index material map) will be examined. The angle, $\theta_{k,i}^{(0)}$, was calculated by finding the gradient between the starting point of the ray (at the camera c_k) and each subsequent point of the discretised ray in the first δ % of the ray-points. The mean of these gradients was found for each ray and this was converted into an angle (measured in degrees), where $0 \leq \theta_{k,i}^{(0)} \leq 360$. The results of this are shown in Figure 4.1 for the cases where $\delta = 10, 30, 50, 70, 90$ and 100 % have been plotted versus the known angle $\theta_{k,i}^{*}$. The figures also include the Pearson correlation coefficient χ and it can be seen that as δ increased so too did χ. The outliers in Figure 4.1 are due to the fact that $0 \leq \theta_{k,i}^{*}, \theta_{k,i}^{(0)} \geq 360$. If for example $\theta_{k,i}^{*}$ is 356 ° and $\theta_{k,i}^{(0)}$ is 5 °, then due to directional statistics this leads to large errors which is the reason for these outliers. Based on these investigations and to reduce the number of outliers, the most robust algorithm was to use all the points of the ray to calculate $\theta_{k,i}^{(0)}$.

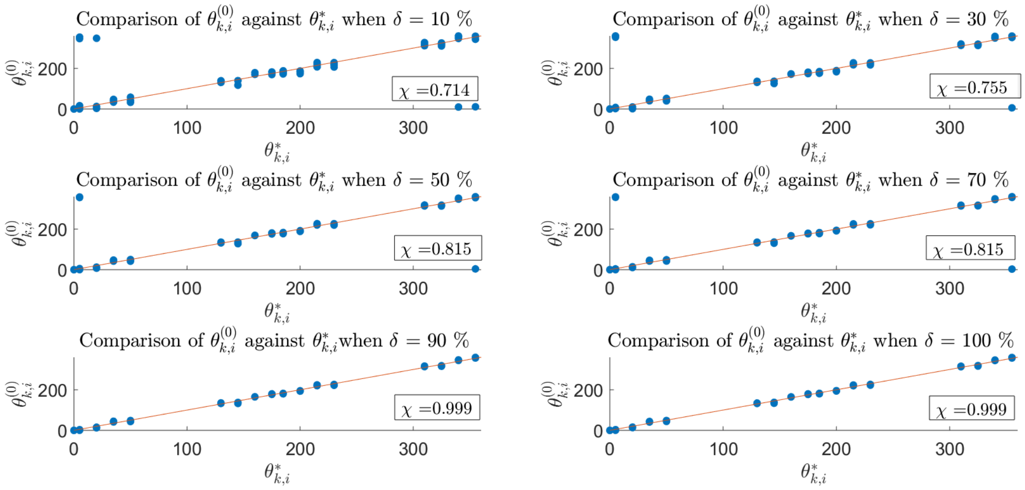

Figure 4.1: Scatter-plots of $\theta^{(0)}_{k,i}$ against $\theta^*_{k,i}$ when $\delta = 10$ %, 30 %, 50 % , 70 %, 90 % and 100 %, where $\theta^*_{k,i}$ is the true angle from the camera (from synthetic data) to the receiver and $\theta^{(0)}_{k,i}$ is the estimated angle from the FMM. The correlation coefficient is given for each percentage of the FMM ray used, δ, and the red line denotes $\theta^{(0)}_{k,i} = \theta^*_{k,i}$.

In addition, the average relative error in the camera-reflector ray angles at iteration zero (of the inversion algorithm) is denoted by $\xi^{(0)}$ where

$$\xi^{(0)} = \left(\sum_{k,i=1}^{N_{rays}} |\theta^*_{k,i} - \theta^{(0)}_{k,i}| / \theta^*_{k,i} \right) / N_{rays} \tag{4.6}$$

where $k, i \in \Phi$, $\theta^*_{k,i}$ is the measured angle and $\theta^{(0)}_{k,i}$ is the angle estimated by the FMM before the first iteration of the inversion algorithm. Since the inversion algorithm is not involved in this metric, then it is independent of the noise parameter $\zeta^{(0)}$. A series of test refractive index maps (denoted by m^*) were created in COMSOL. In this case m^* takes the form of a Voronoi tessellation with ten Voronoi cells. The positions of the Voronoi seeds, $\underline{x}^*_p$, were equal to those in Figure 4.2. The refractive indices, η_p^*, were selected from the set $\{1.005, 1.0075, 1.01, \ldots, 1.0275\}$ and this equates to a refractive index change of 2.2 % relative to the lowest refractive index value, more details of this refractive index map can be found in Section 4.7.

The $\xi^{(0)}$ value when the known map m^* was used was found to be 0.0575 and when there was a homogeneous refractive index map, m^h, $\xi^{(0)}$ was found to be 0.0583. As expected the known refractive index map produced a lower $\xi^{(0)}$ value but not much lower. This is due to the fact that the refractive index map only has changes of 2.2 % and will therefore not lead to large refractive effects and hence large changes in $\xi^{(0)}$. This process was repeated with a series of randomly chosen refractive index maps which could take an unrestricted number of Voronoi cells, but the refractive indices were restricted to the range 1.005 to 1.0275. One hundred samples were collected and a histogram of the values is shown in Figure 4.3. From this figure, it can be seen that there are cases where a random refractive index map produces a lower $\xi^{(0)}$ value than that arising from the known map m^*. This can be attributed to the inversion process using a different ray tracing algorithm (FMM) than COMSOL. It is entirely possible for a refractive index map with a low $\xi^{(0)}$ value to produce an improvement in the uncertainty of the position an object, and that is deemed an acceptable result in this thesis. It should be observed that the value from the known map occurs around the average.

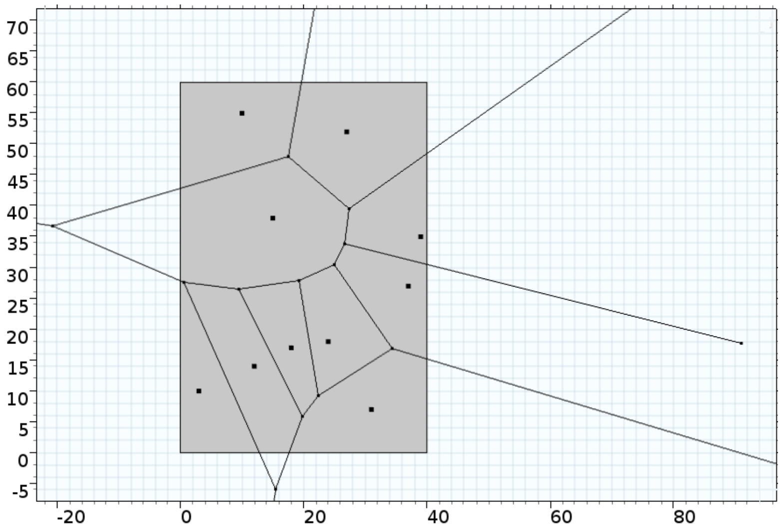

Figure 4.2: This plot shows the Voronoi tessellation that was created in COMSOL with the LiveLink functionality. The black squares within each cell are the set of seeds $P^{(0)}$, the lines are the edges of the Voronoi cells and a bounding box (greyed out area) of 40 m in the horizontal and 60 m in the vertical has been created with the lower left corner positioned at the origin.

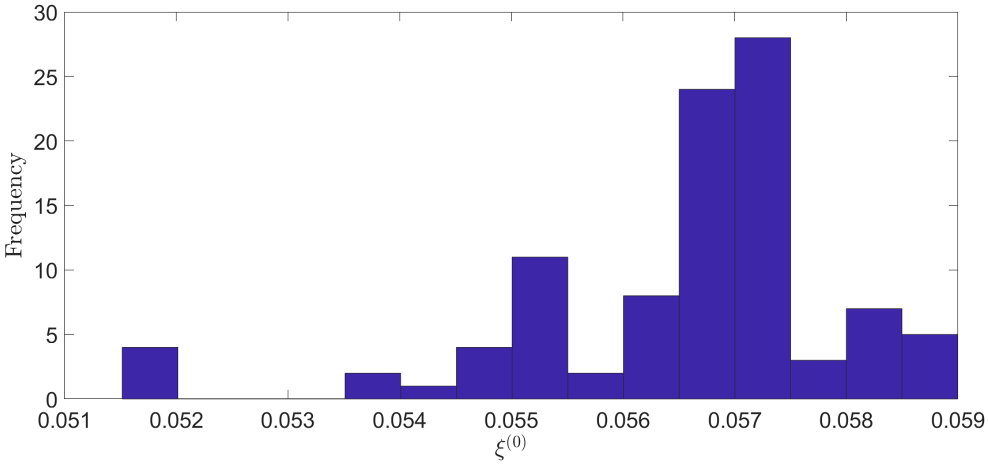

Figure 4.3: Histogram of the average relative error in the angles, $\xi^{(0)}$, (Equation (4.6)) when a random Voronoi tessellation is used and the sample size is 100.

4.4 Recovery of the Refractive Index Map via a Bayesian Approach

The reversible jump Markov Chain Monte Carlo (rj-MCMC) [140] method was employed for the optimisation step. The reversible jump variant of the MCMC was chosen to allow there to be a transdimensional aspect to the model. This means that the number of Voronoi seeds is not fixed throughout the model and allows more flexibility. The rj-MCMC is a stochastic iterative process and is used to create samples from the posterior distribution; the unknown probability distribution describing the likelihood of each Voronoi tessellation being the reconstructed refractive index map. The approach relies on Bayes' Theorem [125]

$$p\left(m^{(j)} \mid \theta^*_{k,i}\right) = \frac{p\left(\theta^*_{k,i} \mid m^{(j)}\right) p\left(m^{(j)}\right)}{p\left(\theta^*_{k,i}\right)}, \tag{4.7}$$

where $p\left(m^{(j)}\right)$ is a probability density function representing the prior knowledge of the model $m^{(j)}$, the likelihood of observing the data $\theta^*_{k,i}$ given a particular model $m^{(j)}$ is $p\left(\theta^*_{k,i} \mid m^{(j)}\right)$, the posterior distribution which describes the probability of $m^{(j)}$ being the refractive index map m^* given the data $\theta^*_{k,i}$ is $p\left(m^{(j)} \mid \theta^*_{k,i}\right)$ and $p\left(\theta^*_{k,i}\right)$ is a probability density function representing observing the known angles $\theta^*_{k,i}$. This then leads to

$$p\left(m^{(j)} \mid \theta^*_{k,i}\right) \propto p\left(\theta^*_{k,i} \mid m^{(j)}\right) p\left(m^{(j)}\right). \tag{4.8}$$

Notice that $p\left(\theta^*_{k,i}\right)$ has been neglected in Equation (4.8) as it is a constant and serves as a normalising factor. The least squares misfit function can then be used to form the likelihood model

$$p\left(\theta^*_{k,i} \mid m^{(j)}\right) \propto \exp\left(\frac{-\gamma^{(j)}\left(\eta_p^{(j)}, \underline{x}_p^{(j)}\right)}{\left(\zeta^{(j)}\right)^2}\right), \tag{4.9}$$

where $\zeta^{(j)}$ is the system noise parameter at model iteration j. There is no noise at iteration $j = 0$, so it is not part of the initial model m^*.

The initial prior probability density function $p\left(m^{(0)}\right)$ is derived from any information which is known a priori, such as the dimensions of the space and the likely range of refractive indices.

At each iteration the Voronoi tessellation model of the refractive index map, $m^{(j)}$ is perturbed to make a new model $m^{(j+1)}$. This can be done in one of five ways: cell birth, cell death, seed move, cell refractive index change or system noise change [100]. There are of course more ways to perturb the model, but this algorithm only uses the aforementioned perturbations. The cell birth step is when an additional Voronoi cell seed is added to the model. The cell death step is the opposite of the birth step and this is where a Voronoi cell seed is removed from the current model. The cell move step is where a randomly selected Voronoi seed $\underline{x}_p^{(j)}$ is moved. The refractive index change step is where a refractive index, $\eta_p^{(j)}$, is changed and lastly the random noise change is when the value of $\zeta^{(j)}$ is changed in Equation (4.5). A change in $\zeta^{(j)}$ is the only perturbation which does not require the rays to be re-traced through the new model $m^{(j)}$. At each iteration of the model a number between 1 and 5 is drawn from a uniform distribution and the outcome determines what perturbation step is taken. When the user is setting up the algorithm in the first instance the range of Voronoi seeds is given as an input. In this thesis, the smallest number of Voronoi seeds that $m^{(j)}$ could have was 5 and the upper limit of the range was 500. As a result of this condition if the algorithm is doing the same perturbation repeatedly this initial condition prohibits the algorithm from getting stuck.

Since the rj-MCMC is an iterative process, at each iteration the algorithm decides whether or not to replace the existing model $m^{(j)}$ with the new perturbed one, $m^{(j+1)}$, using the Metropolis-Hastings criterion [127, 128]. The probability of acceptance depends on the ratio of the probabilities arising from the posterior distributions of $m^{(j)}$ and $m^{(j+1)}$ via

$$p\left(\text{accept}\right) = \min\left(1, \frac{p\left(m^{(j+1)} \mid \theta^{*}_{k,i}\right)}{p\left(m^{(j)} \mid \theta^{*}_{k,i}\right)} \times \frac{q\left(m^{(j)} \mid m^{(j+1)}\right)}{q\left(m^{(j+1)} \mid m^{(j)}\right)}\right) \tag{4.10}$$

where in general terms $q = 1-p$, that is, $q\left(m^{(j)} \mid m^{(j+1)}\right) = 1-p\left(m^{(j)} \mid m^{(j+1)}\right)$. In this case, $q\left(m^{(j)} \mid m^{(j+1)}\right)/q\left(m^{(j+1)} \mid m^{(j)}\right)$ is the ratio of the proposal distributions. Here $q\left(m^{(j+1)} \mid m^{(j)}\right)$ is the probability of moving to model $m^{(j+1)}$ from $m^{(j)}$, this is called the forward step, whilst $q\left(m^{(j)} \mid m^{(j+1)}\right)$ is the reverse step. For a transdimensional move, that is, cell birth or cell death moves, the ratio of the proposal distributions is equal to 1 [90, 100]. This method has been implemented by researchers in the fields of geosciences and non-destructive testing

[90, 101, 131]. The first set of iterations of the model (of the Markov chain) is referred to as the burn-in period. The burn-in period is required to allow the Markov chain to converge to the estimated posterior distribution from which the samples are taken.

From the literature an acceptance rate after the burn-in period of between 25 % and 50 % is desired [95, 143]. However, since this is the first application of this technique to recovering refractive index maps, it is not clear which acceptance rate will be optimal. It can be seen that as the value of $\zeta^{(j)}$ increases in Equation (4.9) then $p\left(\theta_{k,i}^{*} \mid m^{(j)}\right)$ will tend to one, and, as the $\zeta^{(j)}$ value decreases towards zero, $p\left(\theta_{k,i}^{*} \mid m^{(j)}\right)$ will tend to zero. Hence $\zeta^{(j)}$ can be changed to alter the probability of accepting an inferior model (a higher objective function value). This is important as, due to the many local minima present in the objective function hyper-surface, a global optimisation method is required that has a probability of escaping from a local minimum as the method iterates. If the posterior value of the perturbed model, $m^{(j+1)}$, is greater than the value in the current model then the new model is always accepted according to Equation (4.10). However, if the posterior value is lower it is accepted with probability equal to the ratio of the posteriors. So the noise parameter is automatically adjusted as the inversion algorithm iterates to achieve an optimal acceptance rate.

The main output of the inversion process is a reconstructed refractive index map which can be estimated by the mean, median or the maximum-a-posteriori of the posterior distribution on refractive index at each point in the domain. The maximum-a-posteriori (MAP) is in fact the mode of the posterior distribution.

One of the advantages of using a probabilistic method is that higher moments of the posterior distribution of refractive index maps can automatically be accessed and so one can observe where the method is struggling to find an optimal solution (high variance). In addition, statements can also be made about the level of uncertainty associated with any metrology related statements.

4.5 Quantifying the Measurement Uncertainty

To quantify whether or not the recovered refractive index map produced a better estimate of objects of interest (s^*) than the homogeneous refractive index map, a reflector in a fixed, known position s^*, was introduced into the domain to mimic a robot or a component to be worked upon. Let the error in the position of the reflector when the domain is assumed homogeneous be denoted by ε_h, where $\varepsilon_h = \left\| s^* - \hat{s}_h(\theta^*_{k,s}) \right\|_2$ and $\hat{s}_h(\theta^*_{k,s})$ is the estimated position when the domain is assumed to be homogeneous; that is, the rays are assumed to be straight. The position of the object can be estimated using a recovered refractive index map (either the mean, median or MAP of the posterior distribution), which is denoted by $\hat{m}$. The error in position using the recovered map is denoted by ε_α where $\varepsilon_\alpha = \left\| s^* - \hat{s}_\alpha(\theta^*_{k,s}, \hat{m}) \right\|$, where $\hat{s}_\alpha(\theta^*_{k,s}, \hat{m})$ is the estimated position of the reflector; here map $\hat{m}$ is used and so refractive effects are included. In addition the relative improvement of the error in the position of the object of interest when compared to the homogeneous case is defined by $\varepsilon_{imp} = (\varepsilon_h - \varepsilon_\alpha)/\varepsilon_h$. The goal of this work is therefore to find a map such that $\varepsilon_\alpha \ll \varepsilon_h$ and also to reduce the uncertainty, that is, $\mathcal{V}(\varepsilon_\alpha) \ll \mathcal{V}(\varepsilon_h)$, where $\mathcal{V}$ is the error variance, which is calculated by taking the Euclidean distances from each of the line intersections to the true position of the reflector, s^* and calculating their variance. This is implemented in COMSOL and MATLAB, and the method is discussed at the end of this Section. The relative improvement of the variance when compared to the homogeneous case is defined to be $\mathcal{V}_{imp} = (\mathcal{V}(\varepsilon_h) - \mathcal{V}(\varepsilon_\alpha))/\mathcal{V}(\varepsilon_h)$.

One limitation of COMSOL is that it is not possible to define the start and the end point of a ray, as this is an initial value problem; details of this and the equations governing COMSOL can be found in Equation (1.12) and Equation (1.14). Instead the start point, the initial directional vector and the length of the ray are prescribed. The following method for generating camera and reflector positions was devised. This starts with a known refractive index map m^* as shown in Figure 4.4 (creation of the known refractive index map m^* is discussed in Section 4.6).It should be noted that COMSOL is being used in an application that it was never designed to be used for, and as a result, these limitations are due to the application of the software in this particular field of study. From a prescribed spatial position s^*, C rays were released; each with a distinct direction but the same length. The end point of each ray is then used to define the camera positions c_k. The angles $\theta^*_{k,s}$ that each ray from s^* enters the camera c_k was then recorded.

In order to calculate $\hat{s}_h$, a homogeneous spatial domain was then created in COMSOL (the mean refractive index of the above map was chosen but any value will suffice of course). Then from each camera c_k a single straight ray with angle

$\theta^*_{k,s}$ was released; the rays propagate until they reach the edge of the domain. The set of discrete points of each ray were input into MATLAB (version 2017b) [144]. Photogrammetry systems use the method of triangulation to estimate the position of an object in space [39, 48] (see Figure 2.2). All the intersection points of these rays were obtained and then the centre of mass of the resulting point cloud was found and this produced an estimate of $\hat{s}_h$. This process was then repeated for the recovered refractive index map (typically the mean, or median, or mode of the posterior distribution) and an estimate for the reflector position $\hat{s}_\alpha$ was found.

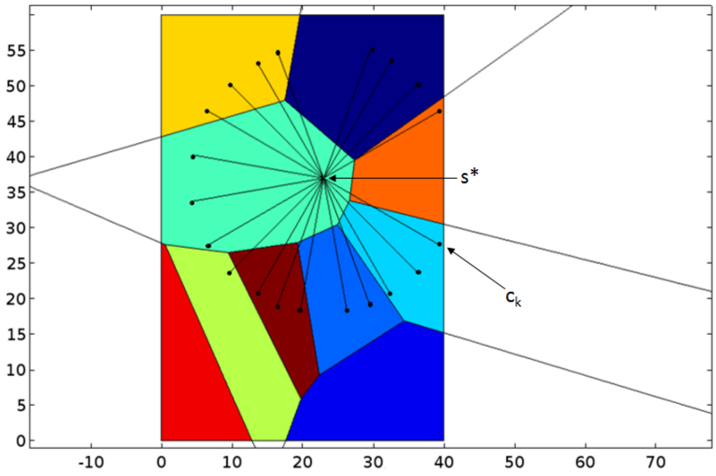

Figure 4.4: A refractive index map in the form of a Voronoi tessellation where the colours represent different refractive index values (in the range 1.005 to 1.0275) in a region of 40 m by 60 m. There are C=20 rays propagating from a known position of a reflector which is mimicking a robot denoted by s^* and positioned at (23, 37) m. These rays have equal length and the small black circles show the end point of each ray which gives the camera positions c_k.

4.6 Generation of Simulated Data

A series of test refractive index maps (denoted by m^*) were created in COMSOL (numerical experiments) A-D; a summary of these can be found in Table 4.6. The typical domain size of each numerical experiment was industrial scale, of the order of 40 m in the horizontal direction and 60 m in the vertical direction and attention was restricted to the 2D horizontal plane case. The generation of these numerical experiments in COMSOL will now be discussed.

A bounding box was created using the *Rectangle* command in the *Geometry* tab in COMSOL; with the bottom left corner positioned at the origin. In numerical experiments A and B, MATLAB was used to generate a random set of Voronoi seeds $\underline{x}_p^{(0)}$ and corresponding refractive indices $\eta_p^{(0)}$ and the co-ordinates of the vertices of each Voronoi cell was output. Due to the computational processing power of the COMSOL Livelink functionality, this method can only be used when the number of Voronoi seeds, P, is small (less than 50) and an alternative method for generating Voronoi tessellations with a large number of seeds is used (see numerical experiment C). The COMSOL Livelink functionality is an additional feature of COMSOL which allows the user to output COMSOL files (.mph) as MATLAB files and edit the files within MATLAB and then save as a COMSOL file. The Livelink functionality does not have the same level of technical support and online documentation as standard COMSOL, so there is a steep learning curve. For numerical experiment A and B, the positions of the seeds, $\underline{x}_p^{(0)}$, were plotted in COMSOL using the LiveLink functionality. This was achieved by programming a loop in MATLAB which adds P *Points* (where P is the number of Voronoi seeds) to the COMSOL Model (the function *Points* is in the *Geometry* tab of COMSOL). The positions of the seeds are shown by the small black squares in Figure 4.2. To add the vertices of the Voronoi tessellation to the COMSOL model a similar method is used. Using the LiveLink functionality another loop is added to the MATLAB code which adds n *Bezier polygons* (defined in the *Geometry* settings of the code) to the model, where n is the number of Voronoi vertices. When the Voronoi tessellation is created in MATLAB the Cartesian co-ordinates of the vertices are stored in two $n \times 2$ matrices. The code works by looping through these vertices and inserting them into the *Polygon Segments* node of the *Bezier Polygon* tab. The material properties of each Voronoi cell are then assigned a constant refractive index $\eta_p^{(0)}$.

As already mentioned in Section 4.5 there are c_k cameras, and the light rays propagate from the reflector positioned at s^* through the known geometry, m^*, with the angle that the light ray leaves the reflector s^* being denoted by $\theta^*_{s,k}$. The end point of each of these rays is a camera position c_k, and these are shown by the small black circles in Figure 4.4. An algorithm was written which estimated the initial ray angle from each camera c_k to the known robot's position s^* due to refraction and hence $\theta^*_{s,k} \neq \theta^*_{k,s}$ typically. The last two co-ordinates of the ray path (the points closest to the camera) and the position of the camera c_k are used to calculate angle $\theta^*_{k,s}$ (the angle from the camera c_k to the reflector mimicking the robot s^*). The first step to calculate this was to export the discrete ray points of the light ray from c_k to s^*. Then the gradient between the last two co-ordinates along the ray (nearest the camera) were calculated. This gradient was then converted to an angle such that $0\ ^\circ \leq \theta^*_{k,s} \leq 360\ ^\circ$.

4.7 Numerical Experiment A

In a typical laboratory, minute refractive index changes can cause sub-millimetre errors in the position of an object of interest which can lead to significant problems [56, 63, 64, 66]. However, before embarking on this weakly heterogeneous case, it is instructive to begin with a more strongly heterogeneous refractive index change. This will allow the methodology to be thoroughly analysed and will be less challenging in demonstrating an improvement in the reflector position error (ε_h), since this error will be more pronounced. Numerical Experiment A will now be formally introduced.

The spatial domain of Numerical Experiment A was defined by a Voronoi tessellation with ten Voronoi cells. This spatial domain was chosen as it is a relatively simple case which can be exploited for initial testing. The subsequent Numerical Experiments have more complex spatial domains. The positions of the Voronoi seeds, $\underline{x}^*_p$, were equal to those in Figure 4.2. The refractive indices, η^*_p, were selected from the set $\{1.005, 1.0075, 1.01, \ldots, 1.0275\}$ and this equates to a refractive index change of 2.2 %. These refractive indices were chosen as they are commensurate with the refractive index of Perspex. Experimentation of light-rays travelling through a series Perspex blocks was scheduled to be carried out during the project because Perspex plastic has a higher refractive index than air and this would allow refraction effects to be observed with the naked eye. However due to time constraints and prioritisation these experiments never materialised. The refractive indices were randomly assigned to each Voronoi cell. The locations of the cameras c_k were found by emitting rays of fixed length from the known retroreflector position s^* with initial angles $\theta^*_{s,k}$, $k = 1, \ldots, C$. The end point of the rays yielded the camera positions c_k. In this numerical experiment (and all subsequent ones) the known position of s^* was (23, 37) m and $C = 20$ rays were released from s^*. As in Section 4.5, the angles that the rays entered each camera were calculated and denoted by $\theta^*_{k,s}$ (recall that $\theta^*_{k,s}$ does not equal $\theta^*_{s,k}$ due to refraction effects and because all angles are measured anticlockwise from the horizontal axis, see Figure 4.5). When the known refractive index map, m^*, was used in the ray tracing algorithm in COMSOL the estimated position of the target was denoted as $\hat{s}^*$. From Figure 4.6a it can be seen that the error in $\hat{s}^*$ is negligible; in-fact the black dot showing its estimated position is the only visible point on the plot. The plot has been enlarged in Figure 4.6b to show the scale of the error; the green dot shows the actual position of the reflector and the black dot is the estimated position of the reflector. In fact, the error in this positioning is $\varepsilon^* = 1.34 \times 10^{-6}$ mm and the variance is $\mathcal{V}(\varepsilon^*) = 3.74 \times 10^{-14}$ mm. The variance is calculated by taking the Euclidean distances from each of the line intersections (the blue dots in Figure 4.6b) to the true position of the reflector, s^* (green dot) and calculating their variance. This result gives confidence in COMSOL as it shows that if the known map m^* was precisely recovered then the error, ε_α, would be negligible. In fact, from the literature not many systems can measure to better than 1:1,000,000 of the working volume.

As described in Section 4.5, the light-rays were then traced from c_k with initial angle $\theta^*_{k,s}$ but this time the refractive index map was assumed to be homogeneous with a constant refractive index of the mean of the refractive indices in the region of interest. These ray-paths are illustrated in Figure 4.7 (a), where it can be seen that the ray paths appear to coalesce at the point s^*. However, it is not until the image is enlarged as in Figure 4.7 (b) that the issue with assuming that the spatial domain is homogeneous is observed. The ray co-ordinates were output and taken into MATLAB and using the method of triangulation an estimate for the

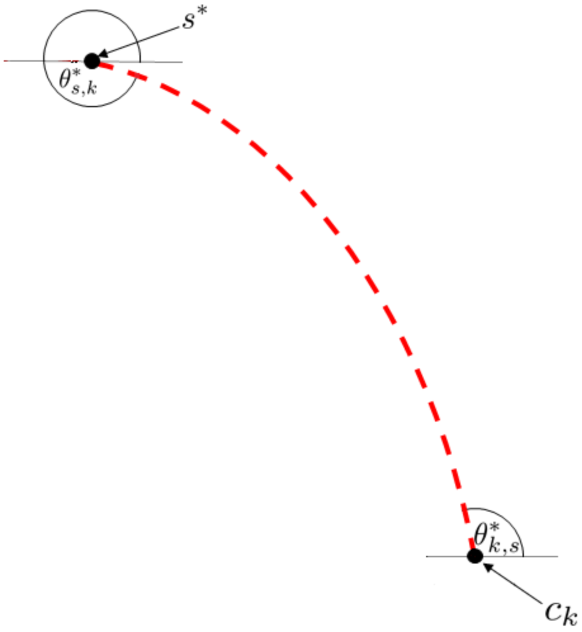

Figure 4.5: Schematic showing $\theta^*_{s,k}$, the angle from the robot at s^* to the camera at c_k and $\theta^*_{k,s}$, the angle from camera c_k to s^*, as shown in this schematic $\theta^*_{k,s} \neq \theta^*_{s,k}$

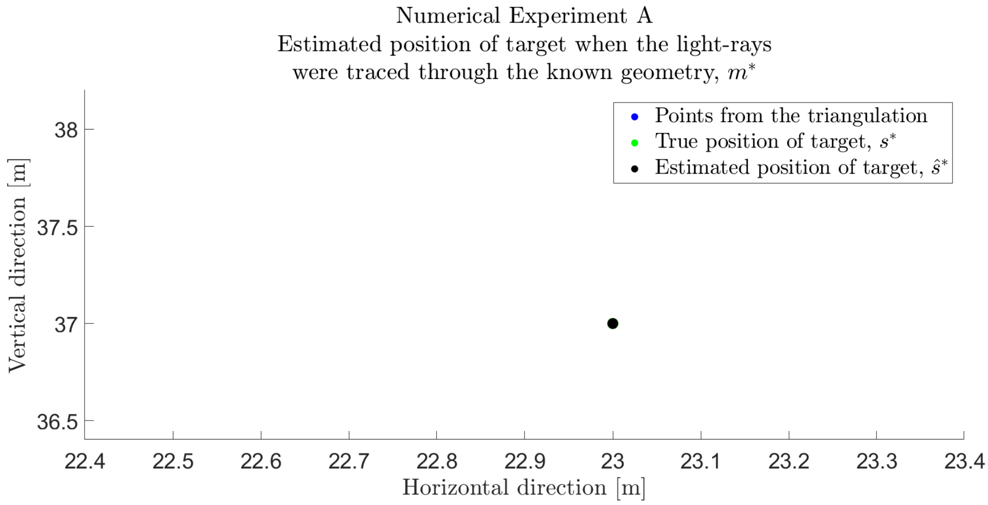

(a)

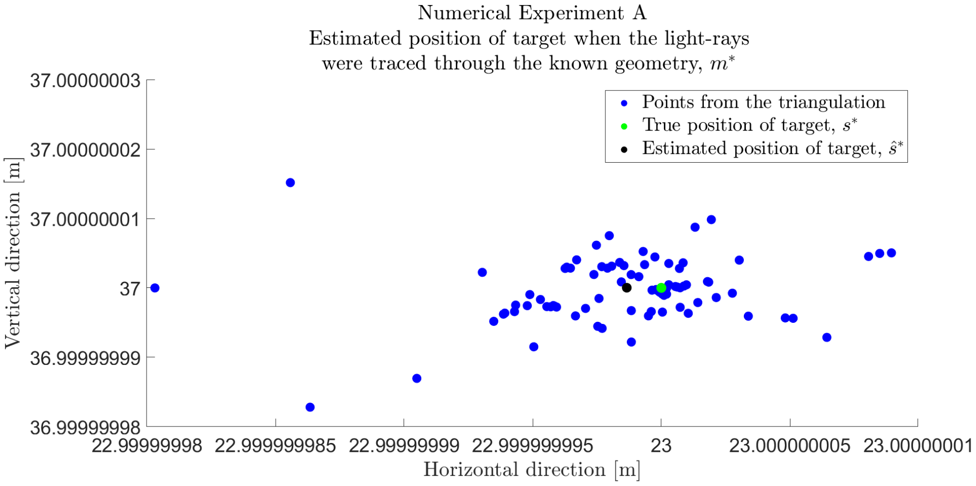

(b)

Figure 4.6: (a) Numerical Experiment A: This plot shows the results of the triangulation method when the light-rays are traced through the known refractive index map, m^*. The error is so small that the true position of the receiver and the points from the triangulation cannot be seen. (b) Numerical Experiment A: This plot shows the results of the triangulation method when the light-rays were traced through the known refractive index map, m^*. The intersection points of the light-rays are shown by the blue points, the estimated position of the reflector ($\hat{s}^*$ is shown by the black dot and the true position (s^*) is shown by the green point.

position of the reflector ($\hat{s}_h$) was found. The cluster of intersection points is shown in Figure 4.8 (blue points) along with the true position of the reflector s^* (shown by the green point) and the estimated position of the reflector $\hat{s}_h$ (illustrated by the black point). In numerical experiment A it was found that the positional error ε_h was 73.3 mm and $\mathcal{V}(\varepsilon_h)$ was 33.9 mm, and these values arise solely from refraction effects caused by the thermal fluctuations in the domain.

It will prove instructive to derive some quantitative measures that characterise the convergence of the inversion algorithm and allow a comparison between COMSOL and the FMM.

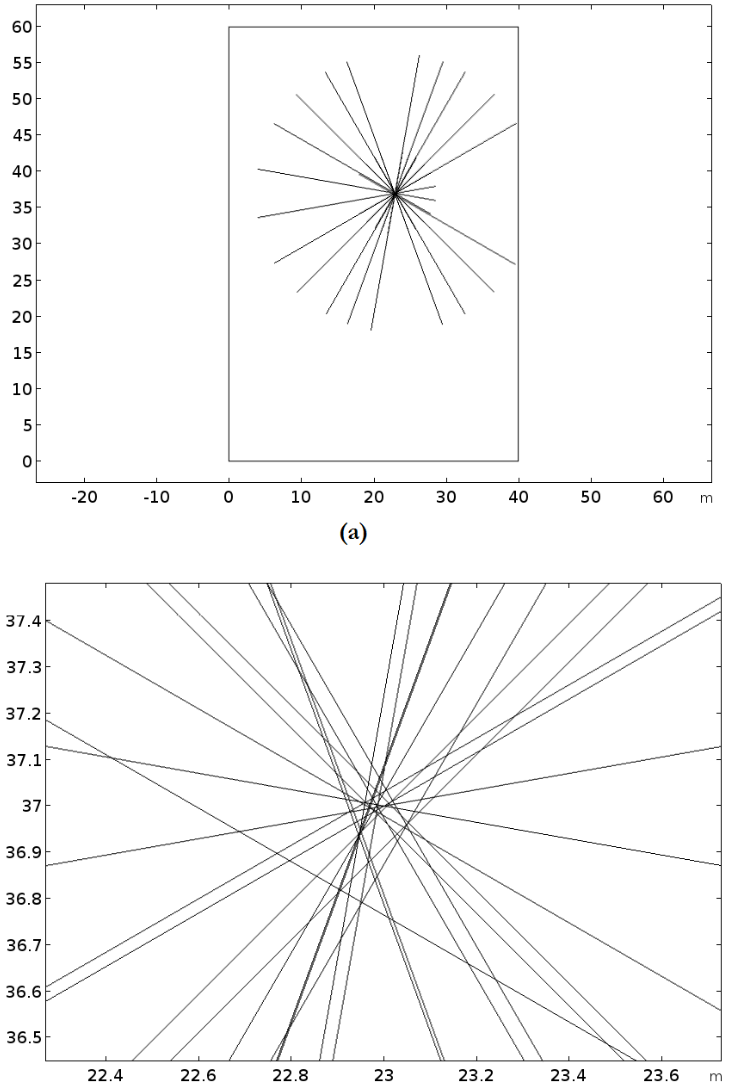

(a)

(b)

Figure 4.7: Numerical Experiment A: (a) Image showing the straight rays propagating through a homogeneous refractive index map from cameras c_k with initial angle $\theta^*_{k,s}$ towards the retroreflector at known position s^*. (b) Shows an enlarged version of (a) to show that the rays do not all intersect at a single point with this homogeneous refractive index map assumption.

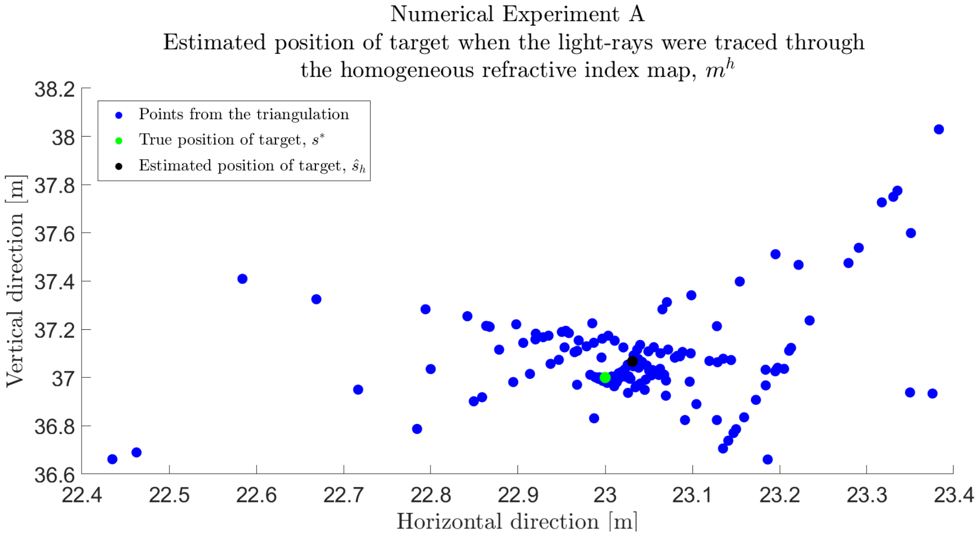

Figure 4.8: Numerical Experiment A: This scatter-plot illustrates the cluster of light-ray intersection points when the light-rays are traced from cameras c_k with initial angle $\theta^*_{s,k}$ through a homogeneous refractive index map. The mean of the light-ray intersection points yields $\hat{s}_h$ (illustrated by the black circle). The true position of the object of interest (s^*) is shown by the green circle.

4.7.1 Discussion of the optimal method to calculate the estimate of the initial ray-angle from the FMM

The sensitivity of the refractive index map to changes in its model parameters (Voronoi cell seed positions and refractive index in each cell) also be examined. Denote the mean relative difference between the initial refractive index material map and the known refractive index map at iteration zero by $\kappa^{(0)}$, where

$$\kappa^{(0)} = \left(\sum_{v=1,w=1}^{VW} |m^*_{vw} - m^{(0)}_{vw}| \right) / \left(\sum_{v=1,w=1}^{VW} m^*_{vm} \right) \tag{4.11}$$

where V and W are the number of pixels in the horizontal and vertical direction respectively of the discretised refractive index map. Recall that the refractive index changes in numerical experiment A only have a 2.2 % difference. It will be seen that the recovered maps can have a larger change. For numerical experiment A the range of refractive index values for the reconstructed maps expressed as a percentage of the mean value was 2.7 %.

The known map, m^*, yields a $\kappa^{(0)}$ value of zero and the uniform refractive index map (homogeneous refractive index map with constant refractive index equal to the mean refractive index) gives a $\kappa^{(0)}$ value of 0.7 %. A histogram of $\kappa^{(0)}$ values is shown in Figure 4.9 arising from 100 randomly chosen Voronoi maps; note that the values have been converted to a percentage. From Figure 4.9 it can be seen that $\kappa^{(0)}$ is left skewed with a maximum at 1.05 % and a peak at 0.95 %.

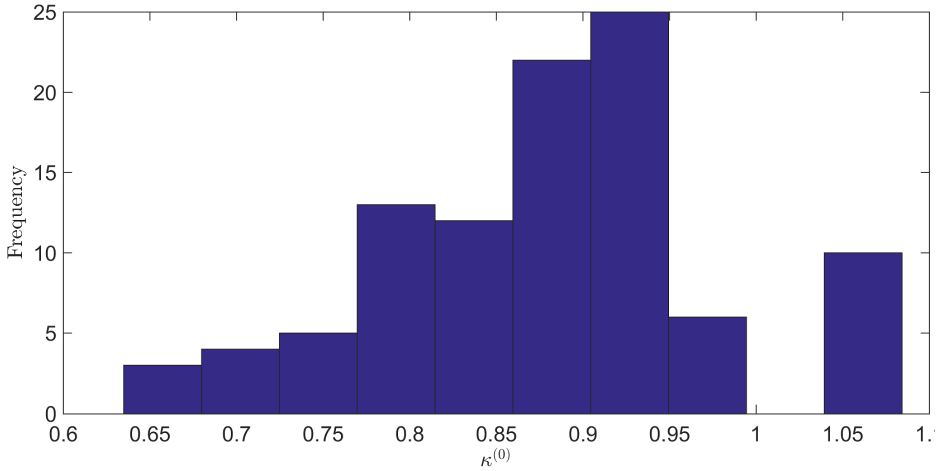

Figure 4.9: Histogram of the mean relative refractive index map difference, $\kappa^{(0)}$, (Equation (4.11)) when a random Voronoi tessellation is used and there is a sample size of 100.

Table 4.1: Table detailing the differences between the average relative error in the angles at iteration zero, mean difference between the refractive index material map and the error and variance of the position of the reflector mimicking the robot s^*, when the known refractive index map m^* and the homogeneous refractive index map m^h are compared.

	$\xi^{(0)}$	$\kappa^{(0)}$	ε	$\mathcal{V}$
m^*	0.0575	0	1.34×10^{-6} mm	3.74×10^{-14} mm
m^h	0.0583	0.007	73.3 mm	32.9 mm

Now that a numerical experiment with a significantly large positional error ($\varepsilon_h = 73.33$ mm) has been generated it can be used to test and develop the refractive index map recovery process. For good coverage of the refractive index map a set of $C = 20$ cameras were positioned around the reflector s^*. As mentioned previously, COMSOL's ray tracing software does not allow the stipulation of the start and end point of a ray. Instead one specifies the starting point of a ray and its initial angle. Therefore to generate a set of camera-reflector pair ray-paths, it is more straightforward to have a distinct set of reflectors for each camera (here four are used) and hence there are in total $R = 4C = 80$ reflectors (and so here $N_{rays} = 80$ too). Another limitation of COMSOL is that all rays which propagate in the domain must have the same length, and the ray lengths are such that all of the R rays remain within the bounded spatial domain (in this case all the rays have length 24 m). This optical path length also ensures that all light rays travel through at least two Voronoi cells. The ray-paths which are simulated in COMSOL are shown by the black lines in Figure 4.10, and from this it can be seen that there is good coverage throughout the domain. The light rays leave camera c_k with initial angle $\theta^*_{k,i}$. In a practical implementation of our methodology the positions of the cameras and the reflectors used for this calibration stage would be known, and the measured angles would be given by the photogrammetry equipment. Hence, $\theta^*_{k,i}$ is used as one of the inputs for the inversion process, along with the position of the cameras and receivers. In a practical situation this would be the calibration stage with known positions for the cameras and reflector. It is assumed that the cameras would remain in a fixed position throughout experimentation. This is the case in the University of Strathclyde's laboratory as the VICON cameras are fixed to a scaffolding (as in [56]), and only 2 of the cameras can be moved onto tripods (as done in the experiments in Chapter 3). To begin with, the known refractive index map m^* was used as the prior; that is the zeroth refractive index map realisation of the rj-MCMC inversion algorithm. Since the rj-MCMC forward model (Fast Marching Method) is a different ray tracing method to that in COMSOL, this first exercise provides another quantitative assessment of the difference between these two methods as captured by the objective function given by Equation (4.5). Ultimately, a uniform refractive index map (so essentially no prior information) will be used as this will be the case in the practical deployment of the methodology.

To allow information to be gathered on the light-rays when they travel through the initial prior refractive index map, the inversion was set to run for zero iterations. The ray-paths produced by the Fast Marching Method were then plotted to check for good agreement with those produced by COMSOL. The ray-paths are plotted in Figure 4.11 and a subset of their light ray paths are compared in Figure 4.12. It can be seen that there is good agreement between these ray-paths

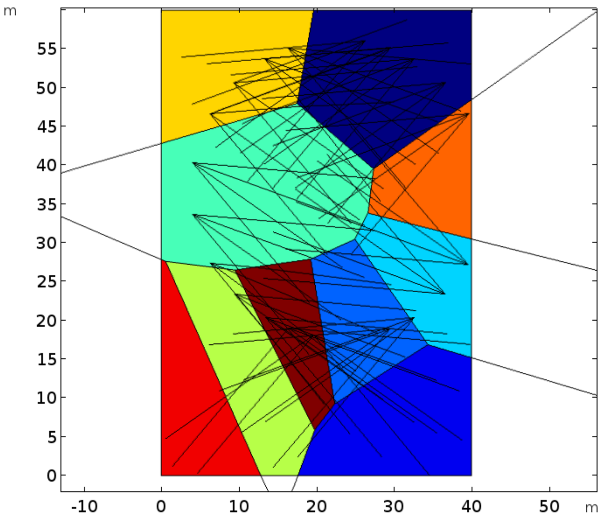

Figure 4.10: Schematic showing the light rays propagating through the known refractive index map m^* from the cameras c_k, to the reflectors r_i, where C=20 and $R = 80$. Four rays propagate from each camera.

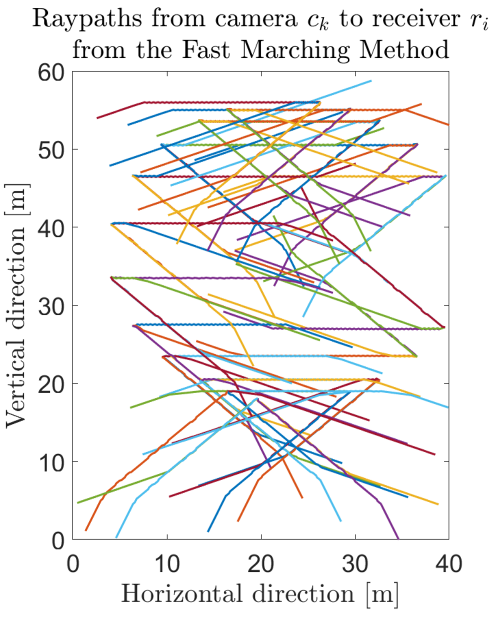

Figure 4.11: A plot showing the ray-paths produced by the Fast Marching Method when the rays are traced from camera c_k to receiver r_i.

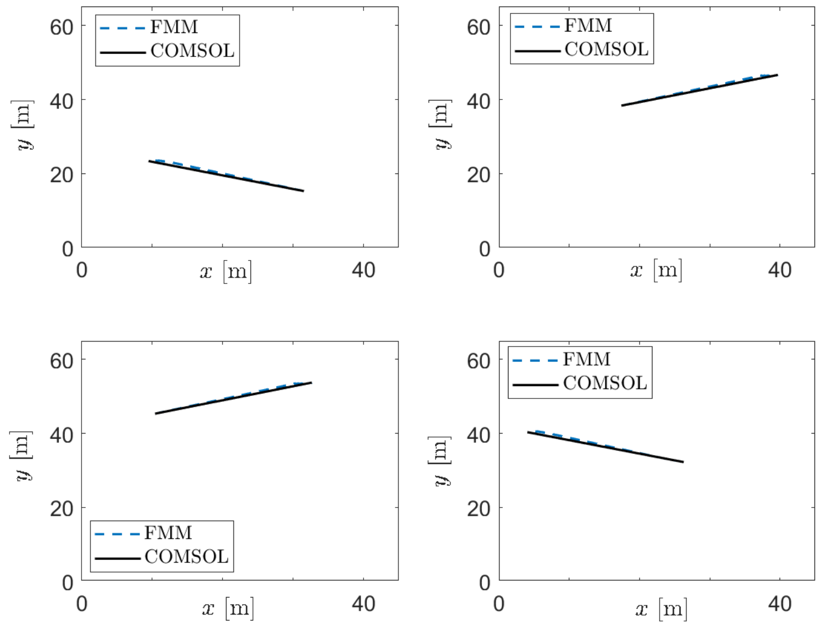

Figure 4.12: Comparing a subset of the ray-paths produced by the FMM (blue dash line) shown in Figure 4.11 and COMSOL (black solid line) shown in Figure 4.10 when the rays are traced from camera c_k to receiver r_i.

(Figure 4.12) and those produced in Figure 4.10. However, Figure 4.13 shows a subset of light-rays with poor agreement. The rays in this Figure exhibit bowing of the ray-path and ray-wriggling. This is one of the reasons why δ was chosen to use 100 % to calculate the angle $\theta_{k,i}$. This plot shows that it is possible for the light-rays to have trajectories which would have never been observed in a real life setting. In addition, these light-ray trajectories do not satisfy Fermat's Principle of the Shortest Path. The reasoning behind this poor agreement is unclear. One reason for this could be that this algorithm was not originally designed for the level of accuracy required for to be applied in a high precision metrology setting. One possible reason could have also been the grid size that the ray is propagating over, however an investigation into this found that when a small grid size was

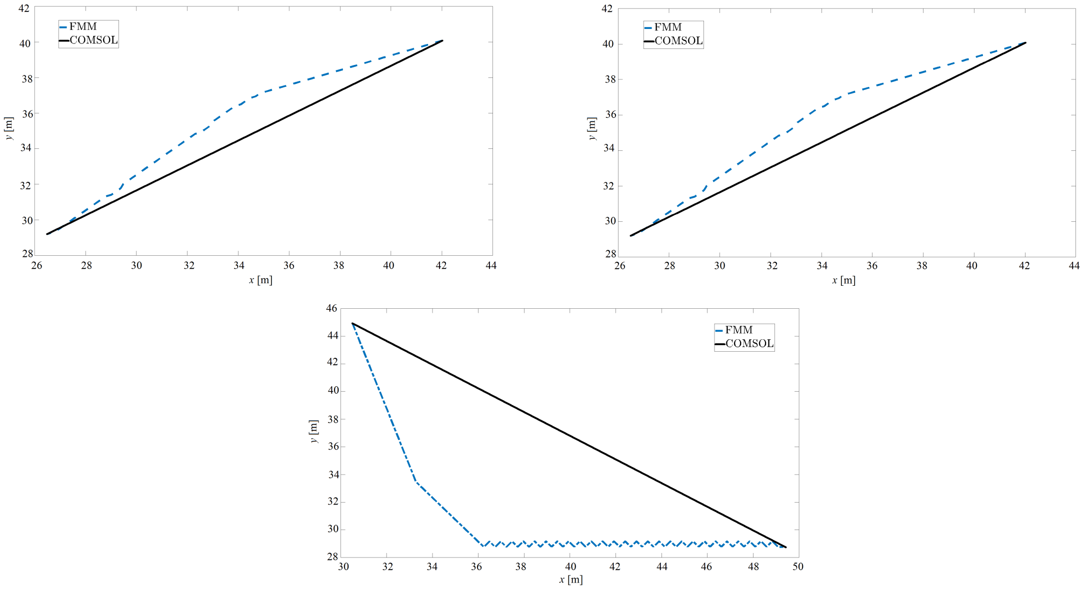

Figure 4.13: Figure showing the ray paths with poor agreement between the FMM (blue dash line) and COMSOL (black solid line) when the rays are traced from camera c_k to receiver r_i.

used these ray-paths were still observed. In Chapter 5, we look at designing a bespoke method which does not use the ray-tracing algorithm. Aside from not always giving good results, it is also the most computationally draining component of the algorithm.

4.7.2 Investigation into perturbing the initial refractive index index map to assess the sensitivity of the objective function

The advantage of using a Voronoi tessellation as the refractive index map to be recovered is that the algorithm can be started from $\kappa^{(0)} = 0$ by choosing the initial refractive index map $m^{(0)} = m^*$. That is, by making the prior refractive index map $m^{(0)}$ of the model the known refractive index map m^*. Another advantage is that a perturbed prior map can be examined and this allows the sensitivity of the objective function to be examined.

Firstly a perturbation in the position of the Voronoi seeds was investigated. Each seed position was perturbed by $m^{(0)} = m^*(x_p^* + \epsilon(L_x/2)$ N(0,1), $y_p^* + \epsilon(L_y/2)$ N(0,1), $\eta_p^*)$ where L_x and L_y are the domain lengths in the horizontal and vertical direction respectively and $\epsilon \in [0, 1]$. As ϵ increased more seed positions lay outside of the domain and for these seeds the known value $\underline{x}_p^*$ was used. The results of this exercise are shown in Figure 4.14 by the blue line. From this plot it can be seen that there is not much variation in the objective function value and it does not go below the unperturbed objective function value at $\epsilon = 0$. One thing to note is that the known refractive index map m^* does not yield a objective function value of 0. The reason for this is simply that $\theta_{k,i}^{(0)}$ does not equal $\theta_{k,i}^*$ due to the different ray-tracing techniques used between COMSOL and the FMM. The fluctuations in the plot are due in part to the fact that as ϵ increases the seed positions are being moved by a higher percentage causing more of them to lie outside of the domain. When this occurs the known seed positions are used for those seeds which is why the objective function value can decrease. In addition, at each ϵ, only a single random realisation was used and to get a more accurate picture a larger number of realisations should be averaged over.

Following on from this, an assessment of the objective function's sensitivity to refractive index changes in each Voronoi cell was also investigated. The refractive indices were perturbed by $m^{(0)} = m^*(\underline{x}_p^*, \eta_p^* + (\eta_{range}/2)\epsilon N(0,1))$, where η_{range} is the range of values which the refractive index can take. As in the previous case, when the value for the refractive index lies outside the pre-specified range of refractive index values the known refractive index value η_p^* is used.

The results of these perturbations are shown in Figure 4.14 by the red line and from this it can be seen that there is not a defining trend in the data. There is a noticeable peak, the reason for which could be that this is the highest ϵ value which results in all the refractive indices changing.

Finally a perturbation of both the cell seed position and the refractive indices was considered. The perturbation is described by $m^{(0)} = m^*(x_p^* + \epsilon(L_x/2)N(0,1)$, $y_p^* + \epsilon(L_y/2)N(0,1)$, $\eta_p^* + (\eta_{range}/2)\ \epsilon N(0,1))$. The results of this are shown in Figure 4.14 by the green line.

It can be seen from Figure 4.14 that the misfit value (γ) is between 5.6 and 5.85 °. This misfit in an industrial setting is extremely large because as the measured distances increases the error will also increase due to the nature of

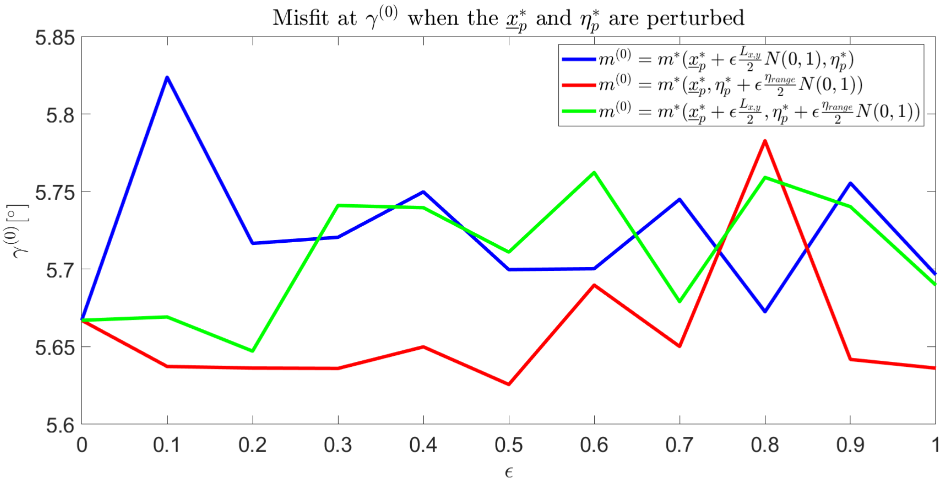

Figure 4.14: Plot showing how perturbations of the Voronoi cell seed positions $\underline{x}_p^*$ (blue line), the refractive indices in each cell η_p^* (red line) and the two of these combined (green line) affect the objective function (misfit) described by Equation (4.5) at iteration zero.

angles. However these misfit values may not be observed in an industrial setting due to the strongly heterogeneous nature of m^*. Numerical experiments B-D will look at industrially relevant test cases.

4.7.3 Numerical Experiment A: The Inversion Process

For each numerical experiment, the inversion process ran for 100,000 iterations (realisations) with a burn-in period of 20,000. There are many inputs into the algorithm, most notably, the position of the cameras, c_k, the position of the reflectors r_i, the angle between these $\theta_{k,i}^*$, a mapping, Φ, detailing which camera sees which reflector, the range of refractive indices the model can choose for each Voronoi cell at each perturbation and the range of the number of Voronoi cells for the model (with the lowest value always set to 5 Voronoi cells). The algorithm naturally looks for the smallest number of Voronoi cells to represent the map, and this was already embedded into the code. This method of using the simplest model is referred to as natural parsimony. It is also possible to prescribe an initial refractive index map (prior) for each inversion which takes the form of a Voronoi tessellation. In this thesis three choices for the initial map were trialled: the known refractive index map m^*, a uniform refractive index map and a random refractive index map.

In the case of the known and uniform priors, their corresponding input files are expressed as the seed positions of the Voronoi tessellation and the velocity in each cell. As mentioned previously this code was initially developed within the seismology community. Since these researchers typically work with ultrasound rays as opposed to light-rays they are able to work in velocities. For this reason all refractive indices are expressed as velocity within the code by using the following result: $\eta = c_\infty / c$ where η is the refractive index, c_∞ is the speed of light in a vacuum and c is velocity in media. However, this equation yields velocities which are far too large and so the resultant velocity is scaled down by a factor of 1000. Alternatively, c_∞ can be scaled down by this factor prior to the calculation. For each numerical experiment it is assumed that the uniform prior has the same number of Voronoi cells as the known refractive index map, m^*. For the random refractive index map the algorithm randomly chooses an initial Voronoi where the number of Voronoi seeds ,P, is somewhere within the specified range mentioned above. Each numerical experiment was repeated three times to allow the algorithm to start from each of the priors mentioned above.

To produce a single map to enable an assessment of how well the inversion has worked a single refractive index map is required. This can take three forms: the mean, the median or the maximum-a-posteriori of the posterior distribution. At each iteration j of the inversion the corresponding Voronoi tessellation is stored within the algorithm and once the inversion is finished the mean, median and MAP value of each pixel in the refractive index map is calculated over j realisations and these values produce the recovered refractive index maps. In addition to these recovered maps the inversion process also outputs the posterior distribution of the noise parameter, $\zeta^{(j)}$, the number of Voronoi cells at each iteration $P^{(j)}$, the objective function $\gamma^{(j)}$ and material map difference $\kappa^{(j)}$.

4.7.4 Numerical Experiment A: Results

To begin with the results for the case where the known map is used as the initial Voronoi map $m^{(0)}$ prior will be discussed. The objective function, $\gamma^{(j)}$ (Equation (4.5)) is shown in Figure 4.15. From this plot it can be seen for the first iterations the objective function is relatively low (around 0.075 degrees) then after time it proceeds to oscillate with a central value of approximately 0.175 degrees.

The mean of the posterior, the median of the posterior and the maximum-a-posteriori of the posterior distribution recovered refractive index maps are shown in Figure 4.16, along with the true refractive index map m^*. Generally speaking the recovered refractive index map for the median, mean and MAP of the sampled refractive index map posterior distribution show no resemblance to m^*; in fact they look very homogeneous. In order to quantitatively assess the material map agreement and decide which map to use for estimating the position of the robot, the material map errors, κ_{mean}, κ_{median} and κ_{max} were found for the respective recovered refractive index maps, where κ is the relative change between the known map m^* and the recovered map. It was found that κ_{median} (see Equation (4.11)) was 0.70 %, κ_{mean} was 0.71 % and κ_{max} was 0.95 %. Therefore, in this instance the median of the posterior recovered refractive index map was chosen as the optimal recovered refractive index map.

The median recovered refractive index map was taken into COMSOL using the *Interpolation* option in the *Functions* tab of the *Global definitions* menu. Following this, the rays were released from positions c_k with angle $\theta^*_{k,s}$ and the co-ordinates of the ray paths were stored. Using the aforementioned triangulation method (see Section 4.5) the value of $\hat{s}_\alpha$ was found and the corresponding ε_α value. The intersection points of the light-rays are depicted by the blue dots in the scatter-plot shown in Figure 4.17, and so too are $\hat{s}_\alpha$ (black dot) and s^* (green dot). After finding the centre of mass of all the intersection points the error in the position was found to be $\varepsilon_\alpha = 33.6$ mm which gives an improvement ε_{imp}

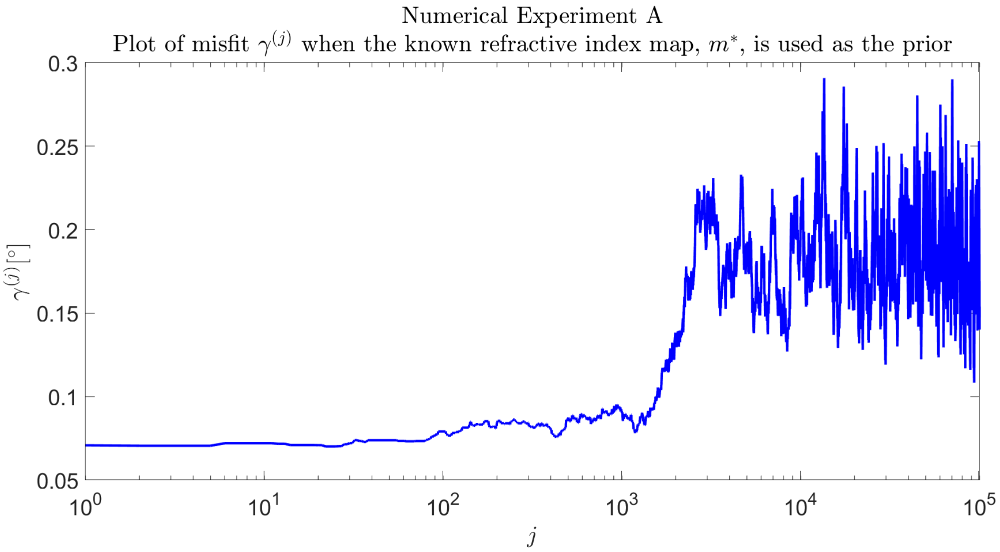

Figure 4.15: Numerical Experiment A: Objective function (misfit) $\gamma^{(j)}$ (Equation (4.5)) when the inversion was set to run for 100,000 iterations with a burn-in period of 20,000, where the known refractive index map, m^*, was used as the prior.

value of 54 %. The variance, $\mathcal{V}(\varepsilon_\alpha)$ was found to be 28.5 mm which gives an improvement $\mathcal{V}_{imp}$ value of 16 % in uncertainty compared to the homogeneous case (see Figure 4.8).

The inversion process was repeated and all values were kept constant aside from the prior. In this instance, the prior refractive index map was that of a uniform refractive index map with a constant refractive index of the mean of the known refractive index map m^*. The inversion algorithm again ran for 100,000 iterations and had a burn-in of 20,000 iterations. The objective function, $\gamma^{(j)}$ for this particular numerical experiment is shown in Figure 4.18. From this plot it can be seen that for the first iterations the objective function is low around 0.075

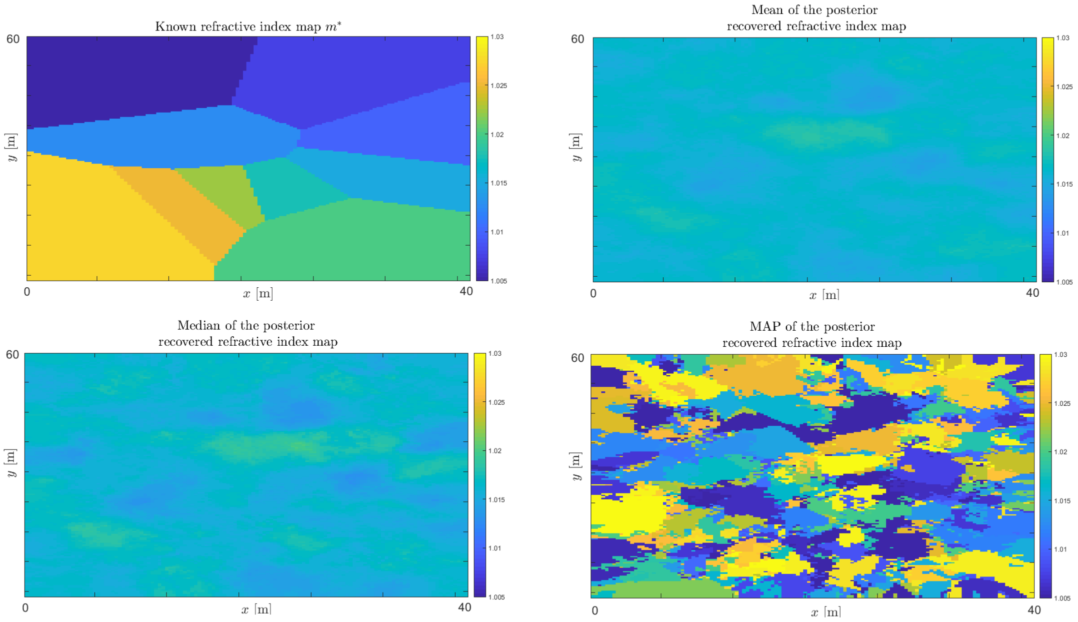

Figure 4.16: Numerical Experiment A: known refractive index map as prior. Top Left: Known refractive index map m^* Top Right: mean of the sampled refractive index map posterior, Bottom Left: median of the sampled refractive index map posterior, (d) maximum-a-posteriori of the sampled refractive index map posterior distribution.

degrees, which is very close to the $\gamma^{(0)}$ value when m^* is used as the initial prior. Then after time it proceeds to oscillate with a central value of approximately 0.175 degrees.

As in the case where the known refractive index map was used as the initial prior, the median recovered refractive index map (see Figure 4.19) had a κ_{median} value of 0.70 % (κ_{mean} was 0.71 % and κ_{max} was 1.02%). Using the triangulation method an estimate for $\hat{s}_\alpha$ was found and the results of the triangulation method are shown in Figure 4.20. The error in the estimated position ε_α was 39.4 mm

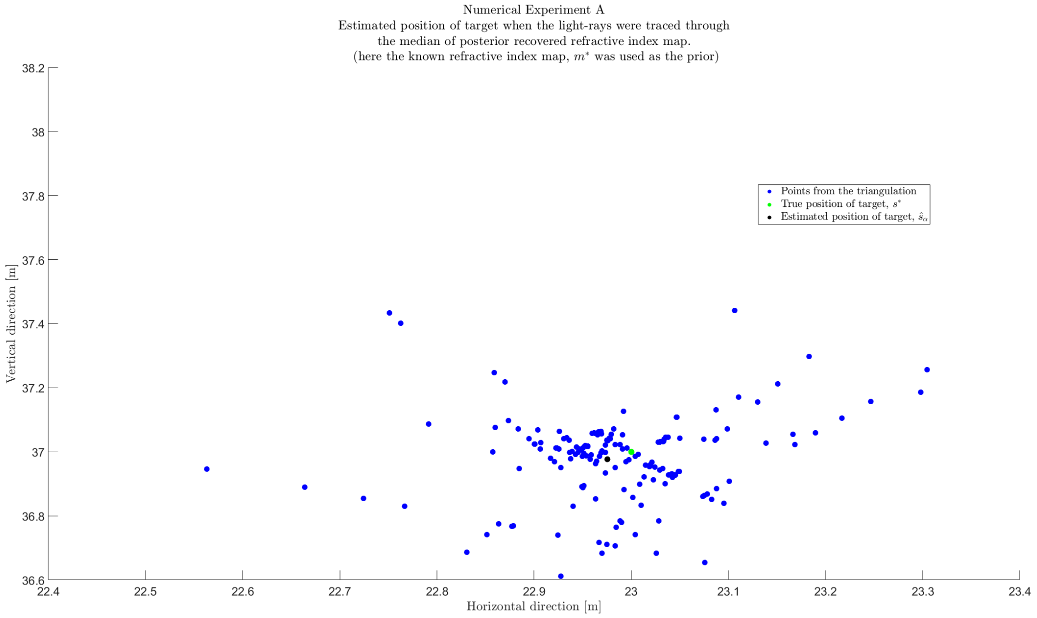

Figure 4.17: Numerical Experiment A: This plot shows the results of the triangulation method when the light-rays are traced through the recovered refractive index map shown in Figure 4.16 (c). The intersection points of the light-rays are shown by the blue points, the estimated position of the reflector ($\hat{s}_\alpha$) is shown by the black dot and the known position (s^*) is shown by the green dot. There are 20 cameras tracking the target s^*.

which leads to an improvement, ε_{imp}, of 46 %. There is also an improvement in the uncertainty, since the variance was found to be 28 mm, which lead to an improvement, $\mathcal{V}_{imp}$, in the variance of 15 %.

A third and final inversion was carried out for numerical experiment A, only this time a completely random refractive index map was chosen as the initial prior. This refractive index map was a Voronoi tessellation with 86 cells and is shown in Figure 4.21. As was seen in the cases where the known and uniform

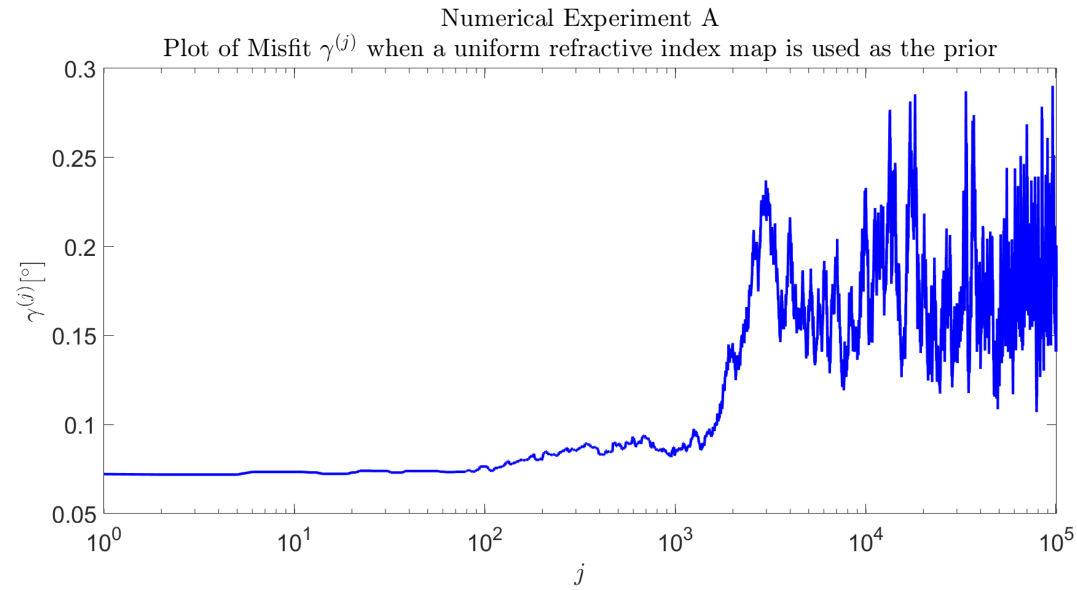

Figure 4.18: Numerical Experiment A: Objective function (misfit), $\gamma^{(j)}$ when the inversion was set to run for 100,000 iterations with a burn-in period of 20,000. In this instance a uniform refractive index map was used as the prior.

refractive index map were used as priors the median recovered refractive index map again had a κ_{median} value of 0.66 % (κ_{mean} was 0.68 % and κ_{max} was 0.86 %).

Following this, the light-rays were traced through Figure 4.22 in order to find the error in the reflector s^*. The results of the triangulation are shown in Figure 4.24, the blue dots show the intersection points of the light rays, the green dot shows the true position of the reflector s^* and the black dot shows the estimated position of the reflector when Figure 4.22 is used as the refractive index map. Interestingly, the error in the position of the reflector, s^*, was found to be 20 mm, that is $\varepsilon_\alpha = 20$ mm, which leads to an ε_{imp} value of 73 %. The variance, $\mathcal{V}(\varepsilon_\alpha)$ was found to be 3.6 mm which gives a $\mathcal{V}_{imp}$ value of 89 %. Whilst it is

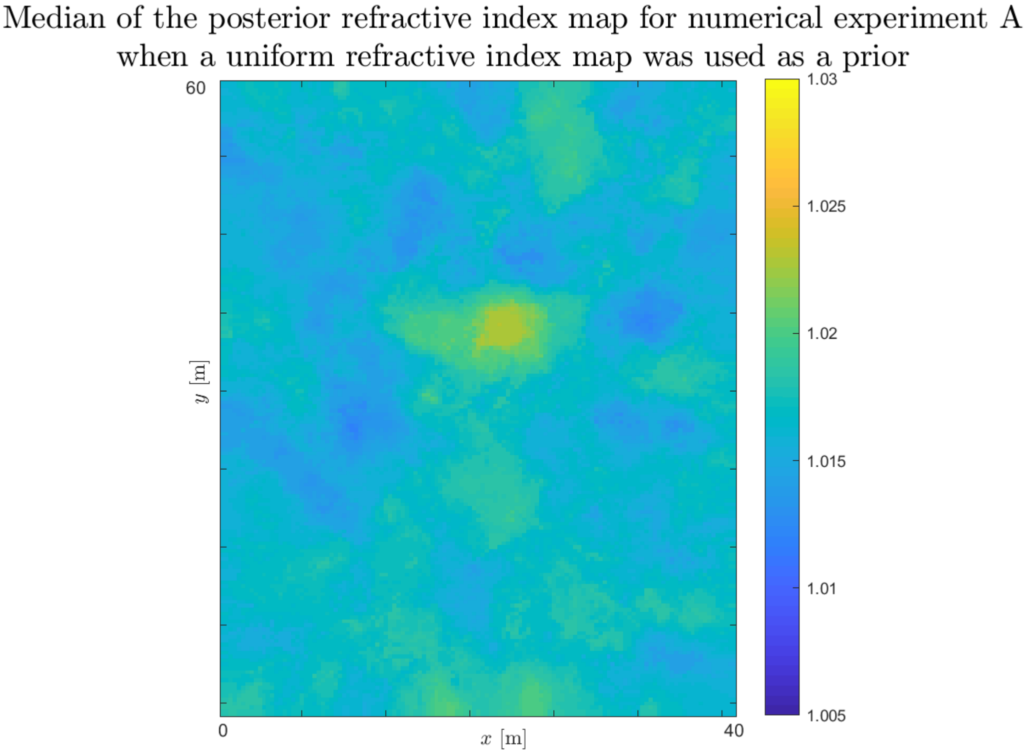

Figure 4.19: Numerical Experiment A: This is the recovered refractive index map for the median of the posterior distribution, achieved from running the inversion process for 100,000 iterations with a burn-in of 20,000 and a uniform prior was used.

unusual that using a random refractive index map as the prior yields a better improvement in position and uncertainty compared to using the known map m^*, Figure 4.26 shows that generally speaking the random prior gives a lower value of κ_{median} compared to the other two cases. One reason for this could be attributed to the robustness of the ray-tracing algorithm.

A comparison of the different $\gamma^{(j)}$ convergence plots is shown in Figure 4.25. The blue line shows $\gamma^{(j)}$ when m^* is used as the prior, the red line shows $\gamma^{(j)}$ when m^h is used as the prior and the green line shows $\gamma^{(j)}$ when the random refractive

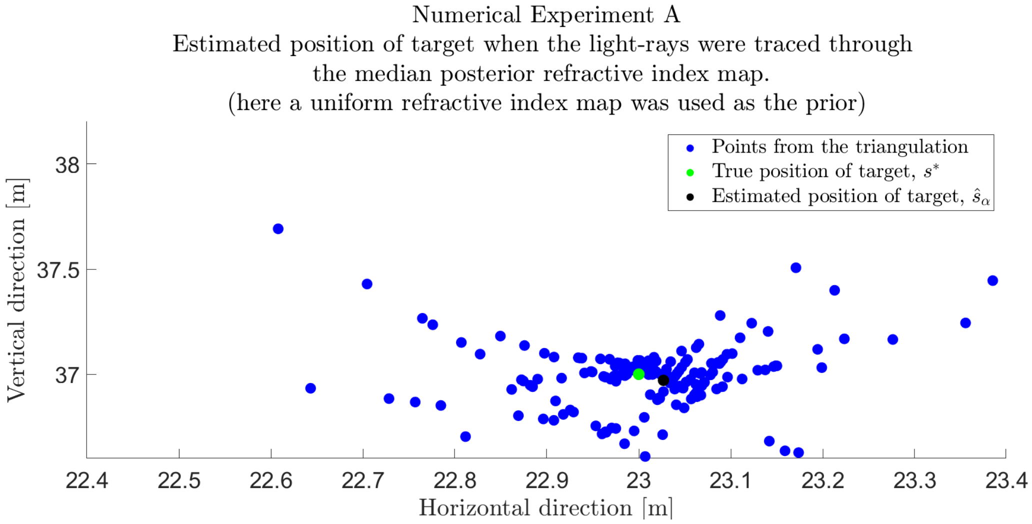

Figure 4.20: Numerical Experiment A, uniform refractive index map as prior. This plot shows the results of the triangulation method when the light-rays are traced through the recovered refractive index map shown in Figure 4.19. The intersection points of the light-rays are shown by the blue points, the estimated position of the reflector ($\hat{s}_\alpha$) is shown by the black point and the true reflector position (s^*) is shown by the green point.

index map as shown in Figure 4.21 is used as the prior. This plot shows that as the number of iterations j increases all three lines converge and then oscillate around the same $\gamma^{(j)}$.

Finally, the mean material map difference is examined in Figure 4.26. The dashed black line in Figure 4.26 is K which is the range of refractive index values expressed as a percentage of the mean value. It can be seen that when the known refractive index map was used as the prior (blue line) at iteration one the objective function is zero (as expected) and then it increases and begins to flatten out. This plot only considers the accepted Voronoi tessellations and in addition only each 1000th Voronoi tessellation over the 100,000 iterations. The red line

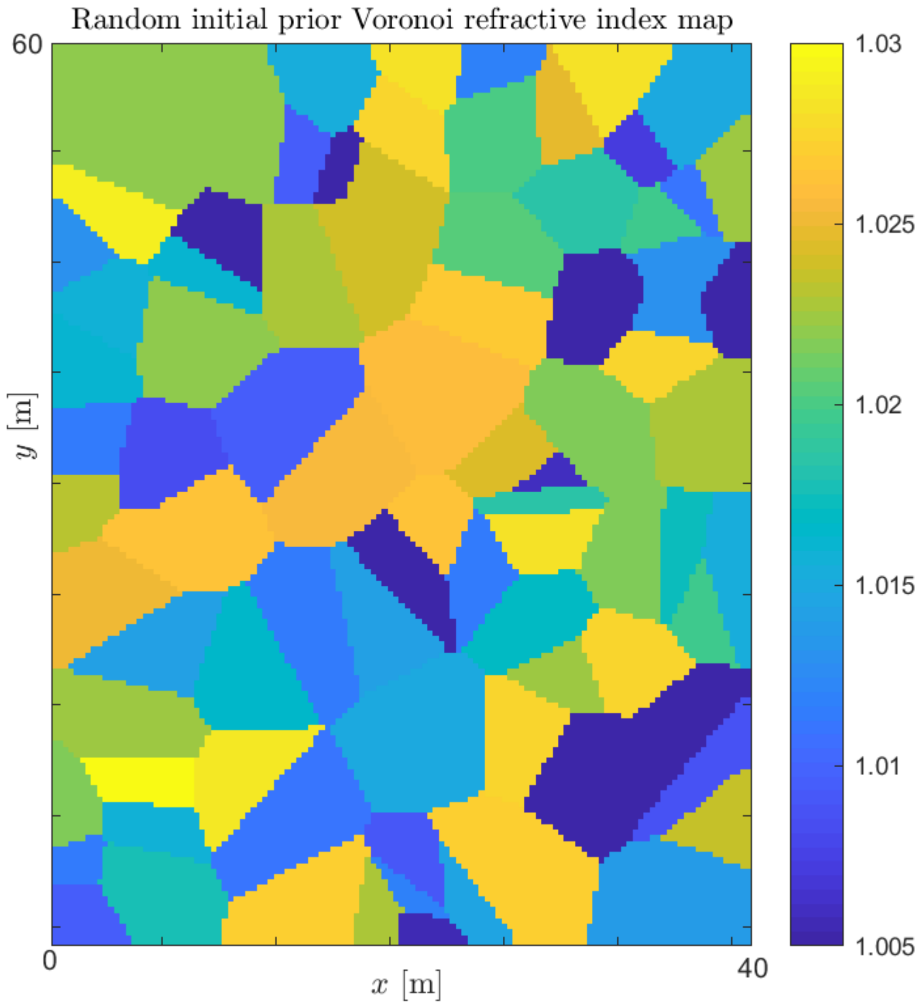

Figure 4.21: Numerical Experiment A: Random initial Voronoi tessellation with 86 cells and the colours in each cell are attributed to a refractive index.

shows the objective function when a uniform refractive index map is used as the prior. As expected this has an initial value which is not equal to zero and this has quite a flat trend. The green line is the equivalent plot for the random initial Voronoi tessellation shown in Figure 4.21.

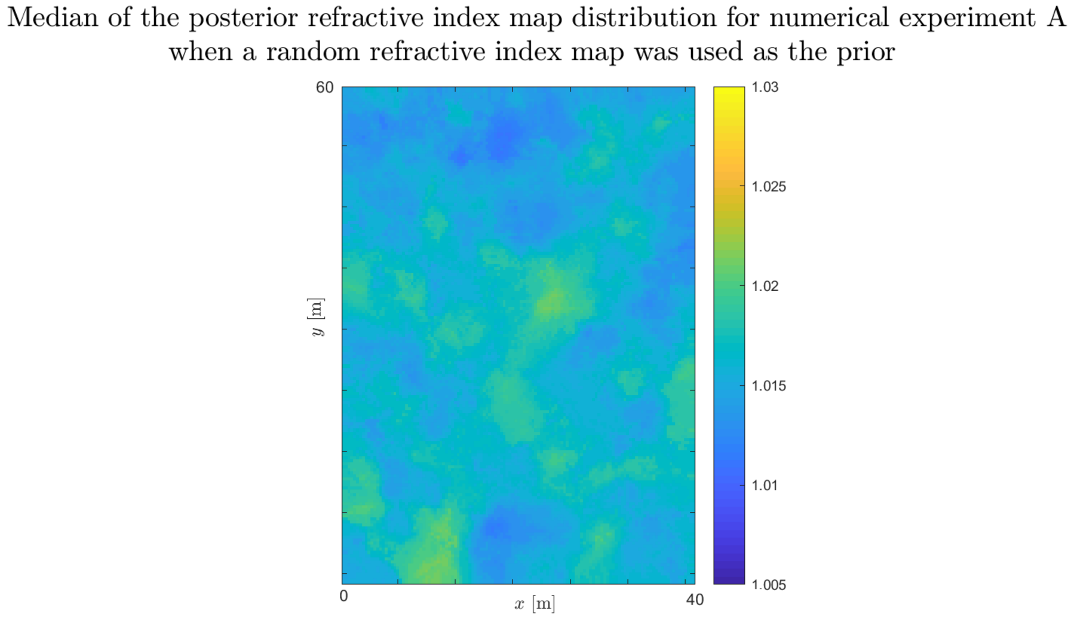

Figure 4.22: Recovered refractive index map when a random refractive index map was used as the prior refractive index map. This was the median of the posterior distribution, achieved from running the inversion process for 100,000 iterations with a burn-in of 20,000.

In terms of acceptance rates the case where the known refractive index map was used as the prior accepted 69.2 % of proposed models, 69.2 % when the uniform refractive index map was used as a prior and 69.6 % when there was a random refractive index map used as the initial prior.

The results from numerical experiment A are encouraging in that the ε_α is much less than ε_h and $\mathcal{V}(\varepsilon_\alpha)$ is much less than $\mathcal{V}(\varepsilon_h)$. One thing that is concerning however is that the ε_α value when a random refractive index map is used as the initial prior is lower than the ε_α when the known map is used as the initial prior. Intuitively this should not be occurring and it suggests that the inversion process is not as robust as one would want.

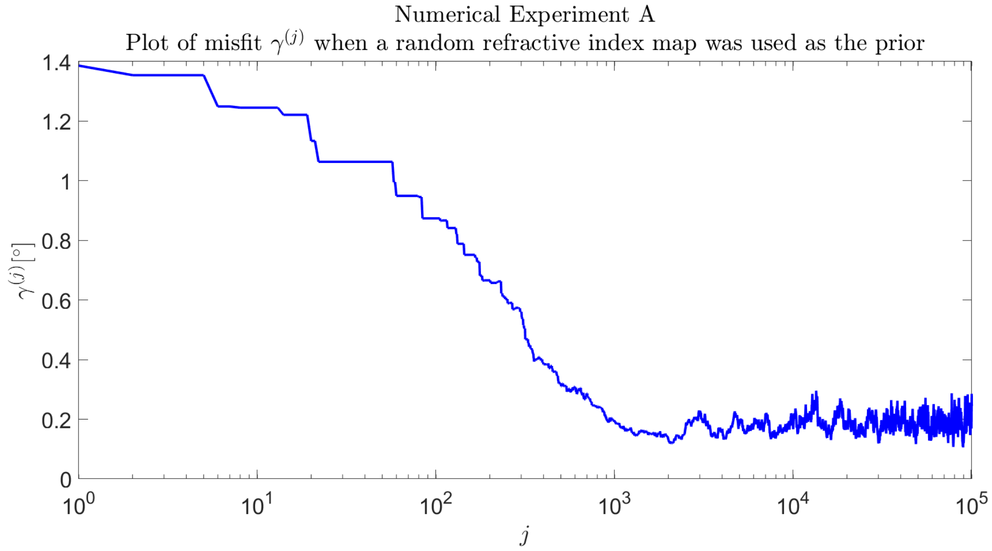

Figure 4.23: Numerical Experiment A: Objective function (misfit), $\gamma^{(j)}$, when the inversion was set to run for 100,000 iterations with a burn-in period of 20,000 and a random refractive index map was set as the prior (Figure 4.21).

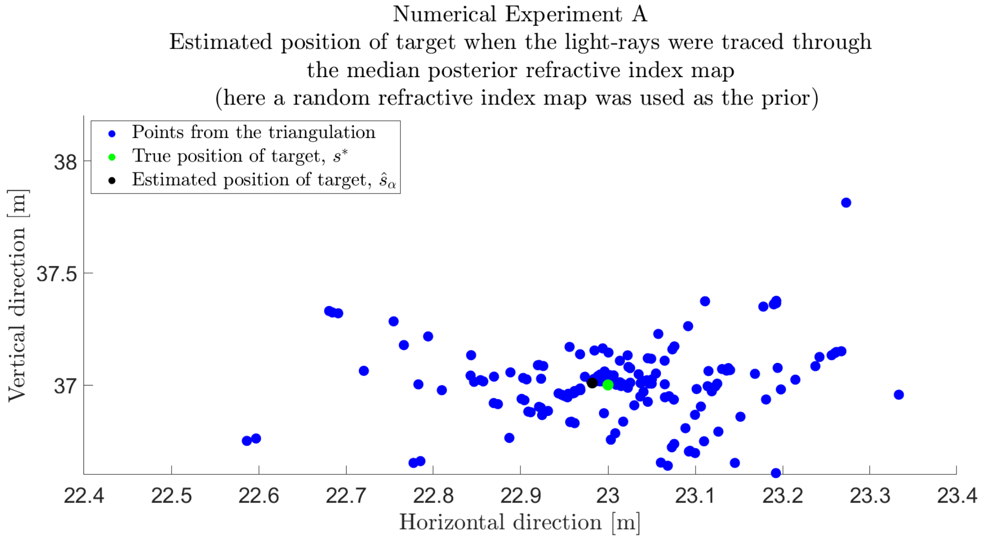

Figure 4.24: Numerical Experiment A, random refractive index map as prior. This plot shows the results of the triangulation method when the light-rays are traced through the recovered refractive index map shown in Figure 4.22. The intersection points of the light-rays are shown by the blue points, the estimated position of the reflector ($\hat{s}_\alpha$) is shown by the black dot and the true position (s^*) is shown by the green dot.

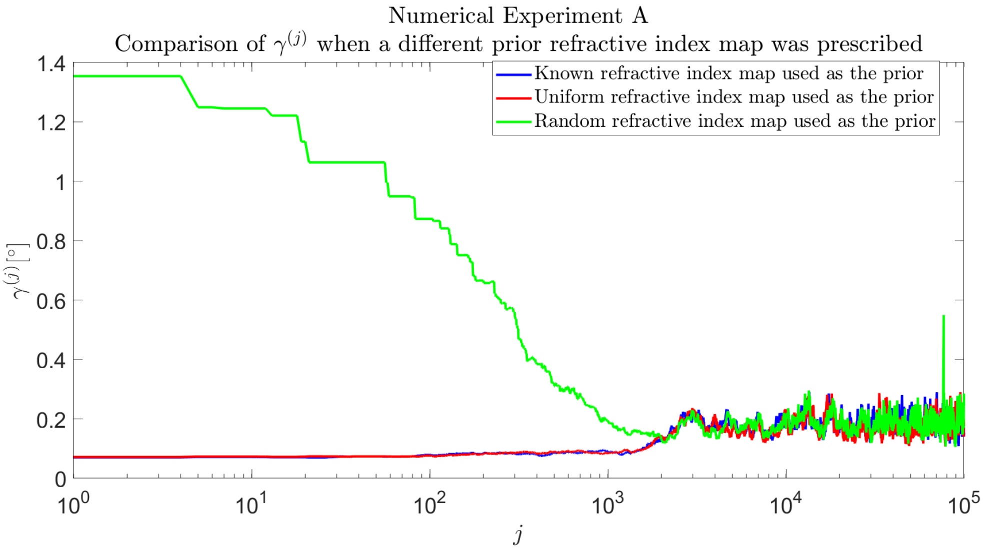

Figure 4.25: Numerical Experiment A: Objective function, $\gamma^{(j)}$, when the inversion was set to run for 100,000 iterations with a burn-in period of 20,000. This plot compares $\gamma^{(j)}$ when m^* was used as the prior (blue line), when m^h was used as the prior (red line) and when a random refractive index map as the initial prior (green line).

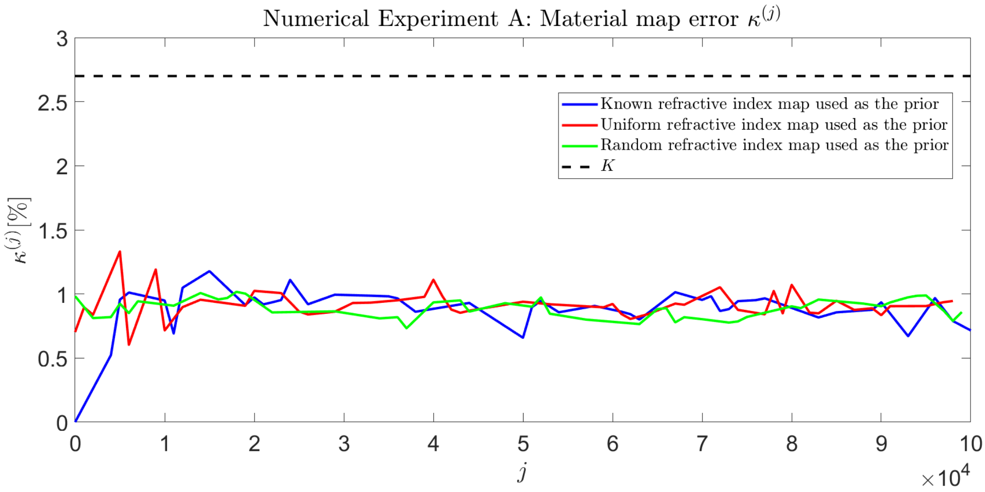

Figure 4.26: Numerical Experiment A: This plot shows how the mean percentage difference between the known map m^* and accepted Voronoi tessellations change as the algorithm progresses. The blue line shows the error in the material map $\kappa^{(j)}$ when m^* was used as the prior, the red line shows the error in the material map $\kappa^{(j)}$ when m^h was used as the prior and the green line shows the error in the material map $\kappa^{(j)}$ when a random refractive index map was used as the prior. The dashed black line is K which is the range of refractive index values expressed as a percentage of the mean value. In this inversion process the algorithm ran for 100,000 iterations and a Voronoi diagram was output every 1000 iterations.

Table 4.2: Table summarising the improvement in uncertainty and position of the object of interest s^* when the light-rays are traced through various reconstructed refractive index maps. These results are for Numerical Experiment A

Spatial domain	ε [mm]	ε_{imp} [%]	$\mathcal{V}$ [mm]	$\mathcal{V}_{imp}$ [%]
m^*	1.3433×10^{-6}	NA	3.74×10^{-14}	NA
Homogeneous m^h	73.3	NA	33.9	NA
Known map as prior	33.6	54	28.5	16
Uniform map as prior	39.4	46	28	17
Random map as prior	20.0	73	3.6	89

4.8 Numerical Experiment B

Now that it has been shown that this method works for a strongly heterogeneous refractive index map, a weakly heterogeneous refractive map will now be considered. Recall that a strongly heterogeneous case is one that would not be observed in an industrial setting due to unrealistic refractive indices. Whereas a weakly heterogeneous case is one that could be observed in an industrial setting. The same 10 cell Voronoi as presented in numerical experiment A will be used, only this time the refractive indices will be commensurate with those observed in an industrial setting. The refractive indices chosen are those associated with a temperature range of 22 to 90 °C and the refractive indices are again randomly assigned to each Voronoi cell. This lower value of 22 °C is commensurate with the ambient temperature of the laboratory in Chapter 3). However, 90 °C is a higher temperature than the maximum temperature observed in Chapter 3, however this value was chosen in an attempt to make ε_h as large as possible and of a similar order to the results obtained in Chapter 3. This value of 90 °C is realistic, as the laboratory where the experiments in Chapter 3 were carried out is also where one of the University of Strathclyde's welding stations is located. Therefore it is not uncommon for high temperatures to be observed in this volume. Since the simulation only focuses on errors coming from thermal fluctuations whereas the positional error in the experimentation is not just caused by thermal fluctuations, the maximum temperature is raised to account for this. Using these temperatures, this led to the range in refractive index values being 8×10^{-3} % compared with 2.2 % in numerical experiment A.

Using the same method detailed in Section 4.7 the error in the position of the reflector (ε_h) and variance ($\mathcal{V}(\varepsilon_h)$) when the refractive index map was assumed to be homogeneous was $\varepsilon_h = 494.9$ μm and $\mathcal{V}(\varepsilon_h) = 43.7$ μm. The ε_h value is in keeping with those observed experimentally (see Table 3.1). Also these values are much smaller than those from Numerical Experiment A. In numerical experiment A ε_h was 73.3 mm and $\mathcal{V}(\varepsilon_h)$ was 33.9 mm

It will now be determined if using the recovered refractive index map yields an improvement in the uncertainty in the position of the reflector and the variance in the position. As in numerical experiment A, with the case where the known refractive index map m^* is used as the prior will be examined first, and the inversion will have 100,000 iterations with a burn-in period of 20,000 iterations. Firstly, $\gamma^{(j)}$ will be considered and this is shown in Figure 4.27, the first thing to note is that the objective function values are significantly smaller than those observed for numerical experiment A, which shows that the method is sensitive to refractive index changes. Furthermore, the number of Voronoi cells for maps $m^{(j)}$ ranged from 5 to 29 which is again a reduction from numerical experiment A. The acceptance rate for this particular instance was 39 % which is within the tolerance of the literature and is much lower than those obtained in numerical experiment A.

As in numerical experiment A, three recovered refractive index maps were output from the inversion algorithm. It was found that the κ_{mean} was the lowest value (1.996 $\times 10^{-3}$ %, compared with 2.077 $\times 10^{-3}$ % and 2.7230 $\times 10^{-3}$ % for the κ_{median} and κ_{max} values respectively) so this was chosen as the map to calculate

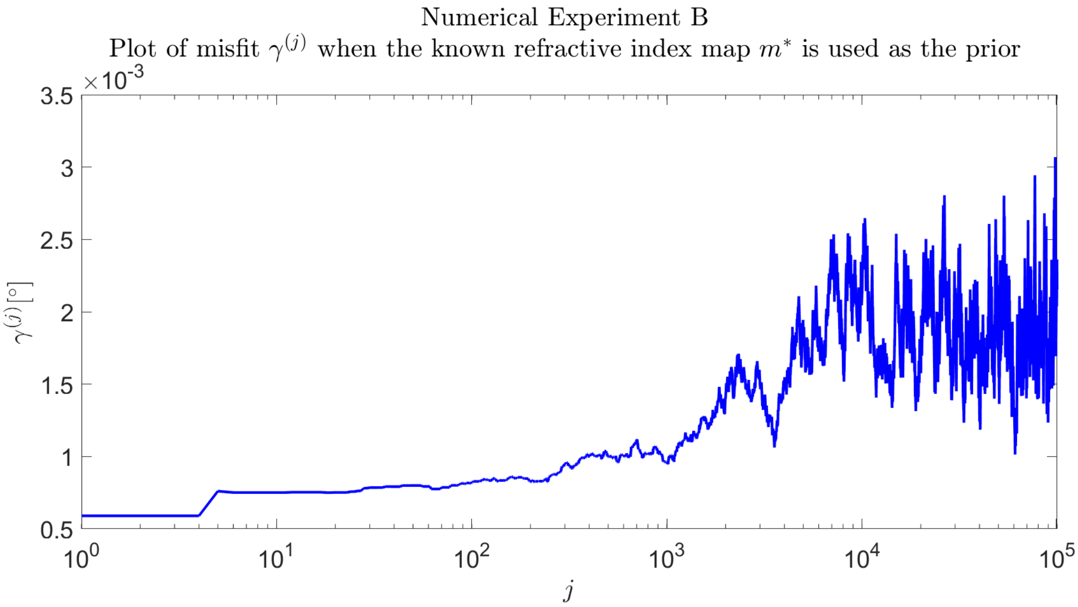

Figure 4.27: Numerical Experiment B: Objective function (misfit), $\gamma^{(j)}$, when the known refractive index map m^* is used as the prior.

ε_α. The recovered refractive index maps for the mean, median and maximum of the posterior distribution are shown in Figure 4.28. In addition, Figure 4.29 shows the temperature maps in degrees Celsius to give an improved readability of the results. The refractive indices have been converted to temperatures using the Ciddor equation.

Following the triangulation method (the results of which are shown in Figure 4.30). The blue dots show the intersection points of the light rays, the green dot shows the true position of the reflector s^* and the black dot shows the estimated position of the reflector when the mean recovered refractive index map is used as the refractive index map. It was found that ε_α was 243 μm which yields an ε_{imp} of 51 % and $\mathcal{V}(\varepsilon_\alpha)$ was 22 μm which is a $\mathcal{V}_{imp}$ of 50 %.

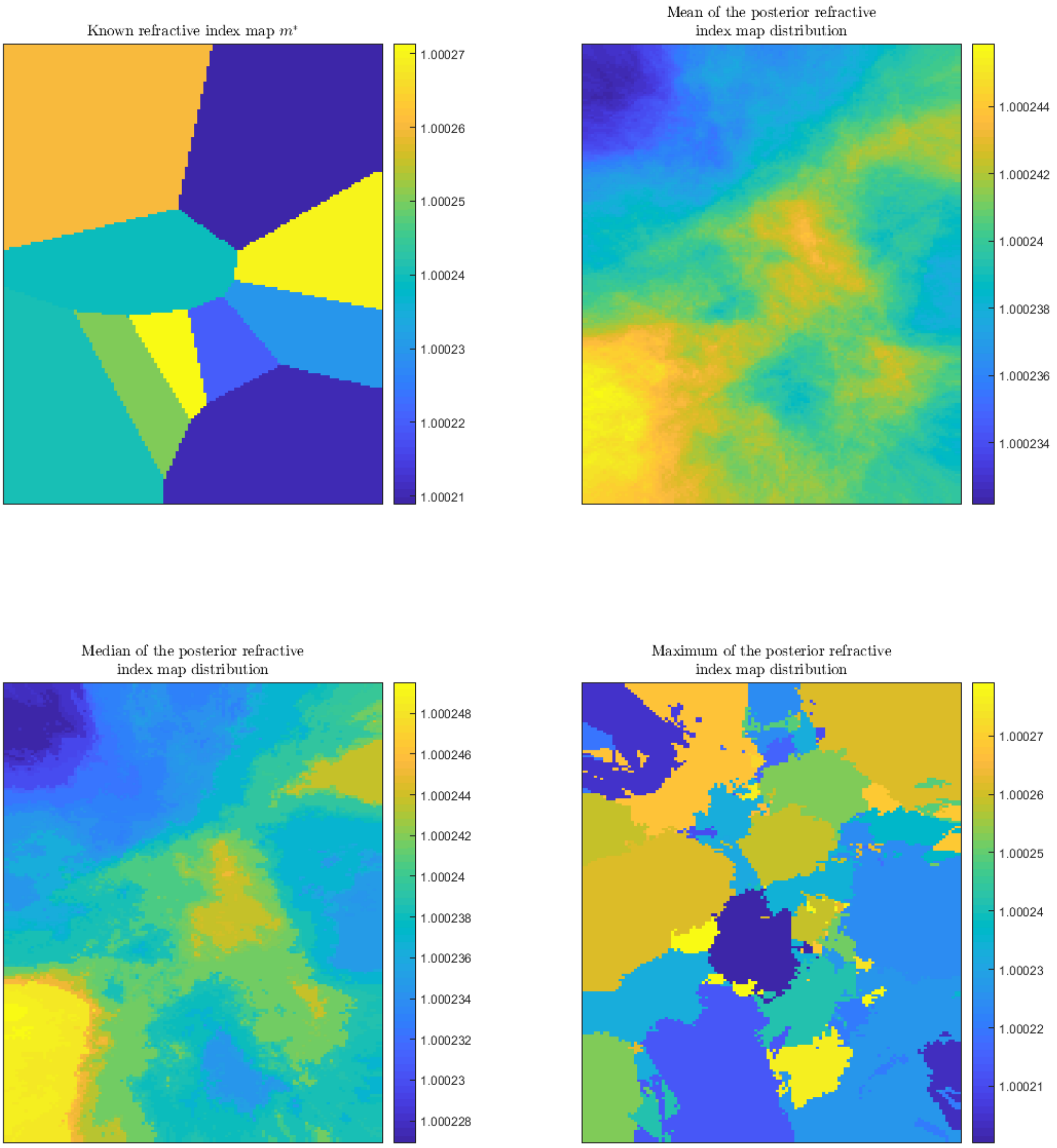

Figure 4.28: Numerical Experiment B: Top Left: The known refractive index map m^*, Top Right: the mean of the sampled refractive index map posterior, Bottom Left: median of the sampled posterior refractive index map and Bottom Right: the maximum-a-posteriori of the sampled posterior refractive index map distribution. In this case the prior was the known refractive index map.

The case where the uniform refractive index map was used as the initial prior will now be examined. The acceptance rate for this inversion was again 39 %. The mean recovered refractive index map had a κ_{mean} value of 1.930 $\times 10^{-3}$ %, compared with 2.005 $\times 10^{-3}$ % and 2.458 $\times 10^{-3}$ % for κ_{median} and κ_{max}) so this was chosen as the map to calculate ε_α. The number of Voronoi cells ranged from 5 to 26 which is a marginally smaller range than when the known refractive index map m^* was used as the prior.

The light-rays were traced in order to find the error in the positioning of the reflector s^*. Using the triangulation method an estimate for $\hat{s}_\alpha$ was found and the results of the triangulation indicated that the positional error in the estimated position ε_α was 260.7 μm which leads to an ε_{imp} value of 47 %. There is also an improvement in the uncertainty, since the variance was found to be 21 μm, which is a $\mathcal{V}_{imp}$ value of 52 %. Interestingly the κ_{median} values is lower for this prior compared with when the known refractive index map is used as the prior, but the ε_α and $\mathcal{V}(\varepsilon_\alpha)$ are higher which seems counter intuitive.

A final inversion was carried out for numerical experiment B, wherein a random refractive index map was chosen as the prior. This refractive index map was a Voronoi tessellation with 138 cells and is shown in Figure 4.21. The acceptance rate was 40 %. The mean recovered refractive index map had a κ_{mean} value (1.885 $\times 10^{-3}$ %, compared with 1.893 $\times 10^{-3}$ % and 2.320 $\times 10^{-3}$ % for κ_{median} and κ_{max} respectively) so this was chosen as the map to calculate ε_α. One thing to note here is that the κ_{mean} and κ_{median} are lower than those calculated when the known and uniform refractive index map m^* is used as the prior.

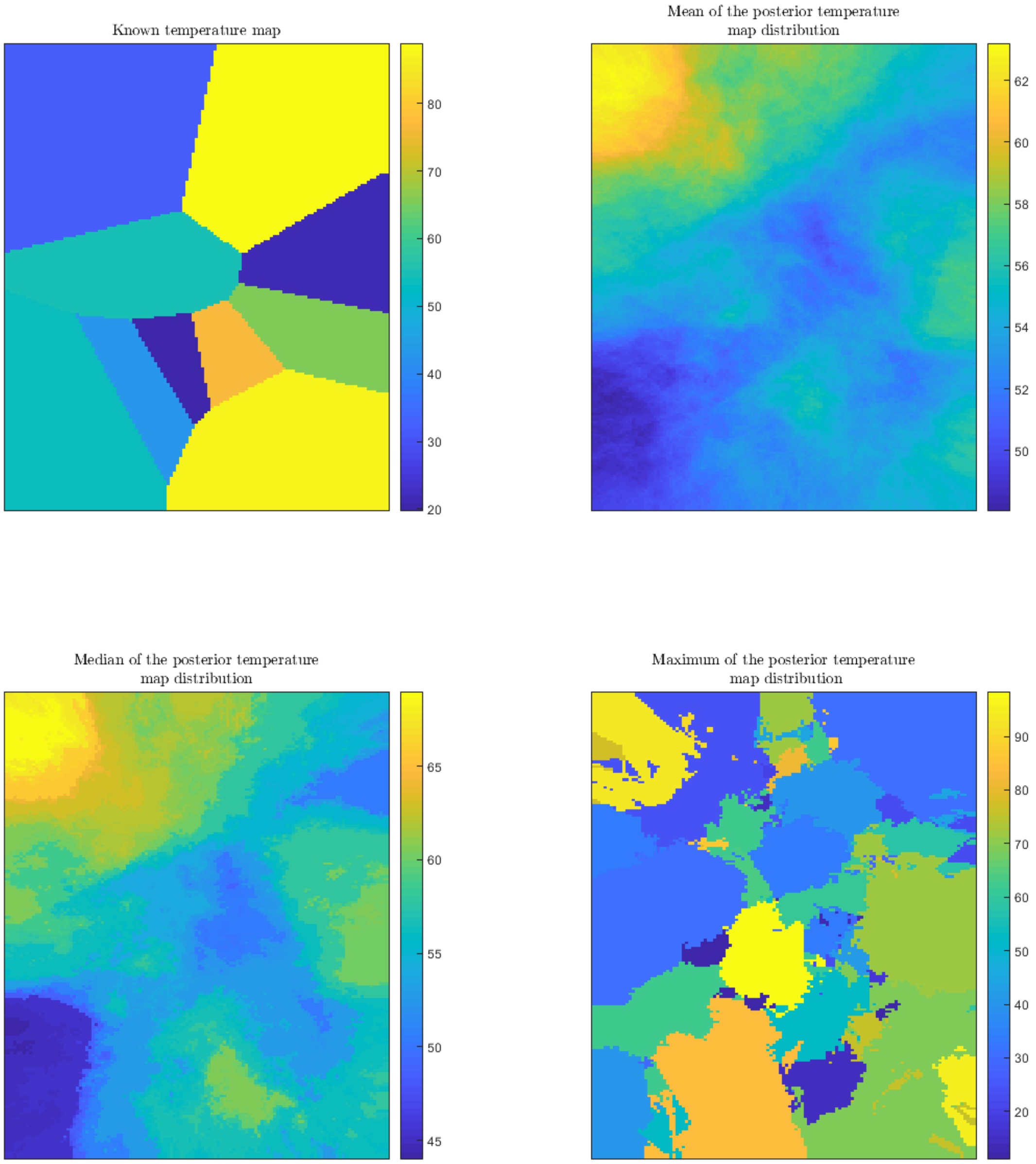

Figure 4.29: Numerical Experiment B: Top Left: The known temperature map, Top Right: the mean of the sampled temperature map posterior, Bottom Left: median of the sampled posterior temperature map and Bottom Right: the maximum-a-posteriori of the sampled posterior temperature map distribution. In this case the prior was the known refractive index map, and have been converted to a temperature in this instance using the Ciddor equation. All of the above temperatures are reported in degrees Celsius.

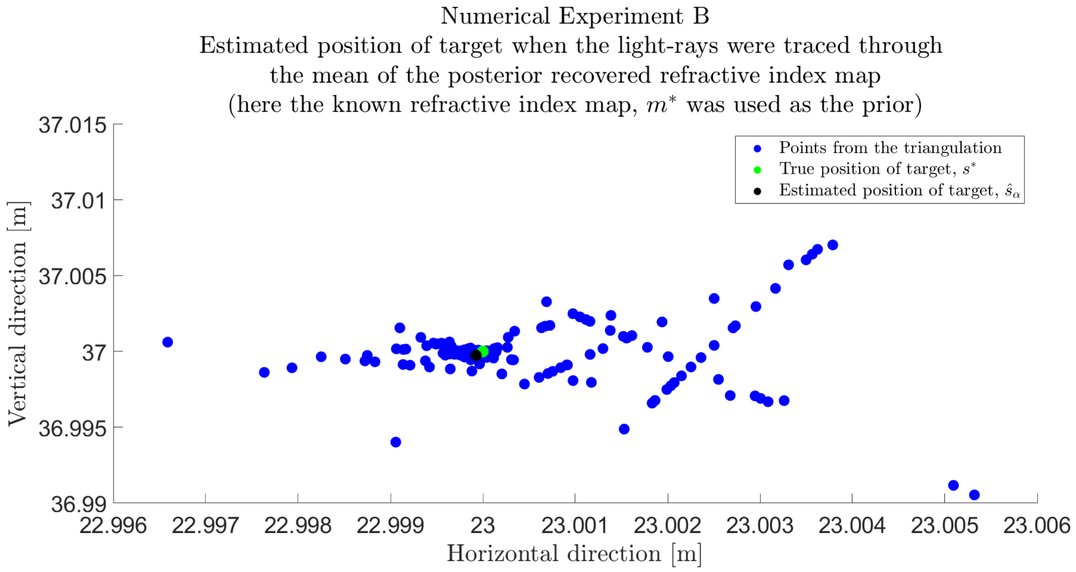

Figure 4.30: Numerical Experiment B: This plot shows the results of the triangulation method when the light-rays were traced through the mean recovered refractive index map. The intersection points of the light-rays are shown by the blue points, the estimated position of the reflector ($\hat{s}_\alpha$) is shown by the black dot and the true position (s^*) is shown by the green dot.

The light-rays were traced through Figure 4.22 in order to find the error in the reflector s^*. Using the triangulation method an estimate for $\hat{s}_\alpha$ was found and the results of the triangulation indicated that the improvement in the estimated position ε_α was 242.7 μm which leads to a ε_{imp} value of 51 %. There is also an improvement in the uncertainty, since the variance was found to be 19 μm, which is a $\mathcal{V}_{imp}$ value of 57 %. A full summary of the results for numerical experiment B can be found in Table 4.3.

Finally, the mean material map difference is examined in Figure 4.31. Recall that K, the range of refractive indices expressed as a percentage of the mean refractive index for the reconstructed refractive index maps is 8 $\times 10^{-3}$ %. In this case at every 500th iteration of the inversion the $\kappa^{(j)}$ value of the corresponding Voronoi tessellation is plotted. It can be seen that when the known refractive index map was used as the prior (blue line) at iteration zero the objective function is zero (as expected) and then it increases and begins to flatten out. The red line shows the objective function when a uniform refractive index map is used as the prior. As expected this has an initial value which is not equal to zero and this has quite a flat trend. The green line is the equivalent plot for the case where a random Voronoi tessellation is used as the prior. Generally speaking the $\kappa^{(j)}$ value for all three cases is approximately 3×10^{-3} %.

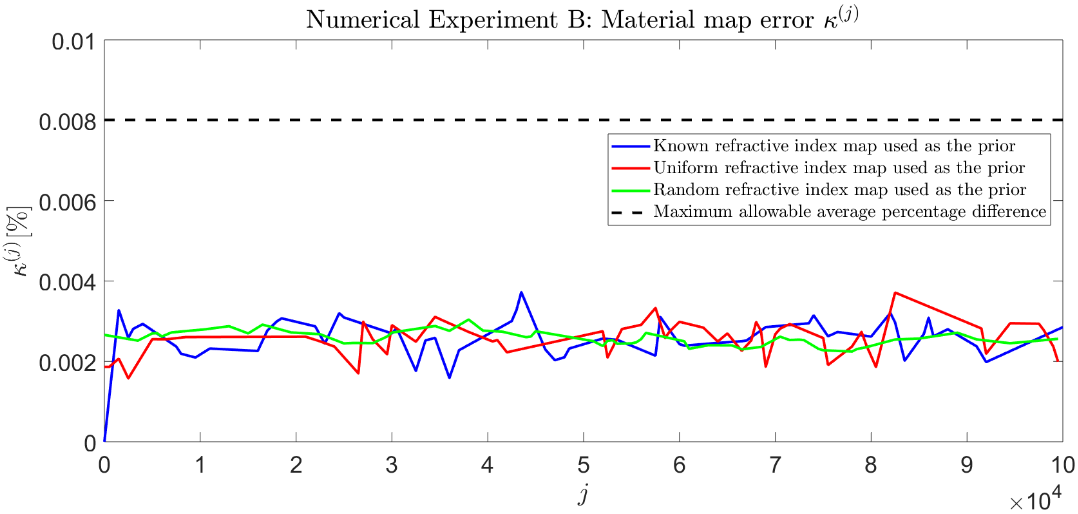

Figure 4.31: Numerical Experiment B: This plot shows how the mean percentage difference between the known map m^* and accepted Voronoi tessellations change as the algorithm progresses. The blue line shows the error in the material map $\kappa^{(j)}$ when the known refractive index map was used as the prior, the red line shows the error in the material map $\kappa^{(j)}$ when a uniform refractive index map was used as the prior and the green line shows the error in the material map $\kappa^{(j)}$ when a random refractive index map was used as the prior. In this inversion process the algorithm ran for 100,000 iterations and a Voronoi tessellation was output every 1000 iterations.

Table 4.3: Numerical Experiment B: Table summarising the improvement in uncertainty and position of the object of interest s^* when the light-rays are traced through various reconstructed refractive index maps

Spatial domain	ε [μmm]	ε_{imp} [%]	$\mathcal{V}$ [/mum]	$\mathcal{V}_{imp}$ [%]
Homogeneous m^h	494.9	NA	43.7	NA
known map as prior	242.9	50	22	51
uniform map as prior	260.7	47	21	52
random map as prior	242.7	51	19	57

4.9 Numerical Experiment C

Due to the success of numerical experiment B, the known refractive index map, m^*, will now take the form of a 100 cell Voronoi, as shown in Figure 4.32. As in numerical experiment B, the refractive indices in each cell, $\eta_p^{(j)}$, will be commensurate with those observed in the real world, indeed. In order to generate this Voronoi the method detailed in Section 4.6 cannot be used due to the large number of cells. Instead, MATLAB is used to generate 100 random seeds and then using Equation (2.16) the temperature in each Voronoi cell is determined and these temperatures were converted to refractive indices using the NIST conversion [145]. This data was then input into the inversion algorithm which was set to run for one iteration. In doing this, a file was obtained containing the specifics of the Voronoi (cell seed positions and corresponding refractive indices) and this file is now in the correct format to import directly into COMSOL and get the image shown in Figure 4.32.

Using the same method detailed in Section 4.7 the error in the position of the reflector (ε_h) and variance ($\mathcal{V}(\varepsilon_h)$) when the refractive index map was assumed to be homogeneous was found, ε_h = 279.3 μm and $\mathcal{V}(\varepsilon_h)$ =2.5 μm. The ε_h value is in keeping with those observed experimentally (see Table 3.1). Also these values are smaller than those calculated in numerical experiment B, showing that this smoother Voronoi tessellation leads to a smaller ε_h and $\mathcal{V}_h$. The reason for this is that a smooth Voronoi will exhibit less refraction effects as the refractive index ratio between the Voronoi cells is reduced.

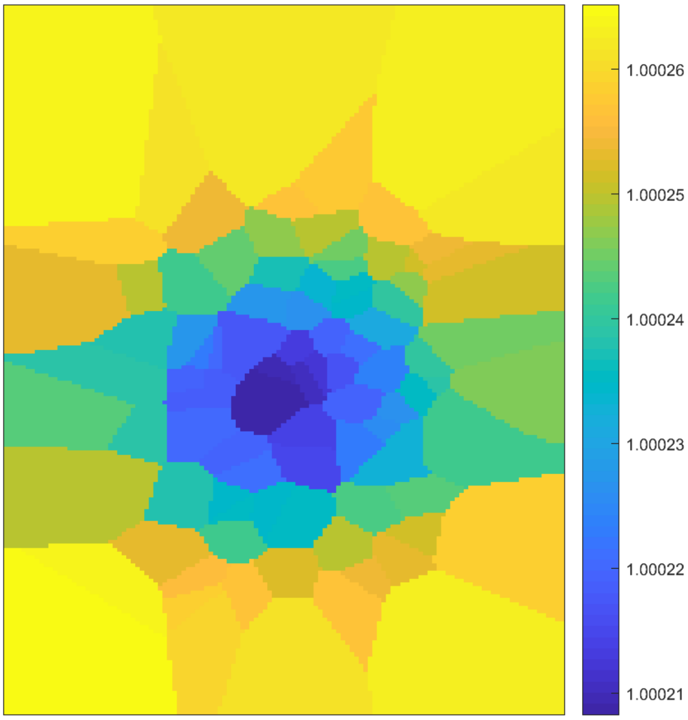

Figure 4.32: 100 cell Voronoi tessellation of a refractive index map which characterises a Gaussian distribution with a central temperature of approximately 363.15 K (90 °C) and a minimum temperature of 295.15 K (22 °C).

It will now be determined if using the recovered refractive index map yields an improvement in the uncertainty in the position of the reflector and the variance in the position. As in numerical experiment A and B, the case where the known refractive index map m^* is used as the prior will be examined first and as in previous, the inversion will use 100,000 iterations with a burn-in period of 20,000 iterations. The objective function, $\gamma^{(j)}$, is shown in Figure 4.33, the first thing to note is that the objective function values are the same order of magnitude than those observed in numerical experiment B. Furthermore, the number of Voronoi cells for model iterations $m^{(j)}$ ranged from 81 to 118 which is a larger range than that of numerical experiment B, which may suggest that the ray tracing part of the inversion lacks the sensitivity to detect the small ray path deviations caused by small refractive index changes when a larger number of Voronoi cells is considered. The acceptance rate for this particular instance was 40 % which is within the tolerance of the literature and is similar to numerical experiment B.

As in numerical experiment A and B, three recovered refractive index maps were output from the inversion algorithm. It was found that the κ_{mean} was the lowest value (1.65 $\times 10^{-3}$ %, compared with 1.79 $\times 10^{-3}$ % and 2.53 $\times 10^{-3}$ % for the κ_{median} and κ_{max} values respectively) so this was chosen as the map to calculate ε_α. Following the triangulation method (the results of which are shown in Figure 4.34). The blue dots show the intersection points of the light rays, the green dot shows the true position of the reflector s^* and the black dot shows the

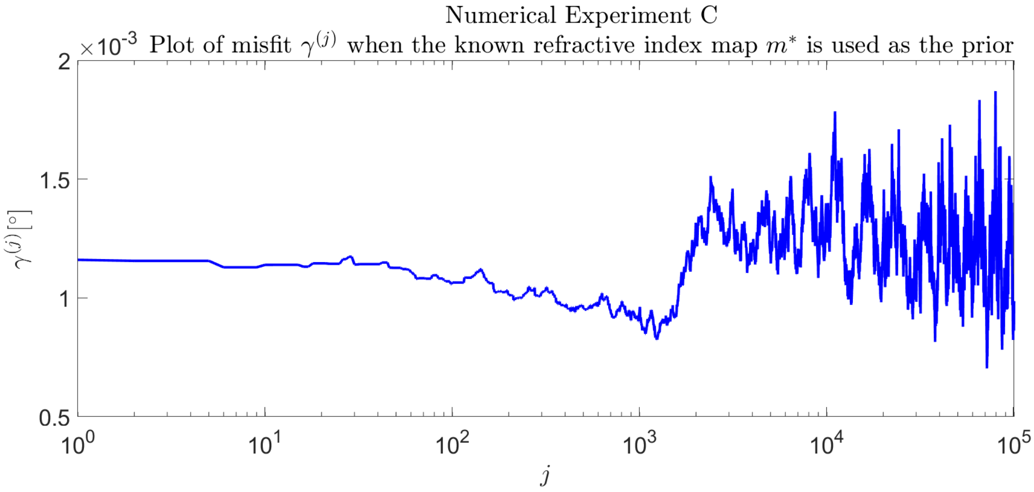

Figure 4.33: Numerical Experiment C: Objective function (misfit), $\gamma^{(j)}$, when the known refractive index map m^* is used as the prior.

estimated position of the reflector when the mean recovered refractive index map is used as the refractive index map. It was found that ε_α was 149 μm which yields an ε_{imp} of 47 % and $\mathcal{V}(\varepsilon_\alpha)$ was 0.7 μm which is a $\mathcal{V}_{imp}$ of 72 %.

The case where the uniform refractive index map was used as the initial prior will now be examined. The uniform refractive index was set to be a 100 cell Voronoi tessellation with each cell having a single refractive index which was the mean of the refractive indices used (this was the same value as in numerical experiment B). The acceptance rate for this inversion was again 40 %. The mean recovered refractive index map had a κ_{mean} value of 1.94 $\times 10^{-3}$ %, compared with 1.99 $\times 10^{-3}$ % and 2.65 $\times 10^{-3}$ % for κ_{median} and κ_{max}) so this was chosen as the map to calculate ε_α. The number of Voronoi cells ranged from 83 to 123 which is a marginally larger range than when the known refractive index map m^* was used as the prior.

As in all the previous numerical experiments, the light-rays were traced through the recovered map in order to find the error in the positioning of the reflector s^*. Using the triangulation method an estimate for $\hat{s}_\alpha$ was found and the results of the triangulation indicated that the error in the estimated position ε_α was 205.8 μm which leads to a ε_{imp} value of 26 %. The variance was found to be 5 μm, which is not an improvement and results in a $\mathcal{V}_{imp}$ value of -100 %.

A final inversion was carried out for numerical experiment C, wherein a random refractive index map was chosen as the prior. This refractive index map was a Voronoi tessellation with 111 cells and the number of Voronoi cells ranged between 90 and 124. The acceptance rate was again 40 %. The mean recovered refractive index map had a κ_{mean} value (2×10^{-3} %, compared with 2.1×10^{-3} % and 2.7×10^{-3} % for κ_{median} and κ_{max} respectively) so this was chosen as the map to calculate ε_α.

The light-rays were traced through the mean of the posterior recovered refractive index map in order to find the error in the reflector s^*. Using the triangulation method an estimate for $\hat{s}_\alpha$ was found and the results of the triangulation indicated that the error in the estimated position ε_α was 226 μm which leads to an ε_{imp} value of 19 %. There is also an improvement in the uncertainty, since the variance was found to be 0.9 μm, which is a $\mathcal{V}_{imp}$ value of 64 %. A full summary of the results for numerical experiment C can be found in Table 4.4.

In summary, for numerical experiment C, every recovered refractive index map yielded an improvement in the positioning of s^* and for the most part the variance was also significantly improved. The main concern with the results is the objective function which struggled to adapt to the smoothness of the Voronoi tessellation, this is due to the ray tracing algorithm of the inversion process. This improvement in the methodology will be looked at in the subsequent chapter. Prior to that a Gaussian refractive index map which is not based on a Voronoi tessellation will be considered.

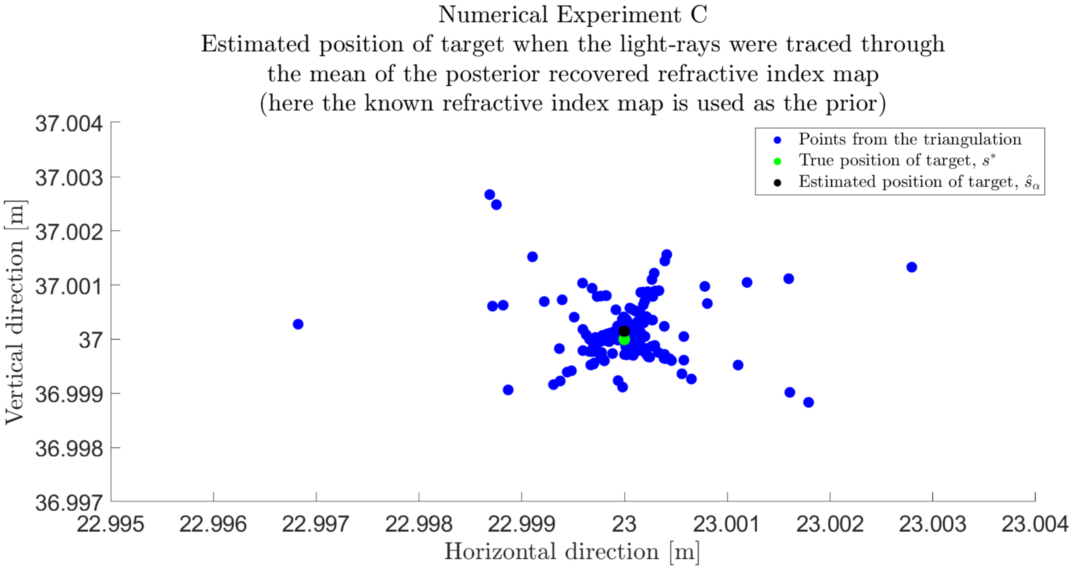

Figure 4.34: Numerical Experiment C: This plot shows the results of the triangulation method when the light-rays were traced through the mean recovered refractive index map. The intersection points of the light-rays are shown by the blue points, the estimated position of the reflector ($\hat{s}_\alpha$) is shown by the black dot and the true position (s^*) is shown by the green dot.

Table 4.4: Table summarising the improvement in uncertainty and position of the object of interest s^* when the light-rays are traced through various reconstructed refractive index maps. These results are for Numerical Experiment C.

Spatial domain	ε [μm]	ε_{imp} [%]	$\mathcal{V}$ [μm]	$\mathcal{V}_{imp}$ [%]
Homogeneous m^h	279.3	NA	2.5	NA
Known map as prior	149.0	47	0.7	72
Uniform map as prior	205.8	26	5.0	-100
Random map as prior	226.2	19	0.9	64

4.10 Numerical Experiment D

To create a refractive index map that is closer even to that observed in an industrial setting, a smooth Gaussian distribution was chosen for the known refractive index map, m^*. This Gaussian distribution was introduced in Subsection 2.2.1 via

$$T(x, y) = (T_{\max} - T_{\min}) \exp\left(-\frac{(x^2 + y^2)}{\sigma^2}\right) + T_{\min} \tag{4.12}$$

where $T(x, y)$ is the temperature at point (x, y) in the domain, σ is the variance of the temperature distribution measured in metres, $T_{\max}$ is the maximum temperature in the domain and similarly $T_{\min}$ is the minimum temperature. This refractive index map was input into COMSOL following the steps outlined in Subsection 2.2.1. In this numerical experiment, $T_{\max}$ was 363.15 K (90 $°C$), $T_{\min}$ was 295.15 K (22 $°C$, this is commensurate with the ambient temperature of the laboratory in Chapter 3) and σ was 20 m, so this is a very plausible industrial setting, for example, in a working volume where welding takes place. The $T_{\max}$ value is larger than that observed in Chapter 3, however this value was chosen in an attempt to make ε_h as large as possible and of a similar order to the results obtained in Chapter 3. This value of $T_{\max}$ is still very plausible in an industrial setting. These temperatures were converted to refractive indices using the Ciddor equation [68]; all other parameters in the equation were set at the NIST average values [136]. The domain size was kept the same as in all previous numerical experiments (40 m × 60 m).

As in all previous numerical experiments, the error when the refractive index map is assumed to be homogeneous was firstly calculated, as this informs whether or not refraction effects cause large enough inaccuracies in the position of s^*. To find this error, ε_h, the rays were traced from camera, c_k, with initial angle $\theta^*_{k,s}$. The triangulation method was used to find the intersection points of the rays and then the centre of mass is found which gives the estimated position of s^* when the domain is assumed to be homogeneous, that is, $\hat{s}_h$. In Figure 4.35 the blue points show the intersection points from the triangulation, the true position of the reflector s^* (shown by the green point) and the estimated position of the reflector $\hat{s}_h$ (shown by the black point). In this case ε_h was 174.2 μm and $\mathcal{V}(\varepsilon_h)$ was 1.4 μm. Comparing this results with those experimentally obtained in Chapter 3 we find that the error is slightly larger than in Experiment 1 and smaller than those obtained in Experiment 2 and 3, but they are all of the same order. In Chapter 3 there were 2 cameras compared to the 20 in this case, increasing the number of cameras gives a smaller error ε_h. The working volume was much smaller in Chapter 3 than in this case. In these simulated experiments there is complete ground truth, whereas experimentation can introduce other types of error. Whilst it is unlikely that an industrial space would have access to twenty cameras, we are simulating with this large number of cameras in an attempt to make the errors solely due to refraction as large as possible.

Unlike numerical experiments A to C, it is not possible to express the known refractive index map, m^*, exactly in terms of a Voronoi tessellation. It is possible to project the Voronoi tessellation onto a piecewise constant if the Voronoi tessellation takes the form of a regular grid. One of the advantages of a Voronoi

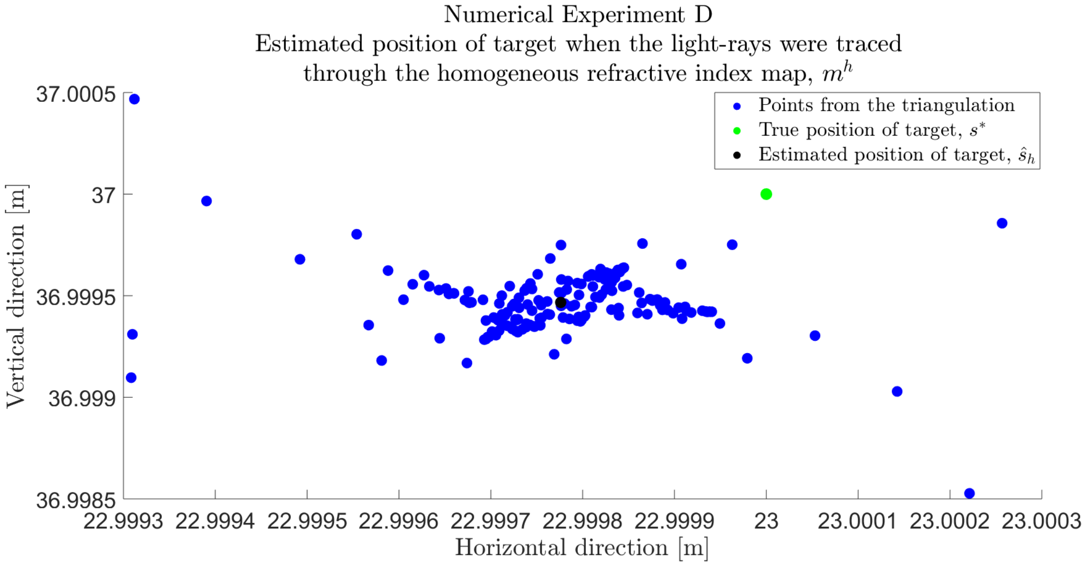

Figure 4.35: Numerical Experiment D: This scatter-plot illustrates the cluster of light-ray intersection points when the light-rays are traced from cameras c_k with initial angle $\theta^*_{s,k}$ through a homogeneous refractive index map. The mean of the light-ray intersection points yields $\hat{s}_h$ (illustrated by the black circle). The true position of the object of interest (s^*) is shown by the green circle.

tessellation is that all the cells are irregular in shape. In order for this piecewise constant to be accurate the grid size would need to be very small (this algorithm struggles with a fine grid size- see Subsection 4.2.1). In addition, this algorithm makes use of natural parsimony and tries to use the smallest number of Voronoi cells and since this would require a large number of Voronoi cells (in the order of thousands), this would not be feasible. This means that for numerical experiment D, the inversion process will only be able to start with a uniform and a random prior. The case where a uniform prior is used will be looked at first.

The uniform prior used in numerical experiment D is the same as the one used in numerical experiment C, that is, a Voronoi tessellation with 100 cells and the refractive index in each cell is the same (this value is the mean refractive index of the known refractive index map in numerical experiment C). As in all previous numerical experiments the inversion ran for 100,000 iterations and had a burn-in of 20,000. The range of Voronoi cells throughout the inversion ranged from 74 to 114 and the acceptance rate was 39.6 %. The objective function is shown in Figure 4.38, it can be seen that this objective function is of the same order as that obtained in numerical experiment C.

It was found that κ_{mean} was the lowest value (3.50 $\times 10^{-3}$) compared with κ_{median} and κ_{max}, 3.57 $\times 10^{-3}$ and 5.5 $\times 10^{-3}$ respectively. Following this, the mean of the posterior refractive index map was used as the spatial map for which the light rays are traced through. These refractive index maps are shown in Figure 4.36 and for increases readability, these refractive indices have been converted to temperatures using the Ciddor equation. The results of this are shown in Figure 4.37. The triangulation method obtained the following results: $\varepsilon_{\alpha} = 110.2$ μm and $\mathcal{V}(\varepsilon_{\alpha}) = 0.1$ μm. This leads to an ε_{imp} of 37 % and $\mathcal{V}_{imp}$ of 89 %.

Finally, a random Voronoi tessellation was used as the prior, the Voronoi had 96 cells. The range of Voronoi cells throughout the inversion varied from 80 to 110, which is a smaller range than when the uniform prior was used for numerical experiment D, but the lowest value is higher in this instance and the acceptance rate was 39.5 %. The objective function is shown in Figure 4.39, and starts off with a large $\gamma^{(j)}$ value and then decreases as j increases and finally begins to oscillate around 2.5 $\times 10^{-3}$ ° which is only slightly higher than the converged value in numerical experiment C.

It was found that κ_{mean} was the lowest value (4.57 $\times 10^{-3}$) compared with κ_{median} and κ_{max}, 5.18 $\times 10^{-3}$ and 6.1 $\times 10^{-3}$ respectively. Following this, the mean of the posterior refractive index map was used as the spatial map for which the light rays are traced through. The triangulation method obtained the following results: $\varepsilon_{\alpha} = 147.2$ μm and $\mathcal{V}(\varepsilon_{\alpha}) = 0.7$ μm. This leads to an ε_{imp} of 15 % and $\mathcal{V}_{imp}$ of 51 %. The results of numerical experiment D are shown in Table 4.5. These results seem more intuitive as these κ values are larger and led to a lower ε_{imp} and $\mathcal{V}_{imp}$ values.

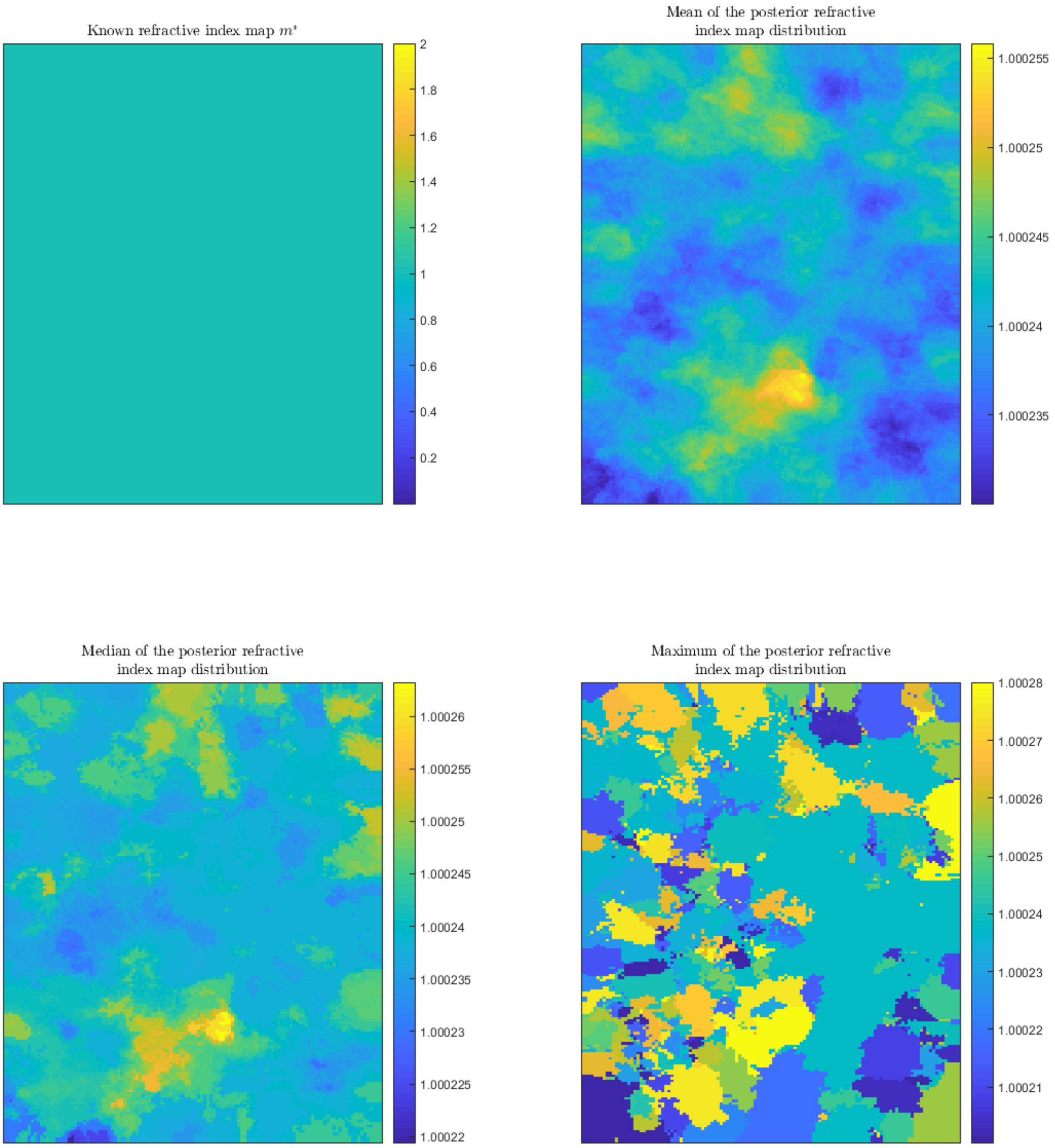

Figure 4.36: Numerical Experiment D: Top Left: The known refractive index map m^*, Top Right: the mean of the sampled refractive index map posterior, Bottom Left: median of the sampled posterior refractive index map and Bottom Right: the maximum-a-posteriori of the sampled posterior refractive index map distribution. In this case the prior was a uniform Voronoi tessellation.

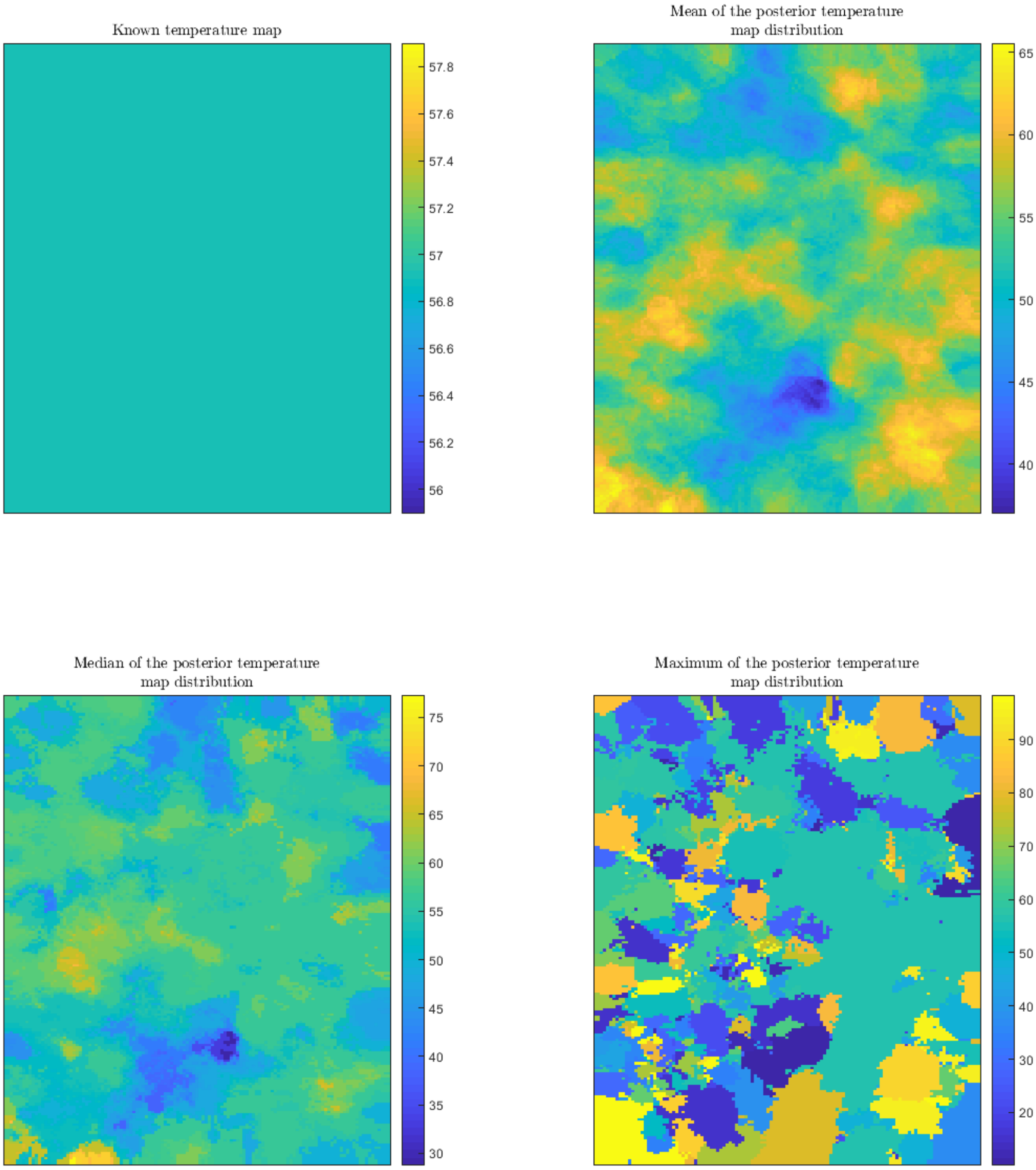

Figure 4.37: Numerical Experiment D: Top Left: The known temperature map, Top Right: the mean of the sampled temperature map posterior, Bottom Left: median of the sampled posterior temperature map and Bottom Right: the maximum-a-posteriori of the sampled posterior temperature map distribution. In this case the prior was a uniform Voronoi tessellation. All of the above temperatures are reported in degrees Celsius

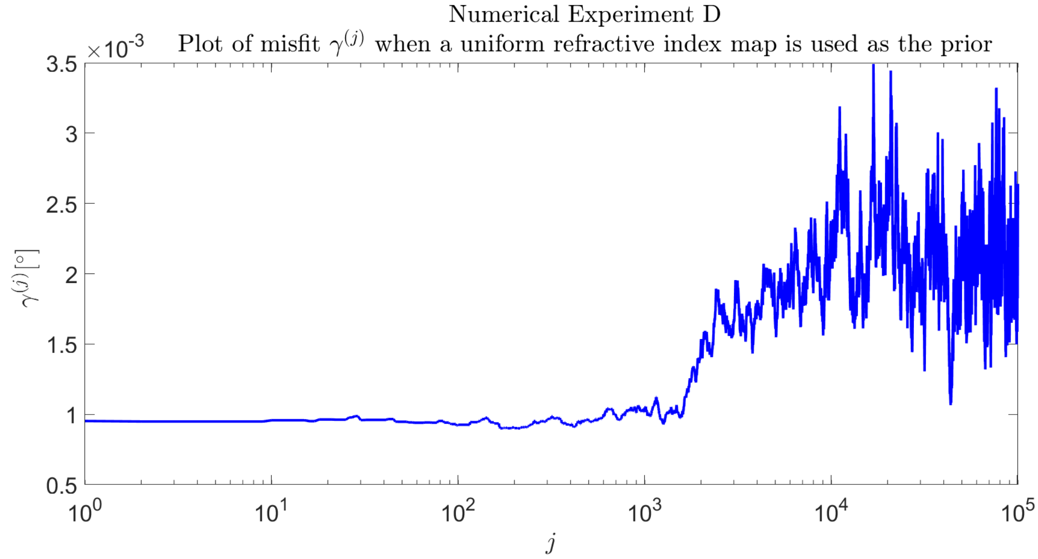

Figure 4.38: Numerical Experiment D: Objective function (misfit), $\gamma^{(j)}$, when a uniform refractive index map is used as the prior.

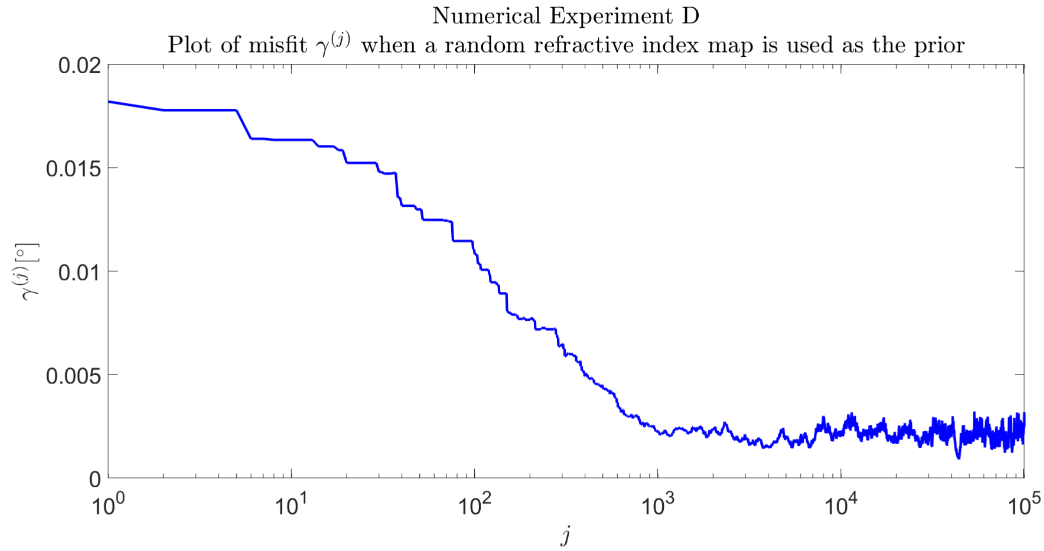

Figure 4.39: Numerical Experiment D: Objective function (misfit), $\gamma^{(j)}$, when a random refractive index map is used as the prior.

4.11 Chapter Summary

This chapter outlined the methodology involved in reconstructing the refractive index map, this methodology is referred to as the δ method. The parametrisation of the refractive index map employed Voronoi tessellations as these require fewer degrees of freedom to describe a heterogeneous map and large regions can be affected by a single perturbation. The forward model was solved using the Fast Marching Method (FMM), which calculates the travel time field between the camera and the reflector and then finds the optical path within this field that the ray takes. The objective function was based on the absolute difference between the experimentally measured angle ($\theta^*_{k,i}$) and the angle calculated at each iteration of the inversion algorithm ($\theta^{(j)}_{k,i}$) as shown in Equation (4.5). The choice of optimisation method was the reversible jump Markov Chain Monte Carlo (rj-MCMC) method. This is an iterative stochastic process which generates a population of solution samples from the posterior distribution. The goal of this is to reconstruct

Table 4.5: Table summarising the improvement in uncertainty and position of the object of interest s^* when the light-rays are traced through various reconstructed refractive index maps. These results are for Numerical Experiment D.

Spatial domain	ε [μm]	ε_{imp} [%]	$\mathcal{V}$ [μm]	$\mathcal{V}_{imp}$ [%]
Homogeneous m^h	174.2	NA	1.4	NA
Uniform map as prior	110.2	37	0.1	89
Random map as prior	147.2	15	0.7	51

Table 4.6: Table giving the description of the spatial domain of each numerical experiment and the corresponding error when the domain is assumed to be homogeneous, ε_h.

Numerical Experiment	Description	ε_h	$\mathcal{V}(\varepsilon_h)$
A	10 cell strongly heterogeneous Voronoi (random cell allocation)	73.3 mm	33.9 mm
B	10 cell weakly heterogeneous Voronoi (random cell allocation)	494.9 μm	43.7 μm
C	100 cell weakly heterogeneous Voronoi (cell refractive index allocation follows a Gaussian distribution)	279.3 μm	2.5 μm
D	Weakly heterogeneous Gaussian distribution	174.2 μm	1.4 μm

the refractive index map such that the positional error, ε_α is smaller than the error that arises when assuming a homogeneous refractive index map, ε_h (which is the current practice).

An initial test case (numerical experiment A) based on a ten cell Voronoi diagram refractive index map was investigated. This refractive index map was strongly heterogeneous and produced a positional error (ε_h) of 73.7 mm arising from a refractive index fluctuation of 2.2 %. Using the median of the refractive index map posterior distribution, a 54 % improvement in the estimated position of the reflector s^* was obtained and a reduction in the variance of 16 %. When there was a uniform prior refractive index map the improvement in the estimated position of the reflector is 46 % and there was a reduction in uncertainty of 17 %. Using a random refractive index map as the prior led to the best improvement in position, 73 % and uncertainty 89 %.

Numerical experiment B had the same Voronoi cell seed position as in A, but the refractive indices were weakly heterogeneous to be commensurate with values observed in an industrial setting. This known refractive index map had a K value of $8 \times 10^{-3}\%$, where K is the range of refractive index values expressed as a percentage of the mean value. When the known refractive index map was used as the initial prior the mean recovered refractive index map was most similar to it and yielded an ε_α of 242.9 μm which is an ε_{imp} of 51 % and $\mathcal{V}(\varepsilon_\alpha)$ was 22 μm which is a $\mathcal{V}_{imp}$ of 51 % . The uniform prior had a ε_α value of 260.7 μm which is an ε_{imp} of 47 % and $\mathcal{V}(\varepsilon_\alpha)$ was 21 μm which is a $\mathcal{V}_{imp}$ of 51 %. The random prior yielded an ε_α of 242.7 μm which is an ε_{imp} of 51 % and $\mathcal{V}(\varepsilon_\alpha)$ was 19 μm which is a $\mathcal{V}_{imp}$ of 57 %. The issue of robustness was questioned as intuitively starting with the known map as initial prior should yield a greater ε_{imp} and $\mathcal{V}_{imp}$ compared when a random Voronoi map is the initial prior.

Numerical experiment C introduced a Voronoi tessellation with 100 cells, with the same refractive index range as in numerical experiment B. For all three priors (known, uniform and random) the uncertainty in the position of s^* was reduced by 47 %, 26 % and 19 % respectively. These results were more intuitive than numerical experiment B as it was expected that starting from the known prior to yield the greatest reduction in the position. When the inversion algorithm started with the known refractive index map, and a randomly generated refractive index map, a reduction in the variance of 67 %, and 64 % respectively, was observed, whereas the uniform prior led to the variance doubling compared to the homogeneous case. One limitation of this numerical experiment was the lack of sensitivity in the objective function. The objective function was the same order of magnitude as numerical experiment B, however in general the refractive index maps were much smoother due to a larger number of Voronoi cells. One potential reason for this is that the ray tracing part of the inversion is not robust enough to deal with small changes in the trajectory of the ray paths.

The final numerical experiment, D, was a more realistic scenario with a single Gaussian distribution representing the heterogeneous temperature distribution. Since this refractive index map cannot be represented as a Voronoi tessellation, the inversion process could only start with a uniform and random prior. Using a uniform prior led to an ε_{imp} of 37 % and a $\mathcal{V}_{imp}$ of 89 %, whereas a random prior resulted in an ε_{imp} of 15 % and $\mathcal{V}_{imp}$ of 51 %.

The following Chapter will introduce a new method for calculating $\theta_{k,i}^{(j)}$ which avoids using the ray tracing algorithm. This new method aims to produce a more sensitive misfit $\gamma^{(j)}$ and reduce computational time.

Chapter 5

Using Time Fields to Reconstruct Refractive Index Maps from Photogrammetry Data

5.1 Using the Time Field to Trace the Ray-paths

The numerical experiments in Chapter 4 suggest that the ray-tracing step that follows the Fast Marching Method (FMM) is computationally very expensive and is not robust. In addition, this algorithm feeds into the objective function which causes it to not be sensitive to small changes in the refractive index. Therefore, to avoid using the ray tracing algorithm in the refractive index map reconstruction algorithm, used in Chapter 4, an alternative method is proposed. This chapter will give details of this proposed method and discuss the results from initial testing. The chapter will repeat Numerical Experiments A through D using the revised method and will report on the comparison between the two methods.

The reason this new revised method is being proposed is two-fold. Firstly, the ray tracing part of the algorithm dominates the computational expense and so this new method will greatly reduce the running time of the algorithm. Secondly, the ray-paths code is not robust and can lead to rays taking trajectories which would never be observed physically; this could be one of the reasons that the recovered refractive index maps do not resemble their respective known refractive index map m^*.

The proposed method still uses the FMM to calculate the arrival times of the ray as the travel time field of the whole domain will be required for the calculations. Due to the weakly heterogeneous nature of the refractive indices which are observed in an industrial setting, the straight ray angle ($\theta^h_{k,i}$) between the camera c_k and the reflector r_i is approximately equal to the experimentally known angle, that is, $\theta^h_{k,i} \approx \theta^*_{k,i}$. We are proposing that the difference, $\phi^*_{k,i}$, where $\phi^*_{k,i} = \theta^h_{k,i} - \theta^*_{k,i}$, between these two angles will be related to the difference between the homogeneous time field and the time field calculated at the j^{th} iteration in the inversion algorithm.

For weakly heterogeneous refractive index maps the degree of ray refraction will be small and so it is assumed that the ray refraction follows a parabolic curve with $0 < \phi \ll 1$. Let us consider a line that is perpendicular to the straight ray path between c_k and r_i and goes through reflector r_i. Due to reciprocity, it can be considered that a spherical wave is emitted from camera c_k, meaning that the arrival time of this wave along this line can be calculated. If the medium was homogeneous then the wave would arrive at r_i first and then the adjacent points on this line and then those adjacent to those and so on. When the medium is heterogeneous the ray bends due to refraction and the arrival times along this line change. Using this change in the arrival times is the basis for this revised approach and it is clear that there is no need now for a ray tracing step (see Figure 5.1, Figure 5.2 and Figure 5.3.

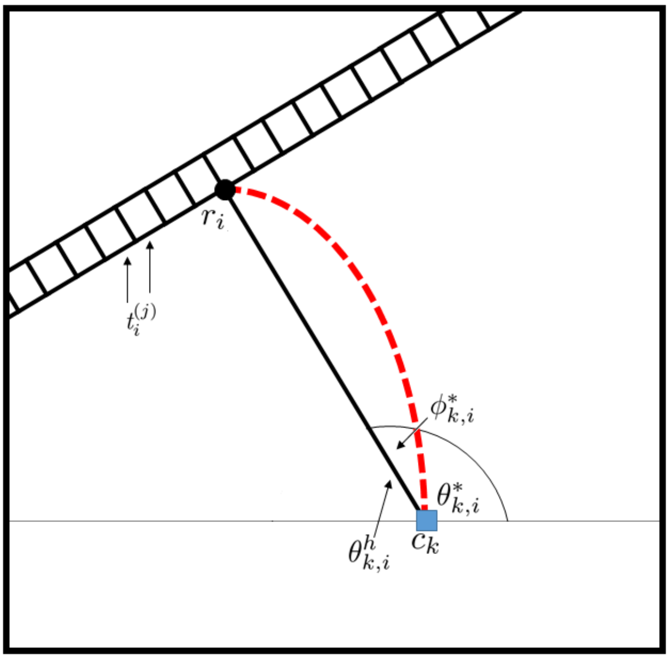

Figure 5.1: Schematic describing the time of flight method, where $\phi^*_{k,i}$ is the difference between the straight ray angle ($\theta^h_{k,i}$) between the camera c_k and reflector r_i and the actual angle that the ray propagates with ($\theta^*_{k,i}$) in the heterogeneous refractive index field. $t_i^{(j)}$ are the entries of the FMM calculated timefield along the line running perpendicular to the straight ray trajectory.

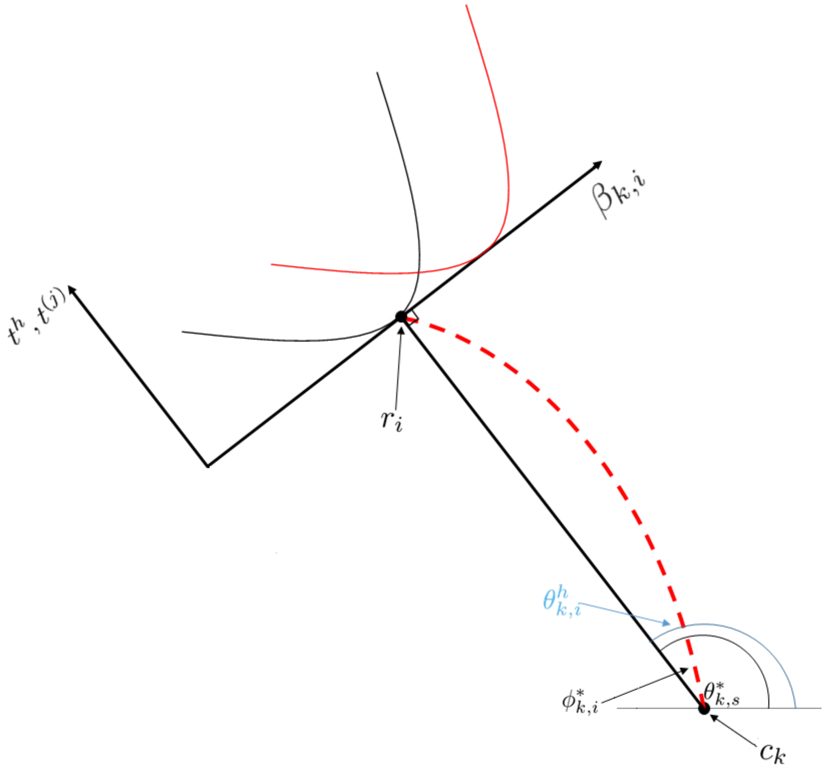

Figure 5.2: Schematic describing the time of flight method, where $\phi^*_{k,i}$ is the difference between the straight ray angle ($\theta^h_{k,i}$) between the camera c_k and reflector r_i and the actual angle that the ray propagates with ($\theta^*_{k,i}$). $\beta_{k,i}$ is the line that lies perpendicular to the straight ray path between c_k and r_i. t^h is the homogeneous time field and $t^{(j)}$ is the time field at iteration j of the inversion.

Denote the line that lies perpendicular to the straight ray path between c_k and r_i by $\beta_{k,i}$. Denote by t^h_i the times of arrival (on the discretised grid used by the FMM) of the spherical wave from c_k on the line $\beta_{k,i}$ when the refractive index

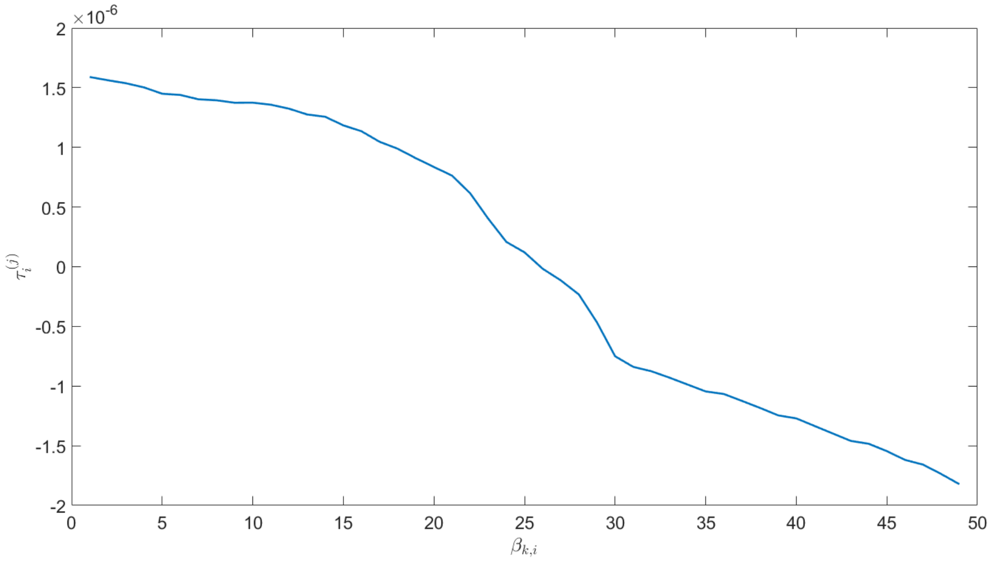

Figure 5.3: Results from initial investigation, showing $\tau^{(j)}$ against $\beta_{k,i}$.

map is homogeneous. Similarly, denote by $t_i^{(j)}$ the times of arrival at iteration j of the inversion process (when the material is heterogeneous). Denote the difference between these two as

$$\tau_i^{(j)} = t_i^h - t_i^{(j)}. \tag{5.1}$$

Following this, the gradient, q, between each adjacent point is found and then the mean of this value is taken

$$q_{k,i}^{(j)} = \frac{\sum_{p=1}^{p-1}(\tau_{p+1}^{(j)} - \tau_p^{(j)})\bar{c}/\Gamma x}{p-1}, \tag{5.2}$$

where Γx is the pixel size of the domain, p is the number of pixels along $\beta_{k,i}$ and $\bar{c}$ is the velocity of the homogeneous domain. This equation is divided by p to ensure that when $\phi^{*}_{k,i}$ and $\theta^{*}_{k,i}$ are compared, values with the same scale and units are being compared. Finally, $\phi^{(j)}_{k,i}$ is calculated by $\phi^{(j)}_{k,i} = \arctan(q^{(j)}_{k,i})$ (see Figure 5.4), $\phi^{(j)}_{k,i} = \theta^{h}_{k,i} - \theta^{(j)}_{k,i}$

If the ray length between camera c_k and r_i is denoted by b from Figure 5.5, then in the homogeneous case at $y = 0$ then $r^h = \sqrt{x^2 + b^2}$ and since $x \approx 0$ then using a Taylor series expansion

$$r^h \approx b + \frac{x^2}{2b} + O(x^4). \tag{5.3}$$

Similarly for iteration j, $r^{(j)} = \sqrt{(x-a)^2 + b^2}$ and since $x \approx 0$ then using a Taylor series expansion

$$r^{(j)} \approx \sqrt{a^2 + b^2} - \frac{ax}{\sqrt{a^2 + b^2}} + \frac{b^2 x^2}{2(a^2 + b^2)^{\frac{3}{2}}} + O(x^3), \tag{5.4}$$

but since $b \gg a$ because of the weakly heterogeneous setting, then $0 < \phi^{(j)}_{k,i} \ll 1$, so b dominates a. Therefore Equation (5.4) reduces to

$$r^{(j)} \approx \sqrt{b^2} - \frac{ax}{\sqrt{b^2}} + \frac{b^2 x^2}{2(b^2)}^{\frac{3}{2}} + O(x^3), \tag{5.5}$$

$$\approx b - \frac{ax}{b} + \frac{b^2x^2}{2b^3} + O(x^3) \tag{5.6}$$

$$\approx b - \frac{ax}{b} + \frac{x^2}{2b} + O(x^3) \tag{5.7}$$

Then $r^h - r^{(j)}$ is

$$b + \frac{x^2}{2b} + O(x^4) - \left(b - \frac{ax}{b} + \frac{x^2}{2b} + O(x^3)\right), \tag{5.8}$$

which is equal to $ax/b + O(x^2)$, showing that $\tan\phi_{k,i}^{(j)} = a/b$, as in Figure 5.5.

The time of flight methodology had to be coded into the inversion algorithm. Prior to running this code the homogeneous time fields have to be found. This is done by running the inversion algorithm for $j = 0$ iterations (this ensures that there is no noise) where the spatial domain is a Voronoi tessellation where every Voronoi cell has an equal refractive index. The refractive index chosen is the median refractive index which occurs in m^*. This file is then saved as a stacked matrix (there is one timefield matrix for each camera, so in this case there are 20 timefield matrices stacked vertically with c_1 at the top and c_{20} at the bottom). This homogeneous timefield dataset is then read into the inversion algorithm at every iteration j.

Following this at each iteration of the code, the algorithm finds the gradient of the line between c_k and r_i and the finds the gradient of the line perpendicular to this and from this the equation of the line is found. This line is then bounded such that it lies in the gridded geometry. The grid is exactly the same one which is used in the FMM. Then determining on the orientation of the line step along the grid horizontally (or vertically) to obtain integer (x, y) co-ordinates of grid points which the perpendicular line intersects and store these co-ordinates. Then read in the homogeneous time field data and obtain the time of flight in each of the stored co-ordinates, repeat this for the heterogeneous time of flight (this is calculated by default earlier in the algorithm for each iteration j). This then gives enough information to calculate $\tau_i^{(j)}$ in Equation (5.1), then using Equation (5.2) and the steps previously detailed $\phi_{k,i}^{(j)}$ is found.

In order to assess whether $\phi_{k,i}^{(j)}$ and $\phi_{k,i}^{*}$ are correlated initial testing was carried out at the zero-th iteration of the inversion algorithm, this was done to ensure complete control over the algorithm. In addition, it was important that the correct initial refractive index map was chosen, the map would have to be smooth and in keeping with what is observed experimentally, for this reason the spatial domain of Numerical Experiment C is chosen (see Table 4.6 and Figure 4.32). This Voronoi tessellation was then taken into COMSOL using the same method used with the reconstructed refractive index maps described in Subsection 4.7.4. Multiple rays of the same length with varying initial angle $\theta_{k,i}^{*}$ were then emitted from cameras c_k to reflectors r_i. The straight ray angle ($\theta_{k,i}^{h}$) between each camera - reflector pair were calculated as well as the value of $\phi_{k,i}^{*}$, where $\phi_{k,i}^{*}$ can be

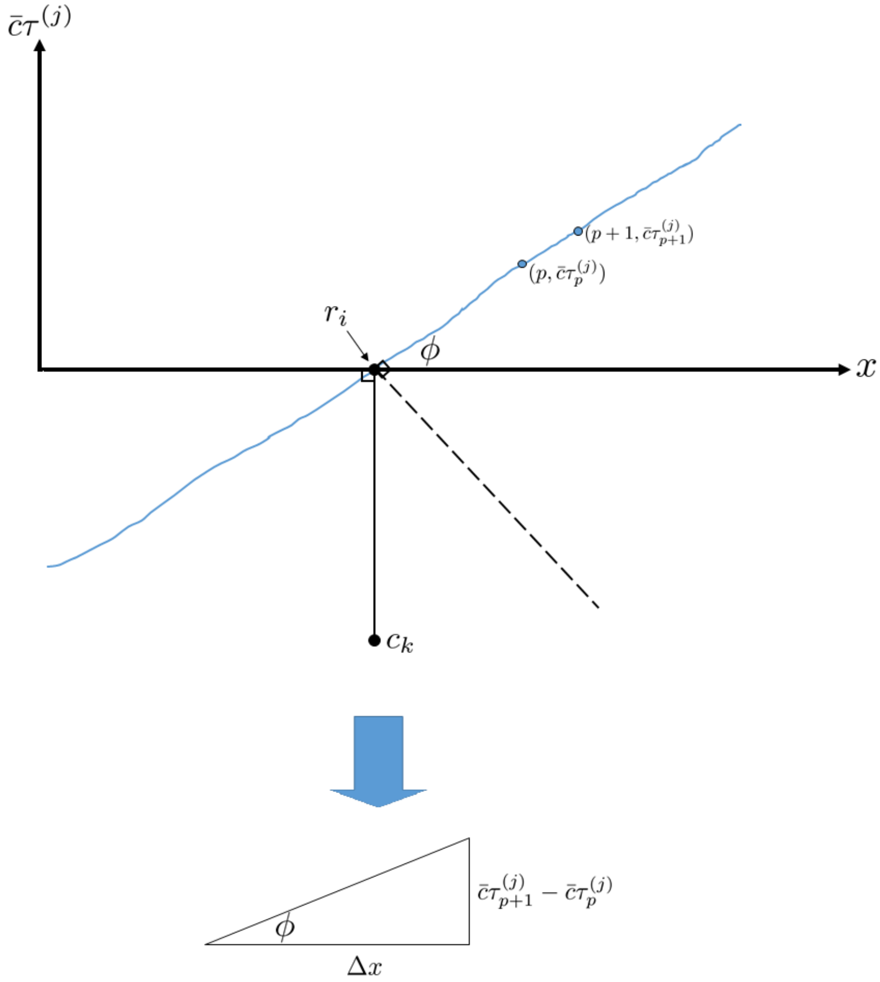

Figure 5.4: A schematic giving more detail of the time of flight method, where $(p, \bar{c}\tau_p^{(j)})$ and $(p+1, \bar{c}\tau_{p+1}^{(j)})$ are two points on the line, Γx is the size of a pixel, $\bar{c}$ is the mean velocity in the spatial domain.

positive or negative. Once these values were calculated, the inversion algorithm was run for zero iterations and the camera and receiver positions, the initial angles $\theta_{k,i}^{*}$ and the extent of the spatial domain were given as inputs. In the inversion algorithm the travel time field matrix is calculated via the FMM for each camera c_k. In the homogeneous case the refractive index map was set equal to the mean

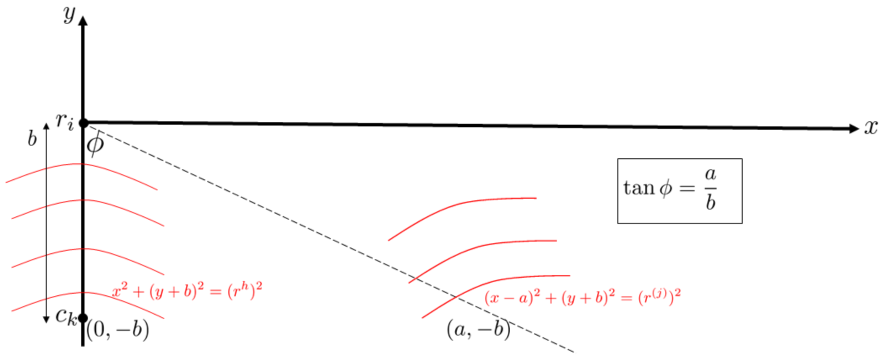

Figure 5.5: A schematic of a light ray emitted as a wave (red curves- equation of each wave is written in red also) from $(0, -b)$ and $(a, -b)$, where b is the ray length between camera c_k and r_i.

of those values in Figure 4.32. The travel time field matrix was then output when the refractive index map was homogeneous (to give t_i^h for each camera-receiver pair) and heterogeneous (to give the corresponding $t_i^{(0)}$).

Once the travel time field matrices were found for the homogeneous and the zero-th iteration, initial testing in MATLAB was carried out. An algorithm was written which calculates the equation of the line perpendicular to the straight ray path ($\beta_{k,i}$), following this the elements of the travel time matrix which lie on the this line are found (t_i^h and $t_i^{(0)}$). Then equations (5.1) to (5.3) are evaluated.

Before presenting the results of this method, a comparison between the δ-method in Chapter 4 and this Time of Flight (TOF) method is provided. The inversion algorithm (at the zero-th iteration) was used to calculate the angle estimates using the δ-method for the same camera-reflector pairs as above with the prior refractive index map being the Voronoi diagram from Figure 4.32 and numerical experiment C. The angle estimated from the algorithm was subtracted from the known angle ($\theta^*_{k,i}$) to give the deviation between the two ($\phi^{\delta}_{k,i}$). This was then plotted against $\phi^*_{k,i}$ in Figure 5.6a. From this plot it is clear to see that the TOF method (blue dots) performs much better than the δ-method (red dots). Closer examination of $\phi^{(0)}_{k,i}$ against $\phi^*_{k,i}$ is plotted in Figure 5.6b. This shows that $\phi^{(0)}_{k,i}$ and $\phi^*_{k,i}$ are positively correlated with each other, with a Pearson correlation coefficient of r = 0.74, which suggests a strong positive correlation.

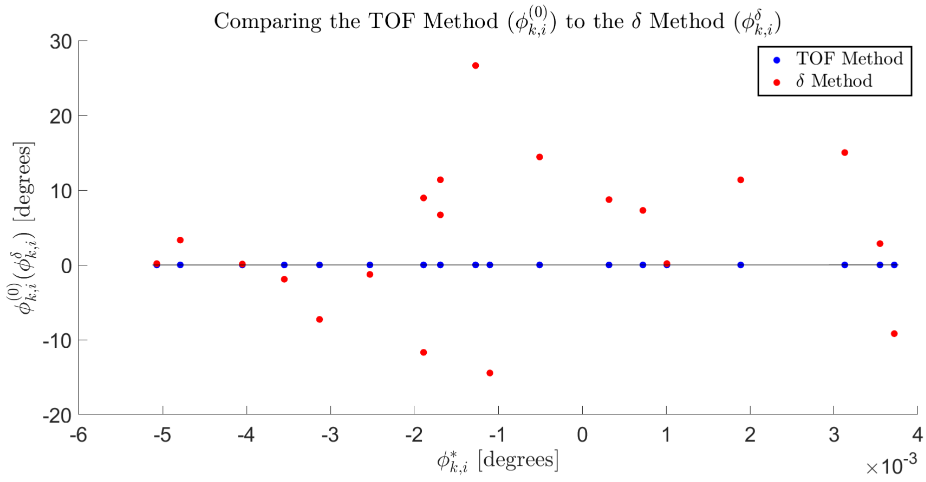

(a)

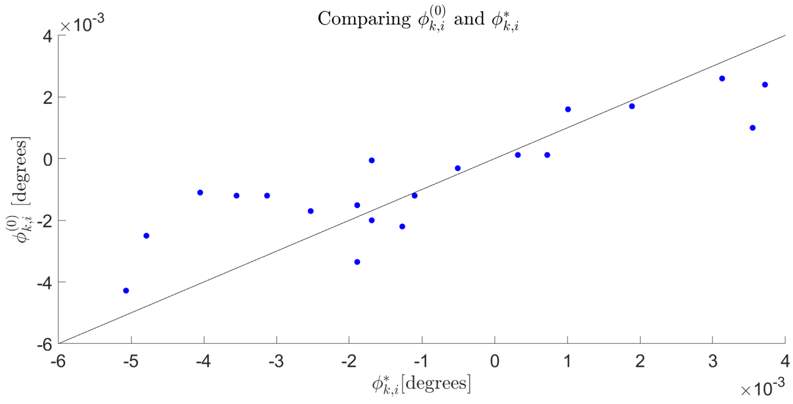

(b)

Figure 5.6: (a) Plot comparing the values that are obtained from using the δ method ($\phi_{k,i}^{\delta}$) detailed in Chapter 4 (red dots) and the time of flight method ($\phi_{k,i}^{(0)}$) presented in this chapter (blue dots) versus the ($\phi_{k,i}^{*}$ prescribed in COMSOL and 20 rays are considered. (b) Plot showing the relationship between $\phi_{k,i}^{(0)}$ and $\phi_{k,i}^{*}$, where $\phi_{k,i}^{(0)}$ is calculated time of flight method.

5.2 Numerical Experiment A

In this section the results of numerical experiment A using the revised TOF method compared with the δ-method results obtained in Section 4.7 will be examined. A comparison between the inversion algorithm performance in both approaches is discussed before presenting the use of the reconstructed refractive index maps in the positioning of the robot at s^*. Note that the computational time when using the TOF method took on average three hours to run 100,000 iterations compared to approximately three days for the δ method took to run. The reason for this is that in the δ method the ray tracing is the most computationally expensive part of the code. However, in the TOF method this part of the code has been switched off, hence the reduction in computational time. The inversion algorithm looks for the smallest number of Voronoi cells ($P^{(j)}$) to represent the map and so tracking this against iteration number j gives an indication of any improvement. The results are plotted in Figure 5.7 using a histogram and it can be clearly seen that the range of $P^{(j)}$ using the TOF method (blue bars) is much smaller than the corresponding values coming from the δ method (red bars).

The second indication of an improvement is a comparison of the objective function value $\gamma^{(j)}$ as expressed in Equation (4.5). Figure 5.8 shows a comparison of the two objective functions obtained from using the known refractive index map as the prior refractive index map when the TOF method is used (blue line)

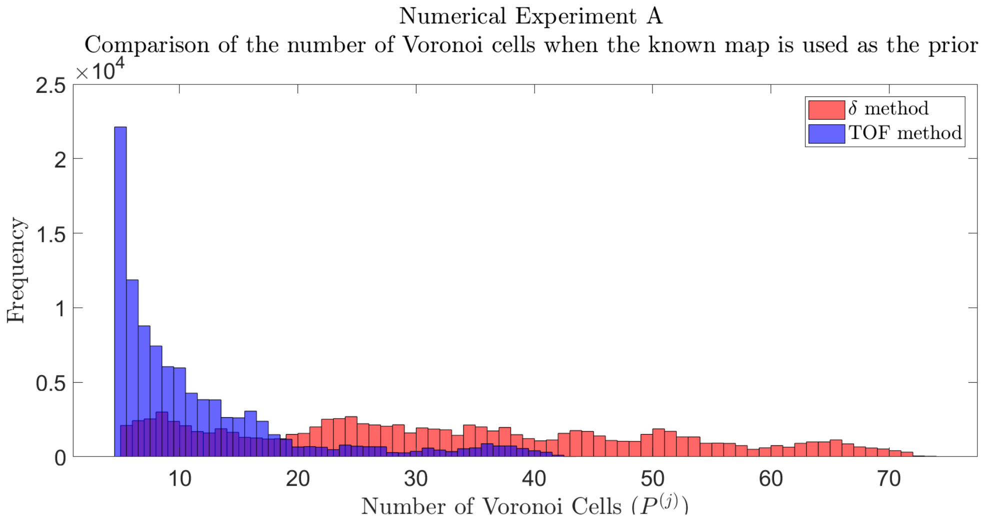

Figure 5.7: Histogram showing a comparison between the number of Voronoi cells $P^{(j)}$ at each iteration, j, of the inversion algorithm when the δ method (red bars) and the TOF method were used (blue bars). These results are based on Numerical Experiment A, when the known refractive index map was used as the prior.

compared with the δ method. It can be clearly seen from Figure 5.8 that the objective function is significantly reduced due to the implementation of the TOF method.

Since the user is ultimately interested in the improvement in the estimation of the position of an object of interest embedded in the domain, the recovered refractive index maps of the posterior distribution will now be considered and these are shown in Figure 5.9. In these plots (a) is the known refractive index map m^*, (b) is the mean of the posterior refractive index map, (c) is median of the posterior refractive index map and (d) the maximum-a-posteriori of the posterior refractive index map distribution. These plots do in fact show some improvement compared with Figure 4.16 particularly the upper left corner of plots (b) and (c) are showing good resemblance to plot (a). However, as in Chapter 4, the MAP

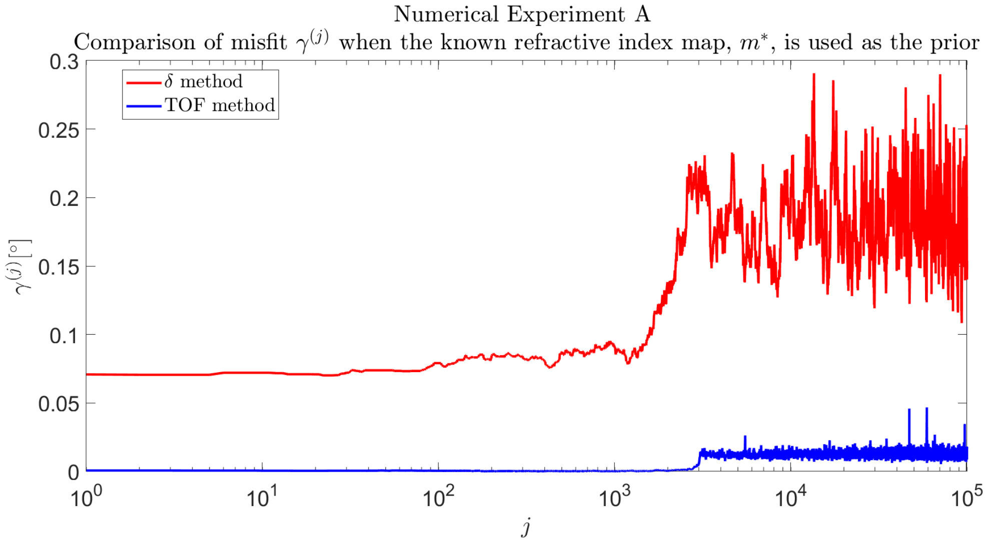

Figure 5.8: Plot showing a comparison between the misfit (objective function) $\gamma^{(j)}$ at each iteration j of the inversion algorithm when the previous δ method (red line) and the new TOF method was used (blue line). These results are based on Numerical Experiment A when the known refractive index map was used as the initial prior.

is not a good representation of the spatial domain. The same metric to assess the material map agreement, that is, κ_{mean}, κ_{median} and κ_{max} is used. It was found that these values were 0.66, 0.65 and 0.77. Since κ_{median} was the lowest value, it is the spatial domain that the rays will be traced through in order to calculate ε_α. As in previous numerical experiments the triangulation method was carried out and the results of this are shown in Figure 5.10 where the intersection points of the light-rays are shown by the blue points, the estimated position of the reflector ($\hat{s}_\alpha$) is shown by the black dot and the true position (s^*) is shown by the green dot. It was found that ε_α was 19.6 mm with a variance $\mathcal{V}(\varepsilon_\alpha)$ of 13.4 mm. These values lead to an ε_{imp} and $\mathcal{V}_{imp}$ of 73 % and 60 % respectively and the full results are expressed in Table 5.1. When these results are compared with those obtained using the δ method in Chapter 4 (Table 4.2), this method has a 42 % improvement in the error of the position and a 53 % improvement in the variance.

Following on from this, numerical experiment A was carried out again however the prior refractive index map was set to be a uniform refractive index map, m^h. The uniform prior has the same Voronoi cell positions as m^* but each cell has the same refractive index value which was the mean refractive index value of m^*. The triangulation method was again carried out to calculate $\hat{s}_\alpha$. It was found that

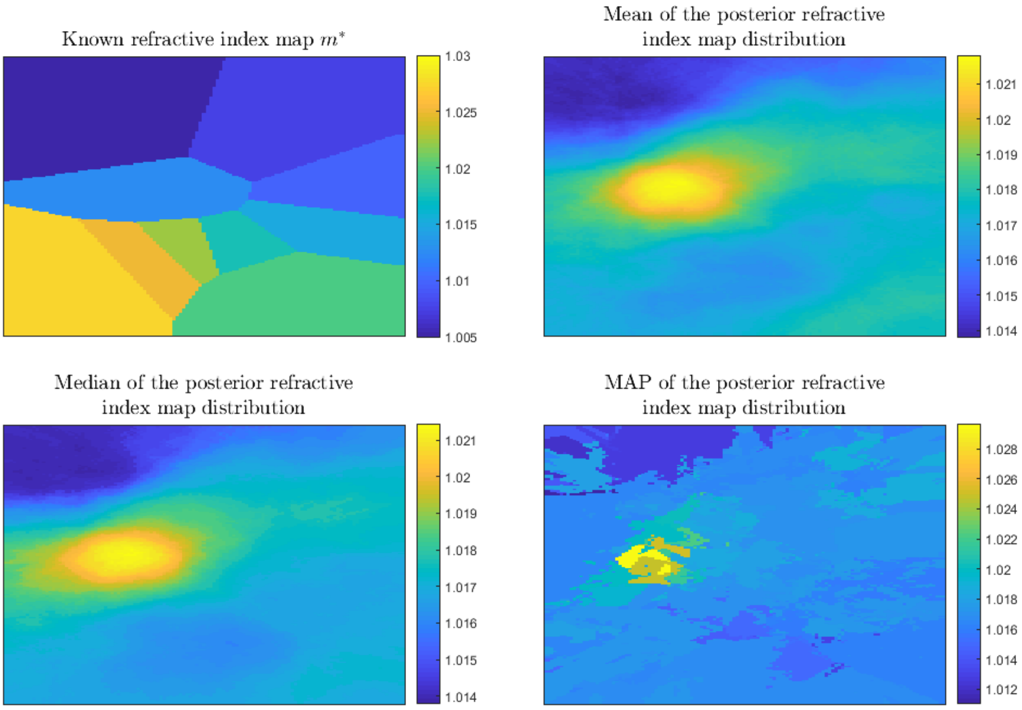

Figure 5.9: Numerical Experiment A: Top Left: The known refractive index map m^*, Top Right: the mean of the sampled refractive index map posterior, Bottom Left: median of the sampled posterior refractive index map and Bottom Right: the maximum-a-posteriori of the sampled posterior refractive index map distribution.

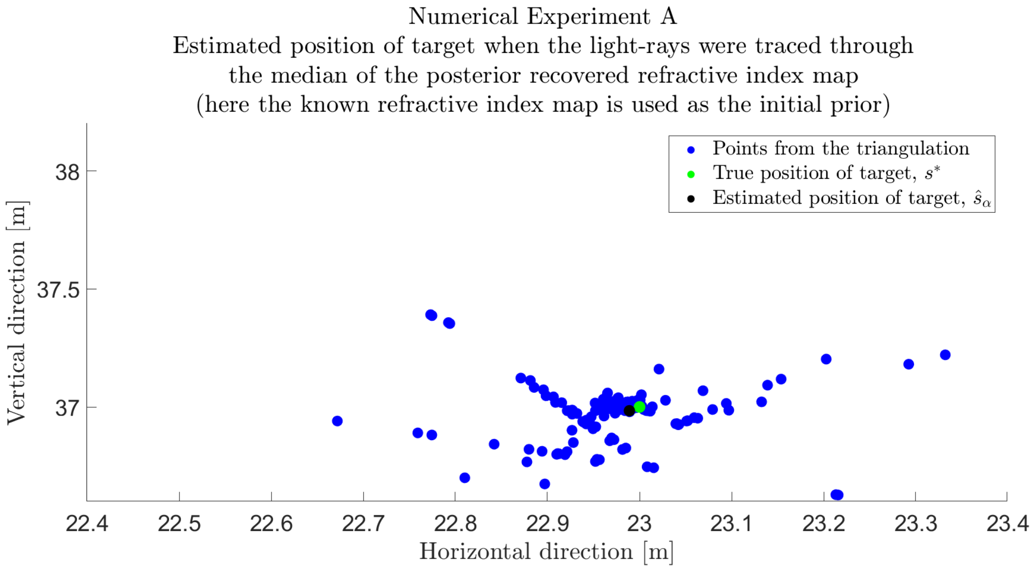

Figure 5.10: Numerical Experiment A: This plot shows the results of the triangulation method when the light-rays are traced through the recovered refractive index map shown in Figure 5.9 (c). The intersection points of the light-rays are shown by the blue points, the estimated position of the reflector ($\hat{s}_\alpha$) is shown by the black dot and the true position (s^*) is shown by the green dot.

ε_α was 23.5 mm with a variance $\mathcal{V}(\varepsilon_\alpha)$ of 12.1 mm. These values lead to an ε_{imp} and $\mathcal{V}_{imp}$ value of 68 % and 64 % respectively and the full results are expressed in Table 5.1. When these results are compared with those obtained using the δ method in Chapter 4 (Table 4.2), this method has a 40 % improvement in the error of the position and a 57 % improvement in the variance.

Finally, Numerical Experiment A was carried out again however the prior was set to be a randomly generated refractive index map chosen by the algorithm. The initial Voronoi diagram that the algorithm chose had $P^{(0)} = 86$ cells which is larger than the maximum value of the range in Figure 5.7. The triangulation method was again carried out to calculate $\hat{s}_\alpha$. It was found that ε_α was 23.8 mm with a variance $\mathcal{V}(\varepsilon_\alpha)$ of 12.2 mm. These values lead to an ε_{imp} and $\mathcal{V}_{imp}$ value of 68 % and 64 % respectively and the full results are expressed in Table 5.1.

These results appear more robust than observed in Section 4.7 as starting with the initial prior gives the lowest ε_α value which is intuitive, which in turn gives the largest ε_{imp} value, giving further validation on the robustness of this method. The acceptance rates when the known, uniform and random refractive index map are used as the prior are 40 %, 40 % and 44 % which are lower than the equivalent numerical experiment for the δ method.

Now that results have been obtained from the known refractive index map, uniform refractive index map and random refractive index map as priors, the objective functions and the material map errors will now be compared. If the former is considered which is shown in Figure 5.11 it can clearly be seen that the objective function is much smaller for the TOF method compared with the δ method, which is very encouraging and shows that TOF is sensitive to the small angle fluctuations observed.

Overall for numerical experiment A there was a 19 % improvement in error in the position in the case where the known prior was used for the TOF method, compared to the δ method and gave a 44 % improvement in the variance. When a uniform refractive index map was used as the prior, there was a 22 % improvement in error in the position in the case where a uniform prior was used for the TOF method, compared to the δ method and a 47 % reduction in variance. Finally, when a random refractive index map was used as the prior, the δ method performed better in terms of reduction in ε_α and $\mathcal{V}(\varepsilon_\alpha)$ (was better by 5 % and 25 % respectively) compared to the TOF method. 2 % improvement in the variance.

Finally the material map error at each iteration j of numerical experiment A, $\kappa^{(j)}$ was calculated (Equation (4.11) shows the formulation for $\kappa^{(0)}$) and the results of this are shown in Figure 5.12 as well as the range of refractive index values expressed as a percentage of the mean value, K,recall $K \approx 2.7\%$). This plot looks remarkably similar to Figure 4.26 although the recovered maps are significantly different (Figure 4.16 compared with Figure 5.9) and there is an improvement in the error in the positioning and the variance for all but one case. It could be possible that because the median and the MAP recovered maps in

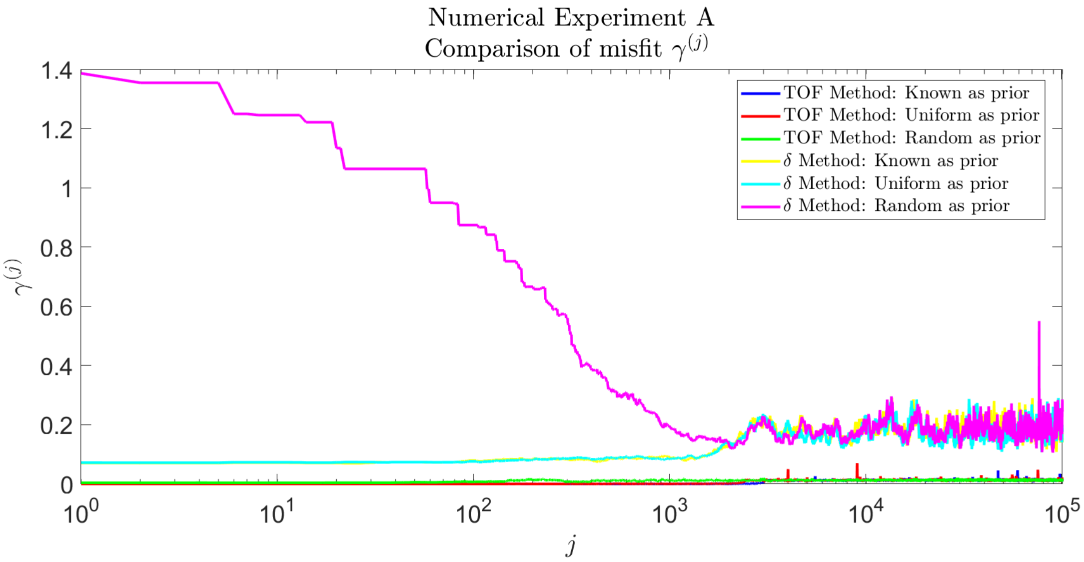

Figure 5.11: Numerical Experiment A: Plot showing a comparison between the misfit (objective function) $\gamma^{(j)}$ at each iteration j of the inversion algorithm when the δ method (yellow, cyan and magenta lines) and the TOF method were used (green, red and blue lines).

Figure 5.9 are very smooth compared to Figure 5.9 that the $\kappa^{(j)}$ value averages out to be the same. One thing to note is that the $\kappa^{(j)}$ looks at only the accepted Voronoi tessellations at each iteration (every 500 due to computational power) and not the mean, median or recovered refractive index maps which could explain why Figure 4.16 and Figure 5.9 are so similar.

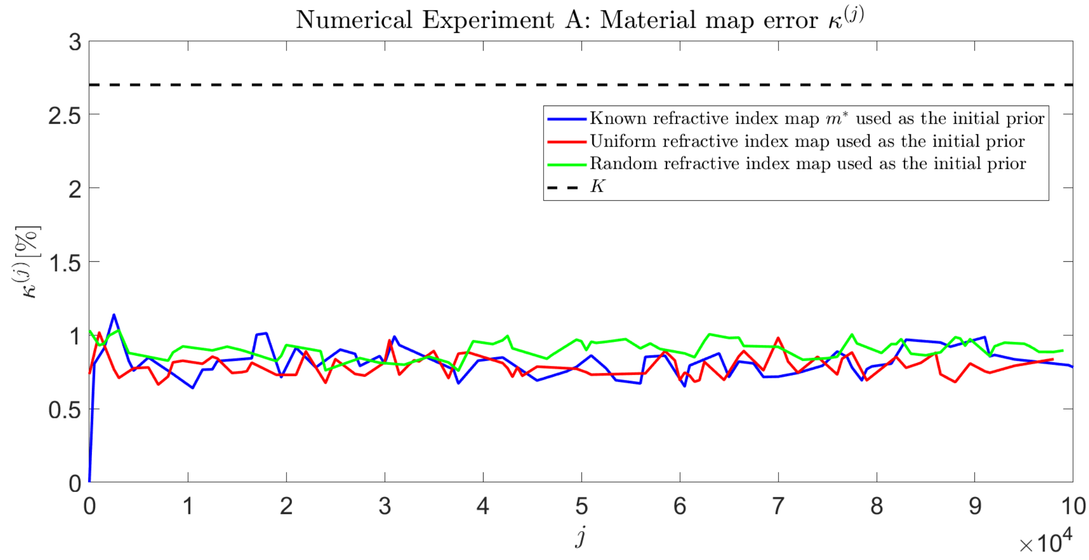

Figure 5.12: Numerical Experiment A: This plot shows how the mean percentage difference between the known map m^* and the accepted Voronoi diagrams change as the inversion algorithm progresses. The blue line shows the error in the material map $\kappa^{(j)}$ when the known refractive index map was used as the prior, the red line shows the error in the material map $\kappa^{(j)}$ when a uniform refractive index map was used as the prior and the green line shows the error in the material map $\kappa^{(j)}$ when a random refractive index map was used as the prior. The dashed black line is K which is the range of refractive index values expressed as a percentage of the mean value. In this inversion process the algorithm ran for 100,000 iterations and a Voronoi diagram was output every 500 iterations.

Table 5.1: Table summarising the improvement in uncertainty and position of the object of interest s^* when the light-rays are traced through various refractive index maps. These results only consider Numerical Experiment A

Spatial domain	ε [mm]	ε_{imp} [%]	$\mathcal{V}$ [mm]	$\mathcal{V}_{imp}$ [%]
m^*	1.3433×10^{-6}	NA	3.74×10^{-14}	NA
m^h	73.3	NA	33.9	NA
known map as prior	19.6	73	13.4	60
uniform map as prior	23.5	68	12.1	64
random map as prior	23.8	68	12.2	64

Table 5.2: Numerical Experiment A: Table summarising the improvement in uncertainty and position of the object of interest s^* when the light-rays are traced through various refractive index maps, this table considers the TOF and δ method.

	Spatial domain	ε [mm]	ε_{imp} [%]	$\mathcal{V}$ [mm]	$\mathcal{V}_{imp}$ [%]
	m^h	73.3	NA	33.9	NA
δ	known map as prior	33.6	54	28.5	16
TOF		19.6	73	13.4	60
δ	uniform map as prior	39.4	46	28.0	17
TOF		23.5	68	12.1	64
δ	random map as prior	20	73	3.6	89
TOF		23.8	68	12.2	64

5.3 Numerical Experiment B

To continue on with the comparison of the method the results of numerical experiment B (defined in Table 4.6) compared with those obtained using the δ method from Chapter 4 will be compared. As in the previous section all of the variables in the inversion have been keep constant aside from the method for calculating $\theta_{k,i}$. The case where the known refractive index map was used as the prior is considered first.

The first metric output by the inversion process is the number of Voronoi cells of the perturbed model, $m^{(j)}$ at each iteration, j. In this case the number of Voronoi cells ranged from 5 to 23, which is a smaller range than the equivalent from Section 4.8. Following this, the objective function is the next metric to be output and a comparison of the objective functions is shown in Figure 5.13 (δ method is the red line and the TOF method is the blue line). It can clearly be seen that $\gamma^{(j)}$is smaller for the TOF method compared with the δ method which is a positive result. In addition, the acceptance rate was 30 % which is lower than the equivalent in Section 4.8, but still within the realms of the literature.

The main assessment into the performance of the inversion algorithm is the improvement of the position of the robot and the variance associated with this. The material map difference, κ_{mean}, κ_{median} and κ_{max} were found to be 1.83 $\times 10^{-3}$ %, 1.89 $\times 10^{-3}$ % and 2.40 $\times 10^{-3}$ % respectively. Since κ_{mean} is the lowest it was the refractive index map which the light rays were traced through for the triangulation method. The recovered refractive index maps are shown in

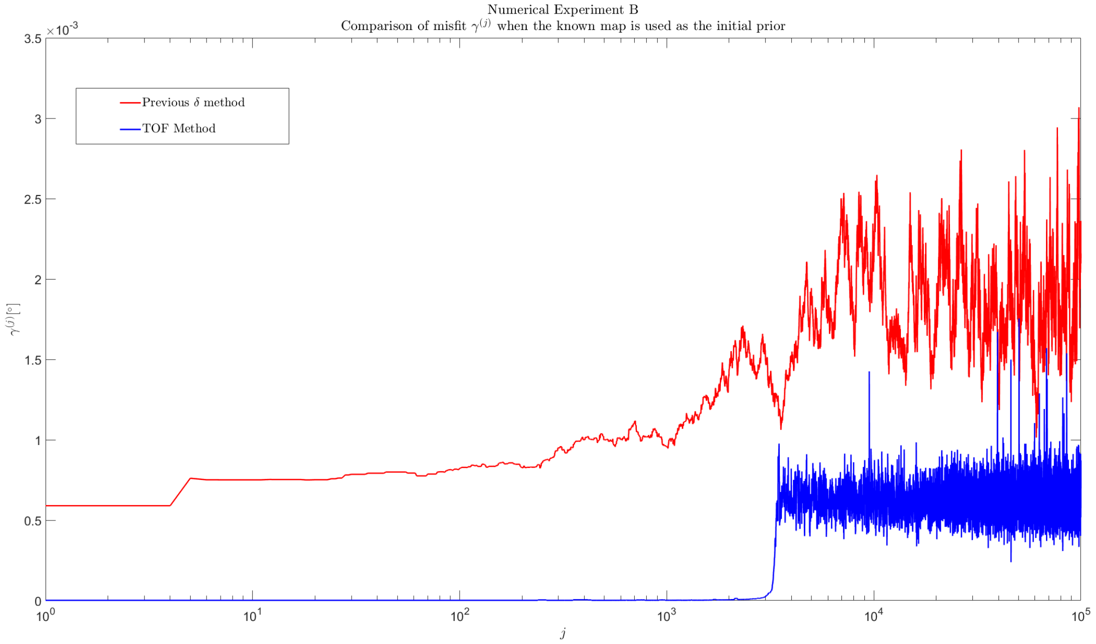

Figure 5.13: Numerical Experiment B: Plot showing a comparison between the misfit (objective function) $\gamma^{(j)}$ at each iteration j of the inversion algorithm when the δ method (red line) and the TOF method was used (blue line). These results are from Numerical Experiment B when the known refractive index map m^* was used as the prior.

Figure 5.14, with the corresponding temperature maps shown in Figure 5.15. If we compare Figure 5.15 and Figure 4.29, then it can be seen that the range of temperatures in the mean of the posterior distribution of Figure 5.15 is lower. Generally speaking the median and maximum of the posterior distribution have a similar range and scale.

The results of the triangulation are shown in Figure 5.16. The intersection points of the light-rays are depicted by the blue dots, $\hat{s}_\alpha$ (black dot) and s^* (green dot). After finding the centre of mass of all the intersection points the error in the position was found to be $\varepsilon_\alpha = 222.0$ μm which gives an ε_{imp} value of

55 %. The variance, $\mathcal{V}(\varepsilon_\alpha)$ was found to be 21 μm which gives a $\mathcal{V}_{imp}$ value of 52 % improvement in uncertainty compared to the homogeneous case (see Table 5.3).

Continuing on with the comparisons, the case where a uniform refractive index map is used as the prior will now be examined. As in previous discussions, this map will have the same number of Voronoi cells as the known refractive index map, m^*, but the refractive index in each cell will be equal to the mean of the refractive indices of m^*. If the number of Voronoi cells is considered, the range is marginally smaller compared to the δ case (range of 21 compared to 22). The objective functions for all of numerical experiment B will be considered at the end of this section. The κ_{mean} value was found to be the lowest (equal to 1.99 $\times 10^{-3}$ compared with κ_{median} of 2.18 $\times 10^{-3}$ and κ_{max} of 2.83 $\times 10^{-3}$. These values are more intuitive than those observed by the equivalent δ method as the κ_{mean} value is larger when the uniform is used as the prior compared with m^*, and this was not the case for the δ method. Following this, the triangulation yielded the following results: ε_α 226.5 μm, $\varepsilon_{imp} = 54$ %, $\mathcal{V} = 21$ μm and $\mathcal{V}_{imp} = 52$ %. The ε_{imp} is larger than the equivalent δ method but the $\mathcal{V}_{imp}$ is unchanged.

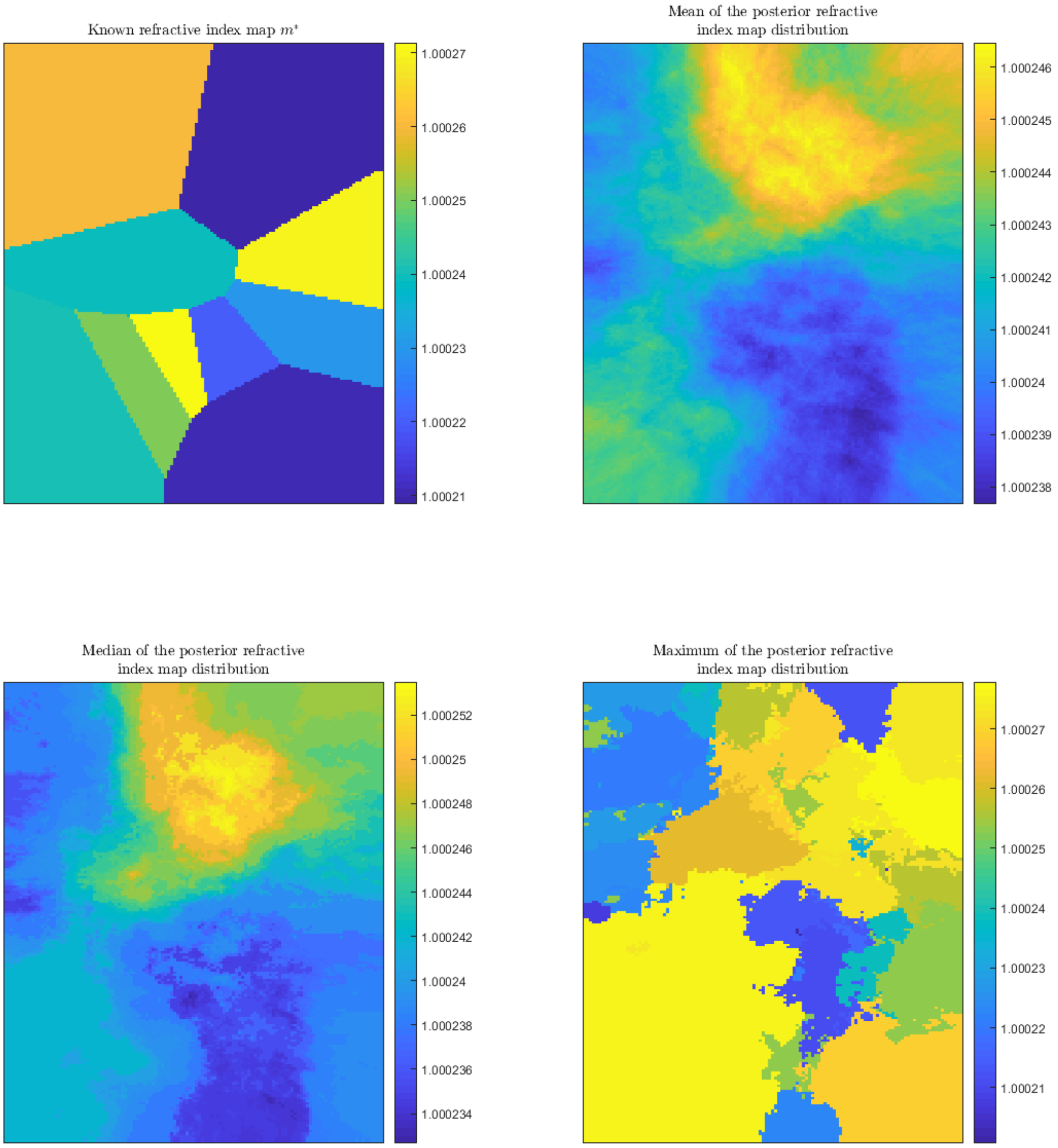

Figure 5.14: Numerical Experiment B: Top Left: The known refractive index map m^*, Top Right: the mean of the sampled refractive index map posterior, Bottom Left: median of the sampled posterior refractive index map and Bottom Right: the maximum-a-posteriori of the sampled posterior refractive index map distribution. In this case the prior was the known refractive index map.

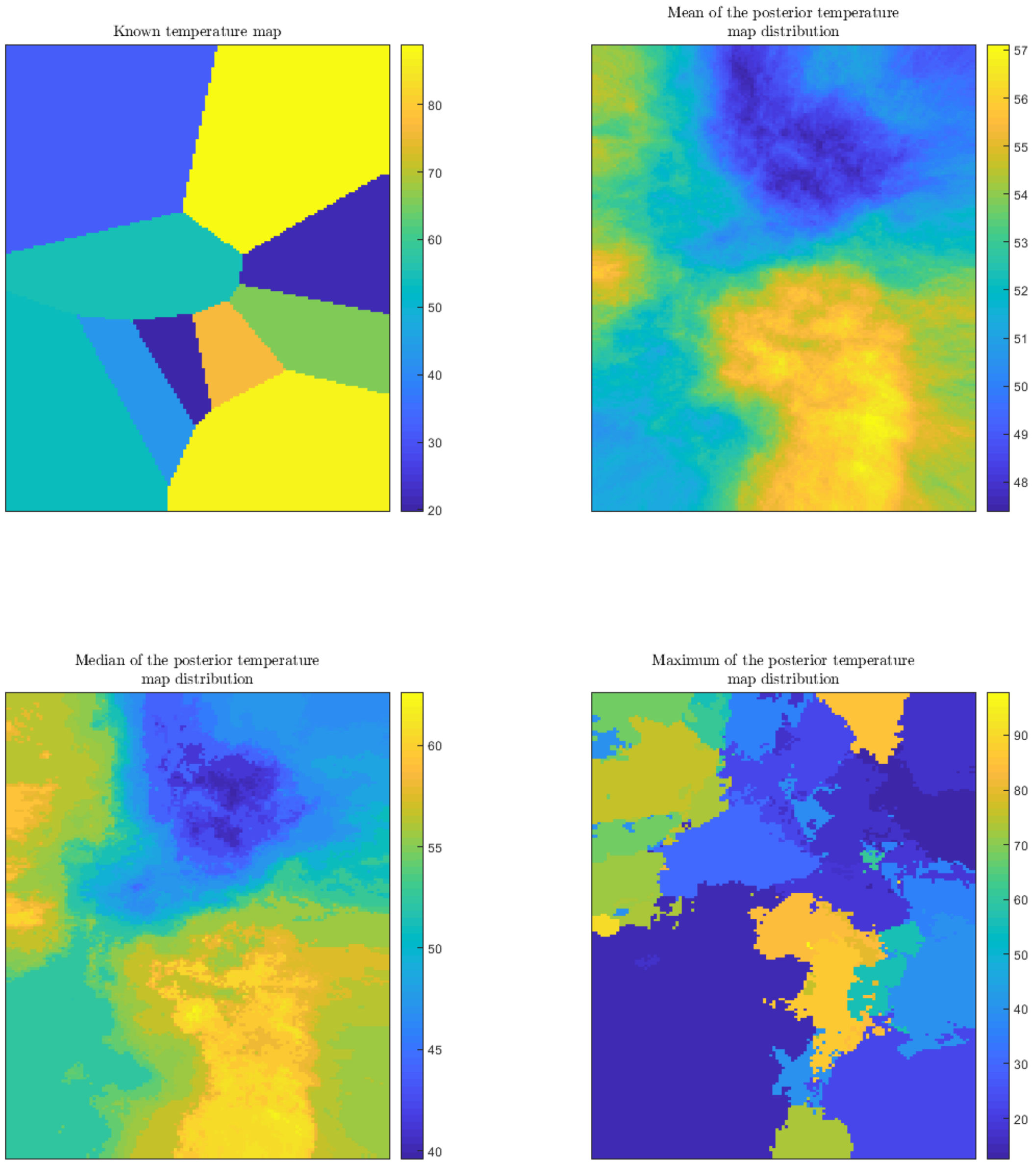

Figure 5.15: Numerical Experiment B: Top Left: The known temperature map, Top Right: the mean of the sampled temperature map posterior, Bottom Left: median of the sampled posterior temperature map and Bottom Right: the maximum-a-posteriori of the sampled posterior temperature map distribution. In this case the prior was the known refractive index map, and have been converted to a temperature in this instance using the Ciddor equation. All of the above temperatures are reported in degrees Celsius.

Finally, a random refractive index map was used as the prior. This initial Voronoi had 107 cells, which is large decrease from the 138 in the equivalent δ method. The number of Voronoi cells throughout the inversion ranged between 107 and 147, which is a much smaller range than the δ method and the values are much lower. The κ_{mean} value was found to be the lowest (equal to 1.90 $\times 10^{-3}$ compared with κ_{median} of 1.94 $\times 10^{-3}$ and κ_{max} of 3.34 $\times 10^{-3}$. These values are larger than those observed by the equivalent δ method. Following this, the triangulation yielded the following results: $\varepsilon_{\alpha} = 239.3$ μm, $\varepsilon_{imp} = 52$ %, $\mathcal{V} = 18$

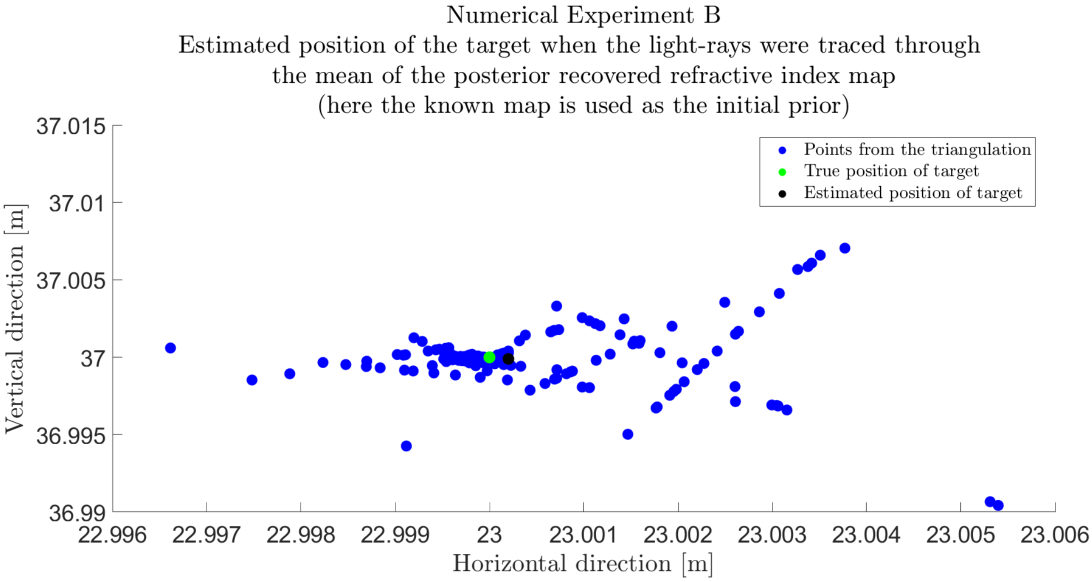

Figure 5.16: Numerical Experiment B: This plot shows the results of the triangulation method when the light-rays were traced through the mean recovered refractive index map. The intersection points of the light-rays are shown by the blue points, the estimated position of the reflector ($\hat{s}_{\alpha}$) is shown by the black dot and the true position (s^{*}) is shown by the green dot.

μm and $\mathcal{V}_{imp} = 59$ %. The ε_{imp} and $\mathcal{V}_{imp}$ are larger than the equivalent δ method, further showing the success of this method. A full summary of the results can be found in Table 5.3.

A comparison of the objective functions between the δ and TOF method for each of the priors as shown in Figure 5.17 will now be discussed. From this plot it can be seen that all $\gamma^{(j)}$ values for the TOF method oscillate around a central value of 0.5 $\times 10^{-3}$ which is one order of magnitude from the oscillation value of the δ method. This plot further shows the success of this method.

Overall for numerical experiment B there was a 4 % improvement in error in the position in the case where the known prior was used for the TOF method, compared to the δ method and gave a 2 % improvement in the variance. When a uniform refractive index map was used as the prior, there was a 7 % improvement in error in the position in the case where a uniform prior was used for the TOF method, compared to the δ method and both methods reduced the variance by the same amount. Finally, when a random refractive index map was used as the prior, there was a 1 % improvement in error in the position for the TOF method, compared to the δ method and 2 % improvement in the variance. Generally speaking for numerical experiment B, the TOF method always performed better than the δ method in terms of reduction of positional error and reduction of variance.

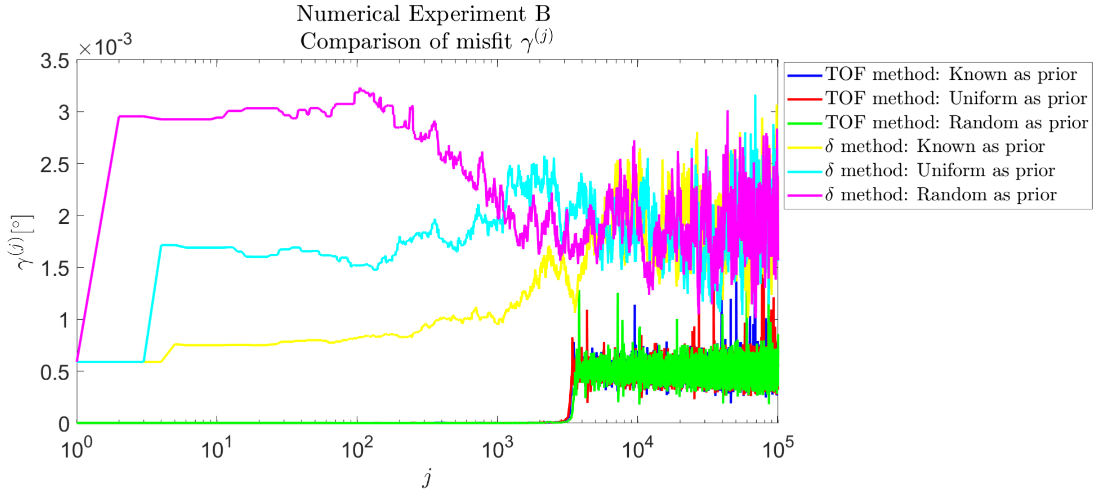

Figure 5.17: Numerical Experiment B: Plot showing a comparison between the misfit (objective function) $\gamma^{(j)}$ at each iteration j of the inversion algorithm when the δ method (yellow, cyan and magenta lines) and the TOF method were used (green, red and blue lines).

Table 5.3: Numerical Experiment B: Table summarising the improvement in uncertainty and position of the object of interest s^* when the light-rays are traced through various refractive index maps, this table considers the TOF and δ method.

	Spatial domain	$\varepsilon[\mu\text{m}]$	ε_{imp} [%]	$\mathcal{V}[\mu\text{m}]$	$\mathcal{V}_{imp}$ [%]
	m^h	494.9	NA	43.7	NA
δ	known map as prior	242.9	51	22	50
TOF		222.0	55	21	52
δ	uniform map as prior	260.7	47	21	52
TOF		226.5	54	21	52
δ	random map as prior	242.7	51	19	57
TOF		239.3	52	18	59

5.4 Numerical Experiment C

The results of numerical experiment C (defined in Table 4.6) compared with those obtained using the δ method from Chapter 4 will now be examined. As in the previous section all of the variables in the inversion have been keep constant aside from the method for calculating $\theta_{k,i}$. The case where the known refractive index map, m^*, was used as the prior is considered first.

The first metric output by the inversion process is the number of Voronoi cells of the perturbed model, $m^{(j)}$ at each iteration, j. In this case the number of Voronoi cells ranged from 87 to 126, which is a slightly larger range than the equivalent from Section 4.9 and it also has a higher lower range value. Following this the objective function is the next metric to be output and a comparison of the objective functions is shown in Figure 5.18, the red line is the δ method and the blue line is the TOF method. It can clearly be seen that $\gamma^{(j)}$ is much smaller for the TOF method compared with the δ method which is a positive result, although it looks relatively flat. Figure 5.19 shows $\gamma^{(j)}$ when the known is used as the prior for the TOF method in more detail. In addition, the acceptance rate was 40 % which is the same as in Section 4.9.

The main assessment into the performance of the inversion algorithm is the improvement of the position of the robot and the variance associated with this. The material map difference, κ was found for the mean, median and maximum-a-posteriori of the posterior distribution, yielding 1.43 $\times 10^{-3}$ %, 1.29 $\times 10^{-3}$ % and 2.16 $\times 10^{-3}$ % respectively. Since the median of the posterior distribution

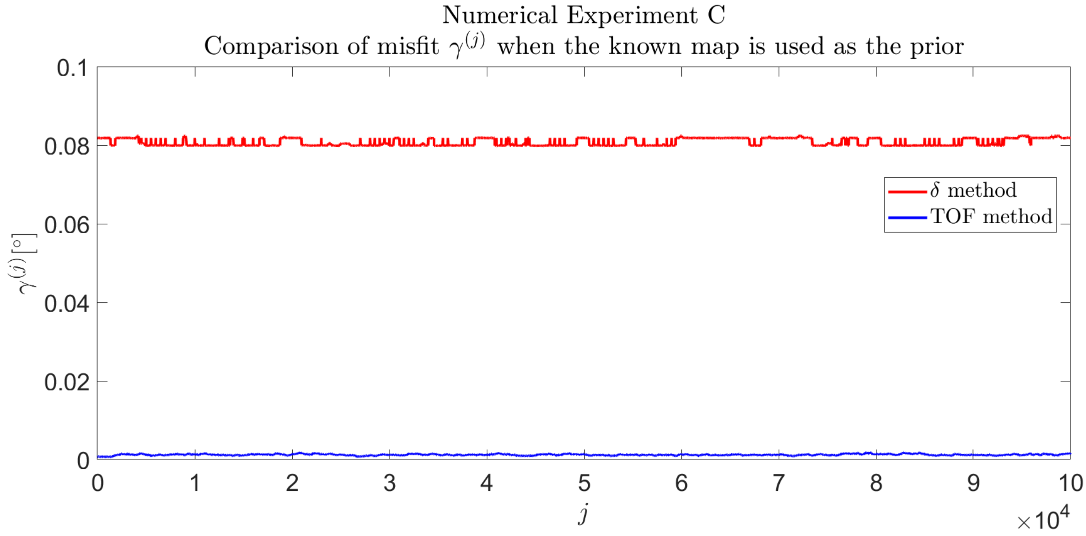

Figure 5.18: Numerical Experiment C: Plot showing a comparison between the misfit (objective function) $\gamma^{(j)}$ at each iteration j of the inversion algorithm when the δ method (red line) and the TOF method was used (blue line). These results are from Numerical Experiment C when the known refractive index map m^* was used as the prior.

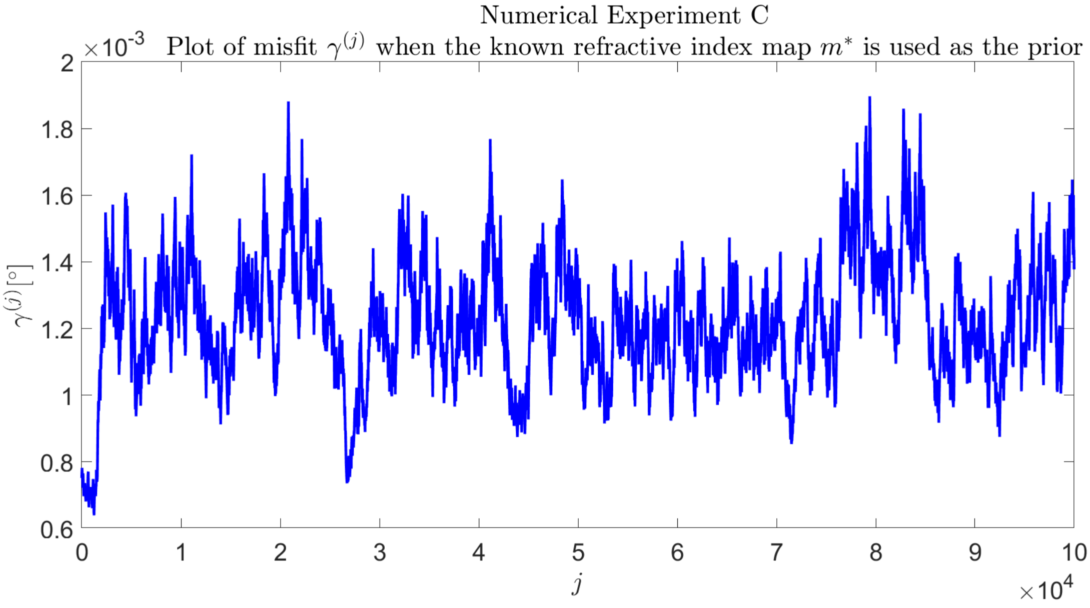

Figure 5.19: Numerical Experiment C: Misfit (objective function) $\gamma^{(j)}$ when the known refractive index map m^* is used as the prior. .

had the lowest κ value it was chosen as the map to perform the triangulation on. Using the triangulation method, it was found that the error in the position, ε_{α} was 91.6 μm which gives an ε_{imp} of 67 %. The variance, $\mathcal{V}(\varepsilon_{\alpha})$ was found to be 0.9 μm which gives a $\mathcal{V}_{imp}$ value of 64 % improvement in uncertainty compared to the homogeneous case (see Table 5.4).

Continuing on with the comparisons, the case where a uniform refractive index map is used as the prior will now be looked at. If the number of Voronoi cells is considered, it can be seen that the range is larger compared to the δ case (range of 57 compared to 41), however the lower bound of the range is lower in the TOF case, 64 compared to 83. The κ_{median} value was found to be the lowest (equal to 1.51 $\times 10^{-3}$ compared with κ_{mean} of 1.54 $\times 10^{-3}$ and κ_{max} of 1.99 $\times 10^{-3}$. These values look reasonable as all κ values are greater than when m^{*} is used as the prior and these values are also smaller than the equivalent δ ones. Following this, the triangulation yielded the following results: ε_{α} 107.9 μm, $\varepsilon_{imp} = 61$ %, $\mathcal{V} =$ 0.6 μm and $\mathcal{V}_{imp} = 76$ %. The ε_{imp} and $\mathcal{V}_{imp}$ are larger than the equivalent δ method.

Finally, a random refractive index map was used as the prior. This initial Voronoi had 107 cells, which is slightly smaller than the 111 in the equivalent δ method. The number of Voronoi cells throughout the inversion ranged between 70 and 127, which is a larger range than the equivalent numerical experiment using the δ method (90 - 124), but the lower bound of the range is lower. The κ_{mean} value was found to be the lowest (equal to 1.91 $\times 10^{-3}$ compared with κ_{median} of 1.93 $\times 10^{-3}$ and κ_{max} of 2.53 $\times 10^{-3}$. These values are marginally smaller than those observed by the equivalent δ method. Following this, the triangulation yielded the following results: $\varepsilon_{\alpha} = 140.8$ μm, $\varepsilon_{imp} = 50$ %, $\mathcal{V} = 2.1$ μm, which gives a $\mathcal{V}_{imp}$ of 16 %. A full summary of the results can be found in Table 5.4.

A comparison of the objective functions between the δ and TOF method for each of the priors as shown in Figure 5.20 will now be looked at. From this plot it can be seen that all $\gamma^{(j)}$ values for the TOF method are again lower than the δ method. In Figure 5.21 only model iteration 500 to 100,000 are considered as it better shows the difference between the objective functions of the two methods. This plot further shows the success of the TOF method and its sensitivity.

Overall for numerical experiment C there was a 20 % improvement in error in the position in the case where the known prior was used for the TOF method, compared to the δ method. However, the δ method provided a better improvement (by 20 %) in variance when the known map was used as the prior compared to the TOF method. When a uniform refractive index map was used as the prior, there was a 35 % improvement in error in the position in the case where a uniform prior was used for the TOF method, compared to the δ method. As in the case when the known refractive index map was used as the prior, the TOF method did not yield a better performance in the variance when compared to the δ method. Finally, when a random refractive index map was used as the prior, there was a 21 % improvement in error in the position for the TOF method, compared to the δ method. Generally speaking for numerical experiment C, the TOF method

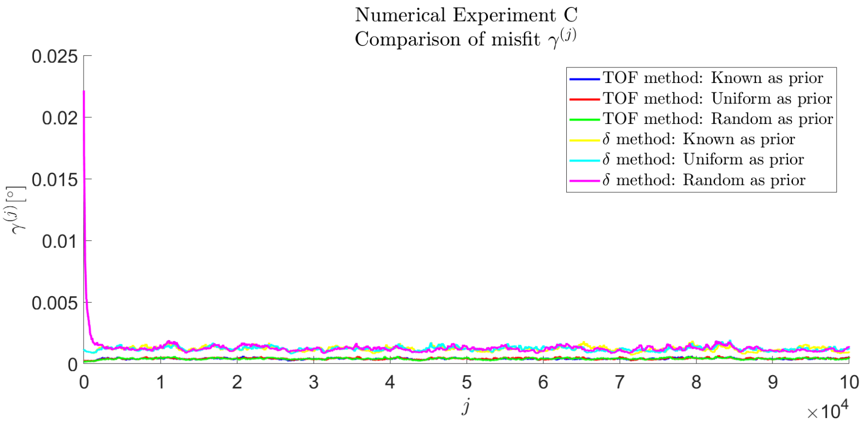

Figure 5.20: Numerical Experiment C: Plot showing a comparison between the misfit (objective function) $\gamma^{(j)}$ at each iteration j of the inversion algorithm when the δ method (yellow, cyan and magenta lines) and the TOF method were used (green, red and blue lines).

always performed better than the δ method in terms of reduction of positional error. However, the δ method always performed better than the TOF method in terms of reduction of variance.

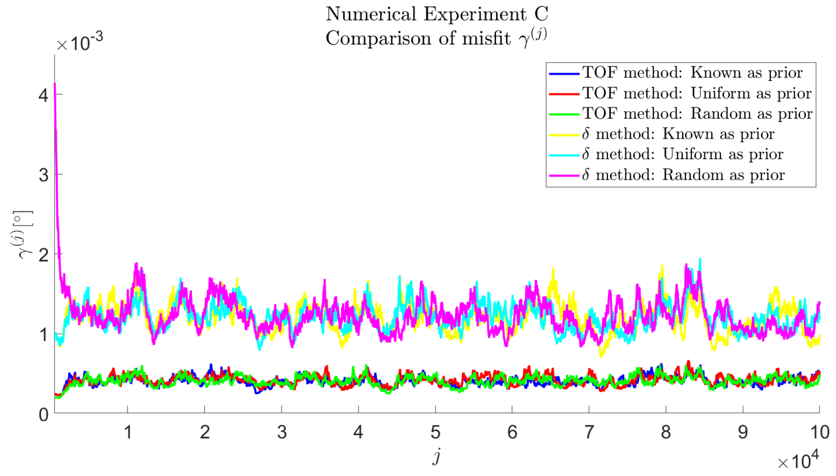

Figure 5.21: Numerical Experiment C: Plot showing a comparison between the misfit (objective function) $\gamma^{(j)}$ at each iteration j of the inversion algorithm when the δ method (yellow, cyan and magenta lines) and the TOF method were used (green, red and blue lines), note that iteration 500 to 100,000 are only considered here.

Table 5.4: Numerical Experiment C: Table summarising the improvement in uncertainty and position of the object of interest s^* when the light-rays are traced through various refractive index maps, this table considers the TOF and δ method.

	Spatial domain	$\varepsilon \mu$m	ε_{imp} [%]	$\mathcal{V} \mu$m	$\mathcal{V}_{imp}$ [%]
	m^h	279.3	NA	2.5	NA
δ	known map as prior	149.0	47	0.7	72
TOF		91.6	67	0.9	64
δ	uniform map as prior	205.8	26	5	-100
TOF		107.9	61	0.6	76
δ	random map as prior	226.2	19	0.9	64
TOF		140.8	50	2.1	16

5.5 Numerical Experiment D

The results of numerical experiment D (defined in Table 4.6) compared with those obtained using the δ method from Chapter 4 will now be examined. As in the previous section all of the variables in the inversion have been keep constant aside from the method for calculating $\theta_{k,i}$. Recall that the known refractive index map, m^* cannot be expressed as a Voronoi, this means that a uniform and random prior can be considered. The case where a uniform refractive index map, was used as the prior will be looked at first.

The first metric output by the inversion process is the number of Voronoi cells of the perturbed model, $m^{(j)}$ at each iteration, j. In this case the number of Voronoi cells ranged from 80 to 121, which is a slightly larger range than the equivalent from Section 4.9 and it also has a higher lower range value. The κ_{mean} value was found to be the lowest (equal to 1.9 $\times 10^{-3}$ compared with κ_{median} of 1.94 $\times 10^{-3}$ and κ_{max} of 2.32 $\times 10^{-3}$. These values are lower than the corresponding δ method for numerical experiment D. The recovered refractive index maps are shown in Figure 5.22 and for easier readability the corresponding temperature maps are shown in Figure 5.23. If Figure 5.23 is compared with Figure 4.37 then the range in temperature scale is the same for the median, mean and maximum of the posterior distribution. The only difference is that the lower and upper bounds of the median of the posterior distribution are lower by 10 ° in Figure 5.23.

Following this, the triangulation yielded the following results: ε_α 68.2 μm, ε_{imp} = 61 %, $\mathcal{V}$ = 0.1 μm and $\mathcal{V}_{imp}$ = 89 %. The ε_{imp} and $\mathcal{V}_{imp}$ are larger than the equivalent δ method.

Finally, a random refractive index map was used as the prior. This initial Voronoi had 108 cells, which is larger than the 96 in the equivalent δ method. The number of Voronoi cells throughout the inversion ranged between 78 and 125, which is a larger range than the equivalent numerical experiment using the δ method (80 - 110). The κ_{median} value was found to be the lowest (equal to 1.91 $\times 10^{-3}$ compared with κ_{mean} of 1.93 $\times 10^{-3}$ and κ_{max} of 2.50 $\times 10^{-3}$. These values are much smaller than those observed by the equivalent δ method. Following this, the triangulation yielded the following results: ε_α 90.3 μm, ε_{imp} = 48 %, $\mathcal{V}$ = 0.6 μm, which gives a $\mathcal{V}_{imp}$ of 59 %. A full summary of the results can be found in Table 5.5.

A comparison of $\gamma^{(j)}$ between the δ and TOF method for each of the priors as shown in Figure 5.24 will now be considered. From this plot it can be seen that all $\gamma^{(j)}$ values for the TOF method are again lower than the δ method. In Figure 5.25 model iteration 500 to 100,000 are solely considered as these iterations better show the difference between the objective functions of the two methods. This plot further shows the success of the TOF method and its sensitivity.

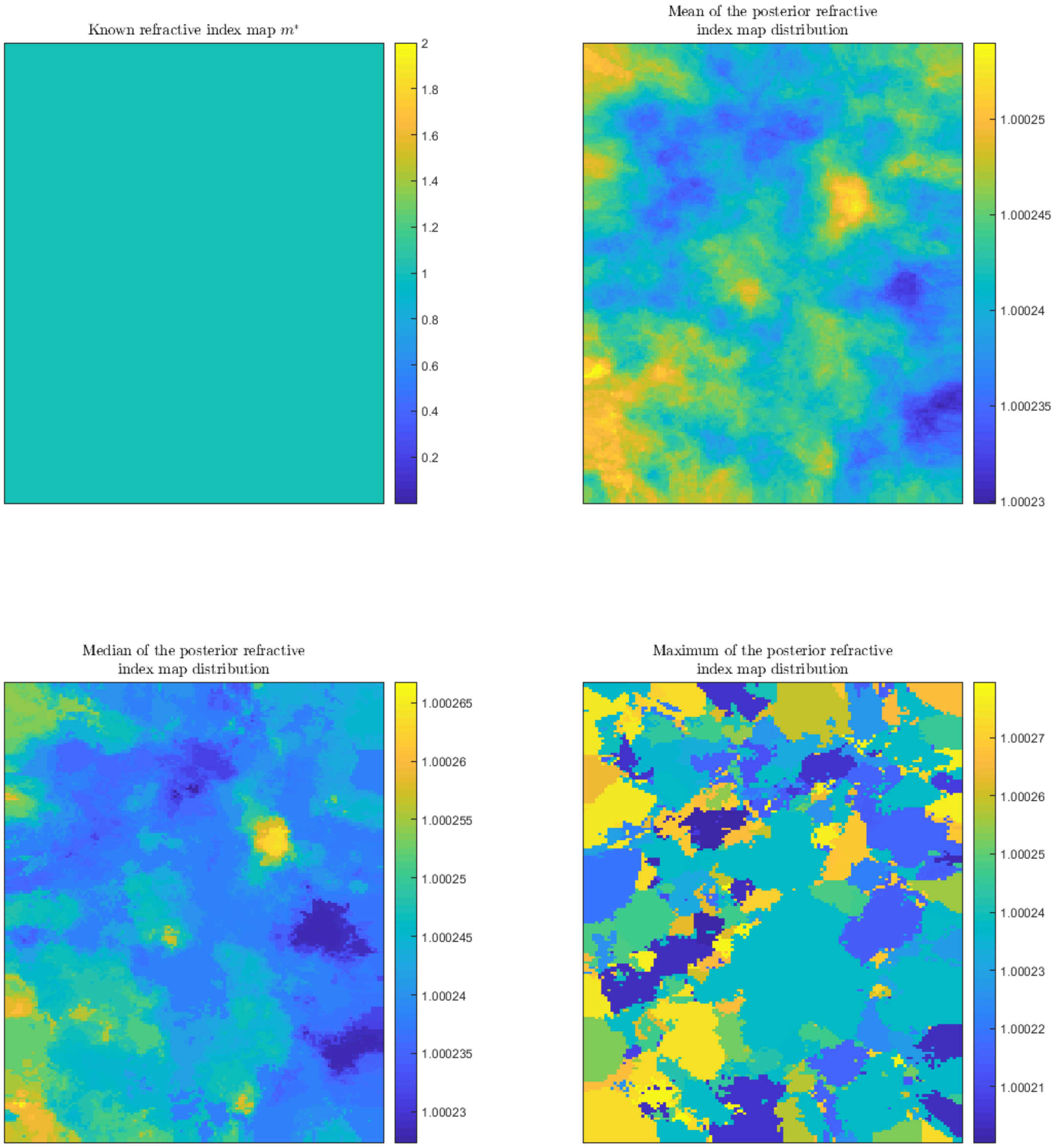
Known refractive index map m^*

Mean of the posterior refractive index map distribution

Median of the posterior refractive index map distribution

Maximum of the posterior refractive index map distribution

Figure 5.22: Numerical Experiment D: Top Left: The known refractive index map m^*, Top Right: the mean of the sampled refractive index map posterior, Bottom Left: median of the sampled posterior refractive index map and Bottom Right: the maximum-a-posteriori of the sampled posterior refractive index map distribution. In this case the prior was a uniform Voronoi tessellation.

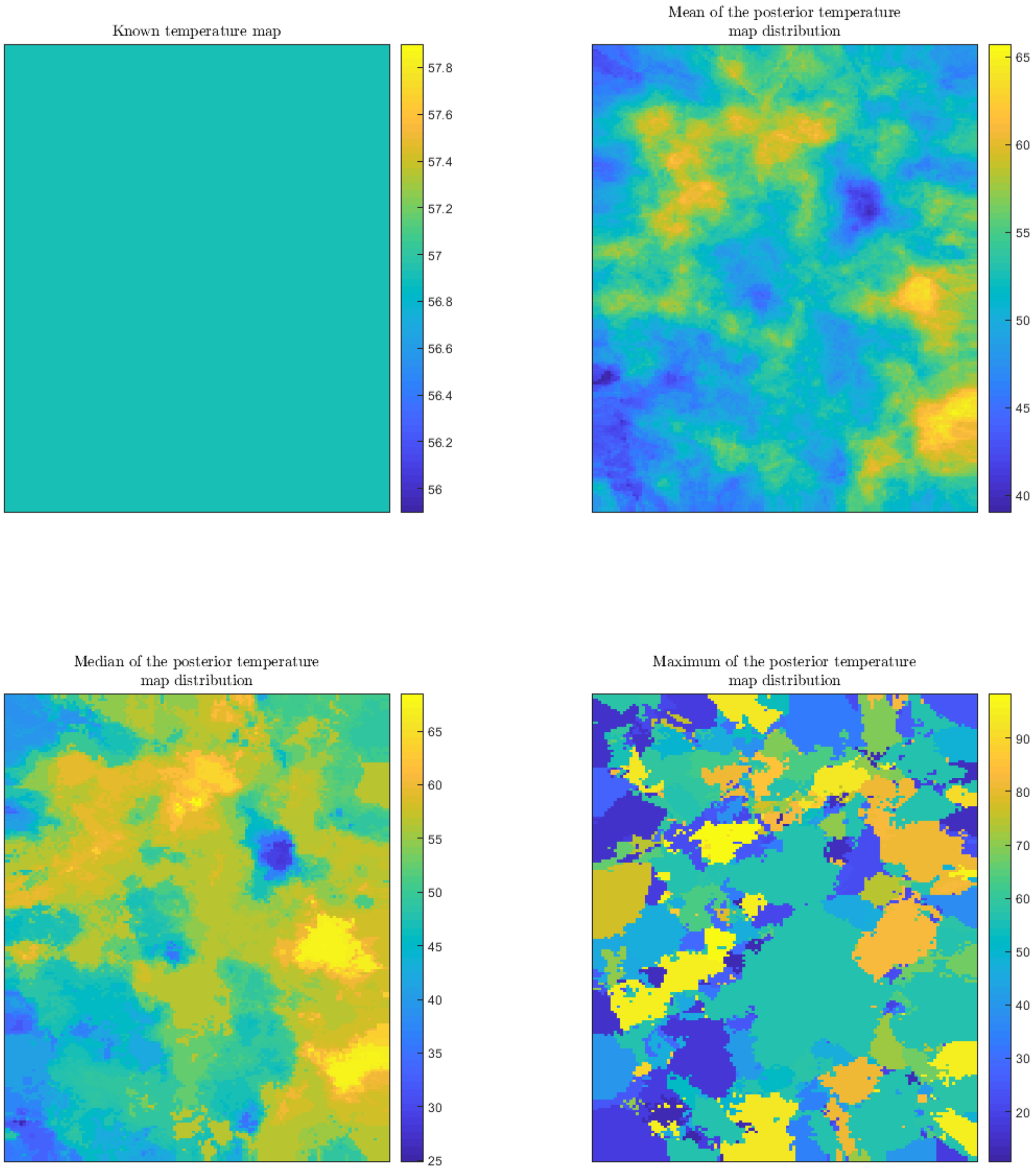

Figure 5.23: Numerical Experiment D: Top Left: The known temperature map, Top Right: the mean of the sampled temperature map posterior, Bottom Left: median of the sampled posterior temperature map and Bottom Right: the maximum-a-posteriori of the sampled posterior temperature map distribution. In this case the prior was a uniform Voronoi tessellation. All of the above temperatures are reported in degrees Celsius.

Overall for numerical experiment D there was a 24 % improvement in error in the position in the case where a uniform prior was used for the TOF method, compared to the δ method and the improvement in the variance was equal for both cases. When a random refractive index map was used as the prior, there was a 33 % improvement in error in the position in the case where a uniform prior was used for the TOF method, compared to the δ method. There was also an 8 % improvement in the variance for the TOF method, compared to the δ method.

A full summary of the results can be found in Table 5.6, this table contains the TOF and δ method for all numerical experiments and includes the computational time associated with each.

5.6 Chapter Summary

This chapter outlined a revised methodology which avoids using the ray tracing algorithm in the inversion. The ray tracing algorithm is computationally expensive and is not robust. The results from this algorithm feed into the calculation of the objective function which in turn leads to the objective function not being sensitive enough. Generally speaking the TOF method takes between 3 and 6 hours to run, whereas the δ method could take up to 3 days. This new method uses the time field calculated by the FMM and examines the profile lying orthogonal to the light ray path.

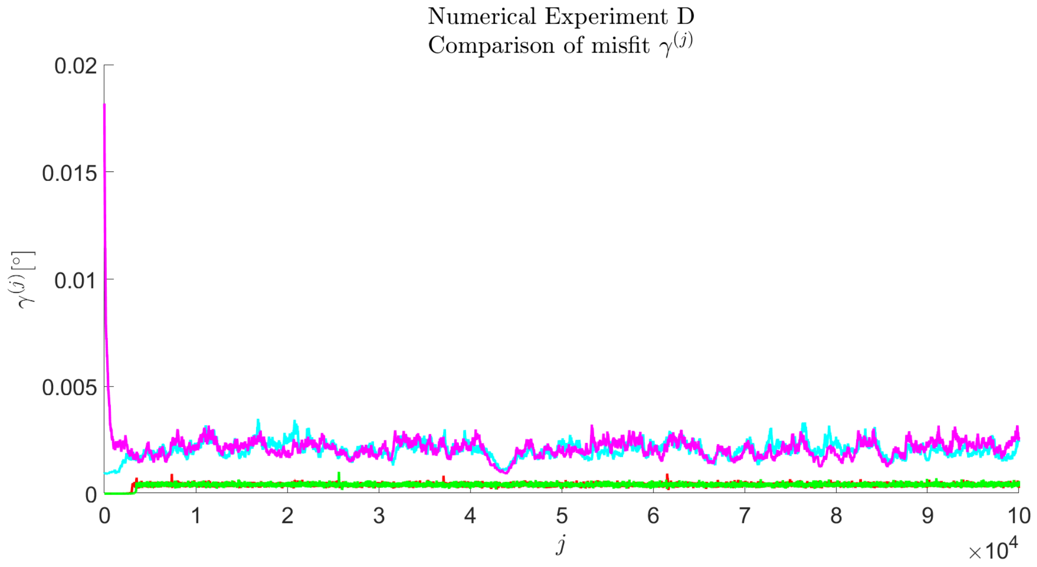

Figure 5.24: Numerical Experiment D: Plot showing a comparison between the misfit (objective function) $\gamma^{(j)}$ at each iteration j of the inversion algorithm when the δ method (yellow, cyan and magenta lines) and the TOF method were used (green, red and blue lines).

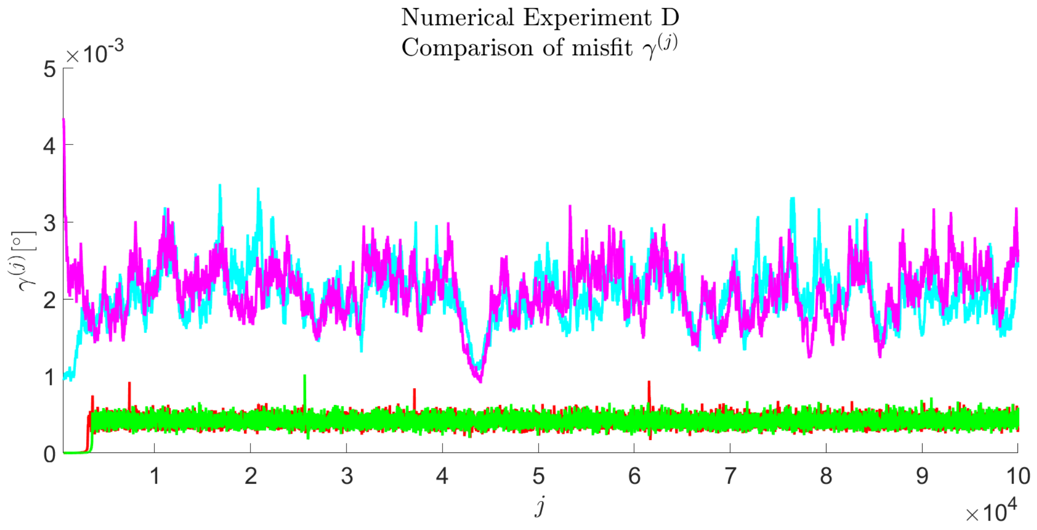

Figure 5.25: Numerical Experiment D: Plot showing a comparison between the misfit (objective function) $\gamma^{(j)}$ at each iteration j of the inversion algorithm when the δ method (yellow, cyan and magenta lines) and the TOF method were used (green, red and blue lines), iteration 500 to 100,000 are the only iterations considered here.

Table 5.5: Numerical Experiment D: Table summarising the improvement in uncertainty and position of the object of interest s^* when the light-rays are traced through various refractive index maps, this table considers the TOF and δ method.

	Spatial domain	$\varepsilon \mu$m	ε_{imp} [%]	$\mathcal{V} \mu$m	$\mathcal{V}_{imp}$ [%]
	m^h	174.2	NA	1.4	NA
δ	uniform map as prior	110.2	37	0.1	89
TOF		68.2	61	0.1	89
δ	random map as prior	147.2	15	0.7	51
TOF		90.3	48	0.6	59

As in the previous chapter the analysis began with numerical experiment A. It was found that the range of Voronoi cells during the inversion were much smaller than that of the equivalent δ method. In addition, the objective function was much smaller than the equivalent δ method, highlighting that the TOF method is sensitive to these small refractive index changes. For the known and uniform priors the TOF method resulted in a larger ε_{imp} and $\mathcal{V}_{imp}$ compared to the equivalent δ method. The random prior still resulted in an ε_{imp} which was positive, and hence better than the homogeneous case.

Numerical experiment B had the same Voronoi cell seed position as in numerical experiment A, but the refractive indices were weakly heterogeneous to be commensurate with values observed in an industrial setting. Using the known refractive index map as prior led to an ε_{imp} of 55 % and a $\mathcal{V}_{imp}$ of 52 %,. Using a uniform refractive index map resulted in an ε_{imp} of 54 % and $\mathcal{V}_{imp}$ of 52 %. Finally, when a random refractive index map was used as the prior ε_{imp} was 52 % and $\mathcal{V}_{imp}$ was 59 %.

Table 5.6: Table summarising the improvement in uncertainty and position of the object of interest s^* when the light-rays are traced through various refractive index maps, this table considers the TOF and δ method for all numerical experiments and includes the computational time associated with each.

Numerical Experiment		Spatial domain	ε [μm]	ε_{imp} [%]	$\mathcal{V}$ [μm]	$\mathcal{V}_{imp}$ [%]	Computational time [hours]
A		m^h	73700	NA	33900	NA	NA
A	δ	known map	33600	54	28500	16	72
A	TOF	as prior	19600	73	13400	60	3
A	δ	uniform map	39400	46	28000	17	72
A	TOF	as prior	23500	68	12100	64	3
A	δ	random map	20000	73	36000	89	72
A	TOF	as prior	23800	68	12200	64	3
B	m^h		495	NA	44	NA	
B	δ	known map	243	51	22	50	72
B	TOF	as prior	222	55	21	52	3
B	δ	uniform map	216	47	21	52	72
B	TOF	as prior	227	54	21	52	3
B	δ	random map	243	51	19	57	72
B	TOF	as prior	240	52	18	64	3
C	m^h		279	NA	2.5	NA	
C	δ	known map	149	47	0.7	72	72
C	TOF	as prior	92	67	0.9	64	6
C	δ	uniform map	206	26	5	-100	72
C	TOF	as prior	108	61	0.6	76	6
C	δ	random map	226	19	0.9	64	72
C	TOF	as prior	141	50	2.1	16	6
D	m^h		174	NA	1.4	NA	
D	δ	uniform map	110	37	0.1	89	72
D	TOF	as prior	68	61	0.1	89	4
D	δ	random map	147	15	0.7	51	72
D	TOF	as prior	90	48	0.6	59	4

Numerical experiment C introduced a Voronoi tessellation with 100 cells, with the same refractive index range as in numerical experiment B. For all three priors (known, uniform and random) the uncertainty in the position of s^* was reduced by 67 %, 61 % and 50 % respectively. There was also an improvement in the variance for all cases, which was not the case for the equivalent δ method. The objective function, $\gamma^{(j)}$ was significantly lower in the TOF method compared to the equivalent numerical experiment using the δ method. This indicates that the TOF method of calculating $\theta_{k,i}^{(j)}$ is more sensitive to the changes in the ray path caused by refraction effects.

Finally numerical experiment, D, was a more realistic scenario with a single Gaussian distribution representing the heterogeneous temperature distribution, since it is not possible to represent this refractive index map as a Voronoi, then the inversion process could only begin with a uniform and random prior. Using a uniform prior led to an ε_{imp} of 61 % and a $\mathcal{V}_{imp}$ of 89 %, whereas a random prior resulted in an ε_{imp} of 48 % and $\mathcal{V}_{imp}$ of 59 %. As in all the previous numerical experiments, the objective function, $\gamma^{(j)}$ was significantly lower in the TOF method compared to the equivalent numerical experiment using the δ method.

The following final chapter provides conclusions of the thesis and looks at future work which could be undertaken.

Chapter 6

Conclusions and Future Work

6.1 Final Conclusions

The thesis began by providing a review of the effects of refraction in large volume metrology. It also introduced current techniques used to recover the refractive index map and ways to model the refractive index maps. There was also an introduction to inverse problems and components involved: spatial domain parametrisation, forward solvers and optimisation techniques.

Following this Chapter 2 looked at how mathematical modelling, and in particular, how a finite element package (COMSOL Multiphysics) can be used to simulate light rays propagating through a spatially heterogeneous refractive index (temperature) map. The equations for calculating transverse temperature gradients were discussed and it was found that transverse gradients dominate ray refraction. A simulation of a Gaussian temperature profile which has light rays propagating through it was studied. An investigation into the effect that varying three parameters (initial angle of the ray, the maximum temperature and the temperature variance) had on the positional error was discussed. It was found that changes in the maximum temperature led to the highest error (approximately 220 μm) relative to changes in the initial angle of the ray and the variance.

Chapter 3 introduced physical experimentation, the aim of which was to show that the Vicon T160 photogrammetry system was sensitive enough to detect the submillimetre errors in position caused by thermal fluctuations. The experiment used two Vicon T160 cameras which tracked a cluster of retroreflectors. It was found that when the heat source was affecting only one of the camera's light ray trajectory, the positional error was 679 μm. These positional errors confirm the findings of Chapter 2 and show that submillimetre sized positional errors can arise in laboratory sized volumes. Mathematical formulae were derived which illustrate the amount that the centroid of a target can move, following the addition of another pixel to the image of the retroreflector. It was found that approximately 99 % of the adjacent centroid movements of the data points captured by the cameras were within the range of movement calculated using the formulae.

Chapter 4 outlined the methodology involved in reconstructing the refractive index map, this methodology is referred to as the δ method. The parametrisation of the refractive index map employed Voronoi tessellations as these require fewer degrees of freedom to describe a heterogeneous map and large regions can be affected by a single perturbation. The forward model was solved using the Fast

Marching Method (FMM), which calculates the travel time field between the camera and the reflector and then finds the optical path within this field that the ray takes. The objective function was based on the absolute difference between the experimentally measured angle ($\theta^{*}_{k,i}$) and the angle calculated at each iteration of the inversion algorithm ($\theta^{(j)}_{k,i}$) as shown in Equation (4.5). The choice of optimisation method was the reversible jump Markov Chain Monte Carlo (rj-MCMC) method. This is an iterative stochastic process which generates a population of solution samples from the posterior distribution. The goal of this is to reconstruct the refractive index map such that the positional error, ε_α is smaller than the error that arises when assuming a homogeneous refractive index map, ε_h (which is the current practice).

An initial test case (numerical experiment A) based on a ten cell Voronoi diagram refractive index map was investigated. This refractive index map was strongly heterogeneous and produced a positional error (ε_h) of 73.7 mm arising from a refractive index fluctuation of 2.2 %. In this numerical experiment, an improvement in positioning and uncertainty of up to 73 % and 89 % respectively were observed.

Numerical experiment B had the same Voronoi cell seed position as in A, but the refractive indices were weakly heterogeneous to be commensurate with values observed in an industrial setting. In this numerical experiment, an improvement in positioning and uncertainty of up to 51 % and 57 % respectively were observed.

Numerical experiment C introduced a Voronoi tessellation with 100 cells, with the same refractive index range as in numerical experiment B. In this numerical experiment, an improvement in positioning and uncertainty of up to 47 % and 67 % respectively were observed. One limitation of this numerical experiment was the lack of sensitivity in the objective function. The objective function was the same order of magnitude as numerical experiment B, however in general the refractive index maps were much smoother due to a larger number of Voronoi cells. One potential reason for this is that the ray tracing part of the inversion is not robust enough to deal with these changes in the trajectory of the ray paths and the unusual ray paths were discussed in Section 4.7.1.

The final numerical experiment, D, was a more realistic scenario with a single Gaussian distribution representing the heterogeneous temperature distribution. Since this refractive index map cannot be represented as a Voronoi tessellation, the inversion process was only able to start with a uniform and random prior. In this numerical experiment, an improvement in positioning and uncertainty of up to 37 % and 89 % respectively were observed.

Finally Chapter 5 outlined a revised methodology which avoids using the ray tracing algorithm in the inversion. The ray tracing algorithm is computationally expensive and is not robust. The results from this algorithm feed into the calculation of the objective function which in turn leads to the objective function not being sensitive enough. Generally speaking the TOF method takes between

3 and 6 hours to run, whereas the δ method could take up to 3 days. This new method uses the time field calculated by the FMM and examines the profile lying orthogonal to the light ray path.

As in the previous chapter, numerical experiment A was considered first. It was found that the range of Voronoi cells during the inversion were much smaller than that of the equivalent δ method. In addition, the objective function was much smaller than the equivalent δ method, highlighting that the TOF method is sensitive to these small refractive index changes. For the known and uniform priors the TOF method resulted in a larger ε_{imp} and $\mathcal{V}_{imp}$ compared to the equivalent δ method. The random prior still resulted in an ε_{imp} and $\mathcal{V}_{imp}$ which were positive, and hence better than the homogeneous case.

In numerical experiment B, an improvement in positioning and uncertainty of up to 55 % and 59 % respectively were observed. In numerical experiment C, an improvement in positioning and uncertainty of up to 67 % and 76 % respectively were observed. The objective function, $\gamma^{(j)}$ was significantly lower in the TOF method compared to the equivalent numerical experiment using the δ method. This indicates that the TOF method of calculating $\theta_{k,i}^{(j)}$ is much more sensitive to the changes in the ray path caused by refraction effects. Then finally numerical experiment D, an improvement in positioning and uncertainty of up to 61 % and 89 % respectively were observed.

6.2 Future Work

Since this was the first attempt at solving this inverse problem there is a lot of scope for future work. The method could be improved by the use of the multi-stencils FMM which is presented in [90, 113]. This update could lead to a more accurate travel time matrix which could lead to an improvement in accuracy to the results obtained in Chapter 5. However, it is unclear how much this would increase the computational time of the algorithm.

The simulations would be straightforward to do in three dimensions and no doubt the ε_h values would increase. However, it would less straightforward to code the inversion algorithm in three dimensions and in turn it would be expected that the computational times would be prohibitive. A deterministic optimisation approach could be employed instead of the stochastic reversible jump Markov Chain Monte Carlo but as the objective function is highly nonlinear (and indeed discontinuous) then this would require very careful treatment and a global optimisation scheme adopted.

One area of future work would be to look at updating the inversion code for another optical based metrology system; most likely the laser tracker system. Experimentation would first need to be carried out to gauge sensitivity of the errors due to heterogeneous refractive index domains. The simulations of a light ray propagating from a laser tracker would be the same as currently presented, however the way in which the errors are calculated would need to be updated for the new optical based metrology system as the laser trackers use distance and angle. In terms of the inversion algorithm, the code would also need to be modified to trace the rays emitted from the laser tracker and calculate the errors associated with this. The main barrier to deploying this using the original method detailed in Chapter 4 is the robustness of the ray tracing algorithm within the forward model. As mentioned in Chapter 4 this method uses FMM to firstly get the time field then finds the path between the camera and the reflector. This method is not robust and since one of the laser tracker outputs is distance the ray paths output by the forward model would be subject to large errors and as a result this would need addressed. In addition the objective function would need to be updated, and as mentioned previously laser trackers use distance and angle in the measurements, so it would be necessary to come up with some sort of weighted objective function, which is not currently implemented.

References

[1] UK Robotics and Autonomous Systems Network, “Manufacturing robotics: The next robotic industrial revolution,” 2016. [Online]. Available: `https://www.ukras.org/wp-content/uploads/2018/10/UK_RAS_wp_manufacturing_web.pdf`, Accessed 2019-08-20.

[2] F. Tobe, “IFR predicts 15 percent industrial robot growth throughout 2018,” 2015. *The Robot Report* [Online]. Available: `https://www.therobotreport.com/news/ifr-predicts-15-industrial-robot-growth-through-2018`, Accessed 2019-08-20.

[3] M. R. Pedersen, L. Nalpantidis, R. S. Andersen, C. Schou, S. Bøgh, V. Krüger, and O. Madsen, “Robot skills for manufacturing: From concept to industrial deployment,” *Robotics and Computer-Integrated Manufacturing*, vol. 37, pp. 282–291, 2016.

[4] H. Park and N. Tran, "An autonomous manufacturing system for adapting to disturbances," *The International Journal of Advanced Manufacturing Technology*, vol. 56, no. 9-12, pp. 1159–1165, 2011.

[5] W. Estler, K. Edmundson, G. Peggs, and D. Parker, "Large-scale metrology–an update," *CIRP Annals-Manufacturing Technology*, vol. 51, no. 2, pp. 587–609, 2002.

[6] International Federation of Robotics, "Robot density rises globally," 2018. [Online]. Available: `https://ifr.org/ifr-press-releases/news/robot-density-rises-globally`, Accessed: 2019-05-23.

[7] Staffing Industry Analysts (SIA), "UK- millions of workers fear robots will take their jobs," 2018. [Online]. Available: `https://www2.staffingindustry.com/eng/Editorial/Daily-News/UK-Millions-of-workers-fear-robots-will-take-their-jobs-study-finds-46974`, Accessed: 2019-05-23.

[8] G. Graetz and G. Michaels, "Robots at work: the impact on productivity and jobs," *The Magazine for Economic Performance*, vol. 447, pp. 13–15, 2015.

[9] M. Muro and S. Andes, "Robots seem to be improving productivity, not costing jobs," 2015. [Online]. Available: `https://hbr.org/2015/06/robots-seem-to-be-improving-productivity-not-costing-jobs`, Accessed 2019-08-20.

[10] M. Rigby, "Future-proofing UK manufacturing: Current investment trends and future opportunities in robotic automation," *Barclays Development Economics*, 2015.

[11] A. Ghosal, *Robotics: fundamental concepts and analysis*. New Dehli, India: Oxford University Press, 2006.

[12] G. M. Mair, *Industrial robotics*. Hertforshire, UK: Prentice Hall, 1988.

[13] T. Bajd, M. Mihelj, J. Lenarčič, A. Stanovnik, and M. Munih, *Robotics*, vol. 43. New York, USA: Springer Science & Business Media, 2010.

[14] J. N. Pires, A. Loureiro, T. Godinho, P. Ferreira, B. Fernando, and J. Morgado, "Welding robots," *IEEE robotics & automation magazine*, vol. 10, no. 2, pp. 45–55, 2003.

[15] M. Abderrahim, C. Balaguer, A. Giménez, J. M. Pastor, and V. Padron, "Roma: A climbing robot for inspection operations," in *Proceedings 1999 IEEE International Conference on Robotics and Automation*, vol. 3, (Detroit, Michigan, USA), pp. 2303–2308, IEEE, 10 – 15 May 1999.

[16] E. Guizzo, "Your next t-shirt will be made by a robot," *IEEE Spectrum*, vol. 55, no. 1, pp. 50–57, 2018.

[17] D. Graham-Rowe, "Robot tailoring: stitched by the sewbot," *New Scientist*, vol. 210, no. 2817, pp. 46–49, 2011.

[18] P. Aronin, "Ultrasonic sewing robots to transform the clothing industry," *Sastra Robotics*, 2018.

[19] W. Wannasuphoprasit, R. B. Gillespie, J. E. Colgate, and M. A. Peshkin, "Cobot control," in *Proceedings of International Conference on Robotics and Automation*, vol. 4, (Albuquerque, New Mexico, USA), pp. 3571–3576, IEEE, 20–25 Apr 1997.

[20] KUKA Robotics, "Cobots in industry," 2018. [Online]. Available: `https://www.kuka.com/en-gb/technologies/industrie-4-0/industrie-4-0-cobots-in-industry`, Accessed: 2019-05-23.

[21] Measurement Sciences Conference, "History of metrology," 2019. [Online]. Available: `https://msc-conf.com/history-of-metrology/`, Accessed: 2019-08-20.

[22] N. Raghavendra and L. Krishnamurthy, *Engineering metrology and measurements.* Oxford, UK: Oxford University Press, 2013.

[23] I. M. Mills, P. J. Mohr, T. J. Quinn, B. N. Taylor, and E. R. Williams, "Redefinition of the kilogram, ampere, kelvin and mole: a proposed approach to implementing CIPM recommendation 1 (CI-2005)," *Metrologia*, vol. 43, no. 3, p. 227, 2006.

[24] R. Davis, "An introduction to the revised international system of units (SI)," *IEEE Instrumentation & Measurement Magazine*, vol. 22, no. 3, pp. 4–8, 2019.

[25] A. Grous, *Applied metrology for manufacturing engineering.* Hoboken, New Jersey, USA: John Wiley & Sons, 2013.

[26] T. M. Adams, “G104-A2LA guide for estimation of measurement uncertainty in testing,” *American Association of Laboratory Accreditation Manual*, vol. 10, p. 1, 2002.

[27] A. Yazici, U. Yayan, and H. Yücel, “An ultrasonic based indoor positioning system,” in *2011 International Symposium on Innovations in Intelligent Systems and Applications*, (Istanbul, Turkey), pp. 585–589, IEEE, 15–18 Jun 2011.

[28] J. Qi and G.-P. Liu, “A robust high-accuracy ultrasound indoor positioning system based on a wireless sensor network,” *Sensors*, vol. 17, no. 11, p. 2554, 2017.

[29] S. Lacroix, A. Mallet, D. Bonnafous, G. Bauzil, S. Fleury, M. Herrb, and R. Chatila, “Autonomous rover navigation on unknown terrains: Functions and integration,” *The International Journal of Robotics Research*, vol. 21, no. 10-11, pp. 917–942, 2002.

[30] P. Lamon, *3D-position Tracking and Control for All-terrain Robots*, vol. 43. Berlin, Germany: Springer Tracts in Advanced Robotics, 2008.

[31] M. Ben-Ari and F. Mondada, *Elements of robotics.* Berlin, Germany: Springer-Verlag, 2018.

[32] S. Liu, L. Li, J. Tang, S. Wu, and J.-L. Gaudiot, “Creating autonomous vehicle systems,” *Synthesis Lectures on Computer Science*, vol. 6, no. 1, pp. i–186, 2017.

[33] D. C. Williams, *Optical methods in engineering metrology.* London, UK: Chapman and Hall, 1993.

[34] G. Peggs, P. G. Maropoulos, E. Hughes, A. Forbes, S. Robson, M. Ziebart, and B. Muralikrishnan, "Recent developments in large-scale dimensional metrology," *Proceedings of the Institution of Mechanical Engineers, Part B: Journal of Engineering Manufacture*, vol. 223, no. 6, pp. 571–595, 2009.

[35] B. Hughes, A. Forbes, A. Lewis, W. Sun, D. Veal, and K. Nasr, "Laser tracker error determination using a network measurement," *Measurement Science and Technology*, vol. 22, no. 4, p. 45103, 2011.

[36] K. C. Lau and R. J. Hocken, "Three and five axis laser tracking systems," Dec. 22 1987. US Patent 4,714,339.

[37] W. Cuypers, N. Van Gestel, A. Voet, J.-P. Kruth, J. Mingneau, and P. Bleys, "Optical measurement techniques for mobile and large-scale dimensional metrology," *Optics and Lasers in Engineering*, vol. 47, no. 3-4, pp. 292–300, 2009.

[38] B. Muralikrishnan, S. Phillips, and D. Sawyer, "Laser trackers for large-scale dimensional metrology: A review," *Precision Engineering*, vol. 44, pp. 13–28, 2016.

[39] T. Luhmann, S. Robson, S. Kyle, and J. Boehm, *Close-range photogrammetry and 3D imaging.* Berlin, Germany: Walter de Gruyter, 2 ed., 2014.

[40] Zygo Optics Business Segment, "Corner cube retroreflectors." [Online]. Available: `http://www.zygo.com/?/opt/components/cornercuberetroreflectors/` Accessed 2019-08-22.

[41] AT401, Leica Absolute Tracker, "ASME B89. 4.19-2006 specifications," 2014. [Online], Available: `https://www.geotech.sk/downloads/Totalne-stanice/AT401/AT401_ASME_specifikacie_presnosti_en.pdf` Accessed 2019-08-22.

[42] American National Standards Institute B89.4.19-2006, *Performance Evaluation of Laser-based Spherical Coordinate Measurement Systems.* New York, USA: American Society of Mechanical Engineers, 2006.

[43] L. B. Brown, D. N. Wells, and J. B. Merry, "Tracking laser interferometer," Dec. 13 1988. US Patent 4,790,651.

[44] Z. C. Z. J. T. Wenyan, "Application of laser tracker on geometric parameters measurement of large dimensional workpieces," *Tool Engineering*, vol. 5, p. 11, 2002.

[45] A. Nüchter, H. Surmann, K. Lingemann, and J. Hertzberg, "Consistent 3D model construction with autonomous mobile robots," in *Advances in Artificial Intelligence*, vol. 2821, pp. 550–564, Berlin, Germany: Springer, 2003.

[46] T. Schenk, "Introduction to photogrammetry," *Department of Civil and Environmental Engineering and Geodetic Science, The Ohio State University, Columbus, Ohio, USA*, 2005.

[47] W. Linder, *Digital photogrammetry.* Berlin, Germany: Springer, 2009.

[48] R. I. Hartley and P. Sturm, "Triangulation," *Computer Vision and Image Understanding*, vol. 68, no. 2, pp. 146–157, 1997.

[49] Geodetic Systems, "Basics of Photogrammetry," 2019. [Online]. Available: `https://www.geodetic.com/basics-of-photogrammetry/#basics-photogrammetry-_Triangulation` Accessed 2019-12-19.

[50] M. R. Shortis, T. A. Clarke, and T. Short, "Comparison of some techniques for the subpixel location of discrete target images," in *Videometrics III*, vol. 2350, pp. 239–250, International Society for Optics and Photonics, 1994.

[51] D. Brown, "A large format, microprocessor controlled film camera optimized for industrial photogrammetry," in *XV International Congress of Photogrammetry and Remote Sensing, Commission V, 29p., Rio de Janerio, Brazil*, 1984.

[52] R. Dosil, X. Pardo, X. Fdez-Vidal, A. García, and V. Leboran, "A new multiresolution blob detector applied to photogrammetry," pp. 109–116, 01 2010.

[53] T. Luhmann, “Close range photogrammetry for industrial applications,” *ISPRS Journal of Photogrammetry and Remote Sensing*, vol. 65, no. 6, pp. 558–569, 2010.

[54] J. Valença, E. Julio, and H. Araujo, “Applications of photogrammetry to structural assessment,” *Experimental Techniques*, vol. 36, no. 5, pp. 71–81, 2012.

[55] Geodetic Systems, “Picture Perfect Measurements: Why V-STARS?,” 2016. [Online]. Available: `https://www.geodetic.com/v-stars/` Accessed 2019-08-22.

[56] R. Summan, S. Pierce, C. Macleod, G. Dobie, T. Gears, W. Lester, P. Pritchett, and P. Smyth, “Spatial calibration of large volume photogrammetry based metrology systems,” *Measurement*, vol. 68, pp. 189–200, 2015.

[57] A. Lewis, G. Hilley, and J. L. Lewicki, “Integrated thermal infrared imaging and structure-from-motion photogrammetry to map apparent temperature and radiant hydrothermal heat flux at mammoth mountain, CA, USA,” *Journal of Volcanology and Geothermal Research*, vol. 303, pp. 16–24, 2015.

[58] H. Handel, “Analyzing the influences of camera warm-up effects on image acquisition,” in *Asian Conference on Computer Vision*, vol. 4844, pp. 258–268, Springer, 2007.

[59] M. Daakir, Y. Zhou, M. P. Deseilligny, C. Thom, O. Martin, and E. Rupnik, “Improvement of photogrammetric accuracy by modeling and correcting the thermal effect on camera calibration,” *ISPRS journal of photogrammetry and remote sensing*, vol. 148, pp. 142–155, 2019.

[60] K. M. Nasr, B. Hughes, A. Forbes, and A. Lewis, “Determination of laser tracker angle encoder errors,” in *EPJ Web of Conferences*, vol. 77, EDP Sciences, 2014.

[61] M. Holá, J. Hrabina, M. Sarbort, J. Oulehla, O. Cíp, and J. Lazar, “Contribution of the refractive index fluctuations to the length noise in displacement interferometry,” *Measurement Science Review*, vol. 15, no. 5, pp. 263–267, 2015.

[62] L. Yan, B. Chen, C. Zhang, Y. Liu, W. Dong, and C. Li, “Measurement of air refractive index fluctuation based on a laser synthetic wavelength interferometer,” *Measurement Science and Technology*, vol. 25, no. 9, p. 095006, 2014.

[63] A. Lewis, “LUMINAR: Large volume in industry.” National Physical Laboratory, London, 2016. [Online]. Available: `http://projects.npl.co.uk/luminar/`, Accessed 2019-08-20.

[64] S. Robson, L. MacDonald, S. Kyle, and M. R. Shortis, “Close range calibration of long focal length lenses in a changing environment,” *International Archives of the Photogrammetry, Remote Sensing & Spatial Information Sciences*, vol. 41, pp. 115–122, 2016.

[65] J. Palmateer, "Effect of stratified thermal gradients on measurement accuracy with application to tracking interferometer and theodolite measurement," in *7th International Metrology Conference*, Metrologie, 1995.

[66] S. Kyle, S. Robson, L. Macdonald, and M. Shortis, "Compensating for the effects of refraction in photogrammetric metrology," in *14th International Workshop on Accelerator Alignment*, (Grenoble, France), 3–7 Oct 2016.

[67] P. Schellekens, G. Wilkening, F. Reinboth, M. Downs, K. Birch, and J. Spronck, "Measurements of the refractive index of air using interference refractometers," *Metrologia*, vol. 22, no. 4, pp. 279–287, 1986.

[68] P. E. Ciddor, "Refractive index of air: new equations for the visible and near infrared," *Applied Optics*, vol. 35, no. 9, pp. 1566–1573, 1996.

[69] B. Edlén, "The refractive index of air," *Metrologia*, vol. 2, no. 2, pp. 71–80, 1966.

[70] K. P. Birch and M. J. Downs, "An Updated Edlen Equation for the Refractive Index of Air," *Metrologia*, vol. 30, pp. 155–162, 1993.

[71] G. Bönsch and E. Potulski, "Measurement of the refractive index of air and comparison with modified Edlén's formulae," *Metrologia*, vol. 35, no. 2, pp. 133–139, 1998.

[72] L. Yan, B. Chen, E. Zhang, S. Zhang, and Y. Yang, "Precision measurement of refractive index of air based on laser synthetic wavelength interferometry with Edlén equation estimation," *Review of Scientific Instruments*, vol. 86, no. 8, p. 085111, 2015.

[73] M. Born and E. Wolf, *Principles of optics: electromagnetic theory of propagation, interference and diffraction of light.* Cambridge, UK: Cambridge University Press, 7 ed., 1999.

[74] D. Williams and H. Kahmen, "Two wavelength angular refraction measurement," in *Geodetic Refraction*, pp. 7–31, Berlin, Germany: Springer, 1984.

[75] S. Gasilov, A. Mittone, E. Brun, A. Bravin, S. Grandl, and P. Coan, "On the possibility of quantitative refractive-index tomography of large biomedical samples with hard X-rays," *Biomedical optics express*, vol. 4, no. 9, pp. 1512–1518, 2013.

[76] M. Sheik-Bahae, A. A. Said, and E. W. Van Stryland, "High-sensitivity, single-beam n_2 measurements," *Optics letters*, vol. 14, no. 17, pp. 955–957, 1989.

[77] P. Hosseini, Y. Sung, Y. Choi, N. Lue, Z. Yaqoob, and P. So, "Scanning color optical tomography (SCOT)," *Optics express*, vol. 23, no. 15, pp. 19752–19762, 2015.

[78] I. Ihrke, *Reconstruction and rendering of time-varying natural phenomena.* PhD thesis, Natural Science and Technology Facility at The University of Saarland, Germany, 2008.

[79] H. J. Kang, B. J. Chun, Y. Jang, Y. Kim, and S. Kim, "Real-time compensation of the refractive index of air in distance measurement," *Optics Express*, vol. 23, no. 20, pp. 26377–26385, 2015.

[80] T. Sun, Q. Ye, X. Wang, J. Wang, Z. Deng, S. Liu, Q. Yang, J. Mei, W. Zhou, C. Zhang, and J. Tian, "Time dependent detection of the refractive index distribution of nonlinear optical materials," *IEEE Photonics Technology Letters*, vol. 28, no. c, pp. 260–263, 2015.

[81] F. Charrière, A. Marian, F. Montfort, J. Kuehn, T. Colomb, E. Cuche, P. Marquet, and C. Depeursinge, "Cell refractive index tomography by digital holographic microscopy," *Optics Letters*, vol. 31, no. 2, pp. 178–180, 2006.

[82] A. Zvyagin, K. K. M. B. Silva, S. Alexandrov, T. Hillman, J. Armstrong, T. Tsuzuki, and D. Sampson, "Refractive index tomography of turbid media by bifocal optical coherence refractometry.," *Optics Express*, vol. 11, no. 25, pp. 3503–3517, 2003.

[83] Z. Kam, B. Hanser, M. Gustafsson, D. Agard, and J. Sedat, "Computational adaptive optics for live three-dimensional biological imaging," *Proceedings of the National Academy of Sciences*, vol. 98, no. 7, pp. 3790–3795, 2001.

[84] K. Meiners-Hagen and A. Abou-Zeid, "Refractive index determination in length measurement by two-colour interferometry," *Measurement Science and Technology*, vol. 19, no. 8, p. 084004, 2008.

[85] A. Belashov, N. Petrov, and I. Semenova, "Accuracy of image-plane holographic tomography with filtered backprojection: random and systematic errors," *Applied Optics*, vol. 55, no. 1, pp. 81–88, 2016.

[86] M. Bertero and P. Boccacci, *Introduction to inverse problems in imaging.* Boca Raton, Florida, USA: CRC Press, 1998.

[87] C. W. Groetsch, *Inverse problems: Activities for undergraduates.* Washington, DC, USA: The Mathematical Association of America, 1999.

[88] A. L. Bukhgeuim, *Introduction to the theory of inverse problems.* Berlin, Germany: Walter de Gruyter, 2000.

[89] S. I. Kabanikhin, "Definitions and examples of inverse and ill-posed problems," *Journal of Inverse and Ill-Posed Problems*, vol. 16, no. 4, pp. 317–357, 2008.

[90] K. M. M. Tant, E. Galetti, A. Curtis, A. J. Mulholland, and A. Gachagan, "A transdimensional Bayesian approach to ultrasonic travel-time tomography for non-destructive testing," *Inverse Problems*, vol. 34, no. 9, p. 095002, 2018.

[91] G. Uhlmann, *Inside out: inverse problems and applications*, vol. 47. Cambridge, UK: Cambridge University Press, 2003.

[92] F. Natterer, "The mathematics of computerized tomography," in *Classics in applied mathematics*, Philadelphia, Pennsylvania, USA: SIAM, 2001.

[93] A. Staniforth and J. Thuburn, "Horizontal grids for global weather and climate prediction models: a review," *Quarterly Journal of the Royal Meteorological Society*, vol. 138, no. 662, pp. 1–26, 2012.

[94] P. A. Ullrich, P. H. Lauritzen, and C. Jablonowski, "Geometrically exact conservative remapping (GECoRe): regular latitude–longitude and cubed-sphere grids," *Monthly Weather Review*, vol. 137, no. 6, pp. 1721–1741, 2009.

[95] T. Bodin, M. Sambridge, and K. Gallagher, "A self-parametrizing partition model approach to tomographic inverse problems," *Inverse Problems*, vol. 25, no. 5, p. 055009, 2009.

[96] G. Voronoï, "Nouvelles applications des paramètres continus à la théorie des formes quadratiques. deuxième mémoire. recherches sur les parallélloèdres primitifs.," *Journal für die reine und angewandte Mathematik*, vol. 134, pp. 198–287, 1908.

[97] A. Okabe, B. Boots, K. Sugihara, and S. N. Chiu, *Spatial tessellations: concepts and applications of Voronoi diagrams.* West Sussex, UK: John Wiley & Sons, 2 ed., 2009.

[98] T. M. Liebling and L. Pournin, “Voronoi diagrams and Delaunay triangulations: Ubiquitous siamese twins,” *Documenta Mathematica Extra volume: Optimization stories*, pp. 419–431, 2012.

[99] E. B. Kurt Mehlhorn, Michael Sagraloff, “Computational Geometry and Geometric Computing: Triangulations ,” *Max Planck Institut, Informatik, Saarbrücken, Germany*, 2009.

[100] T. Bodin and M. Sambridge, “Seismic tomography with the reversible jump algorithm,” *Geophysical Journal International*, vol. 178, no. 3, pp. 1411–1436, 2009.

[101] E. Galetti and A. Curtis, “Transdimensional electrical resistivity tomography,” *Journal of Geophysical Research: Solid Earth*, vol. 123, no. 8, pp. 6347–6377, 2018.

[102] M. Bock, A. K. Tyagi, J.-U. Kreft, and W. Alt, “Generalized Voronoi Tessellation as a Model of Two-dimensional Cell Tissue Dynamics,” *Bulletin of Mathematical Biology*, vol. 72, no. 7, pp. 1696–1731, 2010.

[103] M. Lee and D. Han, “Voronoi tessellation based interpolation method for wi-fi radio map construction,” *IEEE Communications Letters*, vol. 16, no. 3, pp. 404–407, 2012.

[104] J. Snow, “On the mode of communication of cholera,” in *On the mode of communication of cholera*, New York, USA: The Commonwealth Fund, 1903.

[105] L. Ju, T. Ringler, and M. Gunzburger, “Voronoi tessellations and their application to climate and global modeling,” in *Numerical techniques for global atmospheric models*, pp. 313–342, Springer, 2011.

[106] J. Belhadj, T. Romary, A. Gesret, M. Noble, and B. Figliuzzi, “New parameterizations for bayesian seismic tomography,” *Inverse Problems*, vol. 34, no. 6, p. 065007, 2018.

[107] D. M. Mount, “Computational Geometry CMSC 754: Fortune’s Algorithm and Voronoi diagrams,” 2002. [Online]. Available: `http://www.cs.umd.edu/~mount/754/Lects/754lects.pdf`, Accessed 2019-08-23.

[108] L. D. Landau and E. Lifshitz, *The classical theory of fields*, vol. 2. 4 ed.

[109] Multiphysics 5.3a, COMSOL, “COMSOL multiphysics user guide - Ray Optics Interface,” *COMSOL, AB*, 2017.

[110] N. Rawlinson and M. Sambridge, “Wave front evolution in strongly heterogeneous layered media using the fast marching method,” *Geophysical Journal International*, vol. 156, no. 3, pp. 631–647, 2004.

[111] M. S. Hassouna, A. E. Abdel-Hakim, and A. A. Farag, “Robust robotic path planning using level sets,” in *IEEE International Conference on Image Processing 2005*, vol. 3, (Genova, Italy), IEEE, 14 Sept 2005.

[112] K. Siddiqi, A. Tannenbaum, and S. W. Zucker, “A hamiltonian approach to the Eikonal equation,” in *Energy Minimization Methods in Computer Vision and Pattern Recognition*, vol. 1654, pp. 1–13, York, UK: Springer Berlin Heidelberg, 1999.

[113] M. S. Hassouna and A. A. Farag, “Multistencils fast marching methods: A highly accurate solution to the eikonal equation on cartesian domains,” *IEEE transactions on pattern analysis and machine intelligence*, vol. 29, no. 9, pp. 1563–1574, 2007.

[114] J. A. Sethian, “A fast marching level set method for monotonically advancing fronts,” *Proceedings of the National Academy of Sciences*, vol. 93, no. 4, pp. 1591–1595, 1996.

[115] M. Cavazzuti, *Optimization methods: from theory to design scientific and technological aspects in mechanics.* Berlin, Germany: Springer Science & Business Media, 2012.

[116] Y. Eren, İ. B. Küçükdemiral, and İ. Üstoğlu, “Introduction to optimization,” in *Optimization in Renewable Energy Systems: Recent Perspectives*, pp. 27–74, Oxford, UK: Elsevier, 2017.

[117] U. Diwekar, *Introduction to applied optimization*, vol. 22. Berlin, Germany: Springer Science & Business Media, 2 ed., 2008.

[118] D. B. Shmoys and C. Swamy, “Stochastic optimization is (almost) as easy as deterministic optimization,” in *45th Annual IEEE Symposium on Foundations of Computer Science*, pp. 228–237, IEEE, 2004.

[119] M.-H. Lin, J. F. Tsai, and C. Yu, “A review of deterministic optimization methods in engineering and management,” *Mathematical Problems in Engineering*, vol. 2012, 2012.

[120] G. B. Dantzig and M. N. Thapa, *Linear programming 1: introduction.* New York, USA: Springer Science & Business Media, 2006.

[121] D. Aleksendric and P. Carlone, *Soft Computing in the Design and Manufacturing of Composite Materials: Applications to Brake Friction and Thermoset Matrix Composites.* Cambridge, UK: Woodhead Publishing, 2015.

[122] G. R. Liu and X. Han, *Computational inverse techniques in nondestructive evaluation.* Boca Raton, Florida, USA: CRC Press, 2003.

[123] M. Mitchell, *An introduction to genetic algorithms.* Cambridge, Massachusetts, USA: MIT Press, 1998.

[124] W. R. Gilks, S. Richardson, and D. Spiegelhalter, *Markov chain Monte Carlo in practice.* New York, USA: Chapman and Hall/CRC, 1995.

[125] J. A. Rice, *Mathematical statistics and data analysis.* Belmont, California, USA: Thomson Brooks/Cole, 3 ed., 2007.

[126] K. R. Koch, *Introduction to Bayesian statistics.* Berlin, Germany: Springer Science & Business Media, 2 ed., 2007.

[127] N. Metropolis, A. W. Rosenbluth, M. N. Rosenbluth, A. H. Teller, and E. Teller, “Equation of state calculations by fast computing machines,” *The Journal of Chemical Physics*, vol. 21, no. 6, pp. 1087–1092, 1953.

[128] W. K. Hastings, “Monte Carlo sampling methods using Markov chains and their applications,” *Biometrika*, vol. 57, no. 1, pp. 97–109, 1970.

[129] D. Van Ravenzwaaij, P. Cassey, and S. D. Brown, “A simple introduction to Markov Chain Monte–Carlo sampling,” *Psychonomic bulletin & review*, vol. 25, no. 1, pp. 143–154, 2018.

[130] T. Bodin, M. Sambridge, and K. Gallagher, “A self-parametrizing partition model approach to tomographic inverse problems,” *Inverse Problems*, vol. 25, no. 5, 2009.

[131] E. Galetti, A. Curtis, B. Baptie, D. Jenkins, and H. Nicolson, “Transdimensional love-wave tomography of the british isles and shear-velocity structure of the east irish sea basin from ambient-noise interferometry,” *Geophysical Journal International*, vol. 208, no. 1, pp. 36–58, 2016.

[132] N. Rawlinson and M. Sambridge, “The fast marching method: an effective tool for tomographic imaging and tracking multiple phases in complex layered media,” *Exploration Geophysics*, vol. 36, no. 4, pp. 341–350, 2005.

[133] A. Miller, A. J. Mulholland, S. G. Pierce, B. Hughes, and A. B. Forbes, "Positional uncertainty in optical-based metrology systems in large volume manufacturing," *ACTA IMEKO*, 2018.

[134] A. Miller, A. Mulholland, S. Tant, K.M.M. Pierce, B. Hughes, and A. Forbes, "Reconstruction of refractive index maps using photogrammetry," *Inverse Problems in Science and Engineering (IPSE).* In Press.

[135] COMSOL, *COMSOL Multiphysics: Version 5.3a.* COMSOL, 2018.

[136] J. Stone and J. Zimmerman, "Index of refraction of air: Vacuum wavelength and ambient conditions based on the Ciddor equation," 2017. National Institute of Standards and Technology [Online]. Available: `http://emtoolbox.nist.gov/Wavelength/Ciddor.asp`, Accessed 2019-08-20.

[137] Microchip, "MCP9808: ±0.5°C Maximum Accuracy Digital Temperature Sensor Data Sheet ," 2011. [Online]. Available: `http://ww1.microchip.com/downloads/en/DeviceDoc/25095A.pdf`, Accessed 2016-11-11.

[138] Edmund Optics, "Understanding focal length and field of view," 2017. [Online]. Available: `https://www.edmundoptics.com/resources/application-notes/imaging/understanding-focal-length-and-field-of-view/`, Accessed 2017-03-09.

[139] Vicon, “Vicon T series Datasheet,” 2017. [Online]. Available: `https://www.vicon.com/downloads/documentation/go-further-with-vicon-mx-t-series`, Accessed 2019-08-23.

[140] P. J. Green, “Reversible jump Markov Chain Monte Carlo computation and Bayesian model determination,” *Biometrika*, vol. 82, pp. 711–732, 1995.

[141] J. A. Sethian, “Theory, algorithms, and applications of level set methods for propagating interfaces,” *Acta Numerica*, vol. 5, pp. 309–395, 1996.

[142] E. W. Dijkstra, “A note on two problems in connexion with graphs,” *Numerische mathematik*, vol. 1, no. 1, pp. 269–271, 1959.

[143] A. Gelman, G. O. Roberts, and W. R. Gilks, “Efficient Metropolis jumping rules,” in *Bayesian statistics 5*, vol. 5, pp. 599–607, Oxford, UK: Oxford University Press, 1996.

[144] The MathWorks, Inc., “MATLAB and Statistics Toolbox Release 2017b,” 2017. Massachusetts, USA.

[145] NIST, “NIST guide to the SI,” 2016. [Online]. Available: `http://www.nist.gov/pml/pubs/sp811/sec01.cfm` Accessed: 2016-06-15.